Inner disk dynamics of classical T Tauri stars in NGC 2264

Pauline Telles McGinnis Guimarães

Universidade Federal de Minas Gerais - UFMG
Instituto de Ciências Exatas - ICEx
Programa de Pós Graduação em Física

Inner disk dynamics of classical T Tauri stars in NGC 2264

Pauline Telles McGinnis Guimarães

Advisor: Prof. Dr. Sílvia Helena Paixão Alencar, UFMG, Brazil
Co-advisor: Dr. Catherine Dougados, IPAG, France

Tese apresentada ao departamento de Física da Universidade Federal de Minas Gerais, como requisito parcial para obtenção de grau de Doutora em Física
Área de Concentração: Astrofísica

2017

Acknowledgments

This thesis could not have been developed by one person alone. It required investment, support and guidance of many kinds.

First and foremost, I would like to thank Silvia for being not only the best adviser I could hope for, but also a good friend. Thank you for the constant support and for always making me realize how much I progressed when it felt like I was getting nowhere. I could not have come as far as I have without such a great adviser. I would also like to thank Catherine for taking me in with so much enthusiasm in Grenoble and for helping to make the semester I was there such a pleasant and productive one. I've been very lucky to have had these two amazing women who I admire to advise me.

During my doctorate, I've also had the pleasure to work alongside many other wonderful scientists and to learn from them. I hope I've been able to absorb some of their knowledge in the process. I would like to thank them all for the fruitful discussions, especially Jérôme Bouvier and John Stauffer, whose suggestions contributed greatly to the quality of this work. I would also like to thank the CSI2264 team, and everyone who was involved in planning, observing and reducing the fantastic data that I've had the privilege to use in this work.

I thank the physics department at UFMG for the opportunity to develop this thesis, IPAG for receiving me and offering me the support I needed to develop part of it there, and the physics department at UFS for fostering me during my visits. I thank CNPq, CAPES and FAPEMIG for the financial support that allowed for all of this.

Finally, I am nothing without the people who surround me. To my family, thank you for the love, the laughter and all the support. Needless to say, I wouldn't be who I am or where I am without you. To my friends from CSA, my sisters, thank you for always being there when I need you. I thank all my friends in the physics department for the wonderful times, my friends in the lab for making it my second home throughout the years, the friends I made in Grenoble for making my stay that much more fun, the friends I've made at UFS for making me feel welcome, and all the other friends I have who are too many to name.

To Marcelo, my partner in life, my best friend, my eternal counselor. Thank you for the support and for the wonderful life we share. And to my dog, Doze, and my cats, Kiwi and Mia, for the licks and purrs that help me get through stressful times.

Resumo

O aglomerado jovem NGC 2264 é uma região de formação estelar rica, contendo centenas de estrelas jovens de baixa massa com indícios de acreção, chamadas de estrelas T Tauri clássicas (ETTC). Em Dezembro de 2011, este aglomerado foi observado simultaneamente com os satélites CoRoT e *Spitzer*, assim como quase-simultaneamente com vários telescópios no solo, como o CFHT e o VLT, usando o espectrógrafo de multi-objetos FLAMES na faixa espectral que cobre a linha Hα (forte indicador de acreção). NGC 2264 também já foi observado previamente com o CoRoT em Março de 2008 e foi alvo de uma nova campanha do FLAMES em 2014, centrada na linha de emissão proibida [OI] 6300Å, conhecida por traçar jatos e ventos em estrelas jovens. O objetivo desta tese é aproveitar da riqueza de dados disponíveis de NGC 2264 para investigar a dinâmica da parte interna de discos circum-estelares de ETTCs e, com isso, buscar entender melhor os processos de acreção e ejeção de massa que ali ocorrem.

Na primeira parte deste trabalho, investigamos um grupo de ETTCs que apresentam variabilidade fotométrica devido à extinção por material da parte interna do disco. Estes sistemas são observados com altas inclinações e representam uma oportunidade de estudarmos a interação entre a magnetosfera estelar e a parte interna do disco de acreção através de medidas indiretas. Analisamos as curvas de luz simultâneas do CoRoT e do *Spitzer* destes sistemas para investigarmos a distribuição de poeira na região interna do disco e encontramos indícios da presença de grãos maiores que grãos interestelares típicos. Analisamos a variabilidade de velamento nos espectros FLAMES e no índice de cor $u-r$, encontrando em vários casos evidência de manchas quentes associadas a ocultações da fotosfera por material circum-estelar, o que indica que as estruturas responsáveis pelas ocultações podem estar localizadas na base de colunas de acreção. Um modelo de ocultação por uma deformação na parte interna do disco, proposto inicialmente para explicar o comportamento fotométrico da ETTC AA Tau, conseguiu reproduzir os aspectos gerais da maioria das curvas de luz quase periódicas da nossa amostra, encontrando deformações de altura máxima e extensão azimutal semelhantes àquela que foi encontrada para AA Tau. Atribuímos a variabilidade do tipo de AA Tau a um regime de acreção estável e variabilidade semelhante, porém não-periódica, a um regime de acreção instável. Vemos indícios de que uma transição, e até mesmo certa coexistência, entre os dois regimes pode ser comum.

Na segunda parte deste trabalho, investigamos os processos de ejeção através do estudo da linha de emissão proibida de [OI] 6300Å. Separamos a linha de [OI] em três componentes: uma componente de alta velocidade (CAV), uma componente larga de baixa velocidade (CLBV) e uma componente estreita de baixa velocidade (CEBV). Acredita-se que a CAV seja originada em jatos bipolares colimados, porém a origem das componentes de baixa velocidade (CBV) ainda está em debate. Nossas CLBV mostram desvios para o azul consistentes com uma origem em ventos da parte interna do disco. Já foi sugerido que a CEBV seja formada em ventos de fotoevaporação causados pela emissão de raios-X ou radiação UV extrema provenientes do objeto central. Isso é consistente com alguns dos nosso resultados, porém não há evidência suficiente para confirmar este fenômeno. Mostramos que as luminosidades de todas as componentes da linha de [OI] correlacionam positivamente com a luminosidade estelar e de acreção. Também vemos que ETTCs que sofrem acreção no regime instável tendem a apresentam CBV mais largas e CAV mais fortes que aquelas que sofrem acreção no regime estável. Detectamos a CAV apenas entre sistemas com discos internos opticamente espessos, enquanto que a CLBV é encontrada entre alguns sistemas com discos anêmicos e a CEBV é comum entre sistemas com discos internos finos. A razão entre o número de CEBV e CLBV detectadas parece refletir a idade da região de formação estelar, indicando que a CEBV tende a dominar cada vez mais a emissão de [OI] com a evolução do sistema. Também mostramos que propriedades estelares como temperatura efetiva, massa ou rotação estelar não parecem influenciar fortemente a velocidade de propagação ou luminosidade dos jatos, sugerindo que possa ser o disco, e não a estrela, que controla o mecanismo de lançamento dos mesmos.

Palavras-chave: acreção, discos de acreção - ejeção - estrelas: pré-sequência principal - técnicas: fotometria, espectroscopia - aglomerados: NGC 2264

Abstract

The young open cluster NGC 2264 is a rich site of star formation, containing hundreds of young, accreting, low-mass stars known as classical T Tauri stars (CTTS). In December 2011, this cluster was observed simultaneously by the CoRoT and *Spitzer* satellites, as well as quasi-simultaneously by a number of ground-based telescopes, such as the CFHT and the VLT with the FLAMES multi-object spectrograph in a spectral range covering the Hα line (a strong indicator of accretion). NGC 2264 had also been observed previously by CoRoT in March 2008, and it became the target of a new FLAMES campaign in 2014 centered on the forbidden [OI] 6300Å line, a well-known tracer of jets and winds in young stars. The goal of this thesis is to explore the richness of data available for NGC 2264 in order to investigate the dynamics of inner circumstellar disks of CTTSs and, with this, to better understand the processes of mass accretion and mass ejection that occur therein.

In the first part of this work, we investigate a group of CTTSs that present photometric variability indicative of extinction from inner disk material. These systems are viewed at high inclinations and represent an opportunity to study the interaction between the stellar magnetosphere and the inner accretion disk through indirect measurements. We analyze their CoRoT light curves alongside their simultaneous *Spitzer* light curves in order to better understand the dust distribution in the inner disk region, and in this way find indications of the presence of grains larger than typical interstellar grains. We investigate veiling variability in their FLAMES spectra and $u-r$ color variations, and in many cases find evidence of hot spots that are spatially associated with occultations of the stellar photosphere by circumstellar material, indicating that the occulting structures may be located at the base of accretion columns. We find that an occultation model of an inner disk warp, initially proposed to explain the photometric behavior of the CTTS AA Tau, is successful at reproducing the general aspects of most of the quasi-periodic light curves in our sample, finding warps of similar maximum height and azimuthal extension as had been found for AA Tau. We ascribe this AA Tau-like variability to a stable accretion regime and similar but non-periodic variability to an unstable accretion regime. We see indications that a transition, and even certain coexistence, between the two regimes may be common.

In the second part of this work we investigate ejection processes through the forbidden [OI] 6300Å emission line. We separate the [OI] line profiles into three distinct features:

a high-velocity component (HVC), a broad low-velocity component (BLVC), and a narrow low-velocity component (NLVC). The HVC is believed to originate in bipolar, colimated jets, while the origin of the low-velocity components (LVC) is still under debate. Our BLVCs show blueshifts consistent with an origin in inner disk winds. The NLVC has been suggested to arise in X-ray or EUV driven photoevaporative disk winds, which is consistent with some of our findings, but we have insufficient evidence to confirm this. We find that the luminosities of all components correlate positively with the stellar and accretion luminosity. We also find that CTTSs accreting in the unstable regime tend to show broader LVCs and stronger HVCs than stars accreting in the stable regime. We only detect the HVC among systems with optically thick inner disks, while the BLVC is found in a few systems with an anemic disk and the NLVC is common among systems with thin inner disks. The ratio of detected NLVCs to BLVCs seems to reflect the age of the star forming region, indicating that as a system evolves, the NLVC tends to dominate the [OI] emission. We also show that stellar properties such as effective temperature, mass, and stellar rotation, do not seem to influence in a significant way the propagation velocity or luminosity of protostellar jets, and it appears that it is the disk, rather than the star, that governs their launching mechanism.

Keywords: accretion, accretion disks - ejection - stars: pre-main sequence - techniques: photometry, spectroscopy - clusters: NGC 2264

Contents

Resumo I

Abstract III

List of Figures IX

List of Tables X

1 Introduction 1

1.1 Star formation . . . 2

1.2 Classical T Tauri stars . . . 3

1.2.1 Magnetospheric accretion . . . 4

1.2.2 Jets and winds . . . 6

1.3 AA Tau . . . 8

1.4 NGC 2264 . . . 12

1.5 Objectives . . . 14

2 Observations 15

2.1 First CoRoT short run . . . 15

2.2 CSI2264 . . . 16

2.2.1 CoRoT data . . . 16

2.2.2 *Spitzer* IRAC data . . . 16

2.2.3 CFHT MegaCam data . . . 17

2.2.4 USNO data . . . 17

2.2.5 FLAMES spectra centered on Hα . . . 17

2.3 Follow-up FLAMES data from 2013 . . . 19

2.4 FLAMES spectra centered on [OI] 6300Å . . . 20

2.5 Other observations . . . 21

3 The classical T Tauri star population of NGC 2264 23

3.1 Selection of probable members of NGC 2264 . . . 23

3.2 Selection of Classical T Tauri stars . . . 24

3.3 Determination of stellar and accretion parameters . . . 25
3.3.1 Effective temperatures, bolometric luminosities, masses and radii . . . 25
3.3.2 Veiling . . . 28
3.3.3 Rotational velocity projected in our line-of-sight ($v \sin i$) . . . 29
3.3.4 Mass accretion luminosity and mass accretion rate . . . 31
3.4 Photometric variability . . . 32

4 Stars with extinction dominated light curves 41
4.1 Selection of candidates for extinction dominated light curves . . . 42
4.2 Comparing optical and infrared light curves . . . 46
4.3 Color-magnitude diagrams . . . 52
4.4 Variability in the CFHT u and r filters . . . 54
4.5 Veiling variability . . . 58
4.6 Occultation model . . . 64
4.6.1 Co-rotation radii . . . 66
4.6.2 Inclinations . . . 66
4.6.3 Warp parameters and fitted light curves . . . 70
4.6.4 Two occulting structures? . . . 75
4.7 Periodic vs. aperiodic behavior: an indication of accretion regime? . . . 77
4.8 Other characteristics of stars with AA Tau-like light curves . . . 82

5 Spectral signatures of jets and outflows 85
5.1 Recovering the intrinsic [OI] λ6300Å line profile . . . 86
5.1.1 Completion . . . 87
5.1.2 Characterizing [OI] emission line profiles . . . 89
5.2 Line luminosities and correlations with stellar/accretion properties . . . 96
5.2.1 Correlations among [OI] luminosities and stellar/disk properties . . . 97
5.3 Photometric variability and the [OI] line . . . 104
5.4 The low velocity component . . . 107
5.5 The high velocity component . . . 112

6 Conclusions and perspectives 127
6.1 Perspectives . . . 132

A Papers resulting from this thesis 134

B Papers published during the CSI 2264 campaign 158

List of Figures

1.1 Theoretical pre-main sequence tracks in the H-R diagram. 3
1.2 Magnetospheric accretion in CTTSs. 5
1.3 Accretion in the presence of a misalignement between the magnetic and rotation axes. 5
1.4 MHD simultations of the stable and unstable magnetospheric accretion regimes. 6
1.5 Simulation from Zanni & Ferreira (2013) of the star-disk interaction. 8
1.6 AA Tau's light curve and occultation model. 9
1.7 Occultation model proposed for AA Tau. 10
1.8 V-band light curves of AA Tau at different epochs. 10
1.9 Three-color image of NGC 2264. 12
1.10 AA Tau-like light curves found among CTTSs in NGC 2264 by Alencar et al. (2010). 14

2.1 Removal of the nebular contamination from the Hα line in the UVES stellar spectra. 19
2.2 Removal of telluric emission and absorption lines from the stellar spectra centered on [OI]. 21

3.1 Theoretical and observed spectral line ratios. 26
3.2 Comparison of effective temperatures determined using line ratios and spectral types. 27
3.3 Examples of different light curve morphologies found in CTTSs in NGC 2264. 33
3.4 Simultaneous I-band and CoRoT photometry for the AA Tau-like stars Mon-1308 and Mon-250. 34

4.1 Average flux dip depth vs. FWHM/period for AA Tau-like dips and narrow dips. 43
4.2 CoRoT light curves of the stars CSIMon-000056 and CSIMon-001131. 44
4.3 *Spitzer* IRAC 3.6μm and 4.5μm light curves plotted over CoRoT light curves. 47
4.3 Continued. 48
4.3 Continued. 49

4.4 Illustration for anti-correlated optical and infrared light curves. 50
4.5 CoRoT light curves and CoRoT vs. CoRoT-IRAC$_{4.5\mu m}$ color magnitude diagrams of the stars Mon-456, Mon-660, and Mon-1054. 54
4.6 I-band and $u-r$ light curves folded in phase for periodic or quasi-periodic stars. 55
4.6 Continued. 56
4.6 Continued. 57
4.7 CoRoT light curve, Hα line profile, veiling variability, and radial velocity variability of the star Mon-250. 59
4.8 Plots of LiIEW vs. I magnitude for three different stars and their I-band and CoRoT light curves. 62
4.9 Plots of LiIEW vs. I magnitude for the stars in our sample. 63
4.10 Period histogram of CTTSs in NGC 2264 with AA Tau-like or spot-like CoRoT light curves. 68
4.11 Fitted light curves of the star Mon-1308 using an inclination of 55° and 75°. . 70
4.12 Simulated light curves of AA Tau-like stars plotted over CoRoT light curves. 72
4.12 Continued. 73
4.13 2008 CoRoT light curve of Mon-250 and synthetic light curves for two separate accretion funnel flows. 76
4.14 2011 CoRoT light curve of Mon-1054 and fitted light curve of the star Mon-379 in 2011. 77
4.15 Corot light curves of Mon-297 and Mon-774 during their AA Tau phases and aperiodic phases. 79
4.16 CoRoT light curves of Mon-928 in 2008 and 2011. 80
4.17 CoRoT light curves of Mon-297, Mon-456, and Mon-824 during their AA Tau phase. 82
4.18 Mass histograms of CTTSs with CoRoT light curves 83

5.1 Removal of the photospheric contribution from a CTTS spectrum around the [OI] emission line. 86
5.2 HR Diagram of the CTTSs in our sample with detected [OI] emission and without. 88
5.3 Continuum flux at 6300Å vs. T_{eff}, with the peak of the detected [OI] line represented by a color gradient. 90
5.4 Two examples of [OI] emission line profiles found in our sample. 91
5.5 Distribution of FWHM and v_c of all components from all profiles in our sample 92
5.6 Histograms of v_c and FWHM of broad and narrow LVCs ($|v_c| < 30$ km/s) when both are present. 93
5.7 Histograms of v_c and FWHM of BLVCs and HVCs when both are present. . . 94
5.8 Same as Figure 5.6, but with $|v_c| < 50$ km/s. 94

5.9 [OI] line luminosity and luminosity of individual components versus stellar luminosity. . . . 98
5.10 [OI] line luminosity and luminosity of individual components versus accretion luminosity. . . . 99
5.11 [OI] LVC luminosity vs. stellar luminosity and accretion luminosity for our sample and those of R13, N14 and S16. . . . 100
5.12 [OI] line luminosity and luminosity of individual components versus X-ray luminosity. . . . 101
5.13 X-ray luminosity versus stellar luminosity in NGC 2264. . . . 102
5.14 [OI] line luminosity and luminosity of individual components versus the α_{IRAC} index. . . . 103
5.15 [OI] line luminosity and luminosity of individual components versus K-IRAC$_{3.6\mu}$ excess. . . . 103
5.16 Average [OI] line profiles for different types of photometric variability that hint at system inclinations. . . . 105
5.17 Average [OI] line profiles for different types of photometric variability. . . . 106
5.18 BLVC FWHM vs. NLVC FWHM (both normalized by $\sqrt{M_*}$) and BLVC FWHM vs. L_{acc}. . . . 108
5.19 FWHM vs. v_c for NLVCs and BLVCs, with colors indicating inclination or light curve type. . . . 109
5.20 FWHM of the NLVC and BLVC normalized by sqrt(M_*) vs. inclination. . . . 110
5.21 [OI] HVC luminosity vs. stellar mass and mass accretion rate. . . . 113
5.22 [OI] HVC luminosity vs. stellar rotation velocity and Keplerian velocity of the inner disk. . . . 114
5.23 HVC v_c vs. $\cos i$ and deprojected jet velocity vs. Keplerian velocity of the inner disk. . . . 114
5.24 Deprojected jet velocity vs. stellar rotation velocity and stellar mass. . . . 115
5.25 Jet mechanical luminosity vs. accretion luminosity and mass loss rate vs. mass accretion rate. . . . 116
5.26 Gaussian decomposition of the [OI] 6300Å line profiles. . . . 122
5.26 Continued. . . . 123
5.26 Continued. . . . 124
5.26 Continued. . . . 125
5.26 Continued. . . . 126

List of Tables

2.1 Observations from CSI2264 used throughout this work. 16

3.1 Spectral types from the literature and from our analysis with WTTS templates for the stars that showed the largest discrepancy. 29
3.2 Stellar parameters of the CTTSs 35
3.2 Stellar parameters of the CTTSs - continued 36
3.2 Stellar parameters of the CTTSs - continued 37
3.2 Stellar parameters of the CTTSs - continued 38
3.2 Stellar parameters of the CTTSs - continued 39
3.3 Stellar parameters of the WTTSs used as photospheric templates 40

4.1 Stars with AA Tau-like and variable extinction-dominated light curves. . . . 45
4.2 Stellar parameters initially calculated for the AA Tau-like candidates. 67
4.3 Occultation model parameters found for the AA Tau-like candidates. 74

5.1 Information on v_c and FWHM of the different components of the [OI] emission line. 96
5.2 Jet parameters for the stars with detected high-velocity [OI] emission 117
5.3 [OI] 6300Å line luminosities and stellar parameters 118
5.3 [OI] 6300Å line luminosities and stellar parameters - continued 119
5.3 [OI] 6300Å line luminosities and stellar parameters - continued 120
5.3 [OI] 6300Å line luminosities and stellar parameters - continued 121

Chapter 1

Introduction

The subject of star formation has been one of growing interest to astrophysicists in the past decades. One of the strongest motivations in studying young stellar objects (YSOs) is to advance our knowledge of how our own solar system formed, and now with an ever increasing number of known exo-planets, of how such a wide variety of planetary systems are formed. Disentangling the physical processes that dominate the inner region of circumstellar disks around YSOs is one of the major challenges of star formation. Accretion (the flow of circumstellar matter onto a forming star) and outflows (stellar winds, disk winds and protostellar jets) help regulate fundamental stellar properties such as mass and angular momentum, and strongly influence the evolution of circumstellar disks from which planets are formed. Among young, low-mass ($\lesssim 2M_{\odot}$) stars, accretion of matter from the disk to the star is known to take place in the innermost part of the disk (a few 0.1 au from the central object) and is strongly regulated by the interaction between the disk and the stellar magnetic field (Romanova & Owocki 2016). Properties of protostellar jets associated with these low-mass objects also suggest a magnetic origin from the very inner au of the accretion disk (Ferreira et al. 2006; Ray et al. 2007). However, the launching mechanism is not yet well understood, nor is the role of protostellar jets in extracting angular momentum from the star-disk system and their impact on the structure and evolution of the disk.

The inner disk region is where planets have so far been most commonly found[1] (Mayor et al. 2014). Particularly, the current discovery of a Jupiter-sized planet in a close (0.057 au) orbit around a 2Myr-old star (Donati et al. 2016) poses new challenges to our understanding

[1] This is likely due to the strong bias there exists with the two main techniques used to detect exo-planets (i.e., planetary transits and radial velocity measurements) toward finding a planet close to the star.

of planet formation and migration in this region. A strongly magnetized inner disk has serious implications on this matter, therefore it is vital to better understand the dynamics of the inner accretion disk and its interaction with the stellar magnetic field.

1.1 Star formation

Stars are mainly formed in Giant Molecular Cloud (GMC) complexes, structures of typical masses around a few $10^5 M_\odot$ and typical sizes between 50 pc and 100 pc. The gas in these regions is usually distributed in a highly filamentary form, with the existence of many cold, dense ($\gtrsim 10^3 \mathrm{cm}^{-2}$) molecular cloud cores (Hartmann 2009). The process of star formation begins with the collapse of these cores, which occurs when gravity overcomes the resisting forces, such as thermal pressure, turbulent motions, and magnetic fields. This collapse is believed to occur from the inside-out, the central part collapsing first, followed by the outer layers (Shu 1977). Because of the large difference between the dimensions of the core and the final star, any small initial rotational velocity of the cloud core will result in the transfer of a large amount of angular momentum to the forming star. The collapse of a rotating core therefore leads to most of the material depositing onto a flattened surface, rather than onto the central object itself, forming a circumstellar disk. For low-mass stars, most of the matter from this disk is transferred to the central object via disk accretion. Core collapse can also result in fragmentation, leading to the formation of binary or multiple systems (Boss 1995). In these cases a circumstellar disk can form around each star, a circumbinary disk can form around the system, or both may occur.

In the initial stages of collapse, an envelope of dust surrounds the central object and the disk, absorbing radiation emitted from within, making it impossible to observe the central object at optical wavelengths. We refer to these objects as protostars. They are usually detected in the far-infrared, where the stellar radiation absorbed by the surrounding dust is re-emitted (Hartmann 2009). In time (a few 10^5yr), this envelope dissipates and the central object becomes observable at optical wavelengths[2]. These objects are still undergoing gravitational collapse, therefore their radii are larger than the radii of Main Sequence (MS) stars of the same mass. When placed on a Hertzsprung-Russel (HR) diagram, these young objects appear above and to the right of the MS (see Figure 1.1), and for this reason are called Pre-Main Sequence (PMS) stars. During the PMS phase, they evolve on the HR diagram following evolutionary tracks such as the ones shown in Figure 1.1 (Palla 1999). These tracks begin at what is referred to as the birthline, the line that determines where a protostar of a certain mass will first appear on the HR diagram when it becomes optically visible, and end at what is known as the Zero Age Main Sequence (ZAMS), when the right

[2]Unless the star-disk system is observed at such an inclination that the disk is seen edge-on, obscuring the central object. When there is not enough resolution to discern the shape of the disk, this can mimic a protostar.

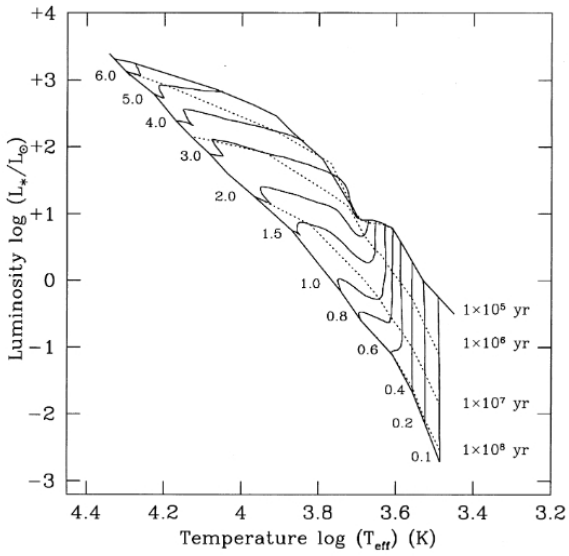

Figure 1.1: Theoretical pre-main sequence tracks in the Hertzsprung-Russel diagram, starting at the birthline (top right solid line) to the ZAMS (bottom left solid line). The numbers beside the ZAMS indicate the stellar mass, in units of $M_{\odot}$, of each evolutionary track. Dotted lines show different isochrones. Figure from Palla & Stahler (1999).

conditions are reached in the object's core for hydrogen fusion to begin and a star is officially born. Before reaching the ZAMS, this object's source of luminosity comes solely from its gravitational collapse (Hartmann 2009).

Pre-Main Sequence objects of low mass ($\lesssim 2M_{\odot}$) are known as T Tauri stars, named after the prototype T Tauri (Joy 1945). They have spectral types M-F, which corresponds to effective temperatures of $T_{eff} \sim 3000 - 7000$K. PMS objects of intermediate mass ($2M_{\odot} \lesssim M_{*} \lesssim 8M_{\odot}$) are known as Herbig Ae/Be stars (Herbig 1960). As the name would suggest, these correspond to A and B-type stars ($T_{eff} \sim 8000 - 30,000$K) with emission lines in their spectra. The name Herbig Ae/Be was adopted in order to avoid confusion with other, more evolved, emission-line A and B-type stars. Stars of higher mass have no observable PMS phase. Their evolution is so rapid that when the envelopes have finished dissipating the stars have already begun hydrogen fusion in their core and are located on the ZAMS (Palla 1999).

1.2 Classical T Tauri stars

T Tauri stars were first identified by Joy (1945) as a type of variable star. They showed irregular photometric variability and broad emission lines, and were found in association with nebulosity. It was the work of Ambartsumian (1947, 1954) that first suggested these were young stars still undergoing gravitational contraction. We now know them to be PMS stars of solar-type masses ($\lesssim 2M_{\odot}$). These stars have been observed to have strong magnetic fields (e.g., Johns-Krull et al. 2001; Donati et al. 2010a, 2011) and X-ray emission (e.g.,

Preibisch et al. 2005; Flaccomio et al. 2006). When they were first discovered, the low spectral resolution made it difficult to detect Hα emission below a certain threshold (equivalent width $\lesssim$ 5 - 10 Å), and all T Tauri stars were thought to have broad emission in this line. With the advancement of X-ray studies in the 1980's, many young stars of late spectral types were found whose optical emission lines were much weaker than the ones classically associated with this class of stars (Hartmann 2009). These then became known as weak-line T Tauri stars (WTTS), and those with broad emission lines became known as classical T Tauri stars (CTTS). The classical T Tauri stars are characterized by broad emission lines, especially in the hydrogen Balmer series; strong ultraviolet (UV) and optical excess compared to a purely photospheric flux; strong excess infrared (IR) flux; and often forbidden emission lines. The weak-line T Tauri stars, on the other hand, present no such characteristics.

1.2.1 Magnetospheric accretion

Magnetospheric accretion models account for most of the observed characteristics of CTTSs (Shu et al. 1994; Hartmann et al. 1994; Muzerolle et al. 2001; Kurosawa et al. 2006; Lima et al. 2010). A schematic picture of the basic principles behind these models is shown in Figure 1.2. Magnetohydrodynamics (MHD) models suggest that the stellar magnetosphere truncates the inner circumstellar disk at a distance of a few stellar radii, where the disk's matter stress equals the magnetic stress (Bessolaz et al. 2008). The material in this region of the disk can no longer move toward the star through the disk plane. Instead, it is forced in the vertical direction and begins to follow the magnetic field lines, leading it to accrete onto the star via what are known as accretion funnel flows (also often called accretion columns). The material accelerated in these funnel flows is adiabatically compressed, heats up and produces the broad emission lines observed in CTTS spectra, such as Hα and Hβ. When the free-falling material reaches the stellar surface, accretion shocks are formed, resulting in the appearance of hot spots that cause the observed UV and optical excess and soft X-ray emission. Other magnetic field lines which are not connected to the disk can produce coronal X-ray emission. Part of the disk material can also be ejected in a disk wind or possibly a bipolar jet, which produces forbidden emission lines. The circumstellar disk emits at IR, sub-mm and mm wavelengths, resulting in a pronounced excess in this part of the spectral energy distribution (SED) of CTTSs.

Magnetohydrodynamics models (e.g., Kulkarni & Romanova 2009; Romanova et al. 2009; Kurosawa & Romanova 2013; Romanova et al. 2013) have proposed that CTTSs can accrete matter from their circumstellar disks through a stable or an unstable regime. In the stable regime, a misalignment between a star's predominately dipolar magnetic field and its rotation axis causes the material present in the region near the disk's truncation radius to fall onto the star via two main accretion funnel flows, following the magnetic field lines connecting the disk to the star (see Figures 1.3 and 1.4, left panel). The interaction between the disk and

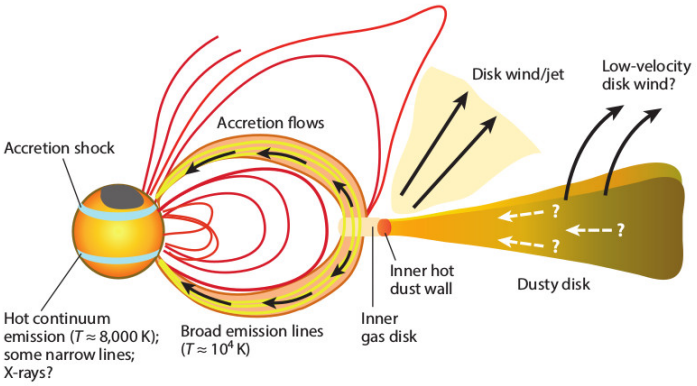

Figure 1.2: Magnetospheric accretion in CTTSs. The stellar magnetosphere truncates the inner circumstellar disk, causing matter to flow toward the star following the stellar magnetic field lines (represented in red), forming accretion columns. The material accelerated in these accretion columns produces broad emission lines, such as Hα and Hβ. The free-falling material collides with the stellar surface, resulting in accretion shocks that produce UV and optical excess. The circumstellar disk is responsible for emission at IR, sub-mm and mm wavelengths. Accretion energy drives disk winds and jets, which produce forbidden emission lines. Figure from Hartmann et al. (2016).

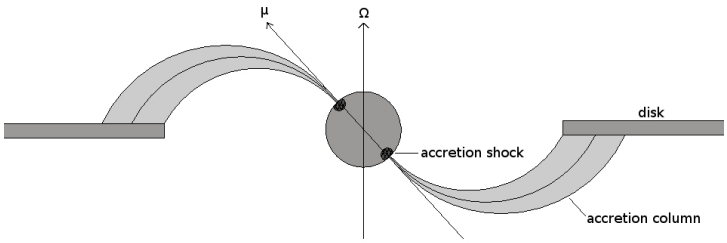

Figure 1.3: When there is a misalignment between the axis of the (predominately dipolar) magnetic field (μ) and the stellar rotation axis (Ω), magnetospheric accretion may occur via the stable accretion mechanism, where two main accretion columns, one in each hemisphere, form at the regions where the stellar magnetic pole is closest to the disk. Two main hot spots due to accretion shocks are located near the magnetic poles.

magnetic field may also lift dust above the disk plane, creating an optically thick warp in the inner disk region near the truncation radius, located at the base of the accretion funnel flows. At the other end of each funnel flow, an accretion shock on the stellar surface results in a hot spot, located at a high latitude. This configuration is able to maintain itself for timescales covering several rotation cycles, leading to relatively periodic photometric variability.

For CTTSs with magnetic fields that do not have a strong dipolar component and/or are not significantly misaligned with the stellar rotation axis, accretion should occur through an unstable regime (Kurosawa & Romanova 2013). In this regime, Rayleigh-Taylor instabilities between an accretion disk and a stellar magnetosphere are expected to cause matter to

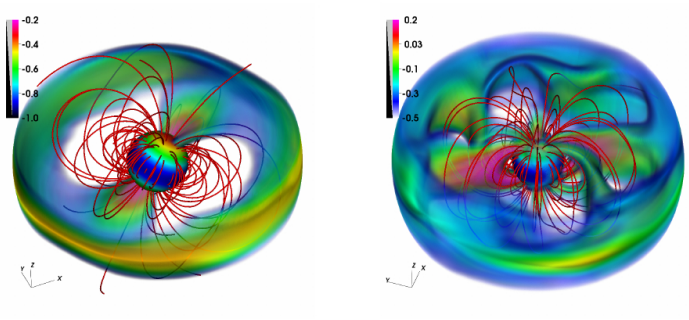

Figure 1.4: MHD simultations of the stable (left) and unstable (right) magnetospheric accretion regimes. Background colors show the volume rendering of the density (in logarithmic scales and arbitrary units). Red lines represent magnetic field lines. Figure from Kurosawa & Romanova (2013).

accrete onto the star via streams that sporadically appear around the star (right panel of Figure 1.4). This is a much more dynamic configuration than the stable regime, and the hot spots resulting from these accretion streams are more randomly distributed around the star. This leads to much more stochastic photometric variability. Magnetorotational instabilities can also lift dust above the disk plane, without necessarily leading to accretion streams (Turner et al. 2010).

Observations of the magnetic fields of CTTSs have shown that a misalignment between the stellar magnetic field and the star's rotation axis is indeed common (Gregory et al. 2012). Studies have also shown that many CTTSs have very complex magnetic fields on the stellar surface, with not only strong dipolar components, but also significant octupolar components (e.g., Donati et al. 2010b, 2011). However, as the distance from the stellar surface increases, higher order multipoles decay much more quickly than the dipole (a dipolar magnetic field decreases with $1/r^3$, while an octupolar magnetic field decreases with $1/r^5$). Therefore, at the inner edge of the accretion disk, generally located a few stellar radii from the star (Gullbring et al. 1998), the dipolar component can often dominate the magnetic field, even if on the stellar surface it is weaker than the octupolar component.

1.2.2 Jets and winds

Outflows are a ubiquitous aspect of star formation. Powerful, highly collimated, bipolar jets are commonly found in association with YSOs of different evolutionary stages. Protostellar jets are often spatially resolved, spanning up to thousands of au from the source. The first indication of the presence of jets near young stars were the Herbig-Haro (HH) objects (Herbig 1951; Haro 1952), a product of high-velocity material shocking with the ambient interstellar medium (Hartmann 2009). The subsequent discoveries of highly collimated jets and molecular outflows in star forming regions added to the picture of matter ejection in YSOs. Signatures of jets are only detected among sources where a disk is still present and

accretion is actively undergoing, which indicates that there is a strong connection between accretion and ejection (Cabrit et al. 1990; Hartigan et al. 1995). Protostellar jets are believed to form as the byproduct of magnetic acceleration from the inner disk region (Ferreira et al. 2006; Ray et al. 2007), but the exact mechanism which drives them is still not well understood (Ray et al. 2007). Since the disk's innermost region is not yet resolved by observations, it is yet to be determined if these jets originate from winds launched at the interface between stellar magnetosphere and accretion disk (the X-wind model, Shang et al. 2007), or in a wide range of disk radii up to a few au from the star (the magneto-centrifugal disk wind, or D-wind model, Pudritz et al. 2007). There are, however, various observable jet properties that can help test these different models, such as the accretion to ejection ratio, collimation, and velocity structure. Statistical studies to test which stellar or disk properties scale with jet properties can help shed light on the matter.

Many similarities are found between jets emanating from more embedded sources and those coming from sources with a more evolved disk, suggesting that the same physical mechanism is at work in different stages of star formation (see, e.g., Cabrit 2002, for a comparison of jets associated with YSOs of different evolutionary stages). Similarities are also found among jets from sources of different masses, though generally at different mass ejection rates, indicating common physical processes over the whole stellar mass range (Ray et al. 2007). The CTTS mass range seems to provide the best efficiency for generating jets, and since they are optically visible and have well defined stellar and accretion properties, these systems provide the best laboratory for testing mass ejection models.

Jets produce highly blueshifted ($\sim 100-200$km/s) forbidden emission lines, such as [OI] 6300, 6363 Å and [SII] 6717, 6731 Å, which can be detected in the spectra of CTTSs and Herbig Ae/Be stars. A redshifted component, emitted by the receding part of the jet, can sometimes also be detected, though in most cases it is obscured by the circumstellar disk. Low-velocity forbidden emission is even more commonly detected among CTTSs (Hartigan et al. 1995; Simon et al. 2016), peaking near the stellar rest velocity or at blueshifts of up to a few tens of km/s. This component seems to originate in slower moving outflows, possibly centrifugally driven MHD disk winds (Kwan & Tademaru 1995) or photoevaporative disk winds (Ercolano & Owen 2010, 2016). Besides forbidden emission lines, winds can also leave their signature on magnetospheric emission lines, such as Hα, or lines produced in the accretion shocks, such as HeI 10830Å, in the form of a blueshifted absorption component. Line profiles with this component can be reproduced using models that combine emission from magnetospheric accretion with absorption in magnetically accelerated winds that arise from the inner disk (e.g., Lima et al. 2010; Kurosawa et al. 2011). These wind features, just as jet signatures, are only detected among accreting T Tauri stars, indicating that they should be powered by accretion (Edwards et al. 2006). There is also evidence for stellar winds among some CTTSs, which also seem to be accretion-driven (Edwards et al. 2006; Matt & Pudritz 2005).

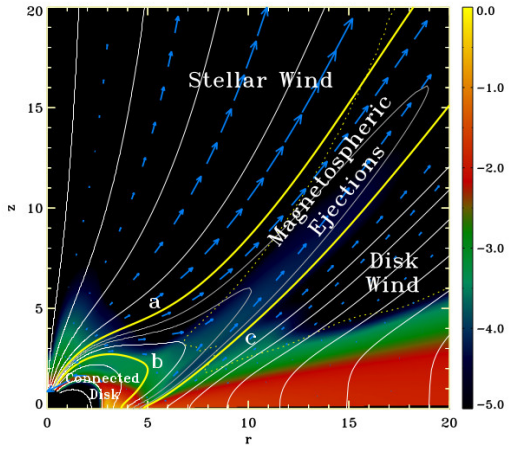

Figure 1.5: Simulation from Zanni & Ferreira (2013) of the star-disk interaction. Colors represent density (in logarithmic scale), blue arrows show poloidal speed vectors, white lines represent magnetic field lines, and thick yellow lines represent the field lines that delimit different components of the system: accretion (in the connected disk region), magnetospheric ejections, stellar winds and disk winds. Figure from Zanni & Ferreira (2013).

During magnetospheric accretion, differential rotation between the star and the disk, and consequently throughout the accretion columns themselves, can result in a distortion of the magnetic field lines, causing them to inflate, twist, and eventually disconnect and reconnect, ultimately restoring the original field configuration. When this happens, material can be ejected from the disk through these disconnected magnetic field lines, leading to outflows known as magnetospheric ejections (Zanni & Ferreira 2013) or conical winds (Romanova et al. 2009). These outflows can remove a significant amount of angular momentum from the star-disk system (Zanni & Ferreira 2013). Figure 1.5 shows simulations of the star-disk interaction from Zanni & Ferreira (2013), where different types of outflows can be identified.

1.3 AA Tau

In 1995, the typical CTTS AA Tau became the object of a photometric, spectroscopic, and polarimetric monitoring campaign, when it was observed for over one month with what was at the time unprecedented photometric cadence (Bouvier et al. 1999). Its light curve was found to present a relatively constant level of brightness interrupted by quasi-periodic dips of around 1.4 magnitudes (see Figure 1.6). The lack of significant color variation and higher polarization level measured during brightness minima indicated that obscuration of the photosphere by circumstellar dust was the likely cause of these flux dips. An attempt to fit a stellar spot model to AA Tau's light curve was unsuccessful, further strengthening the obscuration hypothesis. To account for these quasi-periodic flux dips, the following scenario was proposed: the interaction between the star's predominately dipolar magnetic field, which is inclined in relation to its rotation axis, and the inner circumstellar disk region

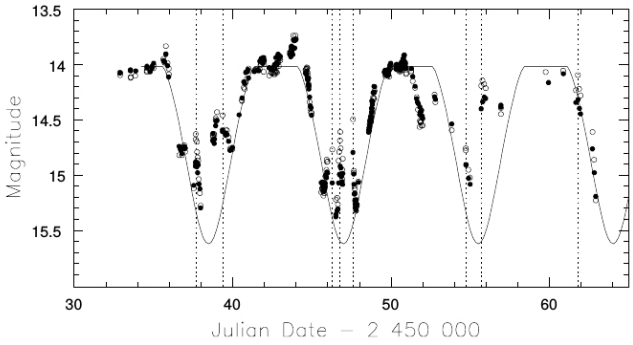

Figure 1.6: AA Tau's V-band (filled dots) and B-band (open circles) light curves from its 1995 observations, along with the synthetic light curve derived using the occultation model proposed for it (solid curve). Figure adapted from Bouvier et al. (1999).

would cause the material in this part of the disk to be lifted, preferentially where the stellar magnetic dipole is closest to the disk, resulting in two arch-shaped walls located opposite to each other, one in each hemisphere (recall Figures 1.3 and 1.4, left panel). This would produce an inner disk warp that occults the stellar photosphere as it rotates around the star, periodically intersecting the line-of-sight (Figure 1.7 demonstrates a simplified model of this warp, showing only the visible hemisphere). This scenario is now associated with the stable accretion regime (Romanova et al. 2013), with dust being lifted at the base of the accretion columns to form a warp.

During the initial studies of AA Tau (Bouvier et al. 1999), a simple geometric model was proposed to explain AA Tau's light curve. This model assumes that, if the star-disk system is viewed at a high inclination (i), an inner disk warp of a given maximum height from the disk plane (h_{max}) and azimuthal extension (ϕ_w), located at the radius of co-rotation with the star (R_{co}), will eclipse the stellar photosphere when it passes through the observer's line of sight. It then generates a synthetic light curve, which resembled the 1995 light curve of AA Tau (Figure 1.6). The location of the warp was at first assumed to be at the co-rotation radius, which was proved to be correct when Bouvier et al. (2007) measured the stellar rotation period of AA Tau from radial velocity variations of photospheric lines in its spectra and of the He I line, which is believed to originate at the accretion shock region on the stellar surface. These periods were both found to be consistent with the photometric period, which represents the Keplerian rotation period of the inner disk warp.

Further monitoring campaigns of the CTTS AA Tau (Bouvier et al. 2003, 2007) showed that, though this inner disk warp persists over timescales of a few years, it can be very dynamic. Figure 1.8 shows AA Tau's light curve during four different observing campaigns in different years. One can see that the quasi-periodic flux dips observed in 1995 are present in 2003 and 2004, but in 1999 they give way to a different configuration, in which two flux dips seem to be present during one stellar rotation cycle. On a few occasions, no flux dip was observed where one was expected. This was interpreted by Bouvier et al. (2003) as

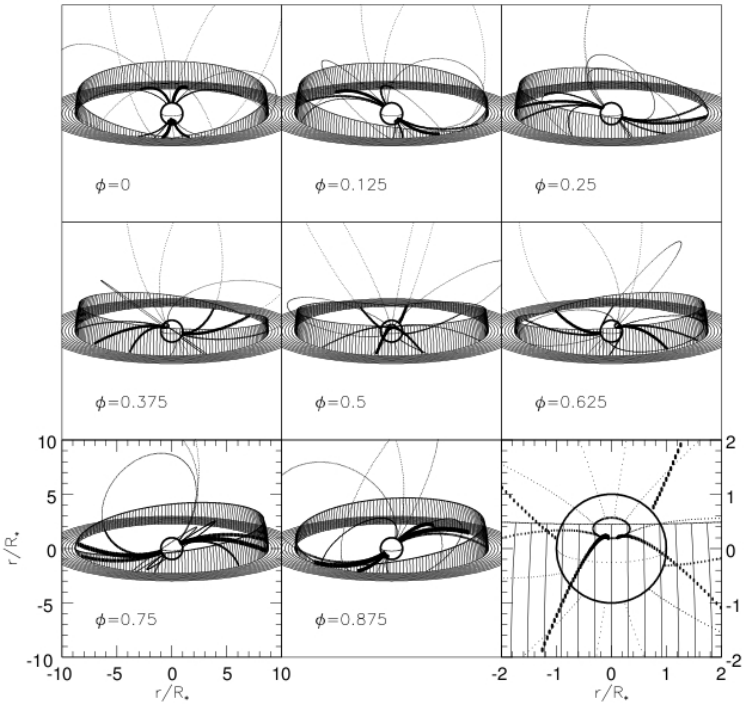

Figure 1.7: Occultation model proposed for AA Tau. A warp of maximum height h_{max} and azimuthal extension of ϕ_w, located at the co-rotation radius (R_{co}) of the accretion disk, eclipses the stellar photosphere when it passes through the observer's line of sight at phase $\phi = 0.5$. The system is seen at inclination $i = 75°$. For clarity, only one hemisphere is shown. Figure from Bouvier et al. (1999).

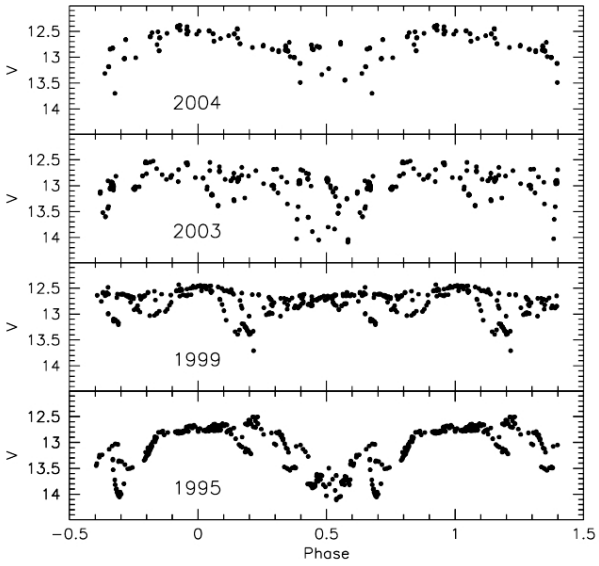

Figure 1.8: V-band light curves of AA Tau at different epochs: 1995, 1999, 2003, 2004. All light curves have been folded in phase using the same period of 8.22 days, but arbitrary origin of phase. Figure from Bouvier et al. (2007).

an indication of the dynamic nature of the interaction between stellar magnetosphere and inner disk. If, because of differential rotation between the star and disk, the magnetic field lines can distort, inflate and eventually disconnect (as is predicted by, e.g., Zanni & Ferreira 2013), then this could be the cause of the variability in shape, width, and amplitude of the flux dips observed over short timescales (days to weeks). The disconnection of the magnetic field lines could result in a strong reduction or even disappearance of the inner disk warp for a few stellar rotation periods, during which no occultation would be observed. Bouvier et al. (2007) also showed that AA Tau exhibits a faint blueing and increase in veiling during the eclipses, indicating that the occulting structure is spatially associated with accretion shocks, as would be expected for an inner disk warp located at the base of accretion columns.

AA Tau's magnetic field was measured by Donati et al. (2010a) using spectropolarimetric data taken with ESPaDOnS (Echelle SpectroPolarimetric Device for the Observation of Stars) at the Canada-France-Hawaii Telescope (CFHT) between December 2007 and January 2009. AA Tau was found to host a magnetic field with a 2-3 kG dipole, inclined $\sim 20°$ with respect to the rotation axis. The octupolar component was found to be much weaker (by a factor of $\sim 5-10$). These measurements provided support to the idea that AA Tau's inner disk warp is a consequence of this inclined, strongly dipolar, magnetic field.

The inner disk warp was later detected macroscopically by Cox et al. (2013) using *Hubble Space Telescope* (HST)/STIS coronographic imagery from 2001 and 2002. They directly measured the inclination of AA Tau's outer disk to be $71° \pm 1°$, consistent with Bouvier et al. (2003) and with the occultation model of Bouvier et al. (1999), and noted that it is misinclined by $4°$ (2σ) with regard to the inner disk, measured at $75° \pm 2°$ by O'Sullivan et al. (2005) using Monte Carlo scattered light models to reproduce the star's photopolarimetric variability. Cox et al. (2013) also detected a faint jet coming from AA Tau, and found that its polarimetric angle near the star is offset by $4°$ from what would be expected based on the outer disk, further supporting the inner disk warp scenario.

After over 20 years of observations often showing the same quasi-periodic behavior, AA Tau's light curve suddenly changed drastically when its average brightness level decreased by over 2 magnitudes in 2011 (Bouvier et al. 2013), at which point it lost its periodicity and became much redder than during its bright phase. Its mass accretion rate, however, did not seem to have suffered any significant change. This dimming episode was attributed to a sudden increase in circumstellar dust extinction in the line of sight, possibly because an unusually dense region of the disk was brought into the line of sight by its Keplerian motion around the star.

This star was the first to provide such unique input into the interaction between the stellar magnetosphere and the inner accretion disk of a CTTS. It became the prototype of a class of variability among these young systems, when many other CTTSs in the young cluster NGC 2264 were discovered to have very similar photometric behavior (Alencar et al. 2010; McGinnis et al. 2015).

Figure 1.9: Narrow-band, three-color image of NGC 2264 obtained by T.A. Rector and B.A. Wolpa (NOAO/AURA/NSF) at the Kitt Peak National Observatory. The filters used for this image were O III (light blue), Hα (red-orange), and S II (blue-violet). The field of view is approximately $0.75° \times 1°$. S Mon can be seen above the center of the image. It is believed to be the ionizing source for the cone nebula, seen in the bottom of the image. Figure from Dahm (2008).

1.4 NGC 2264

NGC 2264 is a young, open cluster belonging to the Mon OB1 association. It is located in the local spiral arm, distant approximately 760 pc from the Sun (Sung et al. 1997). It is a region of active star formation, containing hundreds of YSOs, and is associated with an extensive molecular cloud complex. Its dominant stellar component is the star S Mon, an O7 V spectroscopic binary, believed to be the main responsible for ionizing the surrounding gas, resulting in the nebular emission observed in the region and in the shape of the cone nebula (see Figure 1.9).

This cluster has been the object of a great deal of studies regarding star formation (e.g., Walker 1956; Sung et al. 1997; Flaccomio et al. 1999; Rebull et al. 2002; Lamm et al. 2004; Ramírez et al. 2004; Dahm & Simon 2005; Fűrész et al. 2006; Flaccomio et al. 2006; Sung et al. 2009; Alencar et al. 2010; Teixeira et al. 2012; Affer et al. 2013; Mariñas et al. 2013; Bouvier et al. 2016; Lim et al. 2016) for three main reasons: its relative proximity to the Sun compared with other star forming regions, the low interstellar extinction toward it (Rebull et al. 2002; Venuti et al. 2014), and the existence of a molecular cloud complex associated with it that obscures background objects, making it easier to identify members. Because of the large number of surveys conducted in NGC 2264, spanning wavelengths from centimeter

to X-rays, its stellar population is well defined, with hundreds of likely cluster members cataloged. These members, besides S Mon, consist mostly of M to A-type PMS stars, with a few dozen B-type ZAMS stars. A substellar population of around 230 candidate members has also been cataloged (Kendall et al. 2005). The age of NGC 2264 is estimated to be around 3Myr, though a number of studies have inferred age spreads of at least 5Myr and up to 10Myr (Dahm 2008). Ages of individual objects have been found between 1Myr and 10Myr (Flaccomio et al. 1999; Venuti et al. 2017b), though these are strongly dependent on models of PMS evolution. It has been suggested that sequential star formation has occurred in the cluster (Adams et al. 1983; Venuti et al. 2017b).

In recent years, much attention has been drawn to NGC 2264 since it was observed by the CoRoT satellite (Convection, Rotation and planetary Transits, Baglin et al. 2006) in March 2008, during CoRoT's first short run (Alencar et al. 2010; Affer et al. 2013). This cluster was observed for 23 days, uninterrupted by the day-night cycle, with high-precision ($1-10$mmag) measurements every 512 seconds (or 32 seconds, in some cases). This was the first time a star forming region was observed with such detail and high cadence. This pioneering work resulted in photometry of unprecedented quality for T Tauri stars and Herbig AeBe stars, allowing them to be studied in much more detail than in any previous observational campaign. Among the stars observed in this region, 301 were confirmed as members of NGC 2264, and of these 83 were classified as CTTSs by Alencar et al. (2010). The 83 CTTSs were separated into three groups according to the morphology of their light curves. The first group consisted of 28 periodic, nearly sinusoidal light curves, whose variabilities were attributed to long-lived cold spots; the second consisted of 23 light curves with the same characteristics as those of AA Tau, flat-topped with quasi-periodic flux dips, which became known as AA Tau-like light curves; and the third consisted of 32 non-periodic light curves. Two examples of the AA Tau-like light curves found during this study can be seen in Figure 1.10, shown in full on the left and folded in phase on the right. This study also showed, using *Spitzer* IRAC photometry, that the stars with AA Tau-like photometric variability all present near-IR excess emission, attributed to dust in the inner disk, which is consistent with the scenario of obscuration by an inner disk warp that was proposed for AA Tau.

Following the first CoRoT short run in 2008, a new observational campaign of NGC 2264 was organized in December 2011 with the intention of observing the young cluster simultaneously in a number of different wavelengths and techniques. This campaign became known as the Coordinated Synoptic Investigation of NGC 2264 (or CSI2264) and is described in detail in Cody et al. (2014). It was made possible due to a collaboration between the group responsible for the CoRoT NGC 2264 short run and the YSOVAR team (Young Stellar Object VARiability, Morales-Calderón et al. 2011; Rebull et al. 2014). The simultaneous photometric and spectroscopic observations performed in a range of wavelengths have allowed for young stellar systems to be probed to new depths, helping to better understand the physical processes that govern their variability. New CTTSs were identified according to

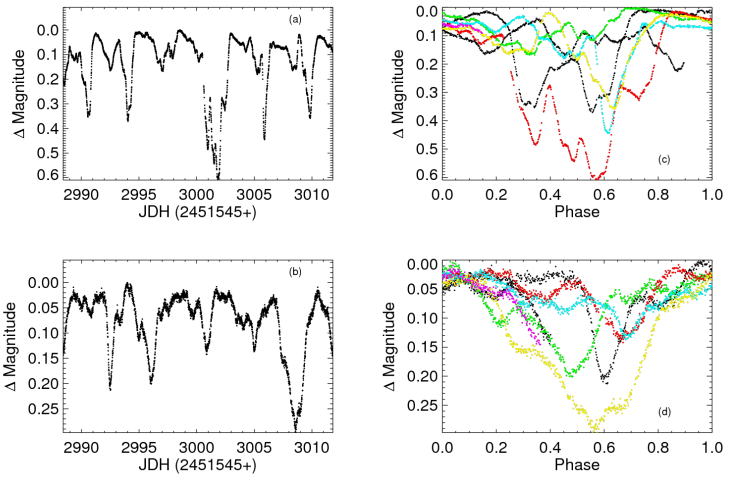

Figure 1.10: Two examples of AA Tau-like light curves found among CTTSs in NGC 2264 by Alencar et al. (2010). (c) and (d) show the light curves (a) and (b), respectively, folded in phase. Different colors correspond to different rotation cycles.

their UV excess (Venuti et al. 2014), new classes of photometric variability among CTTSs were identified (Stauffer et al. 2014, 2015, 2016) and even more stars with AA Tau-like light curves were found (McGinnis et al. 2015), among many other interesting results (Cody et al. 2014; Fonseca et al. 2014; Gillen et al. 2014; Sousa et al. 2016; Venuti et al. 2015, 2017a,b; Guarcello et al. 2017; Zwintz et al. 2017). This campaign and the 2008 CoRoT observations of NGC 2264 provided the foundation for the present study.

1.5 Objectives

The goal of this work is to study the interaction between the inner circumstellar disk and the stellar magnetosphere of classical T Tauri stars in NGC 2264, in order to better understand the physical processes governing accretion and ejection in young low-mass stars. For this purpose, we analyze simultaneous observations in a range of different wavelengths, as well as a combination of photometry and spectroscopy. We propose to improve on magnetospheric accretion models using the observations and to investigate the dust distribution in the inner disk region. We also take advantage of the extensive knowledge available on the CTTSs belonging to NGC 2264 in order to search for correlations between mass ejection and stellar and/or disk/accretion properties, as well as between stellar/disk properties and jet properties inferred from high-velocity forbidden emission. We hope this will provide better constraints for wind and jet launching models.

Chapter 2

Observations

2.1 First CoRoT short run

In March 2008 the CoRoT satellite performed its first short run when it observed the young cluster NGC 2264 for 23 days uninterruptedly. Stars of magnitude down to R $\sim$ 18 were observed with a cadence of 512 seconds, with uncertainties of less than 1% in magnitude. In some cases the data were taken every 32 seconds in order to provide high cadence light curves, but so much detail proved to be unnecessary for the purpose of this work. Therefore, these light curves were re-binned to 512 seconds. CoRoT's field of view was larger than the full extent of the cluster, which fit entirely into one of the CCDs designed for studying exoplanets. It observed in a white light bandpass of approximately 3700Å to 10 000Å. It could, in principle, provide three-color photometry by passing the stellar light through a low-resolution spectral dispersing prism, but for the purpose of this work we used only the integrated white light flux.

After undergoing standard CoRoT pipeline procedures, detailed in Samadi et al. (2006), the data were subsequently processed by Dr. Suzanne Aigrain[1] to remove unwanted effects, such as those caused by Earth eclipses, and to remove measurements affected by the South Atlantic Anomaly using a sigma-clipping filter, taking care not to cut flaring events. In some cases, discontinuities due to detector temperature jumps were present in the photometry, and when possible they were removed manually (for more details on the correction of CoRoT light curve systematics, see Cody et al. 2014).

[1] University of Oxford, UK

2.2 CSI2264

Between December 2011 and March 2013, the Coordinated Synoptic Investigation of NGC 2264 (CSI2264, Cody et al. 2014) took place. It was composed of simultaneous or quasi-simultaneous observations using instruments from fifteen different telescopes (eleven ground-based and four space-based telescopes), including the CoRoT satellite, the *Spitzer* Infrared Array Camera (IRAC, Fazio et al. 2004), the Canada-France-Hawaii Telescope's (CFHT) MegaCam (Boulade et al. 2003), and the FLAMES (Fibre Large Array Multi Element Spectrograph, Pasquini et al. 2002) multi-object spectrograph on ESO's Very Large Telescope (VLT). The observations from the CSI2264 campaign used in this work are detailed in Table 2.1 and in the following subsections.

Table 2.1: Observations from CSI2264 used throughout this work.

Telescope	Instrument	Dates	Band(s)	Time sampling
CoRoT	E2 CCD	2011 Dec 1 - 2012 Jan 3	3000-10 000Å	512 s
Spitzer	IRAC/mapping	2011 Dec 3 - 2012 Jan 1	3.6μm, 4.5μm	101 minutes
Spitzer	IRAC/staring	2011 Dec 3 - Dec 8-9	3.6μm, 4.5μm	15 s
VLT	FLAMES/GIRAFFE	2011 Dec 4 - 2012 Feb 29	6470-6790Å	20-22 epochs
VLT	FLAMES/UVES	2011 Dec 4 - 2012 Feb 29	4800-6800Å	20-22 epochs
CFHT	MegaCam	2012 Feb 14 - 2012 Feb 28	u, r	30 epochs
USNO 40"	CCD	2011 Nov 22 - 2012 Mar 9	I	912-1026 epochs

2.2.1 CoRoT data

NGC 2264 was observed a second time by CoRoT between 2011 December 1 and 2012 January 3, during the satellite's fifth short run. Once again the cluster was entirely observed by the E2 CCD, designed for studying exoplanets, using a cadence of 512s or 32s. The data underwent the same reduction and correction procedures as explained in section 2.1.

2.2.2 *Spitzer* IRAC data

Between 2011 December 3 and 2012 January 1, NGC 2264 was observed by the *Spitzer* Space Telescope in the IRAC 3.6μm and 4.5μm bands, during its Warm Mission mode. A region of $\sim 0.8° \times 0.8°$ centered at R.A. 06:40:45.0, declination +09:40:40 was mapped, with observations occurring approximately twelve times a day. Most objects were observed in both bands, but around 40% fell near the edges of the mapping region and have data from only one band. A region near the center of the cluster was also observed in staring mode, with a cadence of approximately 15 seconds during four blocks of 20, 26, 16, and 19 hours, on 2011 December 3, December 5-6, December 7-8, and December 8-9. The IRAC data reduction procedures and production of IRAC light curves are explained in detail in Cody et al. (2014) and Rebull et al. (2014).

2.2.3 CFHT MegaCam data

The region around NGC 2264 was observed using the Canada France Hawaii Telescope's wide-field imager MegaCam (Boulade et al. 2003) between 2012 February 14 and 2012 February 28. The MegaCam's field of view spans a full 1×1 square degree, covering the cluster with only one pointing. On each observing night, the region was imaged repeatedly, with a cadence between 20 minutes and 1.5 hours, in the u and r bands. A 5-step dithering pattern was used, with single exposures of 3s in r and 60s in u. The data were processed at the CFHT to correct for instrumental signatures, such as bias, dark current, flat, and bad pixels. Aperture photometry was performed, followed by an astrometric and photometric calibration, as explained in detail in Venuti et al. (2014).

2.2.4 USNO data

NGC 2264 was also observed by the US Naval Observatory's (USNO) 40" telescope from December 2011 to March 2012. Approximately 900 epochs of I-band photometric observations were obtained for a field of view of 23'×23' centered approximately on the cluster center. The data were processed by Dr. Ann Marie Cody[2] for standard reduction procedures using bias and dome flat images that were obtained at the beginning of each night. She then performed aperture photometry for all stars in each image, and identified a set of non-variable stars in order to establish zero-points for each CCD frame and construct light curves of the targets using differential photometry.

2.2.5 FLAMES spectra centered on Hα

For 161 stars, 20-22 epochs of VLT FLAMES spectra were obtained between 2011 December 4 and 2012 February 29. Of these, four to six epochs were taken simultaneously with the CoRoT photometry. FLAMES can obtain medium- and high-resolution spectra for multiple objects over a field of view 25 arcmin in diameter. Since this is much smaller than the extent of NGC 2264, even with two pointings, only the central part of the cluster was observed (one pointing centered at R.A. 06:41:04.8, declination +09:45:00, the other centered at R.A. 06:40:58.8, declination +09:21:54).

FLAMES consists of a fiber positioner called OzPoz that feeds the medium-high resolution spectrograph GIRAFFE with up to 132 fibers (in the MEDUSA mode) and the red arm of the high-resolution spectrograph UVES (Ultraviolet and Visual Echelle Spectrograph) with up to 8 fibers. GIRAFFE offers a high resolution mode, with a grating of 316 lines/mm, and a low-resolution mode, with 600 lines/mm. Observations can only take place in a single echelle order at a time. It is equipped with a 2K × 4K EEV CCD with a spatial scale of 0.2 arcsec/pixel in MEDUSA mode, where each fiber has an aperture of 1.2 arcsec on the sky,

[2]NASA Ames Research Center, USA

corresponding to 6 detector pixels. The UVES red arm offers 3 different setups, with central wavelengths of 520 nm, 580 nm, and 860 nm.

For our observations we used the combined UVES+GIRAFFE mode, with the high-resolution HR15N setup of the GIRAFFE/MEDUSA mode, which covers the spectral range from 6470Å to 6790Å, successfully observing the Hα and LiI 6707Å lines with a resolution of R $\sim$ 17,000, and the UVES setup centered on 580 nm, which covers the region from 4800Å to 6800Å with a resolution of R $\sim$ 47,000. The brightest stars were allocated to UVES fibers. A number of GIRAFFE fibers and up to two UVES fibers were allocated to regions of the sky where no star was found. This is done in order to measure the contribution of the sky to the stellar spectra so that it can later be subtracted in order to remove any contamination. There is, for instance, strong nebular emission in the Hα line that contaminates this line's profile and must be correctly removed before it can be analyzed. Since this emission is highly spatially variable in star forming regions like NGC 2264, it was necessary to obtain many sky spectra across each field of observation in order to properly correct for the contamination.

The FLAMES/GIRAFFE spectra were reduced using Gasgano, a Java-based software tool provided by ESO, and FLAMES/GIRAFFE reduction pipelines also provided by ESO. Each stellar spectrum then had the closest sky spectrum subtracted from it in order to remove the contamination by nebular emission lines. They were then normalized by the continuum. The reduction pipelines consist of the following steps: constructing a master bias frame and bad pixel map using a set of bias frames obtained on the night of the observations; constructing a master flat frame in a similar manner, subtracting bias from it and removing bad pixels; wavelength calibration using a slit geometry table, which describes the position of the fibers in the focal plane, and the spectrum of an arc-lamp taken the night of observations to fit a point spread function (PSF) profile to the detected peaks; and extraction of the final science files by applying bias and bad pixel removal, flat-field correction, and wavelength calibration using the output from the previous steps. Optimum (weighted) extraction was performed in order to better subtract the background and remove cosmic rays.

The FLAMES/UVES spectra were reduced using the Reflex pipeline workflows provided by ESO. We then performed sky subtraction and continuum normalization. Sky subtraction in the UVES spectra is not as straightforward as for GIRAFFE spectra, since there are very few UVES fibers placed on the sky (only two fibers during these observations) and they are generally not very close to an observed star. Since the background nebulosity is very irregular in the NGC 2264 region, the spectrum observed in each sky fiber does not necessarily well represent the sky emission present in the spectra of each observed star. In order to circumvent this we first take the average of the two sky spectra and then analyze each portion of this mean spectrum from a particular night in comparison to the stellar spectrum of the same night that we wish to correct. We noticed that some sky features are identical in both spectra, while a few others (e.g., the Hα emission line and the forbidden emission lines NII 6548Å, NII 6584Å, SII 6716Å, and SII 6731Å) are similar in shape but present

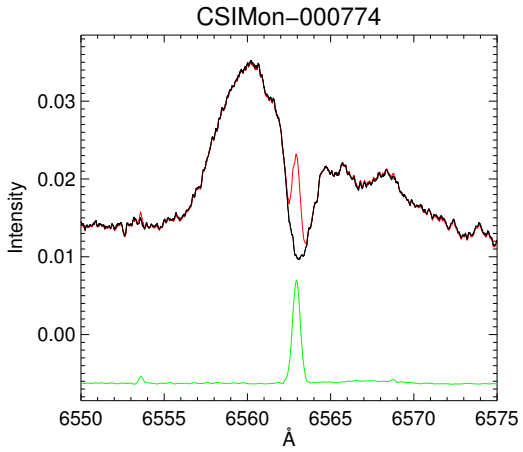

Figure 2.1: Example demonstrating the process to remove the nebular contamination from the UVES stellar spectra. The original spectrum around the Hα line is shown in red; the isolated contamination, taken as the average of 2 sky spectra observed simultaneously with the stellar spectrum and scaled to best reproduce the contamination, is shown below in green; and the result after subtraction is overplotted in black.

different amplitudes. Multiplying the sky spectrum by a specific factor results in a very close approximation between the lines, but different emission lines generally require different factors. Therefore we separated small portions of the mean sky spectrum surrounding these lines (width $\sim$ 1.2Å, centered on the emission line), multiplied each by the optimum scaling factor, and replaced these portions of the mean sky spectrum, thus generating a synthetic sky spectrum that closely resembles the sky contribution observed in the stellar spectrum. Care was taken to maintain the continuum level of the separated multiplied portions equal to the continuum level of the original mean sky spectrum, so as to avoid bumps in the continuum of the final product. We then subtracted this final synthetic sky spectrum from the stellar spectrum to obtain the final sky-corrected product. Figure 2.1 shows an example of this decontamination in the Hα line.

2.3 Follow-up FLAMES data from 2013

In 2013 NGC 2264 was again targeted by FLAMES using the same configuration as the one used during the CSI2264 campaign, in an attempt to obtain spectra for objects that, previously to the CSI2264 campaign, we did not know were interesting. One field centered at R.A. 6:40:47.1, declination +9:40:34.7, with 79 objects allocated to GIRAFFE fibers and 5 objects allocated to UVES fibers, was observed for 13 one-hour runs between 2013 December 22 and 2014 January 3 in queue mode. The remaining GIRAFFE fibers and two UVES fibers were allocated to sky positions and the final UVES fiber was reserved for wavelength calibration using a ThAr lamp. This campaign focused on stars with light curves characteristic of stochastic accretion, those with irregular flux bursts, but many CTTSs with

other types of photometric variability and some WTTSs were observed as well. We used the same configuration as the 2011 FLAMES campaign, the GIRAFFE HR15N setup along with UVES centered at 580nm.

We reduced the FLAMES/GIRAFFE spectra once again using Gasgano and GIRAFFE reduction pipelines provided by ESO. The FLAMES/UVES spectra were again reduced using the Reflex pipeline workflows provided by ESO. The spectra underwent the same sky-subtraction and normalization procedures mentioned in the previous subsection.

2.4 FLAMES spectra centered on [OI] 6300Å

In 2014 the FLAMES multi-object spectrograph was used once again to observe the stellar cluster NGC 2264, this time with the HR13 spectral setup, which covers the spectral region between 6120Å and 6405Å at a resolution of R$\sim$26,500. These new observations focus on the study of jets in CTTSs, and the setup was chosen in order to observe the [OI] 6300Å line, a well-known tracer of jet signatures in these objects. The observations were divided into 4 different fields, two of which were observed with three different fiber configurations in order to include all targets, resulting in a total of 8 different configurations. Each was observed at least once for 40 minute exposures, between September 30, 2014 and February 4, 2015. One configuration was observed 4 times, identified as configuration A1. Since the spectral feature we are interested in for the scope of this work, the [OI] 6300Å emission line, is not expected to vary significantly in the time between these observations, we added the 4 spectra after having removed all contaminating effects, obtaining spectra of larger signal-to-noise ratio for the stars observed in this configuration. A total of 487 stars in the direction of NGC 2264 were observed, including all 159 CTTSs previously observed by the CoRoT satellite. The data were provided by ESO after being treated for standard reduction procedures using ESO pipelines.

The [OI] 6300Å emission line is contaminated by telluric emission and absorption features that must be removed in order to recover the intrinsic line profile. To remove the telluric emission line, we used a χ^2 minimizing technique to identify the three sky spectra that most closely matched the contamination in each stellar spectrum. Only sky spectra observed simultaneously with the stellar spectrum in question were considered. The three sky spectra selected were shifted in wavelength when necessary to best coincide with the contamination. We then took the average of the three profiles and subtracted it from the stellar spectrum (see left panel of Figure 2.2).

We then proceeded to remove the contamination from telluric absorption lines, which affect the wavelength range from approximately 6275Å to 6325 Å. We combined the normalized spectra of two A0-type stars, CSIMon-005644[3] and CSIMon-001235, the first of which

[3]The CSIMon ID is an internal naming scheme devised for the CSI2264 campaign (see Cody et al. 2014), and comprises all cluster members, candidates and field stars in the NGC 2264 field of view.

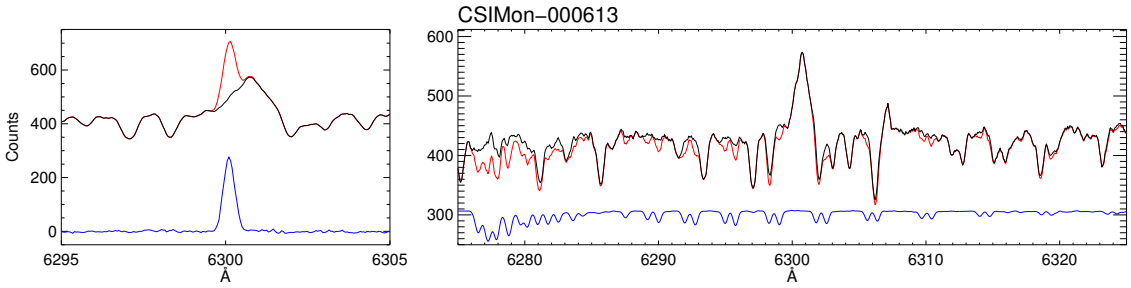

Figure 2.2: Example demonstrating the process to remove telluric emission and absorption lines from the stellar spectra around the [OI] 6300Å line. Left: the original spectrum is shown in red; the isolated contamination, taken as the average of 3 sky spectra that were observed simultaneously with the stellar spectrum, is shown below in blue; and the result after subtraction is overplotted in black. Right: the stellar spectrum, now with the telluric emission line removed, is shown in red; the telluric absorption line template, scaled and shifted vertically to facilitate a comparison with the stellar spectrum, is shown below in blue; and the final decontaminated spectrum is overplotted in black.

was observed 4 times, to create a template. These stars were chosen because they are hot enough that they have no photospheric features in this region, therefore after normalizing to the continuum only the telluric absorption spectrum remains. The telluric absorption spectrum is generally not very variable and this template proved to be a good match for all but one of our observed fields. For the final field a star observed simultaneously was needed. There were no A or B-type stars in this field, therefore the template was created using the G-type star CSIMon-001126. This star has high projected velocity ($v \sin i$), leading to very broad photospheric lines, which could be easily identified and fitted with synthetic spectra. The photospheric contribution could then be subtracted from the original spectrum in order to isolate the telluric absorption lines and create the template. The stellar spectra were then divided by the respective templates in the affected wavelength interval in order to eliminate the contamination (right panel of Figure 2.2).

2.5 Other observations

In order to analyze the Hα line profiles of stars that had no FLAMES spectra from either of our campaigns in that spectral region, we were given access to high-resolution Hectochelle spectra from 2004-2005 by Dr. Gábor Fűrész[4] (Fűrész et al. 2006). They used the 190Å wide order centered at Hα, with a resolution of R$\sim$34,000. These spectra were provided to us fully reduced, sky-subtracted, and normalized. We used them for eight T Tauri stars.

We also had access to HiRES (High Resolution Echelle Spectrometer) spectra from the Keck observatory for one star, CSIMon-000021. This star was observed fifteen times during

[4]Massachusetts Institute of Technology, USA

five days in December 2013, in exposures of 1200 seconds. Spectra in the range between $\lambda = 4776$Å and $\lambda = 6201$Å, with a resolution of R$\sim$48,000, were obtained. These spectra were provided to us by Dr. John Stauffer[5] after already having undergone standard reduction procedures. We further processed them to remove cosmic rays and normalized them to the continuum.

A few classical T Tauri stars that had not been observed by our FLAMES Hα campaigns or by either of these other spectrographs were observed by the ESO-Gaia consortium (Gilmore et al. 2012; Randich et al. 2013) in 2012 using FLAMES/GIRAFFE with the HR15N grating, the same as our 2011 and 2013 observations. These data were downloaded from the ESO science archive under program ID 188.B-3002(K), reduced using Gasgano following the same steps listed in Sect. 2.3, and added to our dataset.

[5]California Institute of Technology, USA

Chapter 3

The classical T Tauri star population of NGC 2264

3.1 Selection of probable members of NGC 2264

Throughout this work, we aim to analyze the processes of accretion and ejection in young stellar objects belonging to NGC 2264. For this it is necessary to select a sample of members of the cluster that are actively accreting, i.e. classical T Tauri stars, to work with. It is also important to analyze a number of weak-line T Tauri stars that will serve as photospheric templates to compare with the CTTSs in order to isolate the spectral signatures of accretion and ejection.

The first step in selecting a proper sample to work with is to identify the members of NGC 2264. Because of the extensive literature available on this cluster and the various surveys conducted in the past, it was possible to obtain a reliable sample of probable cluster members. This sample was selected using the following criteria:

- member according to Lamm et al. (2004) based on narrow-band photometry Hα emission, variability, and location in the I_C vs $(R_C - I_C)$ color-magnitude diagram and $(R_C - \mathrm{H}\alpha)$ vs $(R_C - I_C)$ color-color diagram;

- member according to Ramírez et al. (2004) and Flaccomio et al. (2006) based on X-ray detection from Chandra observations, combined with the location in the I vs $(R - I)$ diagram when optical photometry was available;

- spectroscopic Hα equivalent width greater than 10 Å or Hα width at 10% intensity greater than 270 km/s, in order to identify accreting T Tauri stars (Alencar et al. 2010);
- radial velocity member according to Fűrész et al. (2006);
- member according to Sung et al. (2008) based on Hα emission and location in the I_C vs $(V - I_C)$ color-magnitude diagram;
- identification of *Spitzer* Class I and Class II objects by Sung et al. (2009);
- and candidate members according to Venuti et al. (2014) based on UV excess and variability as signs of accretion.

3.2 Selection of Classical T Tauri stars

After obtaining a reliable sample of probable cluster members, we must identify the ones that show signs of accretion. The following criteria were used to classify objects as CTTSs:

- Hα width at 10% intensity greater than 270 km/s (White & Basri 2003);
- Hα equivalent width higher than a spectral type dependent criterion proposed by White & Basri (2003): EW[Hα] $\geq$ 3 Å for K0-K5 stars, EW[Hα] $\geq$ 10 Å for K7-M2.5 stars, EW[Hα] $\geq$ 20 Å for M3-M5.5 stars, and EW[Hα] $\geq$ 40 Å for M6-M7.5 stars;
- UV excess $E(U-V) < -0.58$ for K0-K6 stars and $E(U-V) < -1.12$ for K7-M3 stars, as proposed by Alencar et al. (2010);
- CTTSs according to Venuti et al. (2014) from their location on various color-color and color-magnitude diagrams ($g-r$ vs $r-i$, r vs $u-r$, $u-g$ vs $g-r$, and $u-g$ vs $r-i$) indicating UV excess caused by accretion; Venuti et al. (2014) also selected a sample of 50 CTTS candidates based on UV excess and photometric variability;
- and detection of forbidden [OI] emission at 6300 Å (detailed in Chapter 5).

Of the objects observed with CoRoT in 2008 and/or 2011, 189 cluster members were classified as CTTSs or CTTS candidates. Of the objects observed by FLAMES in the 2014 [OI] 6300Å line survey[1], a total of 183 members were classified as CTTSs or CTTS candidates. Among these, 159 had also been observed by CoRoT.

[1] This campaign was much more complete than the one centered around the Hα line, which only observed the central region of the cluster.

3.3 Determination of stellar and accretion parameters

After having obtained a reliable sample of accreting and non-accreting T Tauri star members of NGC 2264, we analyzed the available FLAMES spectra in order to derive stellar and accretion parameters for the accreting objects.

3.3.1 Effective temperatures, bolometric luminosities, masses and radii

When determining effective temperatures of CTTSs from their spectra, we often encounter some difficulty due to veiling effects. Veiling occurs as a result of a strong UV and optical excess produced in the accretion shocks on the stellar surface of CTTSs. It is present in spectra when the hot spot caused by these accretion shocks is visible to the observer. This UV and optical excess results in an added blue continuum to the photosphere's spectrum, resulting in shallower absorption lines than those from a pure photosphere. Though the actual line depths are affected by veiling, the ratio between different absorption line depths within a small spectral range is not, since all absorption lines in that range suffer a very similar change caused by the added continuum. Therefore, we can determine a CTTS's effective temperature by analyzing the ratios between photospheric absorption lines that are very sensitive to changes in surface temperature and others that are much less sensitive to these changes.

We initially determined effective temperatures using absorption line ratios for a subsample of 44 stars observed in the first FLAMES campaign. Line ratios of the observed spectra were compared to those of synthetic spectra created using the IDL (Interactive Data Language) routine Spectroscopy Made Easy (SME, Valenti & Piskunov 1996). We used synthetic spectra of temperatures ranging from 3500 K to 6000 K in steps of 500 K, with solar metallicity and $\log g = 4.0$ and 4.5. The value of $v \sin i$ was fixed to the value between 10 km/s and 35 km/s, rounded to the nearest 5 km/s, that resulted in the synthetic spectra that most closely matched the observed spectra. For temperature insensitive lines we used the FeI 6518.4Å and FeI 6633.7Å lines, and for temperature sensitive lines we used the CaI 6471.7Å, CaI 6572.8Å, and VI 6531.4Å lines. We calculated the ratio of each temperature sensitive to temperature insensitive line, then compared these to the theoretical ratios obtained with the synthetic spectra, interpolating between the different temperature steps in order to arrive at a value of effective temperature (see Fig. 3.1 for an example). We calculated the mean of the different values found using each pair of lines in each of the 20 different individual spectra, then took the standard deviation of these values as the uncertainty. In some cases, when a specific line showed an unsatisfactory signal to noise ratio (S/N) in a certain spectrum, the line ratios using that line were ignored.

In parallel to this work, Venuti et al. (2014) analyzed 757 probable members of NGC 2264 (285 CTTSs, 50 CTTS candidates, and 422 WTTSs) that were observed by the CFHT Megacam. They converted spectral types to effective temperatures using the conversion

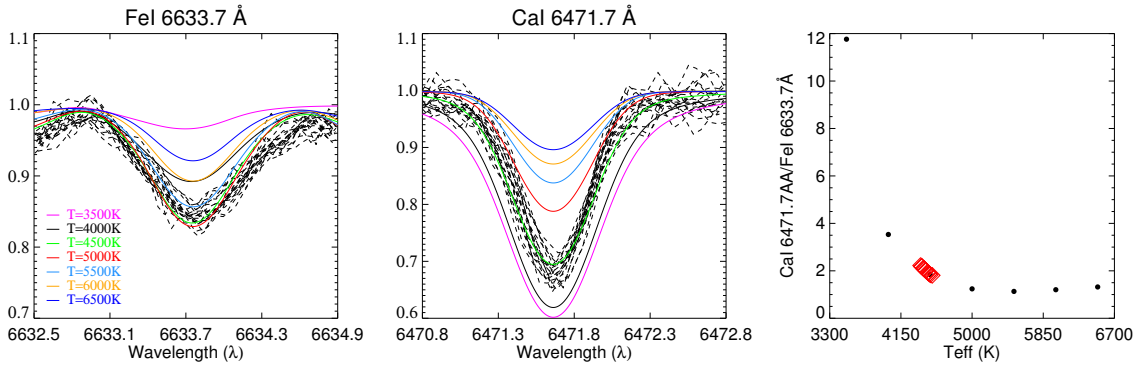

Figure 3.1: Left and middle: theoretical (solid lines) and observed (dashed lines) FeI 6633.7Å and CaI 6471.7Å spectral lines, respectively. Solid lines of different colors represent synthetic spectra of different temperatures, while different dashed lines represent observations of the same star taken on different nights. Right: black dots represent theoretical line ratios as a function of the synthetic spectrum's effective temperature T_{eff}, and red diamonds represent the observed line ratios from different nights as a function of their interpolated value of T_{eff}.

table from Cohen & Kuhi (1979), checked for consistency against that of Luhman et al. (2003). Most of the spectral types were taken from the literature (from Dahm & Simon 2005; Rebull et al. 2002; Walker 1956, in that order of preference), and when none was available they derived the spectral type by comparing dereddened colors with the empirical optical color sequence of Covey et al. (2007). Values of extinction had been calculated by them individually for their stars using CFHT photometry. They estimated bolometric luminosities from de-reddened J-band photometry retrieved from the 2MASS catalog, using J-band bolometric corrections (BC_J) calculated using the temperature-dependent scales of Pecaut & Mamajek (2013) and Bessell et al. (1998). A distance to the cluster of 760pc was used when converting to absolute magnitudes. This distance was initially determined by Sung et al. (1997) and has been strengthened by many studies that followed (Park et al. 2000; Turner 2012; Gillen et al. 2014).

Venuti et al. (2014) placed their values of effective temperature and bolometric luminosity onto an HR diagram and estimated masses and radii for their sample by comparing with the theoretical pre-main sequence model grids of Siess et al. (2000). Though more recent and more physically accurate models are available today, most previous studies of NGC 2264 have used Siess et al. (2000) to determine stellar parameters, making it therefore easier to compare obtained results with previous studies when using this model.

None of the FLAMES campaigns were able to target all of the T Tauri stars included in the CFHT/Megacam campaign, whereas most (98%) of the T Tauri stars targeted by FLAMES were observed by Megacam. The set of stellar parameters measured by Venuti et al. (2014) is therefore much more complete than one we could construct with our values of effective temperatures. Therefore, even though effective temperatures determined from

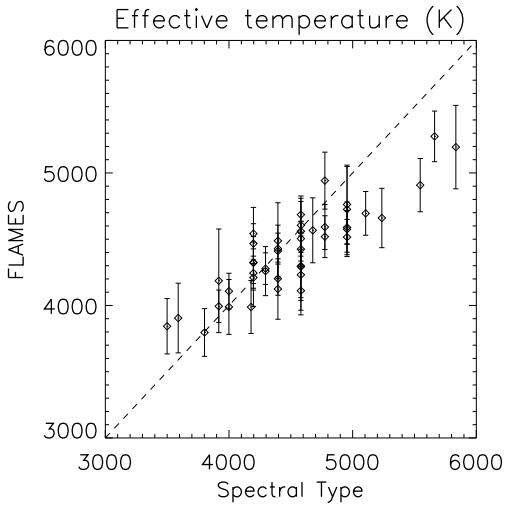

Figure 3.2: Comparison of effective temperatures determined using line ratios in the FLAMES spectra and spectral types given by Venuti et al. (2014).

line ratios in the stellar spectra are more reliable than those converted from photometrically derived spectral types, we found it best to use their values of bolometric luminosities, stellar masses, and stellar radii, in order to have a homogeneously derived set of stellar parameters for all stars in our sample. When comparing these parameters among a large sample of stars, it is important that they were all derived in the same consistent way. We also find it important to maintain consistency among different groups in the collaboration to study NGC 2264. These values of stellar luminosity, mass and radii are given in Table 3.2.

Adopting their values should not affect our results, since the effective temperatures (T_{eff}) determined by the two methods agree within on average $\sim 5\%$, and in the worst cases by $\lesssim 15\%$ (see Figure 3.2). In fact, most ($\sim 55\%$) of the values used by Venuti et al. (2014) fall within our uncertainties. We also note that our values agree well among stars of $T_{eff} \lesssim 5000$ K, whereas for stars where they find $T_{eff} \gtrsim 5000$ K, the values we obtain through line ratios seem to be underestimated. It is among the hottest stars that we find the highest discrepancies between the two values. We must beware of the fact that absorption lines considered to be insensitive to changes in temperature can only be considered as such for small temperature intervals. As we reach higher and higher values, the way these lines are affected by these increases may begin to change more drastically and it becomes necessary to chose a new set of absorption lines to work with. The right panel of Figure 3.1 shows that the CaI 6471.7Å/FeI 6633.7Å ratio is not adequate to distinguish between effective temperatures higher than ~ 5000 K. In this case, for the hottest stars in our sample, our values of stellar mass and radius would have been compromised had we used these temperatures to determine them.

3.3.2 Veiling

In order to measure the amount of excess continuum flux present in a CTTS's spectrum, it is necessary to identify the underlying photospheric contribution and see how much the observed spectrum deviates from it. The best way to do this is to compare a CTTS spectrum to a WTTS spectrum of the same spectral type. WTTSs occupy the same region in the HR Diagram as CTTSs and they are believed to be physically similar to CTTSs. The differences between the two are extrinsic: WTTSs no longer possess thick circumstellar disks and have ceased accretion onto the central object. This means that their spectra are not affected by accretion (nor ejection) related contamination, such as veiling, broad emission lines or forbidden emission lines (they do, however, present some emission lines - for instance, Balmer lines - originating from a highly active chromosphere). WTTS spectra therefore represent almost purely photospheric spectra of young, low-mass objects. This makes them much better photospheric templates for CTTS spectra than, for instance, synthetic spectra created from stellar atmospheric models, which are usually based on Main Sequence stars that are not as closely related to these young, accreting objects as the non-accreting T Tauri stars.

In order to determine the amount of veiling in our CTTS spectra, we analyzed the 2014 FLAMES data set, choosing a sample of WTTS spectra to serve as photospheric templates. We selected WTTSs with spectral types in the same range as our CTTSs and of low $v \sin i$ ($v \sin i \lesssim 15$ km/s). Table 3.3 lists the WTTSs we used as templates and some relevant stellar parameters. Each CTTS spectrum was compared to at least three different photospheric templates, generally one of the same spectral type as the CTTS's, one a subclass earlier and one a subclass later, in order to account for possible misclassifications in the literature when searching for the closest match. In some cases a photospheric template of the same spectral type was not available (usually among the coolest stars of our sample, where spectra with high enough S/N were difficult to find, or among the hottest, where fewer stars were observed) and the three templates of closest spectral type were used instead. The absorption lines in these templates were broadened to adjust for stellar rotation and an extra continuum was added to simulate veiling. We used a goodness-of-fit test to adjust for the amount of veiling and rotational broadening that best matched the observation. We did this by calculating the reduced χ^2 value (χ^2_r) iteratively for pairs of veiling and rotational broadening, in order to find the pair that simultaneously minimized this value, which is defined as

$$\chi^2_r = \frac{1}{n-m} \sum_{i=1}^{n} \frac{(O_i - T_i)^2}{\sigma^2} \tag{3.1}$$

where O_i is the intensity of the observed spectrum at the ith wavelength bin; T_i is the intensity of the veiled, broadened template at the same wavelength bin; σ is the deviation from the mean, measured directly in the continuum of the observed spectrum, in a region where no absorption or emission lines were present; n is the total number of wavelength bins analyzed; and m is the number of fitted parameters (equal to two in this case - veiling

and rotational broadening). Two small wavelength intervals around the [OI] 6300Å and 6363Å emission lines were ignored, in order to fit only the photospheric spectrum. The final combination of WTTS template, veiling and rotational broadening that resulted in the lowest χ^2_r was taken as the best fit. The values of veiling found are given in Table 3.2 as r, the ratio between the continuum excess and the photospheric flux. However, the value of $v \sin i$ from the best fit is not an accurate estimate of the CTTS's true $v \sin i$ because, even though we chose WTTSs of low $v \sin i$ to serve as templates, their rotational broadening cannot necessarily be ignored.

In a few cases we found that the best match for a CTTS used a template of a different spectral type than the one found in the literature. In most cases the discrepancy was small - of only one or two subspectral types, but in three cases we found the difference to be greater than this. We attribute this to a misclassification of the star's spectral type in the literature and provide our values for the correct spectral type in Table 3.1, according to the WTTS template that best reproduced its photospheric absorption lines. For these three stars we recalculated their stellar parameters (effective temperature, bolometric luminosity, mass and radius) in the same way as was described in Section 3.3.1, using the corrected spectral type.

Table 3.1: Spectral types from the literature and from our analysis with WTTS templates for the stars that showed the largest discrepancy.

CSIMon ID	2MASS ID	SpT (literature)	SpT (this work)
CSIMon-000406	06405968+0928438	K3[a]	M1
CSIMon-000795	06411257+0952311	G:V:e[b]	K2
CSIMon-001234	06401113+0938059	K6[b]	K3

[a] Venuti et al. (2014)
[b] Dahm & Simon (2005)

3.3.3 Rotational velocity projected in our line-of-sight ($v \sin i$)

We derived values of $v \sin i$ (stellar rotational velocity projected in our line-of-sight) from the FLAMES spectra using two different methods. Before the more complete FLAMES 2014 campaign took place, we had analyzed the photospheric lines of spectra centered around Hα for a subsample of CTTSs to determine values of $v \sin i$. This subsample focused on stars with particularly interesting photometric variability (discussed in more detail in Sect. 3.4) and these values were published in a series of papers characterizing these types of variability (McGinnis et al. 2015; Stauffer et al. 2015, 2016). After the FLAMES 2014 campaign mapped the cluster and obtained a homogeneous set of spectra for a much larger sample than the previous campaigns, we derived values of $v \sin i$ again for all CTTSs and many WTTSs in this set in a uniform manner. Below we explain in detail the two methods used.

Using spectra centered on Hα We compared FLAMES spectra, when available, and Hectochelle or HiRES spectra otherwise, to synthetic spectra using SME and Oleg Kochukhov's Binmag3[2] IDL routine. The synthetic spectra were created using atomic line files extracted from the *Vienna Atomic Line Database* (VALD[3] Piskunov et al. 1995; Ryabchikova et al. 1997; Kupka et al. 1999, 2000) and the spectrum synthesis code Synth3 (Kochukhov 2007). Synthetic spectra of temperatures between 3500K and 6000K in steps of 250K were created, using log$g$=4.0 and solar metallicity. For each star we chose the synthetic spectrum of effective temperature closest to the star's and applied a broadening correspondent to the instrumental resolution (R=17,000 for FLAMES, R=56,000 for Hectochelle, and R=48,000 for HiRES), with initially no rotational broadening. Using the tools provided by Binmag3, we then applied rotational broadening to the synthetic spectrum and used a χ^2 minimizing technique included in the program to fit the absorption lines in the synthetic spectrum to the photospheric absorption lines of the stellar spectrum. We took care to fit the wings of the absorption lines, rather than their depths, which are more strongly affected by veiling. This was done individually for a number of absorption lines. We then took the mean and standard deviation of the $v \sin i$ values that resulted from these fits as the star's final $v \sin i$ and its uncertainty.

Using spectra centered on [OI] 6300Å As was mentioned in Section 3.3.2, the best photospheric template for a CTTS spectrum is the spectrum of a WTTS of the same spectral type, but when estimating $v \sin i$ the rotational broadening of the WTTS will bring an additional uncertainty into the measure. Therefore we decided to once again compare the stellar spectra to synthetic spectra, created in the same way as described in the previous paragraph, in order to estimate $v \sin i$ values. This time, however, a continuum was added to the synthetic spectra to simulate veiling and both veiling and $v \sin i$ were adjusted simultaneously to find the best fit (lowest value of χ^2_r), as was done using WTTS templates in Section 3.3.2. Small intervals around forbidden emission lines were again ignored during the analysis. Synthetic spectra of at least three different temperatures (the three closest temperatures between 3500K and 6000K, in steps of 250K, to the CTTS's effective temperature as defined in Section 3.3.1) were compared to each stellar spectrum and the one that resulted in the lowest χ^2_r value after adjusting $v \sin i$ and veiling was chosen. The error in $v \sin i$ was calculated during the fitting procedure by finding the values of $v \sin i$ that resulted in $\chi^2_r = \chi^2_{min} + 1$ (where χ^2_{min} is the lowest value found for χ^2_r), while maintaining the veiling constant. We use this because, if we assume that the $\chi^2_r \times v \sin i$ function is approximately Gaussian around the minimum, then $\chi^2_{min}+1$ corresponds to an increase of 1σ (one standard deviation) from the value of minimum χ^2_r. These values of $v \sin i$, which were determined for a much larger sample than using the previous method, are given in Table 3.2.

[2] http://www.astro.uu.se/~oleg/
[3] http://vald.astro.uu.se/

Estimates of $v \sin i$ become more and more uncertain the closer the value is to the spectral resolution. Below this value it is impossible to accurately measure the rotational broadening, we have only an upper limit corresponding to the spectral resolution. Therefore care must be taken whenever using low values of $v \sin i$ in any analysis. In the case of the FLAMES 2014 campaign, we measured this resolution directly from the telluric [OI] emission line in the spectra and found it to be on average 11.3 km/s.

3.3.4 Mass accretion luminosity and mass accretion rate

Most of the values of accretion luminosity and mass accretion rates used throughout this work were calculated by Venuti et al. (2014) from the UV excess luminosity, measured in the CFHT data. Sousa et al. (2016) also calculated accretion luminosities and mass accretion rates from Hα line luminosities for a number of stars that were included in the FLAMES 2011 campaign. Hα line flux ($F_{H\alpha}$) was calculated by multiplying the measured Hα equivalent width (EW(Hα)) by the continuum flux in the Hα region (F_C(Hα)). The Hα line flux was then converted to luminosity using the formula $L_{H\alpha} = 4\pi d^2 F_{H\alpha}$, where d = 760 pc is the distance to the cluster (Sung et al. 1997). Since the FLAMES spectra were not flux calibrated, the continuum flux was estimated from the CoRoT observations that were taken simultaneously with the spectra, where CoRoT magnitudes were converted into R magnitudes using an R-band zero-point of 26.74 magnitudes (Cody et al. 2014). When no simultaneous CoRoT observation was present, the CFHT r-band magnitude measured almost simultaneously with the FLAMES spectra was used instead. The continuum flux was corrected for extinction using the A_V values calculated by Venuti et al. (2014), before being multiplied by EW(Hα) to calculate the Hα flux.

Sousa et al. (2016) then used the relation proposed by Fang et al. (2009) to calculate accretion luminosity (L_{acc}) from $L_{H\alpha}$:

$$\log\left(\frac{L_{acc}}{L_\odot}\right) = (2.27 \pm 0.23) + (1.25 \pm 0.07) \log\left(\frac{L_{H\alpha}}{L_\odot}\right) \tag{3.2}$$

and the relation from Gullbring et al. (1998) to calculate mass accretion rate ($\dot{M}_{acc}$):

$$\dot{M}_{acc,H\alpha}(M_\odot/yr) = \frac{L_{acc} R_*}{G M_* \left(1 - \frac{R_*}{R_{in}}\right)}, \tag{3.3}$$

where the inner radius was set to the commonly used value for disk truncation radius for CTTSs of $R_{in} = 5R_*$ (Gullbring et al. 1998).

In order to estimate $L_{H\alpha}$ and $\dot{M}_{acc,H\alpha}$ for the stars in our sample that were not observed by CoRoT or CFHT simultaneously with the Hα spectra (stars observed by FLAMES around Hα only in the 2013 campaign or whose Hα information we took from the literature), we estimated $F_{H\alpha}$ using the average r-band magnitude from the CFHT 2012 campaign (Venuti et al. 2014). As an estimate of the error bar, we used the amplitude of variability from the

CoRoT light curves. For the brightest stars that saturated in the CFHT observations, we used the mean CoRoT R magnitudes. A comparison of the mean CFHT r and CoRoT R magnitudes in our sample shows that the two coincide very well among the brightest stars ($R \lesssim 14$) and therefore we introduce very little error by using the CoRoT magnitudes for the stars with no CFHT photometry. We corrected the magnitudes for extinction using the individual values derived for each star by Venuti et al. (2014) and, when no value was available, we used the average extinction towards the cluster of $A_R = 0.40$, estimated from all of the stars in our sample with measured extinction. Magnitudes were then converted to flux and multiplied by EW(Hα) in order to retrieve the Hα line flux. We used the same relations as Sousa et al. (2016) to derive L_{acc} and $\dot{M}_{acc,H\alpha}$.

The accretion luminosities and mass accretion rates adopted throughout this work are shown in Table 3.2. The values derived by Venuti et al. (2014) from UV excess are used when available, and those derived from Hα equivalent widths are used otherwise.

3.4 Photometric variability

After CoRoT's second observing run in NGC 2264, all of the light curves of CTTSs observed in either run were analyzed and classified based on their visual morphologies. This was initially done based only on the CoRoT light curves, with no color information. The light curves were classified into more groups than the three initially proposed by Alencar et al. (2010). The two periodic groups identified therein - of spot-like and AA Tau-like light curves - remained, but the third group, that had been described only as aperiodic and irregular, was divided into new groups. In the end, we have the following classification of light curve morphologies:

- Spot-like light curves: characterized by a very regular, nearly sinusoidal, periodic variability (an example is shown in Figure 3.3e). This type of variability was attributed to the rotational modulation of stable cold spots on the stellar surface (Alencar et al. 2010).

- AA Tau-like light curves: these light curves resemble that of the CTTS AA Tau when it was studied in Bouvier et al. (1999). They are characterized by a relatively stable maximum brightness level interrupted by quasi-periodic flux dips (by quasi-periodic we mean they occur with a regular frequency but vary in shape and/or amplitude between rotation cycles - Figure 3.3a,b shows two examples). This behavior has been attributed to quasi-periodic occultation events of the stellar photosphere by an inner disk warp (Bouvier et al. 1999, 2003, 2007; Alencar et al. 2010; McGinnis et al. 2015).

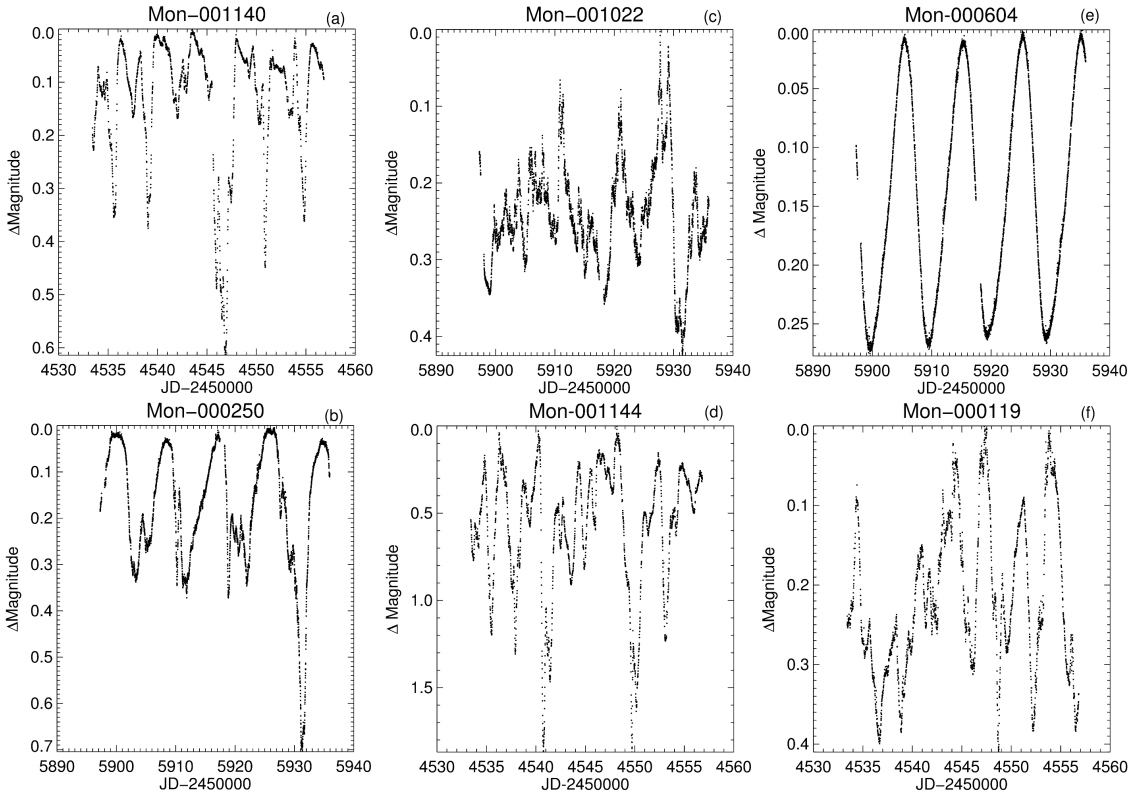

Figure 3.3: Examples of different light curve morphologies found in CTTSs in NGC 2264. (a) and (b) show periodic light curves attributed to circumstellar extinction, (c) shows a light curve dominated by accretion bursts, (d) shows a light curve dominated by aperiodic extinction, (e) shows a spot-like light curve, and (f) shows a light curve whose morphology is complex, probably as a result of a combination of processes.

- Accretion burst-dominated light curves: these light curves present a series of abrupt, irregular flux bursts (see Figure 3.3c for an example) that were attributed to abrupt events of increased accretion, and therefore abrupt increases in the number and intensity of hot spots on the stellar surface (Cody et al. 2014; Stauffer et al. 2014).

- Aperiodic extinction-dominated light curves: similar to the AA Tau-like light curves, but the flux dips do not show a clear period (see Figure 3.3d). We attribute them to the occultation of the photosphere by irregularly distributed material in the disk (McGinnis et al. 2015).

- Complex light curves: their variability is nearly symmetric around the mean flux, meaning they are neither dominated by flux bursts or by flux dips, yet they are not regular enough to be classified as spot-like. They are therefore not easily attributed to one of the other groups and are likely the product of a combination of physical mechanisms (see Figure 3.3f). A portion of these light curves was attributed to time-variable mass accretion (with longer timescales than the accretion bursts) producing transient hot spots on the stellar surface (Stauffer et al. 2016).

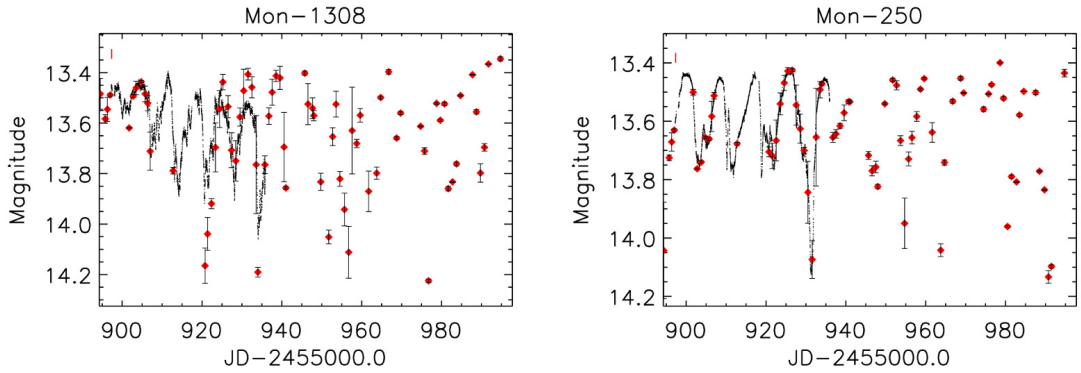

Figure 3.4: Simultaneous I-band and CoRoT photometry, shifted in magnitude to coincide, for the AA Tau-like stars Mon-1308 and Mon-250. The high cadence space-based observations allow the AA Tau-like flux dips to be easily identified, while with even high quality ground-based photometry it is difficult to obtain enough information for the variability to be quantified.

The CSI2264 campaign also identified at least two eclipsing binaries (see, e.g., Gillen et al. 2014), and a small subset of stars with periodic, shallow, short-duration flux dips superposed onto the main features of the light curve (Stauffer et al. 2015). For a more detailed discussion of all of these light curve morphologies, including a statistical analysis of symmetry in the flux and periodicity, see Cody et al. (2014).

Some of these different types of photometric variability were only possible to identify because of the incredible detail present in the CoRoT light curves. To demonstrate the importance of high-cadence space-based observations, we show in Figure 3.4 the CoRoT light curve and USNO I-band light curve, obtained simultaneously, of two stars with AA Tau-like photometric behavior identified during the CSI campaign (McGinnis et al. 2015). It is evident from this Figure that, though the I-band photometry coincides closely with the CoRoT photometry, the lower cadence makes it difficult for AA Tau-like behavior to be identified using only ground-based data. This is likely the main reason why more AA Tau-like systems had not been identified previously to the CoRoT observations of NGC 2264.

Table 3.2: Stellar parameters of the CTTSs (and CTTS candidates) that were included in this work

CSIMon ID	2MASS ID	Sp type	L_{bol} ($L_\odot$)	M_* ($M_\odot$)	R_* ($R_\odot$)	$\dot{M}_{acc}$ ($M_\odot$/yr)	L_{acc} ($L_\odot$)	r	$v \sin i$ (km/s)
CSIMon-000011	J06411725+0954323	K7	0.79	0.70	1.86	1.86e-07	1.72e+00	0.29	14.5± 2.0
CSIMon-000021	J06405944+0959454	K5	0.96	1.20	1.69	9.50e-10§	1.70e-02§	0.05	21.7± 4.2
CSIMon-000056	J06415315+0950474	K5	0.77	1.16	1.52	5.75e-09§	2.18e-03§	0.02	15.8± 2.7
CSIMon-000062	J06422190+0948329	K0	0.50	0.90	0.86	-	-	-	-
CSIMon-000063	J06411193+0959412	M2.5	0.17	0.32	1.19	6.17e-09	4.04e-02	0.35	16.0± 6.2
CSIMon-000064	J06411070+0957424	M1.5	0.39	0.40	1.62	4.68e-09	2.83e-02	0.03	9.5± 2.0
CSIMon-000090	J06410896+0933460	M3	0.58	0.30	2.26	1.10e-08	3.54e-02	0.00	13.5± 3.2
CSIMon-000103	J06405954+0935109	K6	4.10	0.93	3.84	9.61e-09§	5.38e-02§	0.12	33.2± 2.3
CSIMon-000109	J06413743+0937280	K4	2.50	1.51	2.32	-	-	0.13	-
CSIMon-000117	J06405413+0948434	M2.5	0.18	0.32	1.21	3.39e-08	2.21e-01	1.14	32.3±19.1
CSIMon-000119	J06412100+0933361	K6	1.16	0.91	2.04	3.34e-09§	4.19e-02§	0.28	20.8± 1.2
CSIMon-000120	J06411911+0926294	M3	0.50	0.30	2.09	1.70e-07	5.90e-01	0.09	18.2± 4.6
CSIMon-000123	J06410821+0934094	M2.5:M3	1.05	0.31	2.97	5.56e-10§	1.46e-03§	0.41	22.9± 4.8
CSIMon-000126	J06405783+0941201	M0	0.86	0.62	2.02	2.14e-08	1.58e-01	0.12	-
CSIMon-000131	J06404927+0923503	K7	0.70	0.70	1.60	1.10e-08§	1.22e-01§	0.24	14.7± 2.7
CSIMon-000134	J06411441+0926582	M3.5	0.52	0.28	2.20	1.70e-09§	4.77e-04§	0.37	22.8± 5.1
CSIMon-000136	J06411599+0926094	M0	0.84	0.62	1.99	1.58e-08	1.21e-01	-	-
CSIMon-000137	J06404712+0942077	M2	0.25	0.36	1.36	2.88e-09	1.85e-02	0.00	13.0± 6.6
CSIMon-000153	J06405990+0947044	M3	0.21	0.29	1.35	9.12e-09	4.84e-02	1.57	19.1±16.1
CSIMon-000168	J06414287+0925084	K5:M0	0.39	0.90	1.20	1.15e-08	2.11e-01	0.28	10.6± 3.1
CSIMon-000177	J06410620+0936229	G5	3.80	1.48	2.03	9.29e-09§	2.20e-01§	0.00	30.0± 4.0
CSIMon-000192	J06405001+0944545	M3	0.25	0.30	1.49	8.51e-10§	5.96e-04§	0.07	17.2± 4.5
CSIMon-000207	J06405904+0949062	M2:M2.5	0.30	0.34	1.52	5.18e-10§	2.92e-03§	0.00	12.1± 3.0
CSIMon-000212	J06411830+0944067	M2.5	0.21	0.32	1.30	6.46e-10^u	-	0.13	14.1± 4.4
CSIMon-000219	J06411890+0935541	M4	0.14	0.23	1.18	1.91e-09	8.86e-03	0.37	22.8±17.2
CSIMon-000220	J06412454+0937355	M3	0.36	0.30	1.79	2.51e-09	4.33e-03	0.23	55.5±10.1
CSIMon-000225	J06410622+0925036	M5	0.45	0.22	2.30	4.47e-09	1.06e-02	0.28	23.2±13.9
CSIMon-000228	J06405624+0939327	M1	0.57	0.45	1.86	1.66e-08	9.88e-02	0.62	20.7± 2.8
CSIMon-000250	J06410050+0945031	K3	1.23	1.35	1.63	1.44e-09§	1.96e-02§	0.00	14.0± 2.0
CSIMon-000260	J06411099+0935556	K7	0.55	0.71	1.55	1.07e-08	1.18e-01	0.46	11.5± 8.9
CSIMon-000273	J06411837+0939411	M1	0.42	0.45	1.60	2.14e-08	1.48e-01	0.04	12.4± 2.6
CSIMon-000279	J06412119+0932146	M2.5	0.20	0.32	1.28	6.76e-10§	8.72e-04§	0.34	13.4± 8.1
CSIMon-000280	J06404100+0927543	K4	0.45	0.99	1.07	8.91e-10	8.66e-03	0.14	14.2± 3.9
CSIMon-000290	J06405867+0936132	M4	1.10	0.25	3.35	2.95e-08	5.41e-02	0.13	31.2± 7.2
CSIMon-000295	J06404340+0930343	M0	0.25	0.67	1.09	2.75e-09	4.14e-02	0.20	13.4± 3.3
CSIMon-000296	J06405059+0954573	K2	1.57	1.42	1.71	1.73e-09§	4.49e-02§	0.00	15.1± 1.6
CSIMon-000297	J06404516+0928444	K2	1.57	1.42	1.71	5.75e-09§	2.03e-01§	0.01	31.5± 2.7
CSIMon-000314	J06404459+0932261	M3	0.21	0.29	1.35	9.55e-09	4.94e-02	0.42	35.4± 8.7
CSIMon-000318	J06404458+0948126	K6	1.20	0.91	2.07	4.70e-10§	5.20e-03§	0.00	14.3± 2.9

Table 3.2: Stellar parameters of the CTTSs - continued

CSIMon ID	2MASS ID	Sp type	L_{bol} ($L_\odot$)	M_* ($M_\odot$)	R_* ($R_\odot$)	$\dot{M}_{acc}$ ($M_\odot$/yr)	L_{acc} ($L_\odot$)	r	$v \sin i$ (km/s)
CSIMon-000325*†	J06405934+0955201	G5V	-	-	-	-	-	-	-
CSIMon-000326	J06405882+0939187	M0	0.34	0.66	1.27	1.70e-09	2.16e-02	0.46	13.1± 6.5
CSIMon-000328	J06412700+0930131	M1	0.30	0.45	1.34	2.40e-09	1.98e-02	0.00	11.5± 2.4
CSIMon-000330	J06413160+0948328	K2	1.93	1.55	1.89	1.34e-10§	2.76e-03§	0.00	23.2± 1.6
CSIMon-000335	J06413728+0945066	K4	1.45	1.40	1.92	2.31e-09§	4.45e-02§	0.00	15.2± 2.1
CSIMon-000340	J06415593+0940468	M2.5	0.52	0.33	2.05	3.55e-09	1.24e-03	0.00	12.4± 4.2
CSIMon-000341	J06405426+0949203	M0.5	0.56	0.53	1.73	6.17e-08	4.61e-01	0.12	36.3±19.8
CSIMon-000342	J06405573+0946456	M4	0.24	0.25	1.57	1.66e-08	6.32e-02	0.30	22.5± 4.2
CSIMon-000346	J06410908+0930090	K7	0.69	0.70	1.73	2.28e-09§	2.32e-02§	0.54	18.0± 3.0
CSIMon-000347	J06410444+0936433	M2.5	0.26	0.33	1.45	1.12e-08	6.18e-02	0.43	31.2± 6.0
CSIMon-000349	J06404912+0937363	K7:M0	0.42	0.69	1.38	6.46e-09	6.18e-02	0.63	17.1± 4.5
CSIMon-000352	J06412562+0944032	M2	0.33	0.36	1.56	5.01e-09	2.83e-02	0.03	12.1± 2.6
CSIMon-000356	J06410506+0949228	M5	0.21	0.20	1.57	6.46e-10	2.03e-03	0.85	-
CSIMon-000357	J06410574+0931012	K5	1.68	1.20	2.24	1.29e-09§	1.74e-02§	0.18	14.6± 4.5
CSIMon-000358	J06410673+0947275	M3	0.22	0.29	1.39	6.61e-09	3.38e-02	0.07	19.2± 5.4
CSIMon-000359	J06404221+0940110	M0	0.70	0.62	1.83	1.48e-08	1.08e-01	0.17	15.3± 2.2
CSIMon-000361	J06410308+0929045	M	0.17	0.26	1.25	8.71e-10	4.43e-03	0.03	19.1± 5.1
CSIMon-000370	J06405679+0937490	K5	1.57	1.20	2.17	2.55e-08§	4.36e-01§	0.22	12.4± 1.8
CSIMon-000378*	J06405292+0944544	K5.5	0.90	1.06	1.71	5.62e-09	4.84e-02	-	10.4± 0.4‡
CSIMon-000379	J06410497+0950460	K2	2.12	1.60	1.99	1.26e-09§	5.37e-02§	0.03	25.2± 3.6
CSIMon-000406	J06405968+0928438	K3	0.63	0.70	1.59	4.79e-08	1.03e+00	0.93	24.4±18.9
CSIMon-000412	J06404711+0932401	M1	0.79	0.45	2.19	1.05e-07	5.28e-01	0.19	17.2± 2.8
CSIMon-000423	J06411485+0925550	M2.5	0.05	0.26	0.61	1.41e-09	1.48e-02	3.04	-
CSIMon-000424	J06411521+0937576	M1	0.35	0.45	1.45	6.61e-09	5.06e-02	0.07	11.8± 3.4
CSIMon-000425	J06411668+0929522	K5	3.70	1.22	3.34	5.89e-09§	5.41e-02§	0.19	15.7± 3.4
CSIMon-000426	J06411945+0930286	K5	1.42	1.20	2.06	1.75e-08§	2.56e-01§	0.00	12.7± 1.4
CSIMon-000433	J06410111+0934522	M1	0.16	0.44	0.99	1.38e-09	6.77e-03	0.37	14.0± 1.4
CSIMon-000434	J06410406+0935211	M2.5	0.54	0.33	2.08	4.79e-09§	2.15e-03§	0.17	15.1± 3.3
CSIMon-000441	J06405809+0936533	M2	0.50	0.36	1.92	3.63e-09	1.69e-02	0.61	-
CSIMon-000448	J06410360+0930290	M4	0.66	0.25	2.61	1.15e-08	2.71e-02	0.12	30.1± 8.2
CSIMon-000456	J06405154+0943242	K4	1.58	1.41	2.00	5.12e-09§	9.08e-02§	0.03	22.6± 3.1
CSIMon-000457	J06410673+0934459	G6	6.40	1.82	2.70	6.01e-09§	9.24e-02§	0.64	42.1± 2.4
CSIMon-000462	J06404218+0933374	G0	10.06	1.90	2.90	3.16e-08§	5.20e-01§	0.36	35.7± 1.4
CSIMon-000469	J06404114+0933578	K7	0.56	0.71	1.56	7.59e-08	8.43e-01	3.53	-
CSIMon-000474†	J06410682+0927322	G	-	-	-	-	6.64e+00§	0.17	17.5± 1.3
CSIMon-000484	J06410542+0934095	M4.5	0.01	0.13	0.34	9.12e-11	3.18e-04	0.71	-
CSIMon-000491	J06405616+0936309	K3	2.60	1.70	2.36	3.72e-09§	2.20e-01§	0.49	61.9± 4.7
CSIMon-000498	J06404750+0949289	K3	3.90	1.90	2.88	1.00e-08§	1.73e-01§	0.07	26.0± 2.7
CSIMon-000510	J06410429+0924521	M0	0.84	0.62	1.99	9.12e-08	6.90e-01	0.78	14.3± 2.1

Table 3.2: Stellar parameters of the CTTSs - continued

CSIMon ID	2MASS ID	Sp type	L_{bol} ($L_\odot$)	M_* ($M_\odot$)	R_* ($R_\odot$)	$\dot{M}_{acc}$ ($M_\odot$/yr)	L_{acc} ($L_\odot$)	r	$v \sin i$ (km/s)
CSIMon-000525	J06405118+0944461	G0	8.70	1.80	2.82	1.23e-08§	1.97e-01§	0.47	51.8± 4.6
CSIMon-000530	J06411938+0921469	K2.5	0.39	0.82	0.89	1.35e-08	3.02e-01	0.14	13.1± 2.1
CSIMon-000553	J06410303+0937357	M1	1.94	0.45	3.44	9.75e-10§	3.21e-03§	1.02	39.8± 5.8
CSIMon-000558	J06413974+0940279	K4	4.40	1.60	3.35	6.06e-08§	9.00e-01§	0.25	15.4± 2.1
CSIMon-000566	J06405275+0943004	M3.5	0.16	0.26	1.21	2.29e-09	1.18e-02	0.09	18.0± 3.9
CSIMon-000567	J06405639+0935533	K3	1.50	1.45	1.79	3.72e-08	7.38e-01	1.79	21.6± 2.9
CSIMon-000577	J06414382+0940500	K1	2.50	1.62	2.03	2.10e-09§	4.22e-02§	0.03	29.3± 1.7
CSIMon-000578	J06415003+0929322	K6	0.74	0.94	1.63	6.92e-09	9.26e-03	0.13	25.9± 4.1
CSIMon-000590	J06405891+0928528	M1	0.57	0.45	1.86	2.40e-09	1.38e-02	0.00	22.1± 4.8
CSIMon-000598	J06405932+0946165	M1	0.82	0.45	2.24	4.17e-08	2.06e-01	0.34	15.2± 1.8
CSIMon-000613	J06410577+0948174	K6.5	2.05	0.78	2.85	1.92e-08§	1.32e-01§	0.41	14.4± 3.5
CSIMon-000619	J06411475+0934134	K8.5	0.44	0.69	1.41	3.98e-08	4.83e-01	0.43	15.7± 4.8
CSIMon-000628	J06410827+0930228	M3	0.26	0.30	1.51	3.39e-09	1.62e-02	1.26	-
CSIMon-000632	J06404936+0952539	M0.5	0.04	0.49	0.48	4.17e-10	1.01e-02	1.51	-
CSIMon-000636	J06404884+0943256	M0	0.87	0.62	2.03	4.79e-08	3.53e-01	0.16	16.3± 2.7
CSIMon-000637	J06404921+0957387	M1	0.44	0.45	1.64	3.16e-09	2.12e-02	0.09	13.3± 3.0
CSIMon-000650†	J06410098+0932444	K1	-	-	-	-	1.62e-01§	0.22	16.2± 3.1
CSIMon-000654*[4]	J06405949+0929517	M3	0.47	0.30	2.03	6.46e-08	2.36e-01	-	18.0± 3.0‡
CSIMon-000655	J06412313+0937338	M1	0.29	0.45	1.33	1.86e-09	1.55e-02	0.40	16.9± 4.4
CSIMon-000660	J06410051+0929159	K4	1.36	1.40	1.86	1.45e-10§	8.06e-03§	0.02	23.5± 3.3
CSIMon-000667	J06412878+0938388	K3	1.78	1.53	1.95	1.84e-09§	2.25e-02§	0.00	20.5± 2.3
CSIMon-000676	J06414780+0934096	K5	1.81	1.20	2.32	-	-	0.05	15.3± 1.8
CSIMon-000681	J06413111+0926582	K3.5	3.00	1.69	2.65	4.49e-08§	8.47e-01§	0.47	16.1± 1.6
CSIMon-000685	J06404547+0949101	M2	0.50	0.36	1.93	4.37e-09	1.98e-02	-	-
CSIMon-000697	J06413455+0936325	M1	0.33	0.45	1.41	2.40e-09	1.58e-02	0.12	14.2± 3.0
CSIMon-000717	J06411511+0926443	M0.5	0.76	0.53	2.02	2.82e-08	1.81e-01	0.37	18.8± 3.6
CSIMon-000718	J06410416+0920443	M2:M2.5	0.60	0.34	2.16	4.90e-09	1.89e-02	-	-
CSIMon-000727	J06412364+0947163	M2	0.18	0.35	1.15	4.57e-10§	5.61e-04§	0.04	11.4± 3.5
CSIMon-000733	J06404982+0947309	M4	1.12	0.25	3.38	1.41e-08§	7.58e-04§	0.32	12.0± 5.0
CSIMon-000736	J06410689+0929240	M0	0.49	0.64	1.53	2.24e-09	2.31e-02	0.00	14.6± 3.0
CSIMon-000753	J06410597+0939142	M5	0.27	0.21	1.79	3.47e-09	1.01e-02	1.22	47.8± 6.4
CSIMon-000754	J06405302+0952594	M0	0.45	0.64	1.46	1.41e-09	7.24e-03	0.18	75.8± 2.3
CSIMon-000765	J06405363+0933247	K1	1.88	1.45	1.76	6.48e-09§	1.54e-01§	0.01	22.2± 2.4
CSIMon-000766	J06404837+0948385	M0.5	0.41	0.53	1.47	2.14e-08	1.89e-01	0.57	14.6± 4.6
CSIMon-000774	J06405884+0930573	K2.5	3.10	1.83	2.49	5.05e-09§	9.33e-02§	0.02	31.4± 3.5
CSIMon-000795	J06411257+0952311	G:V:e	4.20	1.51	2.11	6.59e-08§	3.77e-01§	0.57	32.2± 7.0
CSIMon-000796	J06405784+0951089	M2.5	0.46	0.33	1.93	3.44e-10§	1.48e-03§	0.00	41.1± 7.8
CSIMon-000798	J06405694+0948407	F9	5.90	1.57	2.30	9.33e-09§	1.60e-01§	0.34	20.2± 5.3
CSIMon-000804	J06405571+0951138	K5.5	0.85	1.06	1.67	6.76e-09	4.32e-02	0.01	18.3± 2.0

Table 3.2: Stellar parameters of the CTTSs - continued

CSIMon ID	2MASS ID	Sp type	L_{bol} ($L_\odot$)	M_* ($M_\odot$)	R_* ($R_\odot$)	$\dot{M}_{acc}$ ($M_\odot$/yr)	L_{acc} ($L_\odot$)	r	$v \sin i$ (km/s)
CSIMon-000808	J06405159+0928445	K4	0.91	1.24	1.52	1.70e-08	3.38e-01	0.14	13.0± 4.0
CSIMon-000810	J06410982+0927122	K5	2.90	1.20	2.95	1.24e-09§	1.41e-02§	0.03	56.7± 3.1
CSIMon-000811	J06404321+0947072	K6	1.08	0.91	1.97	6.75e-09§	6.29e-02§	0.10	15.1± 1.7
CSIMon-000823	J06405014+0957039	M3	0.25	0.30	1.49	7.76e-10	1.36e-04	2.94	-
CSIMon-000824	J06410183+0938411	K4	1.96	1.48	2.23	3.28e-09§	5.09e-04§	0.11	17.1± 1.8
CSIMon-000836	J06404729+0947274	M2	0.18	0.35	1.16	5.25e-10^u	-	0.24	10.3± 4.4
CSIMon-000846	J06411286+0926148	K4	4.21	1.59	2.98	4.77e-07§	6.40e+00§	0.36	16.9± 2.2
CSIMon-000860	J06415492+0942527	M2.5	0.17	0.32	1.18	5.62e-09	3.70e-02	0.59	16.0± 5.7
CSIMon-000861	J06410080+0952075	K8.5	0.47	0.68	1.47	5.62e-08	6.45e-01	0.20	16.5± 3.7
CSIMon-000873	J06411320+0926103	K5	2.70	1.20	2.83	5.77e-08§	6.16e-01§	0.02	46.2± 1.5
CSIMon-000877	J06411678+0927301	K4	1.16	1.33	1.71	2.83e-08§	5.53e-01§	0.20	19.2± 3.3
CSIMon-000879	J06410338+0940448	M1	0.65	0.45	1.99	1.23e-08	3.54e-02	0.00	14.3± 1.9
CSIMon-000893	J06410457+0938308	M3	0.26	0.30	1.52	2.29e-08	1.08e-01	0.90	27.8± 6.3
CSIMon-000904	J06404278+0933350	K7	0.39	0.74	1.30	7.36e-11	7.90e-02	0.20	15.9± 4.7
CSIMon-000914	J06405191+0937558	G0:G5	0.30	-	0.54	-	-	-	-
CSIMon-000919	J06411329+0931503	M4	0.76	0.25	2.80	2.04e-08	4.42e-02	0.07	36.3± 6.8
CSIMon-000926	J06410642+0928388	M1.5	0.25	0.40	1.31	5.01e-09	3.70e-02	0.00	10.1± 4.5
CSIMon-000928	J06412562+0934429	M0	0.58	0.63	1.65	5.62e-09	5.29e-02	0.00	16.2± 2.2
CSIMon-000931	J06411808+0938253	M3	0.23	0.29	1.43	5.62e-10	9.49e-04	1.24	-
CSIMon-000936	J06410715+0927294	K5	1.32	1.20	1.98	7.08e-08	1.05e+00	0.47	14.2± 1.6
CSIMon-000937	J06405255+0952059	K7	1.01	0.69	2.10	1.02e-08	3.88e-03	0.07	26.4± 3.2
CSIMon-000945	J06404989+0936494	K4	1.37	1.40	1.86	7.41e-08	1.38e+00	0.86	12.9± 1.8
CSIMon-000996	J06404131+0951023	K7	0.92	0.69	2.00	2.04e-07	8.62e-01	0.43	14.5± 4.6
CSIMon-001003	J06402564+0959597	M4	0.22	0.24	1.52	2.00e-09	7.74e-03	0.69	11.8± 4.2
CSIMon-001011	J06404052+0935011	M4.5	0.03	0.14	0.57	1.15e-09	6.93e-03	0.68	-
CSIMon-001022	J06403911+0950586	K4	2.07	1.50	2.30	6.31e-09§	8.32e-02§	0.35	14.4± 1.7
CSIMon-001031	J06404005+0935029	K4	1.81	1.46	2.14	1.66e-09§	2.85e-02§	0.77	18.6± 3.7
CSIMon-001033	J06404102+0947577	K7	0.64	0.70	1.67	2.04e-08§	5.84e-03§	0.03	14.1± 2.0
CSIMon-001036	J06403200+0949355	M2	0.27	0.36	1.41	6.17e-08§	2.36e-01§	0.59	-
CSIMon-001037	J06403086+0934405	K1	1.84	1.45	1.74	9.70e-09§	2.03e-01§	0.09	32.2± 1.8
CSIMon-001038	J06402262+0949462	M0	0.32	0.66	1.23	1.51e-09§	7.89e-04§	0.29	14.2± 3.2
CSIMon-001053	J06404113+0952565	K6	1.02	0.91	1.92	8.51e-09	1.32e-01	0.21	13.6± 2.2
CSIMon-001054	J06403652+0950456	M2	0.63	0.36	2.17	2.09e-07	8.26e-02	0.43	12.3± 5.6
CSIMon-001055	J06404041+0950504	K7	2.70	0.68	3.41	4.04e-08§	2.03e-01§	0.00	37.1± 3.0
CSIMon-001059	J06402063+0940499	M5	0.33	0.22	1.97	3.63e-09	-	1.23	5.6± 3.1
CSIMon-001061	J06402416+0934124	M0	0.44	0.64	1.45	4.17e-08	4.51e-01	1.09	14.9± 3.6
CSIMon-001064	J06403518+0951567	M1	0.91	0.45	2.35	1.45e-08§	2.06e-02§	0.00	25.1± 6.9
CSIMon-001076	J06403819+0929524	M1	0.26	0.45	1.25	4.57e-10§	4.15e-04§	0.39	15.3±11.0
CSIMon-001094	J06403164+0948233	K5	0.74	1.14	1.49	1.58e-08§	1.62e-01§	0.22	21.3± 2.1

Table 3.2: Stellar parameters of the CTTSs - continued

CSIMon ID	2MASS ID	Sp type	L_{bol} ($L_\odot$)	M_* ($M_\odot$)	R_* ($R_\odot$)	$\dot{M}_{acc}$ ($M_\odot$/yr)	L_{acc} ($L_\odot$)	r	$v \sin i$ (km/s)
CSIMon-001099	J06404136+0954138	G1	4.80	1.52	2.16	3.23e-09§	1.14e-01§	0.00	26.8± 3.1
CSIMon-001100	J06403934+0934455	K6	2.10	0.90	2.75	3.19e-09§	2.62e-02§	0.72	23.1± 3.2
CSIMon-001114	J06393339+0952017	M1.5	0.85	0.40	2.40	4.27e-08	1.77e-01	0.33	32.6± 4.5
CSIMon-001131	J06393441+0954512	M2	0.55	0.36	2.01	2.14e-08	9.45e-02	0.07	12.3± 4.5
CSIMon-001132	J06402587+0950576	M2.5	0.31	0.33	1.58	2.82e-07	4.32e-02	1.73	12.5± 7.6
CSIMon-001140	J06394147+0946196	K4	1.10	1.31	1.67	7.76e-09^u	-	0.25	22.4± 2.3
CSIMon-001142	J06403446+0935182	M2	0.35	0.36	1.61	6.07e-10§	3.41e-03§	0.44	12.8± 5.0
CSIMon-001144	J06402309+0927423	K5	0.67	1.12	1.42	2.00e-08	3.86e-01	1.15	18.3± 1.5
CSIMon-001149	J06403059+0950147	M3	0.79	0.30	2.63	5.50e-09^u	-	0.19	12.9± 4.0
CSIMon-001156	J06403357+0933363	M2.5:M3	0.15	0.30	1.12	4.27e-09	2.83e-02	1.01	16.0± 9.4
CSIMon-001157	J06402009+0928285	K6	0.63	0.95	1.51	3.98e-09	5.78e-02	0.07	14.4± 2.4
CSIMon-001165*	J06404192+0943551	M3	0.13	0.28	1.07	1.86e-09	4.33e-03	-	16.8± 2.3‡
CSIMon-001167	J06403787+0934540	M3	0.57	0.30	2.23	4.37e-09	3.39e-03	0.00	16.0± 3.1
CSIMon-001171	J06393398+0949208	K7	0.70	0.70	1.75	-	-	0.17	10.5± 3.9
CSIMon-001174	J06401370+0956305	M2	0.58	0.35	2.08	6.17e-08	2.52e-01	0.22	14.7± 4.6
CSIMon-001181	J06401801+0950220	M2	0.22	0.35	1.27	1.58e-10§	1.09e-03§	0.57	37.6± 7.8
CSIMon-001187	J06401417+0934283	M1.5	0.32	0.40	1.46	1.91e-09	1.27e-02	1.47	6.7± 5.4
CSIMon-001197	J06402616+0937092	M2.5:M3	0.19	0.30	1.25	6.61e-10^u	-	1.08	45.1±11.5
CSIMon-001199	J06404184+0951445	K5	1.23	1.20	1.92	2.04e-08§	4.66e-03§	0.00	35.2± 1.1
CSIMon-001201	J06403662+0948229	K5	0.81	1.16	1.56	1.59e-10§	2.97e-03§	0.02	11.8± 2.2
CSIMon-001203	J06393939+0945215	K6	0.83	0.93	1.72	2.82e-08	3.69e-01	0.19	13.3± 2.4
CSIMon-001217	J06403665+0952032	K4	1.23	1.30	1.77	8.91e-08§	1.53e-01§	1.36	17.8± 3.0
CSIMon-001219	J06402744+0952303	M4	0.15	0.23	1.25	3.98e-10§	2.69e-04§	-	-
CSIMon-001223	J06400600+0949426	M2	0.42	0.36	1.77	1.26e-08	6.32e-02	0.25	15.6± 3.6
CSIMon-001234	J06401113+0938059	K6	0.76	0.94	1.65	1.45e-09	2.02e-02	0.91	10.7± 2.1
CSIMon-001241	J06403378+0948438	M3	0.35	0.30	1.75	6.61e-09§	1.87e-03§	0.00	13.6± 4.0
CSIMon-001249	J06402027+0956063	M3	1.03	0.30	3.01	2.95e-08	7.23e-02	0.00	21.3± 4.5
CSIMon-001275	J06402877+0931002	K4	4.60	1.60	3.42	2.51e-08§	1.50e-01§	0.09	15.2± 3.1
CSIMon-001279	J06403123+0931071	K6	1.22	0.91	2.09	4.58e-10§	5.02e-03§	0.10	30.1± 1.9
CSIMon-001296*	J06390374+0940234	K7	0.91	0.69	1.99	7.94e-09	6.61e-02	-	11.0± 1.6‡
CSIMon-001304	J06401361+0924494	K0	6.20	2.17	3.03	-	-	0.16	61.1± 4.6
CSIMon-001308*	J06395924+0927245	M0	0.53	0.63	1.59	1.91e-08	1.85e-01	-	9.9± 2.0‡
CSIMon-001580*	J06410285+1007119	M1	0.27	0.45	1.27	6.46e-09	5.53e-02	-	11.4± 2.0‡
CSIMon-006079	J06392911+0942386	M1	0.57	0.45	1.87	7.59e-09	4.52e-02	3.35	5.7± 3.3
CSIMon-006975*†	J06395318+1001137	M2.5	-	-	-	-	-	-	-
CSIMon-006986*	J06390996+1005127	K7:M1	0.33	0.57	1.31	2.82e-09	2.96e-02	-	-
CSIMon-014132*	J06390355+0916159	M3.5	0.37	0.28	1.88	-	-	-	-

Notes. * Not included in the FLAMES 2014 campaign (centered on the [OI] 6300Å line).

† Not included in the CFHT campaign.

‡ Values of $v \sin i$ determined using spectra centered on Hα, rather than the [OI] 6300Å line, since these stars were not included in the FLAMES 2014 campaign.

§ Values of $\dot{M}_{acc}$ and L_{acc} were derived from EW(Hα).

^{u} Upper limits.

Table 3.3: Stellar parameters of the WTTSs used as photospheric templates

CSIMon ID	2MASS ID	Sp type	L_{bol} ($L_\odot$)	M_* ($M_\odot$)	R_* ($R_\odot$)
CSIMon-000020	J06420924+0944034	K7	0.44	0.71	1.39
CSIMon-000029	J06410328+0957549	K7	0.64	0.70	1.68
CSIMon-000057	J06410393+0958094	M3	0.53	0.30	2.16
CSIMon-000066	J06410357+1000353	M1	0.39	0.45	1.53
CSIMon-000071	J06410025+0958496	K1.5	2.60	1.69	2.14
CSIMon-000104	J06410417+0952020	K6	0.98	0.91	1.87
CSIMon-000145	J06412346+0945586	K7	0.44	0.71	1.39
CSIMon-000172	J06411031+0921495	M2.5	0.55	0.33	2.10
CSIMon-000336	J06411889+0939440	K3	0.34	0.82	0.86
CSIMon-000389	J06404875+0932425	K4	0.96	1.25	1.56
CSIMon-000427	J06404244+0932206	K4	0.66	1.12	1.30
CSIMon-000444	J06414457+0942124	M2	0.41	0.36	1.75
CSIMon-000445	J06420256+0936525	K6	0.58	0.95	1.44
CSIMon-000548	J06410856+0942515	M1	0.45	0.45	1.66
CSIMon-000555	J06412445+0932451	M5	0.18	0.19	1.45
CSIMon-000559	J06412425+0931541	K6	0.63	0.95	1.50
CSIMon-000565	J06410077+0951223	K4.5	1.91	1.35	2.29
CSIMon-000606	J06411446+0933214	K5	1.05	1.20	1.77
CSIMon-000622	J06412179+0945309	K5	0.78	1.16	1.53
CSIMon-000779	J06404819+0927008	M5	0.24	0.21	1.67
CSIMon-000819	J06412918+0939359	G5	5.20	1.65	2.37
CSIMon-000901	J06404335+0950595	K7	0.95	0.69	2.03
CSIMon-001089	J06402989+0950104	K2	1.94	1.55	1.90
CSIMon-001158	J06392625+0941108	M0	0.86	0.62	2.01
CSIMon-001172	J06400637+0939335	K7:M0	0.92	0.65	2.04
CSIMon-001192	J06403878+0921382	K3	0.47	0.93	0.95
CSIMon-001247	J06402894+0942171	K6	0.78	0.93	1.68
CSIMon-001248	J06394672+0940539	G5	3.10	1.39	1.84
CSIMon-001251	J06403183+0936006	M2.5	0.50	0.33	2.00
CSIMon-001256	J06394157+0934405	G0	3.30	1.36	1.73
CSIMon-001264	J06403061+0946106	K4	1.13	1.32	1.70
CSIMon-001307	J06392294+0936168	K0	1.25	1.17	1.36

Chapter 4

Stars with extinction dominated light curves

In this chapter, we will focus on those CTTSs whose photometric behavior is dominated by extinction events that occur when circumstellar material obscures the stellar photosphere. For these phenomena to be observed, the star-disk systems must be viewed at high inclinations[1] in order for the material on or near the accretion disk to occasionally pass in front of the observer's line of sight. In many cases the short periods indicate that the occulting material is located in the innermost region of the accretion disk (few 0.1 au from the stellar surface), where the disk interacts strongly with the stellar magnetosphere and accretion columns or streams are formed. In this way, these systems represent an opportunity to study the interaction between the magnetosphere and the very inner disk through indirect measurements, in a region where direct imaging is not yet possible. By analyzing these systems simultaneously in a range of different wavelengths, we can attempt to better understand the processes that occur in this region.

[1] Throughout this work, inclination refers to the angle between a star's rotation axis and the observer's line of sight: low inclination means a system viewed close to pole-on, while high inclination means a system viewed close to edge-on.

4.1 Selection of candidates for extinction dominated light curves

The first group of stars we are interested in for the current analysis is the one consisting of CTTSs with AA Tau-like light curves. As was mentioned in Section 3.4, these light curves present a relatively stable maximum brightness level interrupted by quasi-periodic flux dips that are neither spot-like nor eclipse-like in nature. These dips vary by on average 25% in width and 30% in amplitude from one rotation cycle to the next. Their periods range from 3 to 10 days, which is consistent with Keplerian rotation near the co-rotation radius (the distance at which the circumstellar disks rotates at the same angular velocity as the stellar surface). Within the main flux dips, there are usually other narrower, shallower flux dips that are not necessarily periodic and can have significant structures.

The light curves we describe as AA Tau-like are based on observations of the CTTS AA Tau that took place in 1995, when it presented this quasi-periodic behavior (Bouvier et al. 1999). However, later studies of this CTTS showed that its photometric behavior varies significantly between observations separated by a few years (Bouvier et al. 2003, 2007, 2013; Cox et al. 2013). At times it shows the quasi-periodic flux dips attributed to an inner disk warp, at times it presents more than one flux dip per stellar rotation period, and at times there is almost no variability at all (see Figure 1.8, page 10). In our sample of CTTSs observed by CoRoT, there are some light curves that are similar to the 1995 AA Tau light curve, but that either do not have a well-defined maximum brightness, or show relatively weak periodicity (for example, see star CSIMon-001054 in Figure 4.14). Cody et al. (2014) do not classify these as AA Tau-like light curves, but they are important in the context of this study because they may represent systems that are undergoing events similar to those that AA Tau underwent across the years. Therefore, we refer to these light curves as candidate AA Tau-like light curves and we analyze these stars' photometric variability in the same way as the stars that present classical AA Tau-like light curves. We wish to try to establish whether the same physical mechanism that was proposed to explain the photometric variability of AA Tau itself, meaning the existence of an inner disk warp brought on by the disk-magnetosphere interaction viewed at a high inclination, could also be responsible for the variability of this group of stars.

The second group of stars that is important to this analysis is the one consisting of CTTSs whose photometric variability is dominated by irregular, non-periodic extinction events from circumstellar material. The phenomenon observed in these light curves is similar to those observed in UX Ori-type objects (UXors), which exhibit deep, non-periodic algol-like minima caused by extinction from circumstellar material in the observer's line of sight (see the review by Grinin 2000). Both the UXors and our stars with aperiodic extinction events show evidence of being seen at high inclinations, which is favorable for circumstellar material located near the disk plane to intersect our line of sight. UXor flux dips typically present larger amplitudes and longer duration than the stars in our sample, probably because of

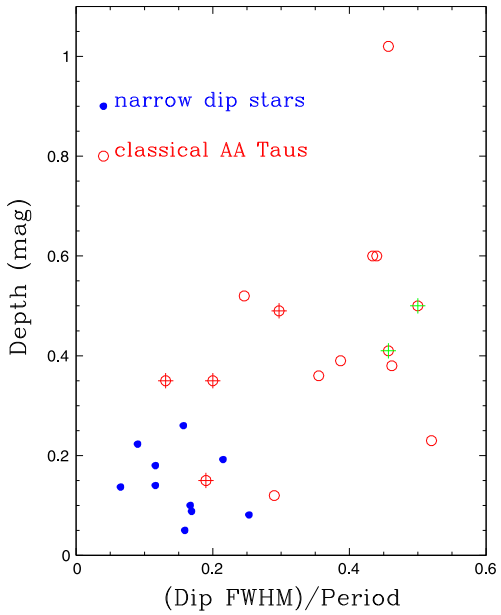

Figure 4.1: Comparison of average flux dip depth vs. the ratio between dip full width at half maximum (FWHM) and period, for AA Tau-like CoRoT light curves and CoRoT light curves with periodic, narrow dips. Stars marked with red crosses represent those whose flux dips are sometimes narrow and sometimes broad. Stars marked with green plus signs represent those that have periodic, narrow flux dips superposed onto AA Tau-like flux dips. Figure from Stauffer et al. (2015).

larger scale disk instabilities. They are also much more common among Herbig AeBe stars, though some CTTSs have been classified as UXors in the past (Herbst & Shevchenko 1999; Grinin 2000). Some of the stars in our sample with this aperiodic behavior could very likely be UXors. At least one of them, CSIMon-000433, has shown a clear blueing during flux minima (Venuti et al. 2015), which is characteristic of UXors.

A final group of stars that present evidence of extinction events in their light curves was studied in detail by Stauffer et al. (2015). These stars present narrow flux dips that are generally shallower than in AA Tau-like light curves, and nearly Gaussian shaped, while AA Tau-like light curves usually show very irregularly shaped dips, often with significant structure in the minima. The narrow flux dips are usually periodic over timescales of tens of days, with periods that are consistent with Keplerian rotation periods of the inner disk region. They are often superposed onto other types of variability, that can be periodic or not. We calculated the depth, in magnitudes, and full width at half maximum (FWHM), in days, of the flux dips in the AA Tau-like light curves and in the light curves with narrow dips, in order to compare the two. Figure 4.1 shows that they seem to represent two different populations whose properties slightly overlap. However, there are many cases where part of a light curve's flux dips can be considered narrow (FWHM/period $\lesssim 0.3$) and part cannot. These are represented by red crosses in Figure 4.1. Green crosses represent light curves

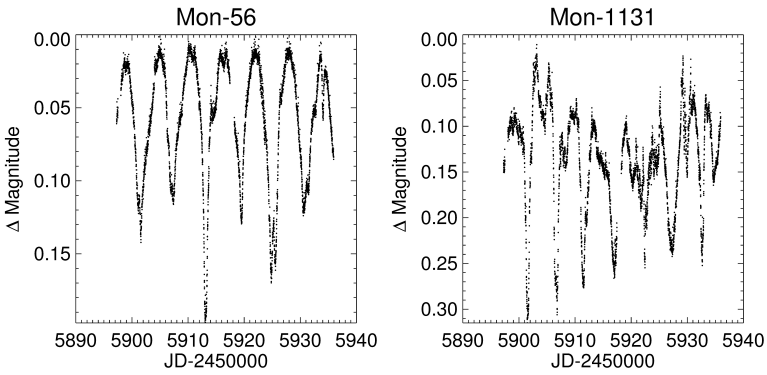

Figure 4.2: CoRoT light curves of the stars CSIMon-000056 (left) and CSIMon-001131 (right). Their light curves resemble AA Tau-like light curves, but the dips' FWHM are small enough for them to be considered narrow dips.

that have narrow dips superposed onto broader, AA Tau-like flux dips. There are also two stars in our sample, CSIMon-000056 and CSIMon-001131 (Figure 4.2), whose light curve classification is not obvious. They are studied in Stauffer et al. (2015) as having narrow flux dips, but since there is no clear lower limit to the width a flux dip produced by an AA Tau-like mechanism should have, these two stars are also studied here and in McGinnis et al. (2015) as stars with possible AA Tau-like light curves. In Stauffer et al. (2015), we discuss whether these narrow dips truly represent a different physical phenomenon than the AA Tau-like light curves, or whether they may be a specific case of the latter.

Table 4.1 shows information on the stars in our sample that are considered to have AA Tau-like or aperiodic extinction-dominated light curves in either epoch, or that present narrow dips in their light curves. The CSIMon ID is an internal naming scheme devised for the CSI 2264 campaign (see Cody et al. 2014), and comprises all cluster members, candidates and field stars in the NGC 2264 field of view. For brevity, throughout the remaining text, we shall eliminate 'CSI' and the leading zeros and replace CSIMon-000xxx with Mon-xxx (for instance, CSIMon-000250 is expressed as Mon-250). The CoRoT ID is the identification number assigned by the CoRoT satellite to all objects it has observed. In some cases where the same star was observed in both epochs, two different CoRoT IDs were assigned to the same star. For these stars we present the ID from the 2008 observation.

The third and fourth columns of Table 4.1 show how the light curve was classified in one epoch or the other. Those labeled with AAT present AA Tau-like light curves, those labeled with AATc are those that were not classified as AA Tau-like by Cody et al. (2014), but that we consider to be candidate AA Tau systems, those labeled as Ap show aperiodic extinction-dominated light curves, and those labeled as ND present narrow dips. For six stars, a possible AA Tau-like variability was found in both epochs, meaning the mechanism responsible for this variability can be stable on a timescale of a few years. Four stars that present AA Tau-like variability were only observed in one epoch. There are thirteen stars

Table 4.1: Stars with AA Tau-like and variable extinction-dominated light curves.

CSIMon ID	CoRoT ID	LC type (2008)	LC type (2011)	P (days) (2008)	P (days) (2011)	$v \sin i$ (km/s)	α_{IRAC}	F_{disk}/F_* at 4.5μm
CSIMon-000021	223980412	ND	ND	3.23	3.16	19.2±1.5	-	-
CSIMon-000056	223994760	AAT/ND	AAT/ND	5.71	5.86	11.1±2.2	-1.21	1.0
CSIMon-000126	616895876	-	Ap	-	0.35[a]	14.0±2.0	-1.04	4.8
CSIMon-000250*	223980688	AATc	AAT	8.32	8.93	9.8±2.2	-2.10	2.1
CSIMon-000296*	500007209	Ap	AAT	2.51[a]	3.91	17.3±2.6	-2.14	1.6
CSIMon-000297*	223976747	AAT	Ap	3.16	-	30.8±1.8	-2.24	1.6
CSIMon-000314	500007930	Ap	Ap	-	3.38[a]	24.0±2.0	-2.61	0.7
CSIMon-000325	605538641	-	Ap	-	-	-	-1.38	-
CSIMon-000358	400007959	Ap	AAT	-	5.86	-	-1.55	1.3
CSIMon-000378	616872605	-	ND	-	11.1	10.4±0.4	-	-
CSIMon-000379*	223981811	Ap	AATc	3.73[a]	3.68	25.0±1.2	-1.91	2.2
CSIMon-000433	616919770	-	Ap	-	-	-	-2.05	-
CSIMon-000441*	223980048	AAT	Ap	4.06	-	-	-1.41	1.0
CSIMon-000456	616872585	-	AAT	-	5.03	19.3±1.5	-1.62	2.5
CSIMon-000498*	500007120	AATc	AAT	4.23	4.28	24.1±2.4	-1.41	2.9
CSIMon-000566	400007955	ND	ND	4.5	4.5	-	-	-
CSIMon-000619	603402479	Ap	Ap	-	-	-	-1.11	11.5
CSIMon-000654*	500007610	AATc	Ap	4.66	-	18.0±3.0	-0.92	-
CSIMon-000660*	223980693	AAT	AAT	5.25	5.25	21.4±2.5	-1.72	3.4
CSIMon-000667*	223987997	Ap	Ap	-	-	24.0±2.0	-0.54	1.5
CSIMon-000717	616943877	-	Ap	-	-	-	-1.43	1.4
CSIMon-000774†	223980264	AAT	Ap	3.46	-	30.7±1.3	-1.25	2.1
CSIMon-000811*	500007460	Ap	AAT	-	7.88	13.5±1.7	-1.08	3.0
CSIMon-000824*	223981023	AAT	-	7.05	-	14.8±1.4	-2.02	-
CSIMon-000928*	223987178	AAT	Ap	9.92	-	20.1±2.8	-1.11	1.4
CSIMon-001037	223973200	Ap	Ap	-	8.93[a]	32.0±3.0	-1.29	11.3
CSIMon-001038	602095739	-	Ap	-	-	-	-1.73	3.0
CSIMon-001054*	400007538	Ap	AATc	-	4.08	20.4±2.0	-1.10	2.0
CSIMon-001076*	400007702	ND	-	5.8	-	9.8±2.4	-	-
CSIMon-001131	223957455	Ap	AAT/ND	5.15[a]	5.18	8.8±1.7	-1.38	1.4
CSIMon-001140	223959618	AAT	AAT	3.87	3.90	19.8±2.3	-2.37	0.8
CSIMon-001144*	223971231	Ap	Ap	-	-	24.0±3.0	-1.73	3.75
CSIMon-001165*	-[b]	-[b]	-[b]	-	-	16.8±2.3	-	-
CSIMon-001167*	400007528	Ap	AATc	8.30[a]	8.78	11.3±2.1	-1.87	1.2
CSIMon-001296	223948127	Ap	AAT	-	9.75	11.0±1.6	-1.47	-
CSIMon-001308	223964667	AAT	AAT	6.45	6.68	9.9±2.0	-1.87	0.7
CSIMon-001580	223981250	ND	-	7.1	-	11.4±2.0	-	-
CSIMon-006975	616803898	-	ND	-	2.8	-	-	-
CSIMon-006986	223950070	AATc	-	6.16	-	-	-1.22	-
CSIMon-014132	602070634	-	AAT	-	4.48	-	-1.50	-

Notes. *There is FLAMES/GIRAFFE spectra in Hα taken simultaneously with the second CoRoT epoch.
†There is FLAMES/UVES spectra taken simultaneously with the second CoRoT epoch.
[a]Low probability periods found during a periodogram analysis of the light curves.
[b]This star was not observed by CoRoT, but was considered to have narrow dips in its *Spitzer* IRAC light curve with a period of $\sim$ 5.5 days (Stauffer et al. 2015).

that were observed in both epochs and classified as AA Tau-like in one and aperiodic in the other. Of these, five displayed AA Tau-like behavior in 2008, yet in 2011 presented aperiodic variability, while the other eight showed the opposite trend. This may be an indication that these stars underwent a change in accretion regime in the less than four years between observations (this possibility is discussed in Section 4.7). Another five stars were classified as having an aperiodic extinction-dominated light curve in both epochs. Five more stars with light curves dominated by aperiodic extinction were only observed in 2011.

It is interesting to note that, though many stars suffered a transition between AA Tau-like and aperiodic extinction-dominated light curves, no star suffered a transition between AA Tau-like or aperiodic extinction and spot-like or accretion burst-dominated light curves (Sousa et al. 2016). This is likely due to the systems' inclinations, as systems viewed at high inclinations would favor extinction events and may hide most of the variability due to spots on the stellar surface, whereas for systems viewed at low inclinations we should observe less extinction events since it becomes difficult for disk material to intersect our line of sight.

The fifth and sixth columns of Table 4.1 show the periods that were measured for each CoRoT light curve in the first (2008) and second (2011) epochs. Periods given for light curves that were classified as aperiodic correspond to low probability periods found during a periodogram analysis of the light curves. The seventh column shows the values of projected rotational velocity ($v \sin i$) measured from the spectra centered on Hα (Section 3.3.3). The eighth column shows the α_{IRAC} index calculated for each star. This index corresponds to the slope of the spectral energy distribution (SED) between 3.6μm and 8μm and it is a good indicator of the amount of dust present in the inner accretion disk (see 4.2). The ninth column shows the ratio of disk flux to stellar flux at 4.5μm, estimated from the stars' SEDs.

4.2 Comparing optical and infrared light curves

Of the 33 stars in our sample that present AA Tau-like or aperiodic extinction-dominated CoRoT light curves, a total of 29 have simultaneous *Spitzer* observations during the CSI2264 campaign in 2011. Figure 4.3 shows these stars' optical CoRoT and infrared *Spitzer* IRAC 3.6μm and 4.5μm light curves plotted together. CoRoT flux was transformed into magnitude using its largest value as magnitude zero, then shifted to overlap the *Spitzer* IRAC data. Of these 29 stars, we see that the 4 stars Mon-660, Mon-811, Mon-1140, and Mon-1308 show very similar behavior in both bands, with their AA Tau-like modulation appearing in the infrared (IR) as well as in the optical. Another five stars, Mon-297, Mon-314, Mon-433, Mon-441, and Mon-456, also present similar behavior in the two bands, with minima and maxima generally coinciding in the IR and optical, but their light curves do not overlap as well as the first group. There are nine stars that correlate in some parts of their IR and optical light curves, while other parts behave differently, even showing an anti-correlation at times. They are Mon-56, Mon-126, Mon-358, Mon-654, Mon-717, Mon-774, Mon-1054,

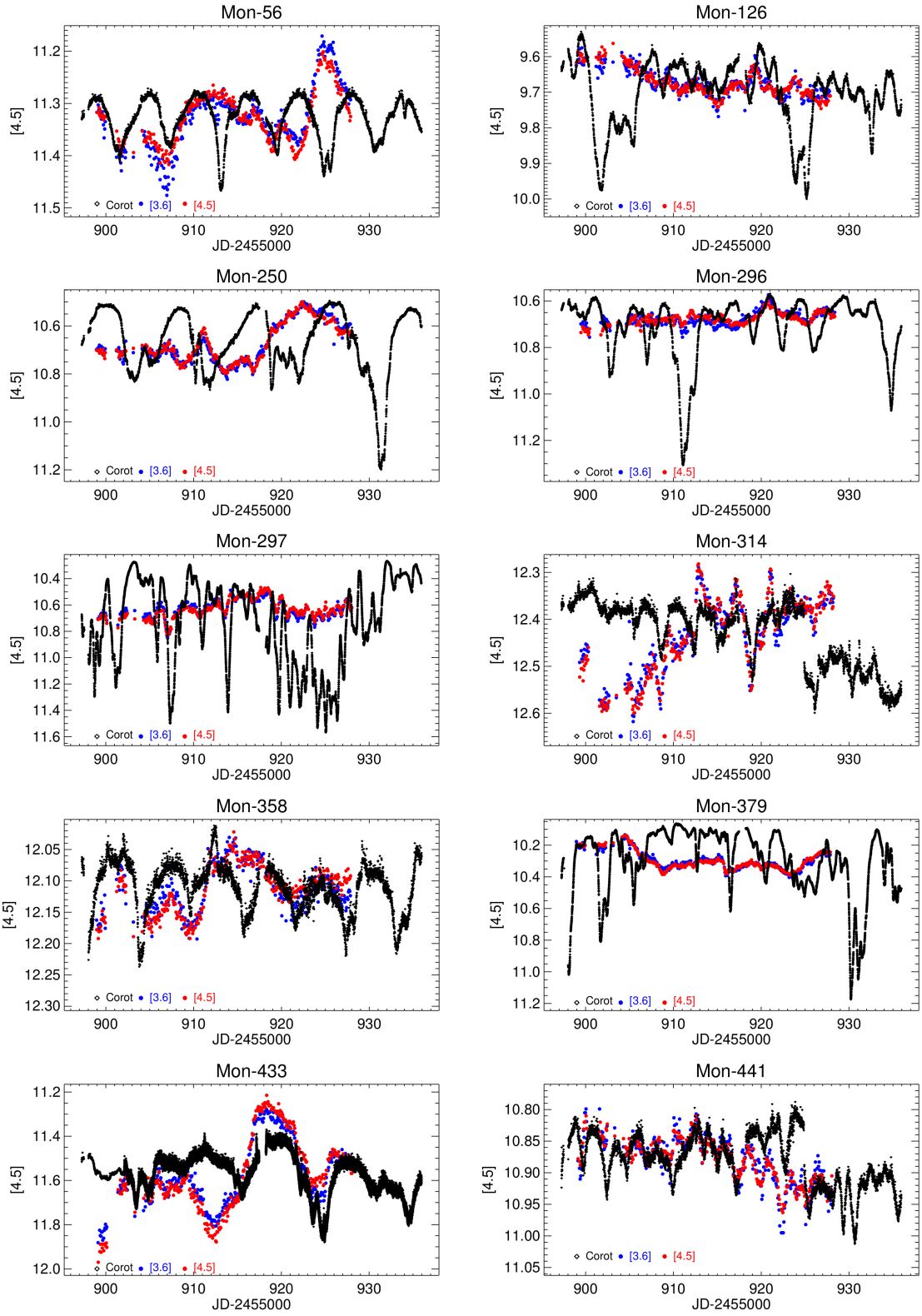

Figure 4.3: *Spitzer* IRAC 3.6μm and 4.5μm light curves (blue and red filled circles, respectively) plotted over CoRoT light curves (black circles). The CoRoT and IRAC 3.6μm light curves were shifted in magnitude for easier comparison.

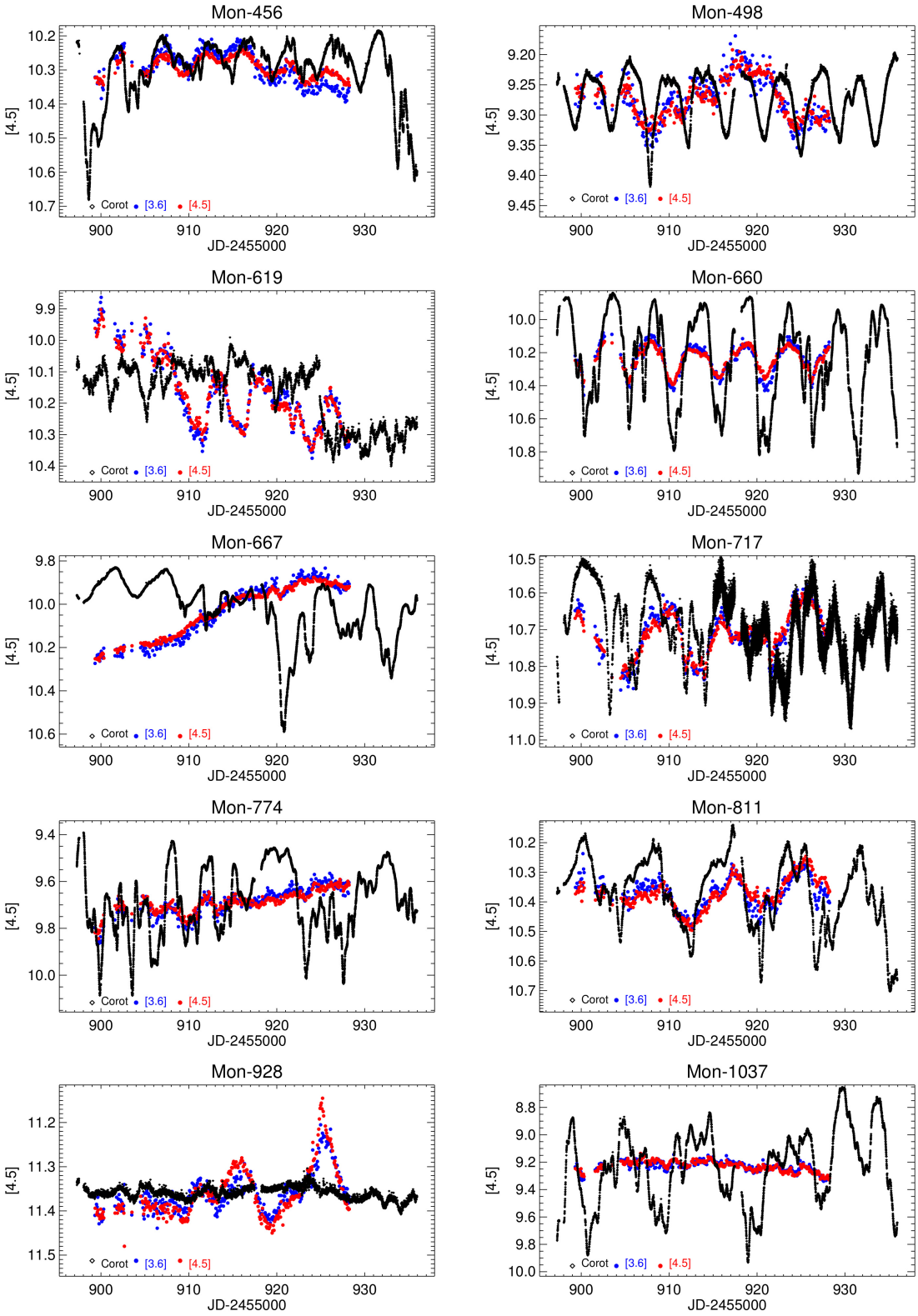

Figure 4.3: Continued.

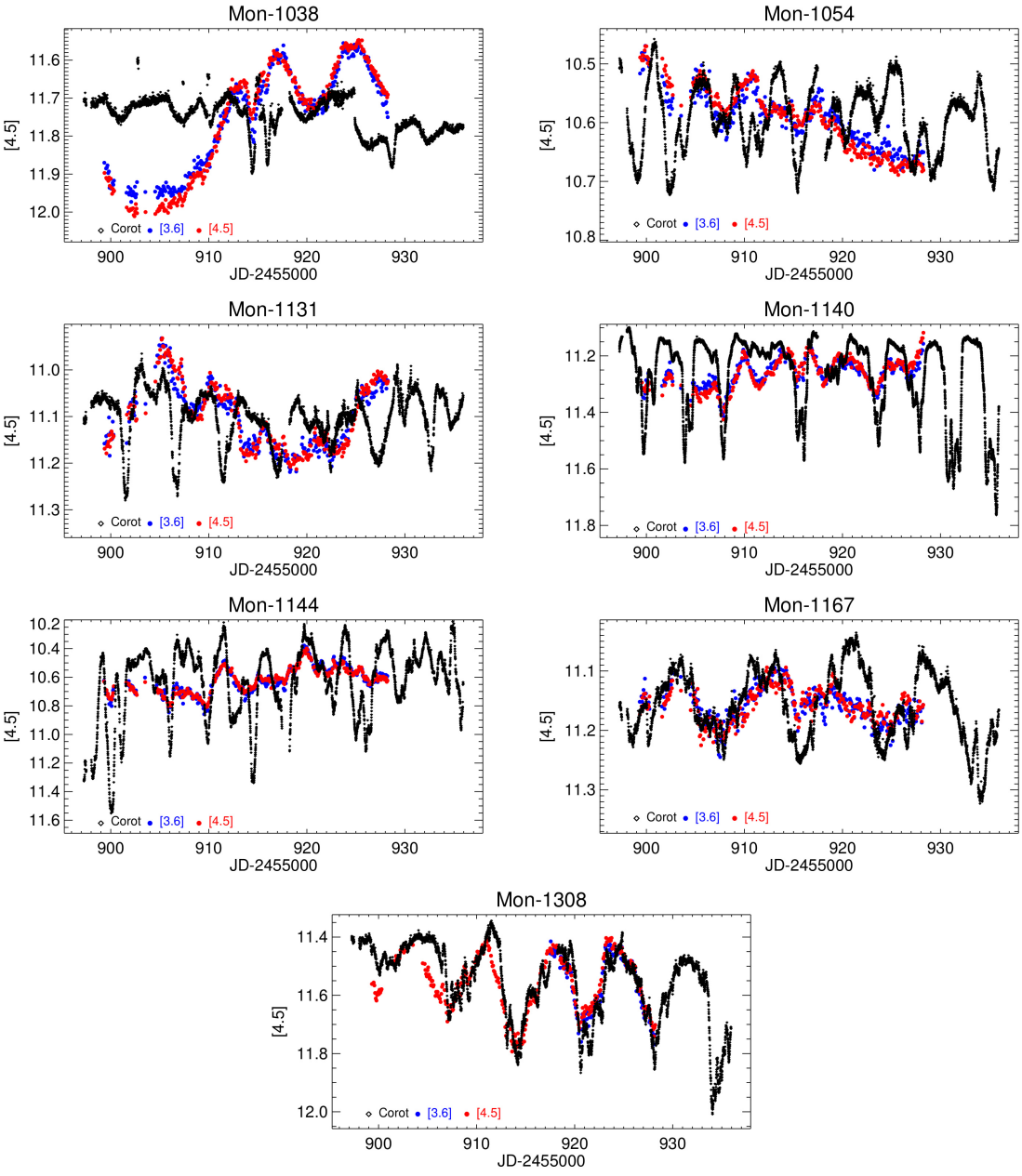

Figure 4.3: Continued.

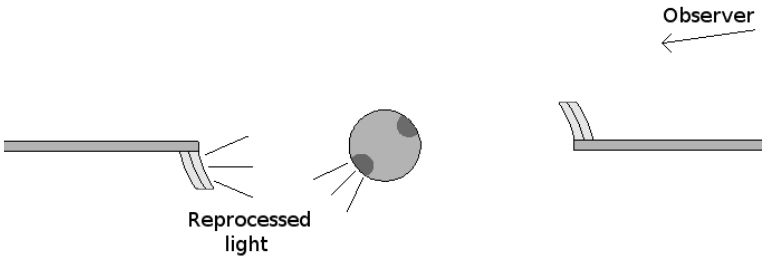

Figure 4.4: When one side of the inner disk warp occults the stellar photosphere, the hot spot and photosphere on the opposite side illuminate the part of the warp on that side. The light is absorbed by the dust and is re-emitted at longer wavelengths.

Mon-1144, and Mon-1167. Another group of 10 stars (Mon-296, Mon-325, Mon-379, Mon-498, Mon-619, Mon-667, Mon-928, Mon-1037, Mon-1038, and Mon-1131) present entirely different IR and optical light curves, showing very little or no feature in common.

One star, Mon-250, shows an almost anti-correlation between its CoRoT and *Spitzer* IRAC light curves throughout most of the simultaneous observations. Its *Spitzer* IRAC maxima tend to coincide with its CoRoT minima, meaning this variability cannot possibly be the consequence of hot or cold spots on the stellar surface, since any variability on the photosphere should be present in all wavelengths. This photometric behavior is also observed in a few other light curves, during one or two rotation cycles (see e.g., Mon-56 in Figure 4.3 between MJD 55923 and MJD 55928, or Mon-1054 between MJD 55909 and MJD 55913). A possible explanation for this increase in IR emission during optical occultations is illustrated in Figure 4.4, and comes from the radiation transfer model of Whitney et al. (2013) applied to a scenario where an accretion shock is associated with an inner disk warp. This is the case of a system accreting in the stable regime, as discussed in the Introduction. Two main accretion columns are formed opposite each other, one in each hemisphere. Each is associated with a hot spot on the stellar surface where an accretion shock is located. The base of each accretion column is associated with part of the inner disk warp. When one part of the warp intersects our line of sight occulting the stellar photosphere, the hot spot opposite it, as well as the rest of the stellar photosphere on that side of the star, illuminates the other part of the inner disk warp. The dust located there would then absorb the light from the hot spot and photosphere and re-emit it at longer wavelengths, causing an increase in emission in the infrared.

The α_{IRAC} index gives us an idea of how much dust is present in the inner accretion disk. Lada et al. (2006) established a criterion to classify the inner disk structures of systems according to this index. Stars with $\alpha_{IRAC} < -2.56$ are considered naked photospheres (systems devoid of dust within a few 0.1 au), those with $-2.56 < \alpha_{IRAC} < -1.80$ are classified as having anemic disks (their inner disk region is optically thin), those with $-1.8 < \alpha_{IRAC} < -0.5$ are classified as having optically thick inner disks, stars with $-0.5 < \alpha_{IRAC} < 0.5$ are clas-

sified as flat spectra sources, and stars with $\alpha_{IRAC} > 0.5$ are considered Class I protostellar objects. Unfortunately, no *Spitzer* IRAC observations were made in 8μm simultaneously with the 2011 CoRoT-*Spitzer* campaign, since by this time *Spitzer* was already operating in its warm mission. Therefore there are no measurements of α_{IRAC} simultaneously with the CoRoT light curves. However, Teixeira et al. (2012) determined α_{IRAC} values for 14 of our 29 stars with simultaneous CoRoT and *Spitzer* observations. For the stars that were not included in Teixeira et al. (2012), we use values of α_{IRAC} calculated by Dr. Luisa Rebull[2] using archival IRAC and Multiband Imaging Photometry for *Spitzer* (MIPS) data (McGinnis et al. 2015). The values are given in Table 4.1.

We note that the objects in our sample whose CoRoT and *Spitzer* light curves correlate best are generally in the transition region between optically thin and optically thick inner disks, with values of α_{IRAC} between -1.4 and -1.9. If there is too much dust within a few au of the star (higher values of α_{IRAC}), the *Spitzer* light curves would be dominated by emission from warm circumstellar dust, rather than occultation of the stellar photosphere. On the other hand, if the portion of the disk occulting the star has very little dust, then the flux dips at IRAC wavelengths would be much shallower than at optical wavelengths, or even non-existent. This may be the case for Mon-296, whose *Spitzer* light curve is relatively constant except for a very shallow dip occurring during the optical light curve's lowest minimum, and a small burst near one of its maxima (Figure 4.3). This star has an anemic disk, according to its value of α_{IRAC}. The star Mon-250, mentioned in the discussion above, also has an anemic disk. It has a value of $\alpha_{IRAC} = -2.10$, among the lowest in this sample. This may seem to conflict with the explanation given for its IR behavior, since a large amount of dust in the inner disk would be necessary for the light that is reprocessed in this region to contribute significantly to the IRAC light curve. However, though its value of α_{IRAC} is relatively low, it is still large enough to indicate that there is some dust in the inner disk, and the scenario depicted in Figure 4.4 may be more related to the geometry of the system than to its α_{IRAC} value. From its SED we estimate that the disk contributes much more than the star to the flux at 4.5 μm (approximately twice as much).

Finally, in order to investigate the distribution of dust in the inner part of accretion disks, we compared the optical and IR light curves that positively correlate with one another and attempted to find which extinction law would be necessary to transform one to the other. We used a very simple approach, assuming an optically thin regime. We estimated extinction laws by measuring the ratio between the depths (in magnitudes) of the dips in the IR and optical light curves (analyzing only those dips where a correlation was observed). We found extinction laws A_λ/A_R (where $\lambda = 3.6\mu$m and 4.5μm) between 0.28 and 0.77.

Interstellar matter (ISM) is typically found to have extinction around $R_V = 3.1$, where $R_V = A_V/E(B-V)$. This corresponds to $A_{3.6}/A_V = 0.05$ and $A_{4.5}/A_V = 0.04$ (from the

[2]California Institute of Technology, USA

relations of Cardelli et al. 1989). Since the CoRoT filter is centered close to the center of the R Johnson filter, we transform these values to A_λ/A_R to better compare with our observations, finding typical interstellar extinction laws of $A_{3.6}/A_R = 0.07$ and $A_{4.5}/A_R = 0.05$. This is much lower than the range of values we found for the stars in our sample, implying that the distribution of dust grains in the inner circumstellar disk region should be very different from ISM, possibly containing larger grains.

The *Spitzer* light curves were not corrected to remove the contribution of disk emission, which is significant in these wavelengths. In order to derive more accurate extinction laws for the inner disk material, an analysis of these stars' SEDs should be conducted in order to determine how strong the contribution of the disk is in these two IRAC bands and attempt to isolate the stellar contribution, as Fonseca (2016) did for the star V354 Mon[3]. She assumed that the main cause of the flux dips in the IR and optical light curves of V354 Mon is occultation of the photosphere by inner disk material and showed that, when only the stellar contribution to the *Spitzer* IRAC light curves is considered, the amplitude of the flux dips becomes very similar to the amplitude measured in the optical CoRoT light curves. This color-neutral extinction indicates that the occulting material is indeed composed of much larger grains than the ISM.

Dr. Luisa Rebull (private communication) estimated the ratio of disk flux to stellar flux at 4.5μm for some of the stars in our sample from their SEDs (the values are given in Table 4.1). However, these SEDs use data from various different observations taken over timescales of a few years. Since these stars are very variable, the ratios of F_{disk} to F_* estimated from these SEDs does not necessarily represent the systems at the time when simultaneous CoRoT and *Spitzer* observations were taken. In order to properly conduct this analysis, simultaneous or quasi-simultaneous data should be used to build the SEDs, as was done for V354 Mon. This is left to a future study. We can, however, state that correcting for the fraction of IR light emitted by the disk would only increase our values of A_λ/A_R, leading to even larger discrepancies with the ISM. We can also see in Figure 4.3 that some of the systems in which the disk contribution at 4.5μm is lowest (Mon-56, Mon-314, Mon-441, and Mon-1308) show light curves with variability amplitudes that are very similar in both IR and optical bands. This is consistent with what Fonseca (2016) found for V354 Mon.

4.3 Color-magnitude diagrams

We constructed color magnitude diagrams using the simultaneous CoRoT and *Spitzer* data for stars that present AA Tau-like light curves or light curves dominated by aperiodic extinction. CoRoT magnitude was plotted against CoRoT magnitude minus *Spitzer* IRAC 4.5μm magnitude. This method alone does not allow us to clearly distinguish between photometric variability due to extinction and variability caused by a configuration of hot and/or cold

[3]This star is known as CSIMon-000660 in this work.

spots on the photosphere. Nevertheless, if we assume that extinction is the main source of the flux dips present in both the CoRoT and IRAC light curves, then we can use these color magnitude diagrams to estimate extinction laws from the slopes[4] of the distributions (Figure 4.5), using the following relation:

$$C = B * (C - I_{4.5}) \tag{4.1}$$

where B is the slope of the distribution, C is the CoRoT magnitude, and $I_{4.5}$ is the IRAC magnitude at 4.5 μm. In this way,

$$\frac{C}{C - I_{4.5}} = B \rightarrow \frac{1}{B} = 1 - \frac{I_{4.5}}{C} \rightarrow \frac{I_{4.5}}{C} = 1 - \frac{1}{B} = \frac{A_{4.5}}{A_R} \tag{4.2}$$

It is important to perform this analysis only on the parts of the light curves where the same phenomenon is responsible for the variability in the optical and infrared bands, because it is invalid otherwise. For this reason, we calculated slopes using linear regression only for the parts of the data where the CoRoT and IRAC light curves correlate reasonably well. We separated various parts of each light curve and calculated the slopes of different flux dips and different parts of the flux dips separately, as shown in Figure 4.5 (different colors correspond to the analysis of different parts of the light curve). We did this in order to verify if different parts of the disk warp would present different extinction laws. We found that entrances into and exits from the occultations show the same slopes, within the uncertainties. In one case, Mon-456 (see top panels of Figure 4.5), slightly different slopes were found for different flux dips. This might be due to factors such as variable disk emission interfering with the IRAC light curves.

We were able to estimate extinction laws for ten of the stars in our sample using this method, finding values between those consistent with ISM ($A_{4.5\mu m}/A_R \sim 0.05$) and up to $A_{4.5\mu m}/A_R \sim 0.29 \pm 0.04$. We disregarded any slope of value less than 1, since the extinction laws derived would be nonphysical. In these cases, other factors such as variable disk emission in 4.5μm or a configuration of hot and/or cold spots on the stellar surface could be strongly interfering with the distribution of points in the color magnitude diagrams. It is possible that variable disk emission is also influencing our derived extinction laws even when the values found are physically plausible. This might be the reason why we find lower extinction laws than those estimated in Section 4.2. These results are another indication that the dust distribution in inner accretion disks differs from that of the ISM, but the values found for extinction laws cannot be relied upon to be very precise. More accurate estimates would require a more extensive study of these and other color magnitude diagrams.

[4] If extinction is indeed the main cause of the flux dips observed in these light curves, then the slopes in these SEDs represent the extinction vector of the occulting material.

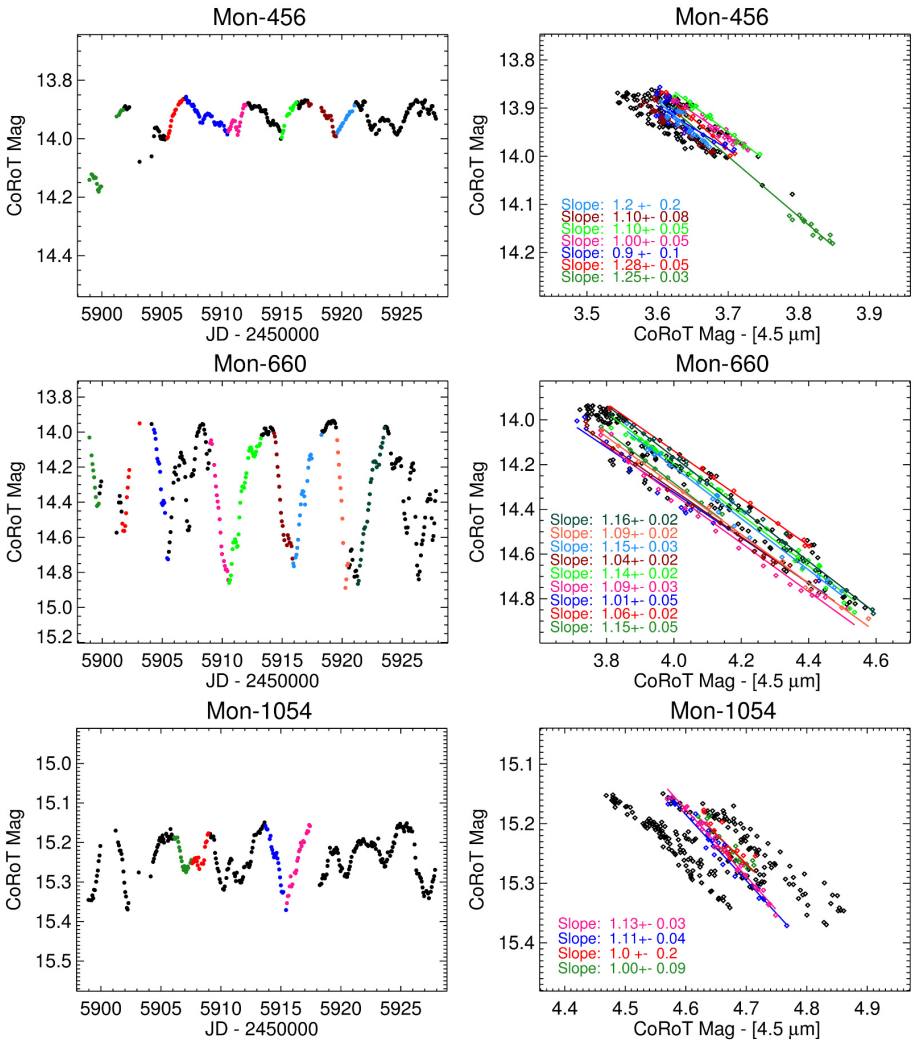

Figure 4.5: Left: CoRoT light curves of the stars Mon-456, Mon-660, and Mon-1054. Right: CoRoT vs. CoRoT-IRAC$_{4.5\mu m}$ color magnitude diagrams of the same stars. Slopes were calculated for various parts of the light curves where CoRoT and *Spitzer* IRAC data best correlate. Different colors show different parts of the light curves for which slopes were calculated.

4.4 Variability in the CFHT u and r filters

We checked for color variation in the periodic and quasi-periodic stars of our sample by comparing CoRoT or I-band light curves with $u-r$ for the stars whose light curves were classified as AA Tau-like or AA Tau candidates in 2011. Their simultaneous I-band light curves and $u-r$ variability are plotted in phase in Figure 4.6, using the periods determined from the CoRoT data (Table 4.1) and using the same initial date. When the I-band light curve did not show enough detail to allow for a proper identification of the flux dips, we plotted the CoRoT light curve in Figure 4.6 instead. Though the CFHT data were not taken simultaneously with CoRoT, the photometric variability of these objects is not expected to have changed significantly in the few weeks between the CoRoT and CFHT observing runs.

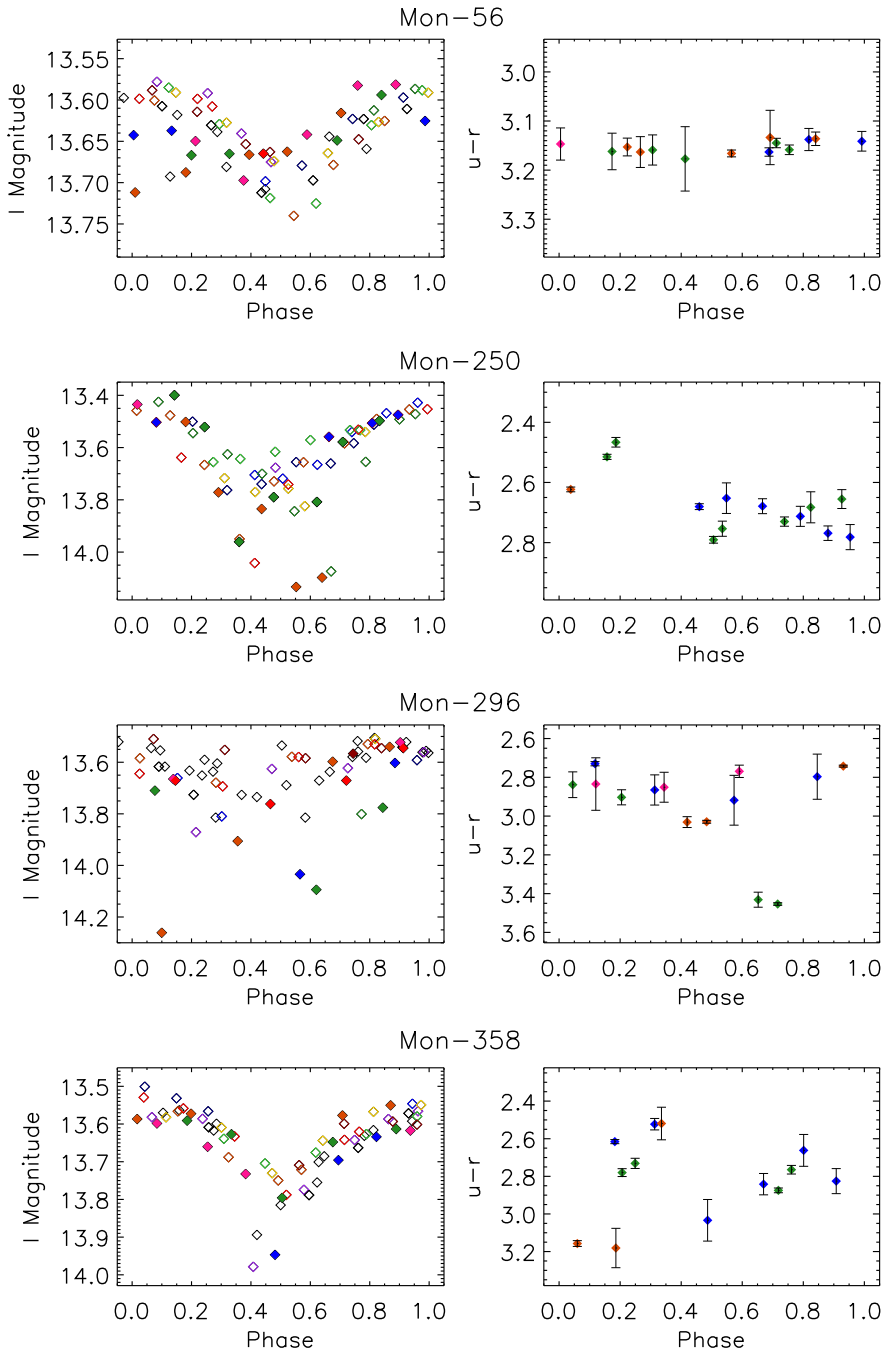

Figure 4.6: I-band and $u-r$ light curves folded in phase for periodic or quasi-periodic stars. Colors used for $u-r$ represent the same rotation cycle as filled diamonds of the same color in I. It was not possible to identify flux dips in the phase-folded I-band light curves of Mon-1037, Mon-1296, Mon-1308, and Mon-14132, because of insufficient cadence, so the phase-folded CoRoT light curves are shown instead. In these cases colors do not represent the same phase in both plots.

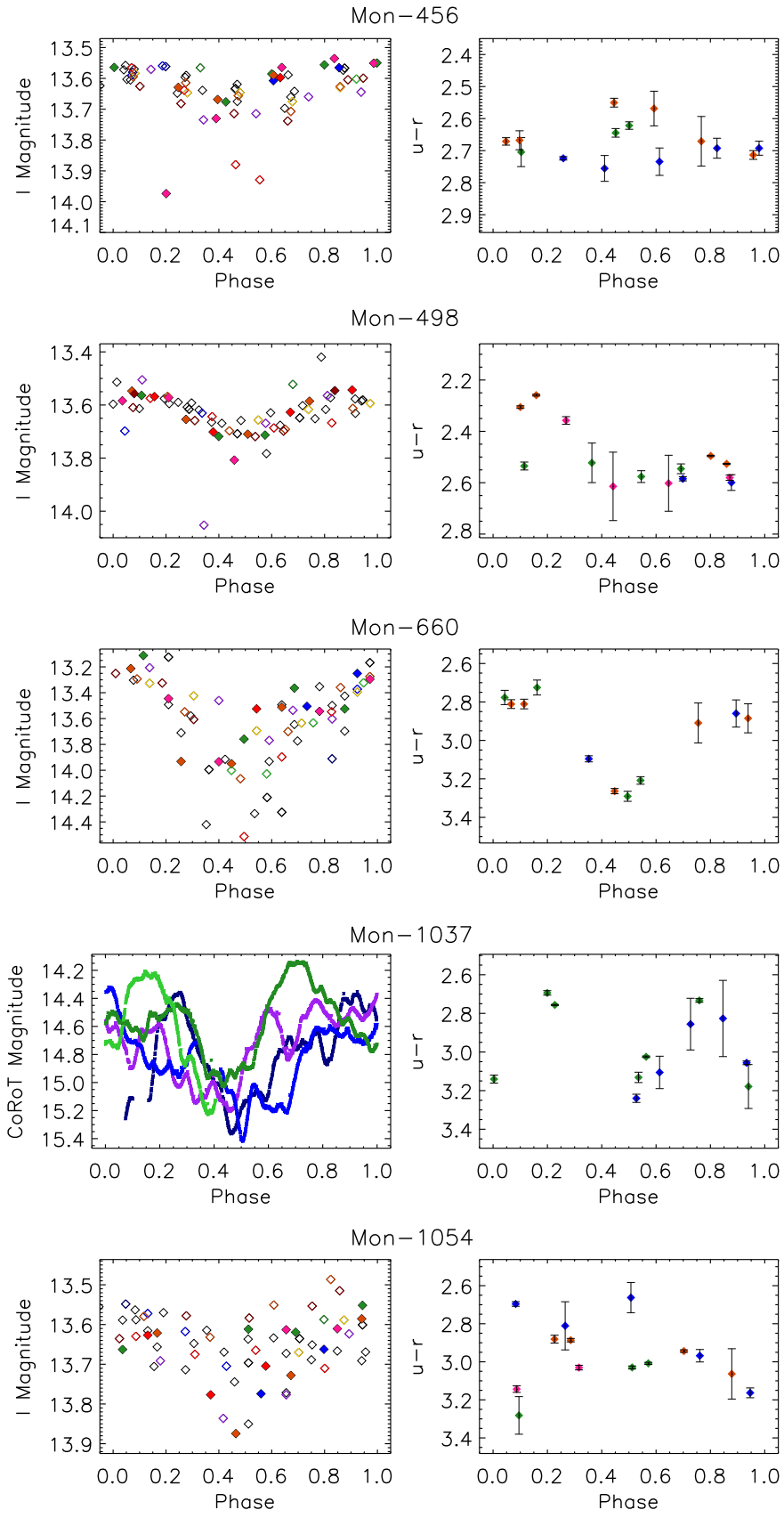

Figure 4.6: Continued.

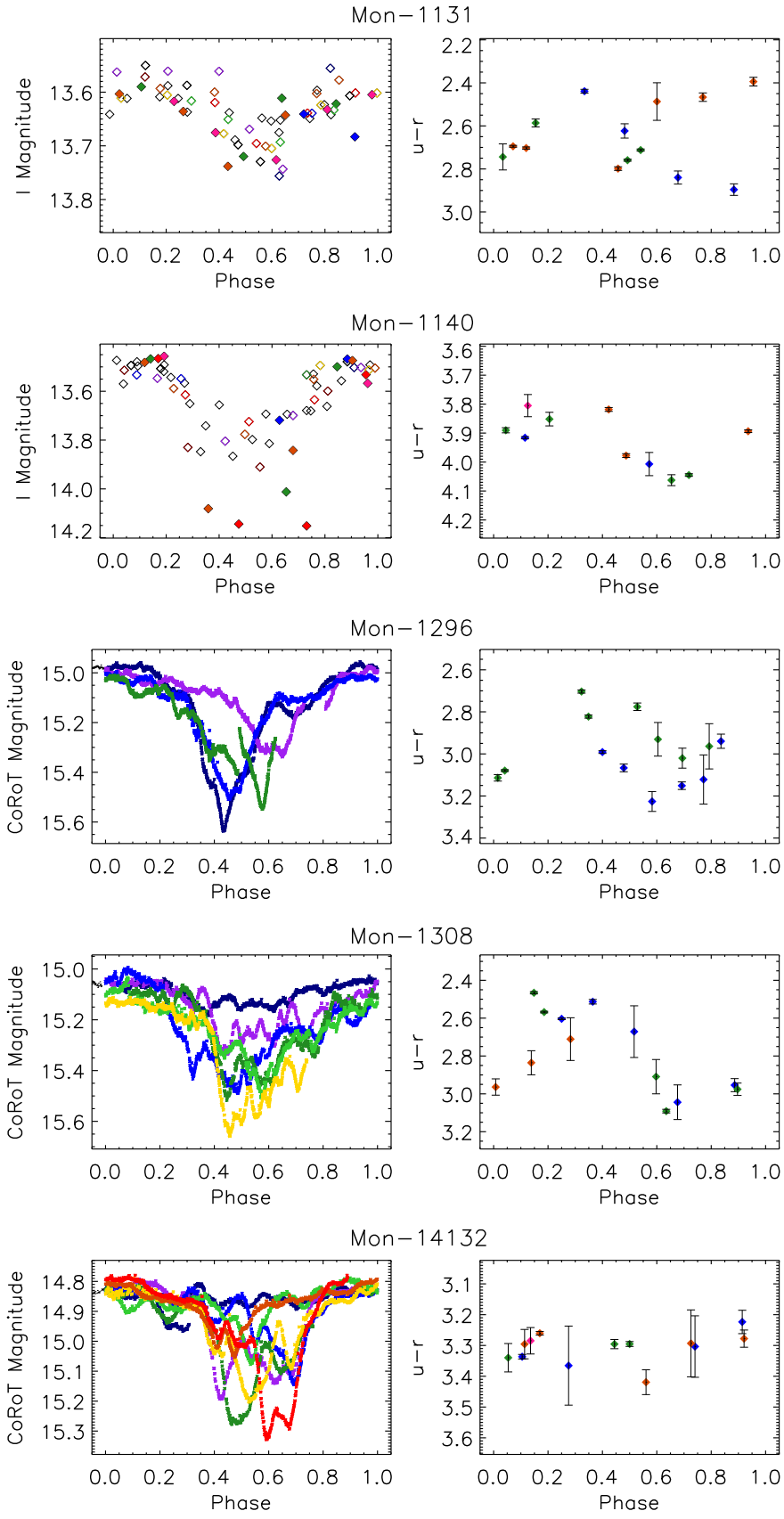

Figure 4.6: Continued.

Therefore, by folding the light curves in phase using the same initial date and period, we can see how a system's color varies during the flux dips.

For most stars, we see a reddening during the flux dips (at phase 0.5), as would be expected for an extinction event (Figure 4.6). However, for four stars (Mon-250, Mon-358, Mon-456, and Mon-1054), we can observe the system becoming bluer during one or two flux dips, while the other rotation cycles either maintain relatively constant color or become slightly redder at phase 0.5. This effect was observed in AA Tau (Bouvier et al. 2003), which showed little color variation except during some minima, when it became bluer. This blueing effect was attributed to the appearance of hot spots on the stellar photosphere during occultations from the inner disk warp, and indicates that the warp is spatially associated with an accretion shock. The fact that we observe the same phenomenon in these four stars is evidence that they may be undergoing the same physical process as AA Tau did during its stable accretion phase. Another three stars undergo a similar phenomenon, where they become slightly bluer during the beginning of the flux dips, then become redder. This could also be evidence that a hot spot associated with an accretion shock is partially appearing, but in this case it is soon occulted by the inner disk warp. These stars are Mon-1140, Mon-1308, and Mon-1167. The final two stars, Mon-56 and Mon-14132, demonstrate little to no change in color. Figure 4.6 shows these light curves and $u-r$ color diagrams folded in phase.

4.5 Veiling variability

As was discussed in Section 3.3, veiling occurs due to excess optical and UV emission contributing to the stellar spectra. This excess emission comes from hot spots on the stellar surface that are caused by accretion shocks. Veiling should, therefore, only be detected in the spectrum of a star when accretion shocks are visible in the observer's line of sight. Veiling was measured in each of the 20 FLAMES spectra of the CTTS Mon-250 by comparing line depths to those of a WTTS of the same spectral type, in order to determine what fraction of the observed continuum should be due to hot spots. In McGinnis et al. (2015) we showed that this star's veiling almost always increases as the photometric flux decreases, as shown in Figure 4.7c, which is evidence of an accretion shock large enough to produce measurable veiling appearing in our line of sight at the same time the photosphere is being obscured. The radial velocity measured from this star's photospheric lines were also shown to vary with a period of 8.6 ± 0.5 days (Figure 4.7d). Variability in the radial velocity of photospheric lines is often caused by spots on the stellar surface, therefore the period measured from this variability represents the stellar rotation period[5]. This derived period is consistent with the one found from the CoRoT light curve that was obtained around the same time as

[5]Variability in the radial velocity of photospheric lines can, of course, also indicate a spectroscopic binary, but the two effects are distinguishable from one another. A binary or a planetary companion will cause the center of the lines to shift as the objects rotate around each other, whereas spots on the stellar surface will affect the shapes of the lines, rather than their central velocities, causing them to appear slightly deformed.

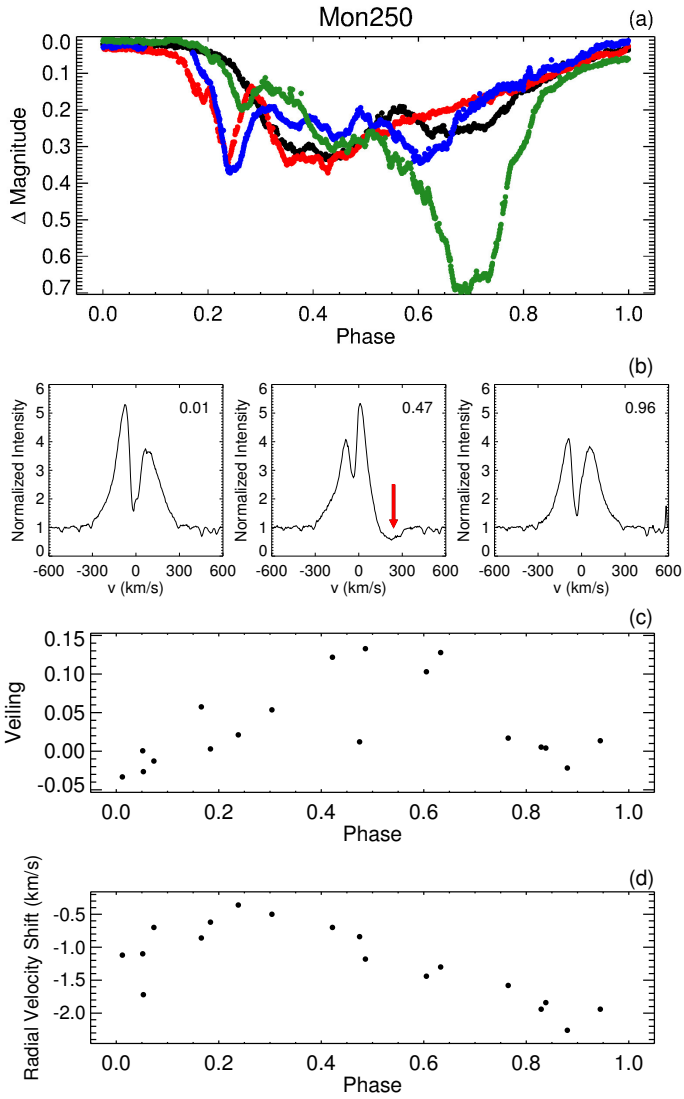

Figure 4.7: Mon-250. a) 2011 Corot light curve folded in phase. b) Hα line profile during different rotational phases, indicated in each panel. A redshifted absorption component seen only near phase 0.5 is indicated by a red arrow. c) Measured veiling folded in phase. d) Radial velocity shift with regard to the rest velocity of the standard WTTS, measured from photospheric lines in the spectra, folded in phase. In all four panels, the same period of 8.6 days, determined from the radial velocity variation of photospheric lines, was used to calculate the phase and the same initial date was used.

the FLAMES observations ($P_{CoRoT} = 8.93 \pm 0.50$ days), which indicates that the structure producing the flux dips in the light curve is located at or near the disk's co-rotation radius, as was the case for AA Tau (Bouvier et al. 2003, 2007).

McGinnis et al. (2015) also showed that the Hα line profile of the star Mon-250 presents a redshifted absorption component in several spectra, but only during the light curve minima, as can be seen in Figure 4.7b (the redshifted component is indicated by a red arrow). This is clear evidence that an accretion funnel flow appears in front of our line of sight during the

photometric flux dips, since the infalling material responsible for the absorption is moving away from us. Figure 4.7 thus illustrates that whatever is responsible for occulting this star's photosphere periodically is spatially associated with an accretion funnel flow and accretion shocks. This is a strong indication that this system possesses an inner disk warp located at the base of an accretion column, possibly as a result of the interaction between an inclined stellar magnetic field and the inner disk.

Unfortunately, such a detailed analysis of veiling and radial velocity variability was only possible for this star, since it was the only one with a high enough variability amplitude in a direct veiling measurement and in radial velocity to draw significant conclusions. For the other CTTSs in NGC 2264 for which we obtained FLAMES spectra simultaneously with CoRoT observations, veiling was estimated using the equivalent widths of the Li I 6707.8Å and Fe I 6633.4Å lines (Sousa et al. 2016). As veiling increases, their measured equivalent widths should decrease. These lines were chosen since they are the absorption lines with the best signal-to-noise ratio in these spectra.

Many of these CTTSs show at least some variability in these lines' equivalent widths. Depending on the physical processes occurring on and around a CTTS, we may expect for this variability to correlate (or anti-correlate) on some degree with its photometric variability. For example, if a star's photometric variability is dominated by hot spots, we would expect the observed veiling to increase with increasing brightness (provided these hot spots produce enough excess emission for veiling to be measurable in our data). As the amount of hot spots visible to the observer increases, veiling would increase as well as the total optical flux measured. This is believed to be the case for the light curves dominated by accretion-driven flux bursts (discussed in Stauffer et al. 2014). The reoccurring sudden increases in brightness are likely due to an increase in accretion luminosity, which is associated with an increase in veiling. Therefore for these systems an increase in brightness should be accompanied by a decrease in the absorption lines' equivalent widths. On the other hand, if a star's photometric variability is due to the rotational modulation of stable, cold spots on the photosphere, then the veiling would not be expected to vary, since cold spots do not result in any measurable excess emission. In this case the measured equivalent widths of photospheric absorption lines would remain constant.

For photometric variability caused by the scenario proposed for AA Tau, in which an inner disk warp located at the base of an accretion column obscures the photosphere as the system rotates, we could expect two possible trends in the veiling. If accretion shocks are never visible to the observer because they are obscured by the warp, or if the veiling caused by these shocks is too small to be accurately measured, then there should be no considerable variability in the observed absorption line equivalent widths. If, however, an accretion shock appears in the observer's line of sight producing measurable veiling, then it should appear at the same time as the inner disk warp, since both are associated with the accretion column. In this case, as the inner disk warp occults the star, causing the flux minima, the veiling should

increase thanks to the appearance of a hot spot caused by the accretion shock. Therefore, for an AA Tau-like system, the equivalent width of photospheric absorption lines should either remain relatively constant or increase with increasing brightness.

To illustrate these different behaviors we show in Figure 4.8 plots of Li I equivalent width (LiIEW) vs. I-band magnitudes (left panels) for three different cases, alongside their CoRoT and I-band light curves (right panels). We used USNO I-band magnitudes rather than CoRoT magnitudes because they had better time coverage, despite the lower cadence. Only the first few FLAMES observations took place while CoRoT was still observing NGC 2264, so there are at most 6 spectra of each CTTS with a simultaneous CoRoT measurement, whereas the USNO observations spanned the entire FLAMES campaign, providing us with 20-22 simultaneous spectra and I-band magnitudes. The I-band measurements taken on the same night were averaged and matched with the equivalent width derived from the FLAMES spectrum taken on that night. The USNO and VLT are separated by little more than 40° in longitude, so the observations were likely taken within a few hours of each other on most nights.

The top panels of Figure 4.8 show a star whose veiling increases (LiIEW decreases) with increasing brightness. Its light curve was classified as being dominated by flux bursts attributed to variable accretion events, in accordance with its veiling variability. The middle panels of Figure 4.8 show a star whose veiling decreases (LiIEW increases) with increasing brightness, a tendency we attribute to occultation of the photosphere by an inner disk warp that is associated with the accretion mechanism. Its light curve was indeed identified as possibly AA Tau-like (see Table 4.1), though this is one of the systems that were not obvious to classify and was not considered as an AA Tau-like light curve in other papers (Cody et al. 2014). The bottom panels of Figure 4.8 show a star whose veiling does not vary considerably, which means the photometric variability could be due to a configuration of cold spots on the surface, or to obscuration by an inner disk warp that either fully occults any accretion shock associated with it, leaving the veiling unaltered during occultations, or that presents relatively low accretion and does not generate large enough UV excess for veiling to be measured with precision. This CTTS presents little UV excess, consistent with either of these scenarios. Its light curve was classified as AA Tau-like, but we cannot confirm if the material occulting the photosphere is associated with accretion shocks or not. This light curve is very unlikely to be caused by cold spots, since they usually result in a much more regular photometric variability.

Figure 4.9 shows plots of LiIEW vs. I-band magnitudes for the rest of our CTTSs with extinction-dominated CoRoT light curves (both AA Tau-like and aperiodic) that were observed by both FLAMES and USNO. In many cases the veiling variability is very irregular and we cannot see a clear pattern (e.g., Mon-498), while some present relatively constant veiling (e.g., Mon-379, shown in Figure 4.8). For six objects, there is a hint of a decrease in veiling (increase in Li I equivalent width) as the CTTS's brightness increases, which

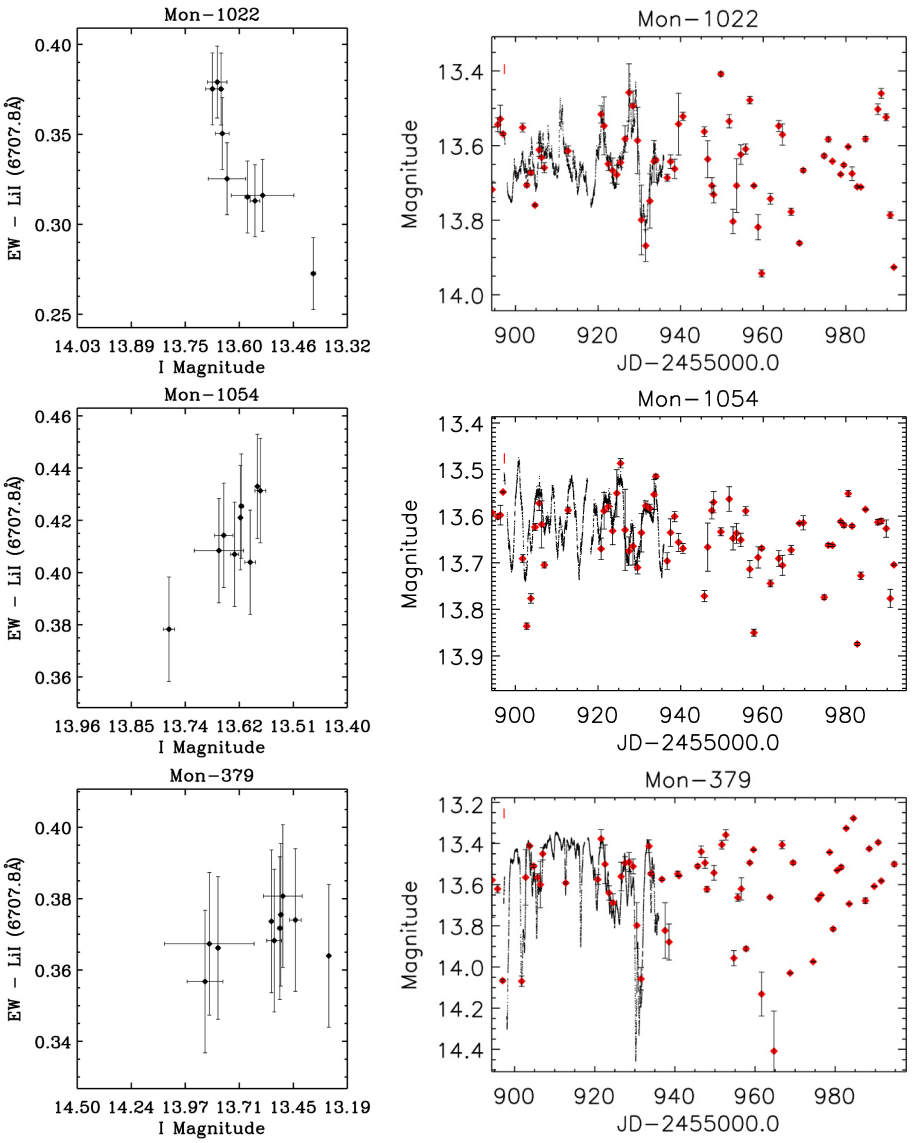

Figure 4.8: Left: plots of LiIEW vs. I magnitude for three different stars. Right: I-band and CoRoT light curves, shifted in magnitude to coincide, of the same three stars. Top panels: the star has an accretion-burst dominated light curve, and veiling variability that supports the variable accretion scenario. Middle panels: the star has a light curve that presents aperiodic extinction events, and veiling variability that supports a scenario in which the occulting structures are associated with accretion shocks. Bottom panels: the star has a light curve with AA Tau-like characteristics, while its near lack of veiling variability can neither confirm nor refute the hypothesis that it is an AA Tau-like system.

could indicate that they are being obscured by circumstellar disk material that is spatially associated with accretion shocks. This is the case for Mon-250, Mon-441, Mon-660, Mon-811, Mon-1054, and Mon-1144.

The star Mon-811 was outside the USNO field, and therefore we have no I-band information for it. For this one star, we made a plot of LiIEW vs. CoRoT flux counts instead. This

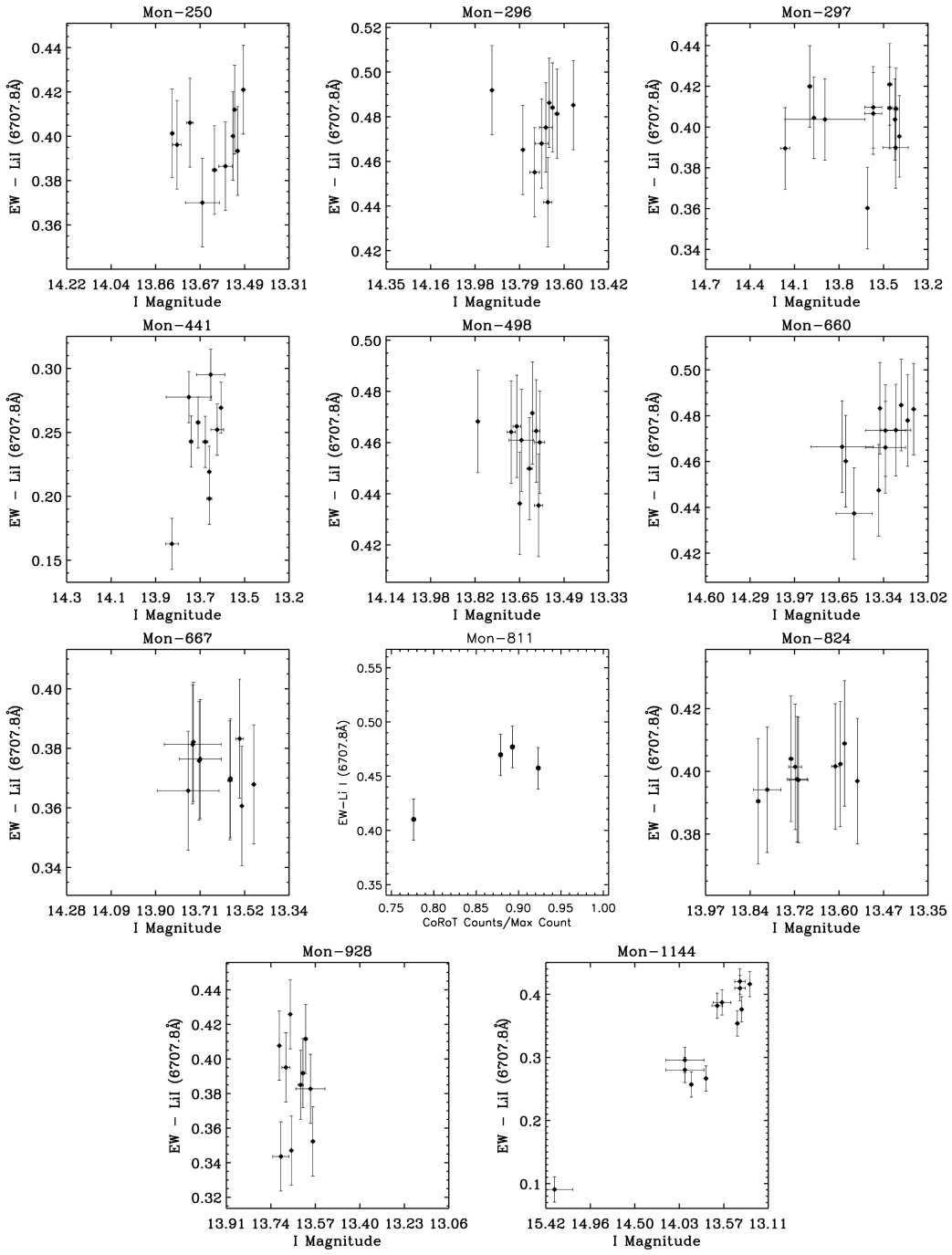

Figure 4.9: Plots of LiIEW vs. I magnitude for the stars in our sample.

plot was not nearly as well sampled, since very few FLAMES spectra were taken during the CoRoT observations, but it shows a tendency similar to the middle panels of Figure 4.8.

The CTTS Mon-1144 has the largest variability amplitude in veiling (LiIEW varies by up to ~ 0.3 Å), meaning there should be significant hot spots on the stellar surface. It is also the one with the clearest trend of increased veiling with decreased stellar flux. It has the highest UV excess among the CTTSs in our sample for which veiling was measured, which could be expected, since the hot spots associated with the accretion shocks on the surface of the star should produce a considerable UV excess. This is also one of the objects with no clear period in its light curves. Mon-441 also presents aperiodic extinction-dominated light curves and an apparent increase in veiling as the flux decreases. These two cases indicate that the material occulting the photosphere in these aperiodic systems could also be spatially associated with accretion shocks, and therefore with accretion funnel flows. The occultations in these light curves could be caused by dust lifted above the disk plane at the base of the irregularly distributed accretion streams that are associated with an unstable accretion regime, in a manner analogous to the inner disk warp that is located at the base of an accretion column that is associated with a stable accretion regime.

Measures of veiling using the FeI 6633.4 line proved to be much less accurate than LiI 6707.8, since it is shallower in these stars and therefore suffers more from noise in the spectra. For this reason veiling was only measured using FeI for a small subset of these stars with FLAMES spectroscopy. In these cases the observed tendencies agree with those determined using the LiI line.

4.6 Occultation model

In this section we aim to verify if the occultation model proposed to explain the light curve of AA Tau in Bouvier et al. (1999) (described in the Introduction) is also capable of reproducing the light curves we have classified as AA Tau-like in NGC 2264. It consists of a simplified geometrical model, which reproduces the variation in flux that would be caused by an optically thick clump, located in the inner accretion disk, that periodically occults the stellar photosphere of a system observed at inclination i as this system rotates (see Figure 1.7). This clump is assumed to be located at the disks's radius of co-rotation with the star (R_{co}) and to have a height that varies according to the azimuthal angle (ϕ):

$$h(\phi) = h_{max} \left| \cos\left(\frac{\pi(\phi - \phi_0)}{\phi_w} \right) \right|, \text{for} - \phi_w/2 \leq \phi \leq \phi_w/2, \tag{4.3}$$

where h_{max} is the maximum height reached by the clump, ϕ_0 is the azimuth at that maximum height, and ϕ_w is the clump's total azimuthal extension. The clump height is equal to zero for all values of $|\phi| > \phi_w/2$.

The warp found by Bouvier et al. (1999) to best reproduce the light curve of AA Tau had a maximum height of $h_{max} = 0.3 R_{co}$ and an azimuthal extension of 360°. We apply this

model to our AA Tau-like light curves (and candidate AA Tau-like light curves) from both CoRoT observing runs and compare the values we find with these. For the stars that showed AA Tau-like behavior in both CoRoT observing runs, we also compare the results obtained in each and check if they are consistent with occulting structures of similar characteristics. If so, this would mean that this structure can persist over timescales of a few years.

In order to reproduce the observed light curves with the occultation model, the following parameters must be constrained:

- the radius (R_w) at which the warp is located,
- the star-disk system's inclination i,
- the warp's maximum height h_{max}, and
- the warp's azimuthal extension ϕ_w.

If we know the system's inclination and the warp's radial location in the disk, then finding the best warp to reproduce a certain CTTS's light curve is a simple matter of varying its maximum height and azimuthal extension in order to fit the modeled light curve to the observation. To determine the radius at which the warp is located, we assume that the periods we measured from the CoRoT light curves are the Keplerian rotation periods of the occulting material orbiting the star. We can thus use Kepler's third law in the following form to find R_w:

$$R_w^3 = GM_* \left(\frac{P_{kep}}{2\pi}\right)^2, \tag{4.4}$$

where M_* is the star's mass, P_{kep} is the Keplerian rotation period, and G is the gravitational constant. For stellar mass we use the values derived in Section 3.3.1 (reproduced in Table 4.2). The values calculated for R_w are given in Table 4.2.

Determining a system's inclination is not trivial. Ideally, we would use inclinations measured from direct observations of the protoplanetary disks. However, we do not have direct measurements of the disks in our sample because, at the distance to NGC 2264 (taken here as 760 pc, Sung et al. 1997), this would require an angular resolution below 0.1 arcsec. This is difficult to achieve even with modern instruments and has not yet been attempted. So instead, we use stellar rotation properties to estimate these inclinations. We apply the following relation between $v \sin i$, stellar radius R_*, and stellar rotation period P_{rot}:

$$v \sin i = \frac{2\pi R_*}{P_{rot}} \sin i \rightarrow \sin i = \frac{P_{rot}}{2\pi R_*} v \sin i. \tag{4.5}$$

The derived inclination estimates are given in Table 4.2. The values of $v \sin i$ used were the ones determined from the spectra centered on Hα in Section 3.3.3 (shown again in Table 4.2). For stellar radii we use the values derived in Section 3.3.1 (also shown in Table 4.2).

4.6.1 Co-rotation radii

For the CTTS AA Tau, the inner disk warp was found to be located at (or very near) the co-rotation radius, as had initially been assumed. Its stellar rotation period was measured using the radial velocity of the HeI 5876 emission line and of photospheric lines, revealing a value consistent with AA Tau's photometric period (Bouvier et al. 2003, 2007). In our sample, we found the same result for the star Mon-250 in Section 4.5. We found a spectroscopic period of $P_{rot} = 8.6 \pm 0.5$ days, a value consistent with the periods found from its CoRoT light curves of $P_{kep} = 8.3 \pm 1.0$ days in 2008 and $P_{kep} = 8.9 \pm 0.5$ days in 2011. The same period of 8.6 days was also found by Sousa et al. (2016) in both the Hα and the HeI 6678 lines. This indicates that the structure responsible for the flux dips in the CoRoT light curves of Mon-250 is located at or near the co-rotation radius.

Unfortunately we could not directly measure the stellar rotation periods of the other stars in our sample, since their radial velocities did not present significant variability within our errors. In order to estimate their stellar rotation periods, we can assume that, if they truly represent systems similar to AA Tau, then their inner disk warps may also be located very close to the co-rotation radius. This would allow us to use the periods found from their CoRoT light curves as rotation periods as well. To investigate if this assumption is reasonable, we compare the CoRoT periods of the AA Tau-like light curves with those found for stars with spot-like light curves. Spot-like photometric variability occurs because of the rotational modulation of stable configurations of spots on the stellar surface. Their periods therefore represent stellar rotation periods, whereas the periods of AA Tau-like light curves represent the Keplerian rotation periods of the material that occults the stellar photosphere. If the values of the two groups are similar, then our assumption that the periods of AA Tau-like light curves may also represent stellar rotation periods is not too far off. Figure 4.10 shows a histogram of the periods of CTTSs in NGC 2264 with CoRoT light curves classified as spot-like (shown in blue) and AA Tau-like (shown in red). We see that, though the distributions are not identical, the periods of AA Tau-like light curves fall within the region where rotational periods are found, meaning our assumption is valid.

We henceforth assume that the inner disk warp is located at the disk's co-rotation radius for all of our possible AA Tau-like systems, and use the periods determined from their CoRoT light curves to calculate their inclinations. The only exception is Mon-250, for which we use the spectroscopic period. For the stars observed to be periodic in both CoRoT epochs, but for which a slightly different period was found in each, we use the value with the smallest error. These periods are shown in Table 4.2.

4.6.2 Inclinations

System inclinations estimated from stellar rotation properties are subject to very large errors. This is especially true when dealing with high inclinations, in which case even a small error

Table 4.2: Stellar parameters initially calculated for the AA Tau-like candidates.

CSIMon ID	L_{bol} ($L_\odot$)	M_* ($M_\odot$)	R_* ($R_\odot$)	P_1 (days)	P_2 (days)	$v \sin i$ (km/s)	$\sin i$	Inclination (°)	$R_{w,1}$ (R_*)	$R_{w,2}$ (R_*)
CSIMon-000056	0.77	1.16	1.52	5.71	5.86	11.1±2.2	0.85±0.38	58^{+32}_{-30}	9.29	9.45
CSIMon-000250	1.23	1.35	1.63	8.32	8.93	9.8±2.2	1.02±0.49	62±28	11.71	12.28
CSIMon-000296	1.57	1.42	1.71	–	3.91	17.3±2.6	0.78±0.33	51^{+39}_{-24}	5.11	6.86
CSIMon-000297	1.57	1.42	1.71	3.16	–	30.8±1.8	1.13±0.40	69±21	5.95	–
CSIMon-000358	0.22	0.29	1.39	–	5.86	15.0±4.0	1.25±0.54	68±22	–	6.51
CSIMon-000379	2.12	1.60	1.99	–	3.68	25.0±1.2	0.91±0.30	66^{+24}_{-28}	5.95	5.89
CSIMon-000441†	0.50	0.36	1.92	4.06	–	–	–	–	3.97	–
CSIMon-000456	1.58	1.41	2.00	–	5.03	19.3±1.5	0.96±0.21	74^{+16}_{-33}	–	6.92
CSIMon-000498	3.85	1.90	2.88	4.23	4.28	24.1±2.4	0.71±0.26	45^{+31}_{-19}	4.73	4.77
CSIMon-000654	0.47	0.30	2.03	4.66	–	18.0±3.0	0.82±0.37	55^{+35}_{-28}	3.87	–
CSIMon-000660	1.36	1.40	1.86	5.25	5.25	21.4±2.5	1.16±0.44	68±22	7.64	7.50
CSIMon-000774	3.10	1.83	2.49	3.46	–	30.7±1.3	0.84±0.28	57^{+33}_{-23}	4.73	–
CSIMon-000811	1.08	0.91	1.97	–	7.88	13.5±1.7	1.07±0.35	64±26	–	8.19
CSIMon-000824	1.96	1.48	2.23	7.05	–	14.8±1.4	0.92±0.40	68^{+22}_{-37}	7.90	–
CSIMon-000928	0.58	0.63	1.65	9.92	–	20.1±2.8	2.38±1.05	90	10.09	–
CSIMon-001054	0.63	0.36	2.17	–	4.08	20.4±2.0	0.76±0.28	49^{+41}_{-28}	–	3.52
CSIMon-001131	0.55	0.36	2.01	–	5.18	8.8±1.7	0.45±0.21	27±14	4.44	4.46
CSIMon-001140	1.10	1.31	1.67	3.87	3.90	19.8±2.3	0.91±0.34	66^{+24}_{-35}	6.79	6.83
CSIMon-001167	0.56	0.30	2.23	–	8.78	11.3±2.1	0.88±0.42	62^{+28}_{-35}	5.18	5.37
CSIMon-001296	0.91	0.69	1.99	–	9.75	11.0±1.6	1.07±0.48	63±27	–	8.52
CSIMon-001308	0.53	0.63	1.59	6.45	6.68	9.9±2.0	0.82±0.37	55^{+35}_{-28}	7.86	8.04
CSIMon-014132†	0.37	0.28	1.88	–	4.48	–	–	–	–	3.98

Notes. $P1$ and $P2$ are the Keplerian periods found from the CoRoT light curves in 2008 and 2011, respectively, while $R_{w,1}$ and $R_{w,2}$ are the warp's radial locations found using $P1$ and $P2$, respectively. The stars identified with a † either have no observed spectrum, or the S/N is too low to determine $v \sin i$, and so we cannot estimate their inclinations.

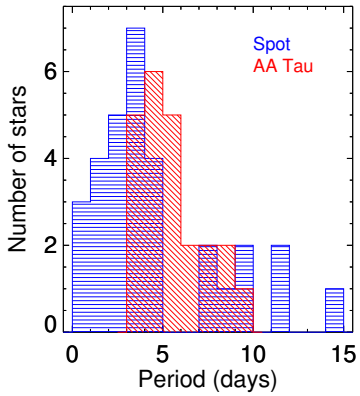

Figure 4.10: Period histogram of CTTSs in NGC 2264 whose CoRoT light curves were classified as AA Tau-like (blue) or spot-like (red). The periods of spot-like light curves represent stellar rotation periods, while those of AA Tau-like light curves represent Keplerian rotation periods at the warp location.

in $\sin i$ translates into a large error in i. Unfortunately our errors in $\sin i$ themselves are relatively large to begin with, therefore these estimates of i are very imprecise.

Obtaining precise values for the radii of CTTSs is challenging for various reasons. They present strong variability, spectrum veiling and surface spots, which all contribute to the difficulty in accurately determining temperature and luminosity. Besides these factors, determining the distance to young stars that are not close enough for accurate parallax measurements introduces further uncertainties in the estimates of luminosity and therefore radius. Hartmann (2001) discusses these difficulties and argues that typical errors in radius determination are on the order of 20%. Meanwhile, Rebull et al. (2002) find errors of around 12% for TTSs in the spectral range K5-M2. In this study we consider the more conservative value of 20% when determining our errors in radius.

Our errors in $v \sin i$ were determined for each CTTS individually and are typically on the order of 10% - 12%. Though this is relatively low, it may be underestimated. The projected rotational velocity is not as simple to determine as one might expect. Various factors can cause absorption lines to broaden, and if we do not take them into account correctly we could be under- or over-estimating $v \sin i$. Furthermore, the closer these values are to the spectral resolution, the more uncertain they become. Thus, low values of $v \sin i$ ($\lesssim 20$ km/s) cannot be strongly relied upon.

Errors in photometric periods are low, because of the incredible detail managed with CoRoT. They were calculated as the half width at half maximum of the peak in each periodogram and are typically around 5% to 7%. However, assuming that they represent the stellar rotation period may introduce further errors in our estimates of inclination if the photometric variability does not come from the stellar surface or the disk's co-rotation radius. All of this contributes to the inaccuracy of this method, but as it is our only way of estimating these systems' inclinations we proceed with it. In all, we find errors on the order

of 35% in $\sin i$, which are high, but consistent with other studies of TTS inclinations (e.g., Artemenko et al. 2012).

Although the values themselves are imprecise, estimating inclinations in this way allows us to at least distinguish between systems observed at low inclinations from those observed at medium to high inclinations, since for low inclinations the errors in $\sin i$ do not translate into such large errors in i as they do with high inclinations. In Table 4.2 we can see that all but one star in our AA Tau-like sample are consistent with high inclinations, as the model of occultation by an inner disk warp requires. The exception is Mon-1131, which appears to be seen at a low inclination (Table 4.2). We can consequently rule out the proposed occultation mechanism as the primary cause for its photometric variability, unless its radius, period or $v \sin i$ is wrongly determined. Its $v \sin i$ is very low, which is consistent with a low inclination, but also means that this value is very uncertain[6]. On the other hand, it is possible that there are two structures obscuring the photosphere, separated by 180°, making it seem as if the period were half its true value. If this were the case this system's inclination would be $64^{\circ}{}^{+26}_{-36}$, consistent with the occultation scenario. Further investigation would be needed to determine if this is the case, so for the time being this system has been excluded from further investigation using the occultation model. It is studied as a system with narrow flux dips in Stauffer et al. (2015), where different mechanisms are proposed to explain its variability.

We found many systems with an estimated $\sin i$ that is larger than 1. In most cases a reasonable interval of values within the error bars falls below 1. For these, we argue that the sine of the system's true inclination should be anywhere between the lowest value within its determined uncertainties ($\sin i - \Delta \sin i$, where $\Delta \sin i$ is the uncertainty in $\sin i$) and $\sin i = 1$. Therefore the inclination is a value between $\sin^{-1}(\sin i - \Delta \sin i)$ and 90°. We then take the mean value in this interval as the inclination, and $90^{\circ} - i$ as the error bar. For example, a star of $\sin i = 1.07 \pm 0.32$ has an inclination of $69^{\circ} \pm 21^{\circ}$, since the inverse sine of the lowest value, $\sin i = 1.07 - 0.32 = 0.75$, is 48°.

There is one star for which, even when considering the error bars, the estimated $\sin i$ is much larger than 1. This is the case of Mon-928. It is possible that the material occulting this star is located farther away from the star than its co-rotation radius, in which case the Keplerian period found from its CoRoT light curves is larger than the stellar rotation period, resulting in a larger value of $\sin i$. It is also possible that its true period is actually 4.96 days, half the value we used, which would lead to an estimated inclination of $66^{\circ} \pm 24^{\circ}$. There is an additional, smaller, flux dip in its 2008 light curve located between the second and third larger flux dips (see Figure 4.12), which would justify using a period of 4.96 days, rather than 9.92 days, though we gave preference to the latter since it coincides with the period found in the literature of 9.48 ± 2.34 (Lamm et al. 2005). In either case, it is probably safe to consider that this system is viewed at a high inclination. Therefore, we use the occultation

[6]It should be noted, however, that this star's $v \sin i$ was determined using Hectochelle spectra, rather than FLAMES spectra, which has considerably higher resolution.

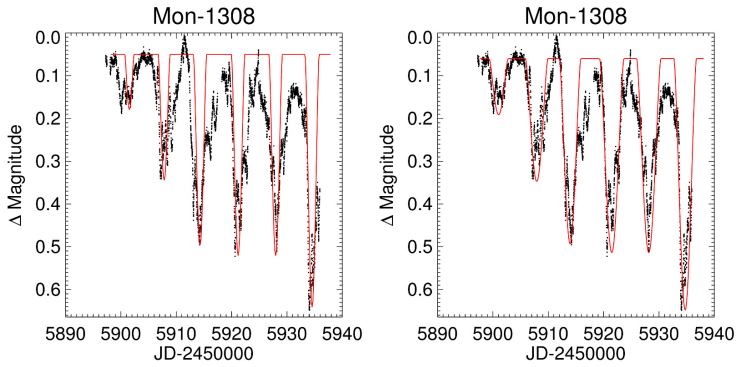

Figure 4.11: Fitted light curves of the star Mon-1308 using an inclination of 55° (left) and 75° (right). In both cases the values of warp maximum height and azimuthal extension were set to those that best fit the width and amplitude of the minima, without extrapolating to unphysical values.

model itself to find which interval of inclinations results in the best fit for the light curve, and consider this to be the system's inclination. This was also done for the two stars in Table 4.2 for which we have no measure of $v \sin i$, where we assume without proof that the systems are seen nearly edge-on. The new values are presented in Table 4.3.

For the rest of the AA Tau-like stars, we used the occultation model in this way to provide a better estimate for the inclination. In many cases it was not possible to successfully reproduce the observed widths of the flux dips using the whole range of values of i initially calculated, unless we extrapolated the other parameters to unphysical values (such as azimuthal extension $\phi_w > 360°$). Therefore, we took all values of i within the error bars and considered only the interval that could successfully reproduce the widths of the observed light curves with physically possible values of ϕ_w. This restricted the inclinations much more than the original calculation, resulting in much smaller error bars, as can be seen in Table 4.3. Figure 4.11 shows an example of the best fits for a light curve using the originally calculated value of inclination (restraining ϕ_w to $\leq 360°$) and the new value presented in Table 4.3. It is easy to see that this inclination is much better at reproducing the widths of the flux dips.

4.6.3 Warp parameters and fitted light curves

We used the occultation model interactively to simulate the CoRoT AA Tau-like light curves. We fixed the warp's radial location at the co-rotation radius and allowed the warp maximum height and azimuthal extension to vary, in order to fit the simulated flux dips to the observed ones. Inclination was maintained as a semi-free parameter, constrained to vary only within the error bars presented in Table 4.2. Inclinations were determined first, as described above, by verifying for which values we could reproduce the width of each minima without having to resort to unphysical values of azimuthal extension. We adopted a maximum inclination

of 77°, as larger inclinations would likely result in the inner disk region being overshadowed by the outer flared disk[7] (Bertout 2000), making it impossible to observe occultation of the photosphere by an inner disk warp. Error bars in warp maximum height and azimuthal extension were calculated by modeling the flux dips with the value of inclination fixed at its lowest and highest possible values, and finding the best fit in each case.

Each minimum of each light curve was fitted independently to account for any possible change in the warp from one rotation cycle to another. This allows us to identify how the warp must vary between rotation cycles in order to account for the variability in the widths and amplitudes of the flux dips. It also allows us to assess the changes on timescales of years by comparing the warp parameters found from the 2008 and 2011 light curves of the same star. The synthetic light curves reproduced by the occultation model are shown in Figure 4.12 and the derived warp parameters are shown in Table 4.3. Since they vary from one rotation cycle to another, the intervals of the values found for each light curve are presented.

Most values found for the warp's maximum height and azimuthal extension are similar to the ones given for AA Tau. The ratio between the warp's maximum height and the radius at which it is located ranges from 0.10 to 0.34 for individual flux dips, with an average value of $h_{max}/R_w = 0.23$ (it was found to be $h_{max}/R_w = 0.30$ for AA Tau in Bouvier et al. 1999). The azimuthal extension of the warp varies from as low as 110° to very often a full 360°, with an average of $\phi_c = 300°$. For AA Tau it was maintained at 360° for all flux dips. Inclinations generally need to be greater than $\sim 65°$ for the occultation model to successfully reproduce the widths of the minima, but in some cases may be as low as 60° for relatively large warp heights or shallow flux dips.

The warp maximum height must vary between rotation cycles by on average 11%, and at times by up to 57%, to account for the variations in amplitude of the light curves. The warp's azimuthal extension needs to vary by on average 17%, and up to 65%, from one rotation cycle to the other to account for the variations in the width of the flux dips present in the CoRoT light curves. If the photometric variability of these stars is indeed caused by an inner disk warp that is a product of the interaction between the magnetosphere and the inner disk region, as we propose, then these values demonstrate how dynamic this interaction must be. This dynamic nature is predicted by MHD models (e.g. Kulkarni & Romanova 2013).

The occultation model initially proposed for the CTTS AA Tau appears to be adequate at reproducing the general aspects of the AA Tau-like light curves of our sample. It is capable of reproducing the widths and amplitudes of the flux dips using values of inclination, warp maximum height, and azimuthal extension that are consistent with those found for AA Tau itself, with only a few stars showing values of warp height and azimuthal extension that are significantly lower.

[7] This effect may not be as significant for sources that have very little dust in their inner disks, since they may possess flatter outer disks. However, this is not the case for any of our systems with AA Tau-like light curves.

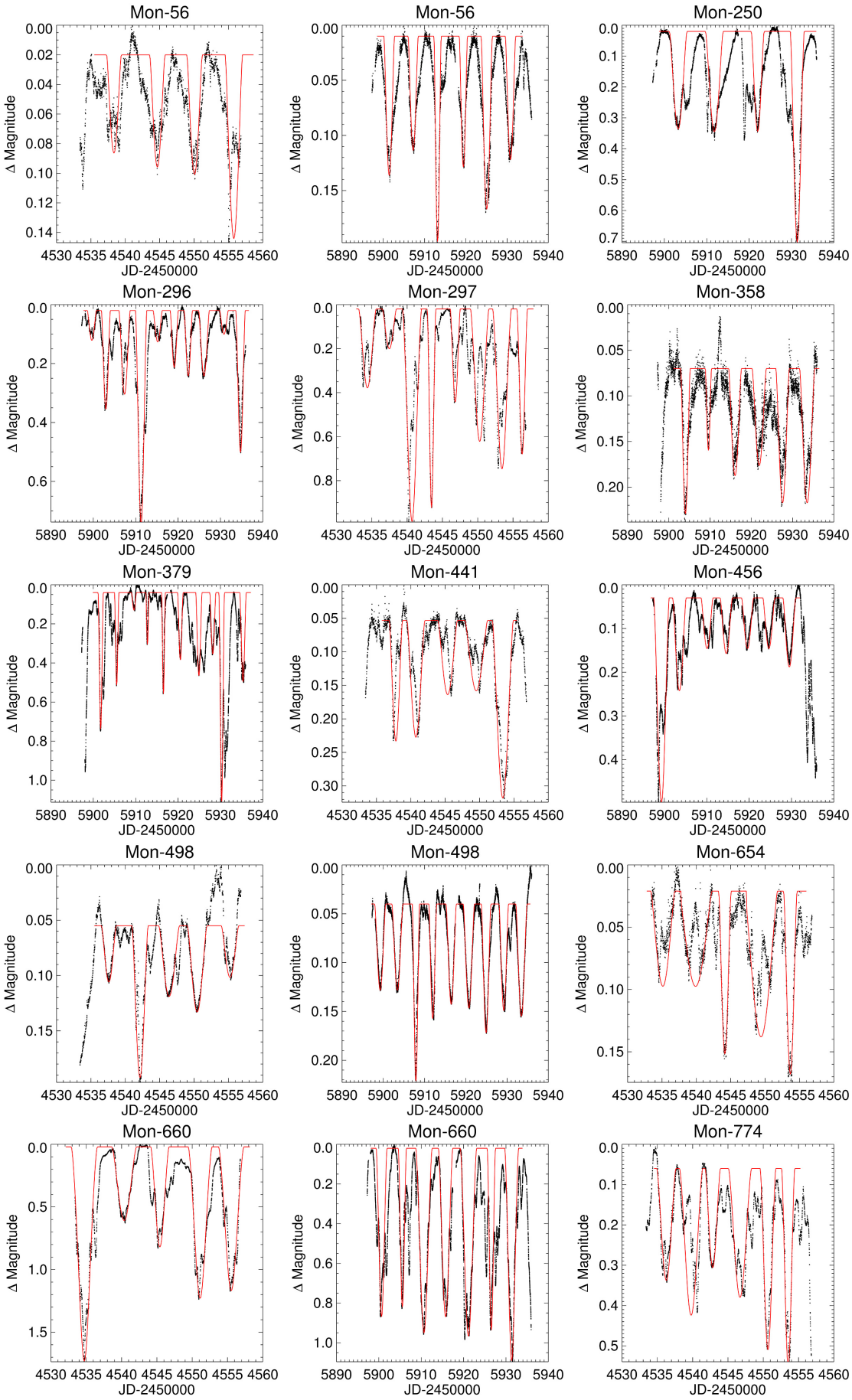

Figure 4.12: Simulated light curves of AA Tau-like stars (red) plotted over CoRoT light curves (black).

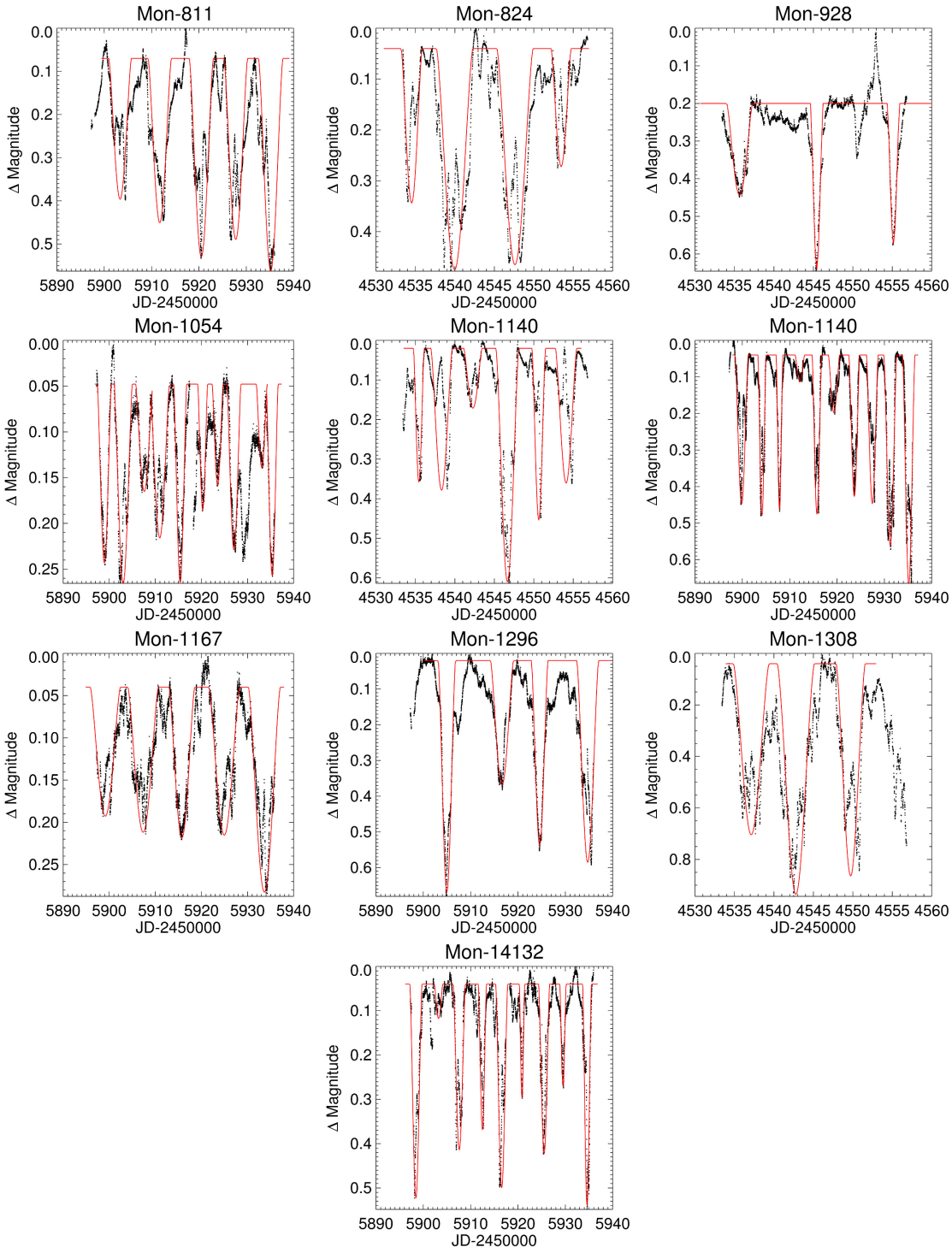

Figure 4.12: Continued.

Table 4.3: Occultation model parameters found for the AA Tau-like candidates.

CSIMon ID	Epoch	$R_w(R_*)$	h_{max}/R_w	$\phi_w(^\circ)$	Inclination ($^\circ$)
CSIMon-000056	2008	9.29	0.24-0.25 ($\pm$0.10)	320 ($\pm$40) - 360	71$\pm$6
CSIMon-000056	2011	9.45	0.24-0.26 ($\pm$0.10)	290 ($\pm$70) - 360	71$\pm$6
CSIMon-000250	2008	11.71	0.23-0.28 ($\pm$0.05)	140 ($\pm$30) - 360	74$\pm$3
CSIMon-000250	2011	12.28	0.24-0.27 ($\pm$0.05)	270 ($\pm$30) - 360	74$\pm$3
CSIMon-000296	2011	6.86	0.21-0.31 ($\pm$0.09)	290 ($\pm$40) - 360	72$\pm$5
CSIMon-000297	2008	5.95	0.17-0.28 ($\pm$0.04)	180 ($\pm$30) - 360	75$\pm$2
CSIMon-000358	2011	6.51	0.17-0.19 ($\pm$0.06)	210 ($\pm$50) - 360	73$\pm$4
CSIMon-000379	2011	5.89	0.22-0.34 ($\pm$0.12)	110 ($\pm$30) - 270 ($\pm$90)	70$\pm$7
CSIMon-000441	2008	3.97	0.17-0.23 ($\pm$0.11)	160 ($\pm$20) - 310 ($\pm$50)	70$\pm$7
CSIMon-000456	2011	6.92	0.18-0.24 ($\pm$0.05)	360	74$\pm$3
CSIMon-000498	2008	4.73	0.17-0.21 ($\pm$0.10)	145 ($\pm$35) - 165 ($\pm$15)	70$\pm$6
CSIMon-000498	2011	4.77	0.19-0.22 ($\pm$0.10)	130 ($\pm$50) - 165 ($\pm$15)	70$\pm$6
CSIMon-000654	2008	3.87	0.10-0.13 ($\pm$0.06)	180 ($\pm$60) - 310 ($\pm$50)	73$\pm$4
CSIMon-000660	2008	7.64	0.25-0.33 ($\pm$0.04)	260 ($\pm$20) - 360	74$\pm$3
CSIMon-000660	2011	7.50	0.27-0.29 ($\pm$0.05)	200 ($\pm$30) - 360	74$\pm$3
CSIMon-000774	2008	4.73	0.15-0.21 ($\pm$0.03)	220 ($\pm$40) - 360	75$\pm$2
CSIMon-000811	2011	8.19	0.26-0.28 ($\pm$0.08)	360	72$\pm$5
CSIMon-000824	2008	7.90	0.24-0.27 ($\pm$0.08)	260 ($\pm$40) - 360	72$\pm$5
CSIMon-000928	2008	6.36	0.28-0.30 ($\pm$0.10)	120 - 300 ($\pm$60)	71$\pm$6
CSIMon-001054	2011	3.52	0.16-0.21 ($\pm$0.09)	270 ($\pm$70) - 360	70$\pm$5
CSIMon-001140	2008	6.79	0.16-0.24 ($\pm$0.03)	190 ($\pm$20) - 360	75$\pm$2
CSIMon-001140	2011	6.83	0.14-0.24 ($\pm$0.03)	190 ($\pm$20) - 360	75$\pm$2
CSIMon-001167	2011	5.37	0.15-0.18 ($\pm$0.05)	330 ($\pm$30) - 360	74$\pm$3
CSIMon-001296	2011	8.52	0.31-0.34 ($\pm$0.13)	260 ($\pm$80) - 330 ($\pm$30)	69$\pm$8
CSIMon-001308	2008	7.86	0.28-0.30 ($\pm$0.06)	330 ($\pm$30) - 360	73$\pm$4
CSIMon-001308	2011	8.04	0.20-0.27 ($\pm$0.06)	340 ($\pm$20) - 360	73$\pm$4
CSIMon-014132	2011	3.98	0.18-0.32 ($\pm$0.14)	120 ($\pm$40) - 290 ($\pm$80)	68$\pm$9

Notes. R_w is the radius where the warp is located, assumed to be at the co-rotation radius (i.e., $R_w = R_{co}$); h_{max} is the maximum warp height found for each flux dip, expressed in stellar radii R_*; and ϕ_w is the azimuthal extension of the warp found for each flux dip. The inclinations shown here were constrained using the occultation model.

For the stars whose light curves are classified as AA Tau-like in both CoRoT epochs, the values we found of warp maximum height and azimuthal extension are always in the same range. This means that, although the occulting structure should be variable on timescales of days to weeks, it can persist on timescales of a few years. For these stars, the periods found in each observing run are very similar to each other, most being equal within their uncertainties. In all of these cases the radius where the occulting structure should be located differs by less than 4% from one epoch to the other, and most by less than 2%, which is well within the uncertainties. It is possible that these structures move somewhat in radius over timescales of a few years, but if this is the case then they apparently do so by very little.

Though the occultation model is able to reproduce the widths and amplitudes of the light curve minima, it is unable to account for the exact shape of the flux dips, which are much more complex than the nearly Gaussian shapes reproduced by the model. This is a very simple model, based on a symmetric warp of homogeneous optical thickness, which likely does not reflect the reality of these systems. Short term brightening episodes were found in the light curves of AA Tau during its occultation events, and were attributed to inhomogeneities of the optical thickness in the occulting material (Bouvier et al. 1999). We also observe these brightening episodes in many of the light curves in our sample. Our light curves' flux dips present significant structure, which could be due to inhomogeneities in the material occulting the star, to the existence of a configuration of hot spots visible during the occultations, or to non-steady accretion within the funnel flows, which would lead to variable emission during the flux dips. We would need to apply a model that takes into account all of these different effects if we wished to properly reproduce the details of our light curves, which is not the aim of this work.

4.6.4 Two occulting structures?

We note that, in our AA Tau-like light curves, there are sometimes two flux dips where we would expect to see only one for the AA Tau scenario. For instance, in the 2008 CoRoT light curve of the star Mon-250 (left panel of Figure 4.13), we see two very deep flux dips between MJD 54541 and MJD 54549, which spans only one rotation cycle. This caused its period to be initially estimated as half of its true period, which was only determined more precisely in 2011, when its photometric variability proved to be more stable and its rotation period of 8.6 days was determined spectroscopically (see discussion in Section 4.5). Therefore, the 2008 light curve spans only three rotation cycles, though we observe more than three flux dips. We could speculate that the two middle dips are part of a single occulting structure, as the last two dips would be as well, and that the increase in emission in the middle of the flux dips is due either to the appearance of a large hot spot or to a very inhomogeneous warp. Unfortunately, there is no color information simultaneous with this light curve to verify these scenarios. However, we are unable to reproduce a single large flux dip that encompasses both

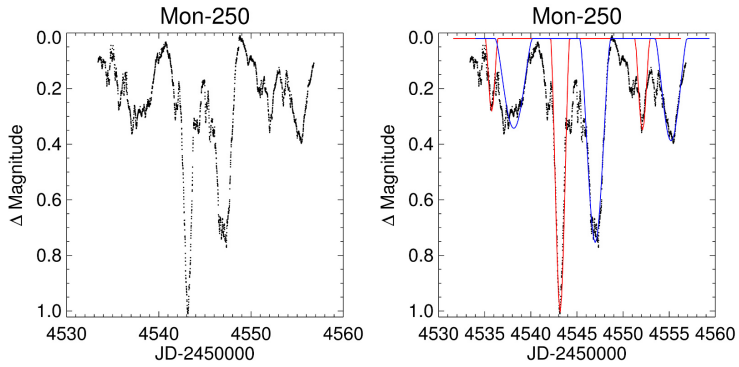

Figure 4.13: Left: 2008 CoRoT light curve of Mon-250. Right: synthetic light curves generated with the occultation model for two separate accretion funnel flows (blue and red) plotted over the 2008 CoRoT light curve of Mon-250.

of the middle dips seen in the 2008 light curve with the occultation model, using physically plausible parameters. We can reproduce each dip separately, however, if we consider that there are two accretion funnel flows, separated by 160° (i.e., nearly opposite each other), causing two distinct clumps of optically thick material to be lifted above the disk plane. This is illustrated in the right panel of Figure 4.13. For this reason, we propose that it is possible for the main accretion funnel flow to at times give way to two accretion funnel flows as a result of increased instability of the accretion process.

This same behavior was observed in AA Tau in 1999, when its quasi-periodic flux dips gave way to two flux dips per stellar rotation cycle (recall Figure 1.8, page 10). This may also be occurring in the star Mon-1054, which presents several double dips in its 2011 light curve, shown in the left panel of Figure 4.14. Arrows point to moments where we observe two flux dips when we would expect to see only one in a typical AA Tau-like scenario. Its veiling features support the AA Tau-like scenario as the primary cause for its photometric variability (see Section 4.5). The occultation model is capable of reproducing some of its double dips with only one accretion funnel flow, assuming that another mechanism is responsible for the emission within the dip, but it is not able to do so for the fifth double dip indicated in the left panel of Figure 4.14. In this case, only two funnel flows of similar height and azimuthal extension, separated by 160°, can successfully reproduce both minima in the light curve. This may be an indication that the accretion process this CTTS is undergoing is suffering from increased instabilities.

This may be the case as well for the star Mon-379 during the 2011 CoRoT observations (right panel of Figure 4.14), where we can observe additional extinction events occur alongside its periodic AA Tau-like dips. These periodic dips are easily reproduced by the occultation model. The additional extinction events may be due to random accretion streams appearing around the star, coexisting with the main stable accretion funnel flow. For this particular star, some of the dips are quite narrow and the occultation model finds values for

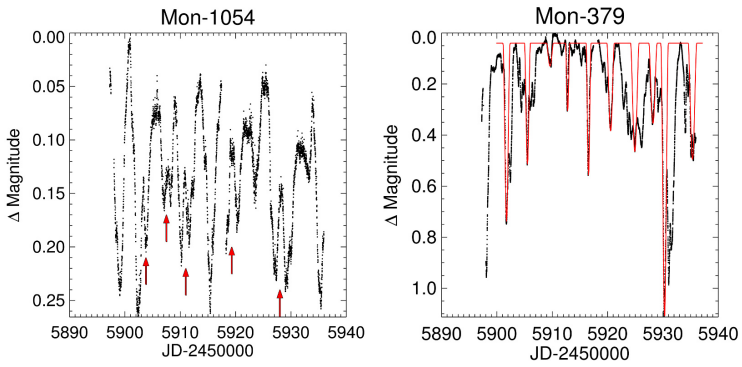

Figure 4.14: Left: 2011 CoRoT light curve of Mon-1054. Arrows show moments when two flux dips are present where we would expect to see only one in a typical AA Tau-like scenario. Right: Simulated light curve (red) plotted over the 2011 CoRoT light curve of Mon-379 (black).

its azimuthal extension as low as 110°, unlike the majority of other AA Tau-like systems, where this value is between 260° and 360°. These factors may all be an indication of the declining stability of this CTTS's accretion process. This possibility will be discussed further in the next Section.

4.7 Periodic vs. aperiodic behavior: an indication of accretion regime?

In this section, we discuss the main differences between the stars with quasi-periodic AA Tau-like photometric variability and the stars whose light curves are dominated by circumstellar extinction, but have no obvious periodicity. AA Tau-like photometric behavior has been associated with the stable accretion regime (Bouvier et al. 2007; Romanova et al. 2013; McGinnis et al. 2015), in which the interaction between a strongly bipolar stellar magnetosphere and the inner accretion disk would result in an inner disk warp, which would occult the stellar photosphere periodically as the system rotates. In McGinnis et al. (2015) we proposed that the stars whose light curves are dominated by aperiodic extinction may be associated with the unstable accretion regime, in which case the material that is randomly occulting the stellar photosphere could be circumstellar disk material lifted above the disk plane at the foot of irregularly distributed accretion streams. Our findings in Section 4.5 for Mon-441 and Mon-1144 provide strong support to this hypothesis. If this is indeed the case, then the change in light curve morphology between the two CoRoT observing runs that we observe for some stars (see Section 4.1 and Table 4.1) would indicate a change in their accretion regimes.

As reported by Kurosawa & Romanova (2013), a transition between regimes can be expected if one or a few of the factors that determine instability change with time within a

certain system. According to their models, the parameters that are important in determining through which of these regimes a CTTS will accrete are: mass accretion rate ($\dot{M}_{acc}$), truncation radius, stellar rotation rate, the inclination angle β between the stellar rotation axis and the axis of the magnetic field (Ω and μ, respectively, in Figure 1.3), and the α-parameter, which describes viscosity in the disk. Therefore if, for instance, the truncation radius R_{mag} becomes smaller than the co-rotation radius R_{co} because of a decrease in the stellar magnetic field, accretion flows tend to become unstable. The mass accretion rate can also affect the ratio R_{mag}/R_{co}, since higher mass accretion rates lead to smaller truncation radii, therefore leading to more unstable configurations. The viscosity parameter (α) controls the global mass accretion rate. The higher α is, the higher the mass accretion rate is, leading to more instabilities. According to Kulkarni & Romanova (2009), the transition from a stable to an unstable regime occurs around critical values of mass accretion rates. They state typical critical values for stars with $R_{mag} \approx 2 - 3R_*$ to be around $\dot{M}_{acc} = 1.7 \times 10^{-7}$, and for stars with $R_{mag} \approx 4 - 5R_*$, around $\dot{M}_{acc} = 2.1 \times 10^{-8}$.

A larger angle β can lead to more stable configurations, since at large β the magnetic poles become closer to the inner disk rim, lowering the potential barrier in the vertical direction that the material must overcome to be lifted into the accretion funnel flows. According to MHD models, values of $\beta > 25°$ usually lead to stable configurations (Kulkarni & Romanova 2009; Romanova et al. 2014).

Venuti et al. (2014) showed that mass accretion rates in CTTSs can vary considerably over time. They calculated mass accretion rates for stars in NGC 2264 using data from December 2010 and January 2012, the latter being nearly simultaneous with the CoRoT observations. They showed that many of the stars in our sample had mass accretion rates vary by up to 50% in little over one year. Unfortunately, there is no estimate of mass accretion rate simultaneous with the 2008 CoRoT observations, but it is possible that a variation such as this contributed to a transition between accretion regimes. However, Venuti et al. (2014) also show that long term changes in mass accretion rates are not necessarily larger than short term changes. The variability they observed in timescales of years is in the same range as the one observed in timescales of days to weeks, which is consistent with other studies (e.g. Costigan et al. 2014). So if these changes were to influence the stability of the accretion regime, then this influence would be on shorter timescales as well.

The other factor that could be responsible for these transitions is the stellar magnetic field configuration. It has already been shown observationally that the magnetic field of a CTTS can change significantly over the years. The CTTS V2129 Oph (Donati et al. 2011), for example, had its magnetic field measured in two different epochs, nearly four years apart, and the magnetic field strength was shown to vary greatly from one epoch to the other. The dipolar component was found to be about 3 times stronger in the second observation, and the octupolar component 1.5 times stronger than four years earlier. Donati et al. (2011) found that the ratio R_{mag}/R_{co} had nearly doubled in that time.

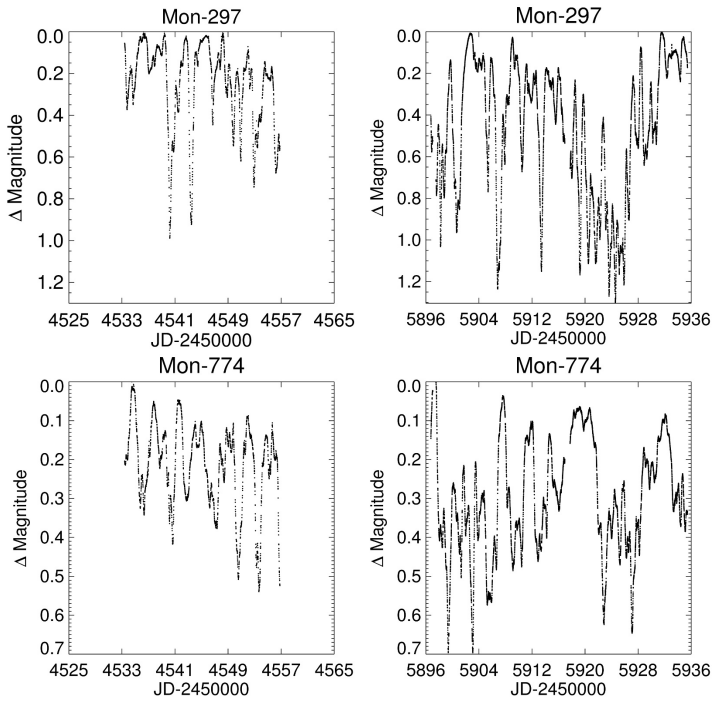

Figure 4.15: Corot light curves of Mon-297 and Mon-774 during their AA Tau phases (left) and aperiodic phases (right).

In our study we see that $38\%^{+14\%}_{-11\%}$[8] (5/13) of the stars that in 2008 showed photometric variability similar to AA Tau were observed again in 2011, this time showing aperiodic variability due to extinction from circumstellar material. Of the stars that were observed in 2008 to have aperiodic photometric variability due to circumstellar extinction, $62\%^{+11\%}_{-15\%}$ (8/13) were observed again in 2011 with variability similar to AA Tau. If our proposed scenario is true, then this points to a transition from a stable to an unstable accretion regime, or vice-versa, in less than four years for $57\%^{+9\%}_{-11\%}$ [8] of our sample of possible AA Tau-like stars (i.e., out of the 23 stars that presented a light curve similar to AA Tau in at least one CoRoT observation, 5+8 suffered this transition). An example of two of the stars that appear to have undergone this transition is shown in Figure 4.15.

There is one specific case which is different from the others. The star Mon-928 presents AA Tau-like flux dips in 2008 which disappear entirely in 2011. Its light curve observed in the second CoRoT run is not characteristic of circumstellar extinction, but instead resembles the small scale variabilities seen in between the flux dips of its 2008 light curve (Figure 4.16). The period of 9.92 days found during the first epoch is similar to periods previously measured for this star in the literature (Lamm et al. 2005), yet it is non-existent in the 2011 light curves.

[8] Throughout this work we assign Poisson uncertainties to fractions whenever the sample considered is large (at least 100 objects). These uncertainties are determined as $\sqrt{N_{det}}/N_{tot}$, where N_{tot} is the total number of objects considered and N_{det} is the number of detections. For smaller samples the Poisson approximation is not valid and asymmetric uncertainties must be assigned. In these cases we follow the approach described in the appendix of Burgasser et al. (2003).

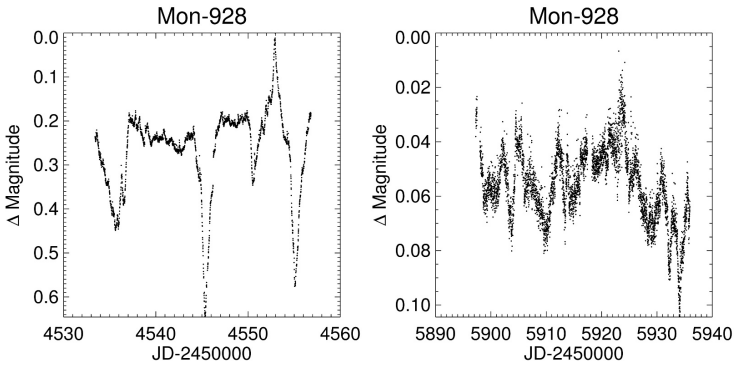

Figure 4.16: CoRoT light curves of Mon-928 in 2008 (left) and 2011 (right).

One possibility is that in 2011 the inner disk warp did not reach high enough altitudes above the disk to occult the stellar photosphere. At the inclination of 71° we estimated for this system (see Section 4.6), our simulations using the occultation model show that if the warp found to best reproduce the 2008 CoRoT light curve decreased in height by at least 26%, the occultations observed in 2008 would no longer occur. This amount of variation in warp height is well within the range we observed for these objects in Section 4.6.3, and could be caused, for instance, by an increase in the mass accretion rate leading to a more unstable configuration in 2011 and therefore a less pronounced warp.

For the 13 stars that changed between periodic and aperiodic photometric behavior, we performed a periodogram analysis of their light curves from both CoRoT epochs using the Scargle periodogram as modified by Horne & Baliunas (1986). If the material occulting the photosphere during the periodic phase is close to the corotation radius, as was the case for AA Tau, then the period found during this phase represents the stellar rotation period. It is possible that even during the aperiodic phase a weak signal corresponding to the stellar rotation period may be recovered. Therefore we analyzed the periodograms of each epoch separately and compared them to see if this was the case. For 11 stars, during the epoch of unstable accretion at least a weak signal was present at the period found for the AA Tau phase. For eight of these stars, this peak was the only one present, or the strongest, despite being much weaker than the one present during the AA Tau phase. The only exception was the star Mon-441, which shows a weak signal during its unstable phase, but this signal does not correspond to the period found in the AA Tau phase, or to a multiple of it.

We measured the amplitudes of the variable flux dip depths during both the AA Tau-like and the aperiodic phases and compared them. In most cases the amplitudes during the aperiodic phase are smaller by 20% to 60% than those measured during the AA Tau phase. However, for 4 of these 13 stars, the flux dip depths remained nearly the same in both epochs, and for 2 more stars the variability amplitude during their aperiodic phase was larger by 20% to 30% (the stars shown in Figure 4.15). This means that, at least in some cases, during the unstable accretion phase dust must be lifted above the disk plane at

similar, and sometimes even higher, altitudes as during the stable accretion phase.

It has also been noted that these stars are often fainter when in the aperiodic phase than during their AA Tau phases, by up to a few 0.1 magnitudes. We propose the following to explain this effect: in the unstable accretion regime there are several accretion streams surrounding the star, lifting material at different points around the circumstellar disk that occult the photosphere. It is possible that there is always a clump of material intercepting our line of sight, causing us to never observe the full photospheric flux of the star. This would not be the case during the stable accretion regime, since we would then expect the stellar photosphere to be observable during some rotational phases, when the inner disk warp passes behind the star.

A system's instability at a certain moment can perhaps be quantified by some aspects of its light curves. For systems seen at low or medium inclinations, for instance, Kurosawa & Romanova (2013) predict that the more unstable is the system's accretion regime, the higher the frequency of flux peaks per stellar rotation period one would observe in its light curve, thanks to the presence of a larger number of accretion shocks on the photosphere. It is fair to assume that, for systems seen at high inclinations, a higher frequency of flux dips would also be observed for more unstable scenarios because of the larger number of accretion streams present around the star, whose base could contain dust that can occult the photosphere. Of the stars in our sample that changed from one regime to the other, most present two to three flux dips per stellar rotation period during their unstable accretion phase, while some show up to seven flux dips per rotation period. This may be an indication of the degree of instability of these star-disk systems. The two stars that show the highest frequencies of flux dips during their unstable accretion phases are the two that have the lowest masses in our sample of possible AA Tau-like stars. As discussed in Section 4.8, low mass stars appear to present more unstable accretion, possibly as a result of magnetic field configurations. On the other hand, these high frequencies of flux dips can also be caused by dust lifted above the disk plane as a result of magnetorotational instabilities that do not necessarily lead to accretion streams (Turner et al. 2010; Hirose & Turner 2011).

Of the 23 stars that present AA Tau-like behavior, only six maintain this behavior in both 2008 and 2011. Many appear to show some signs of weak instability even during their AA Tau phase, sometimes presenting two or three flux dips in one rotation cycle. A few examples are Mon-297, Mon-456, and Mon-824 (Figure 4.17). Most of our stars show many small secondary flux dips in the light curve, indicating a possible coexistence of secondary accretion streams with the main accretion funnel flows. This is predicted by MHD models such as that of Blinova et al. (2016), who separate the unstable accretion into two regimes, ordered and chaotic. In the ordered unstable regime, two accretion funnel flows can form, sometimes both carrying similar amounts of matter flux, sometimes one carrying more. These two funnel flows can persist over a few rotation cycles, and can alternate with one main accretion funnel flow in similar timescales. This seems to be the case of Mon-250 and

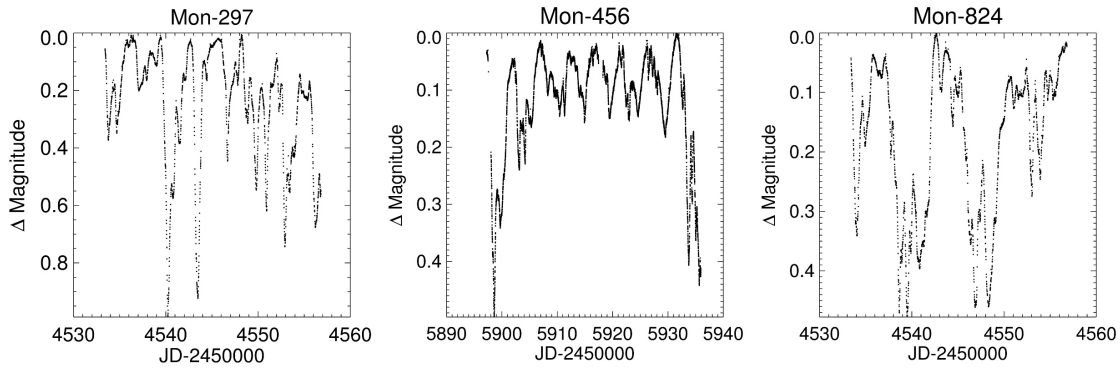

Figure 4.17: CoRoT light curves of Mon-297, Mon-456, and Mon-824 during their AA Tau phase. These stars sometimes present two, or even three, flux dips per rotation period, and often secondary flux dips are present alongside the main flux dips, indicating a possible coexistence between unstable accretion streams and stable accretion funnel flows.

Mon-1054, which sometimes presented two flux dips during one rotation cycle (Figure 4.13 and 4.14).

4.8 Other characteristics of stars with AA Tau-like light curves

We noticed that the CTTSs that present AA Tau-like light curves in either CoRoT observing run tend to have higher masses, on average, than those that showed only aperiodic behavior. This can be seen in Figure 4.18. The left panel shows a histogram of the masses of stars with AA Tau-like light curves (red) and stars with aperiodic extinction-dominated light curves (purple), plotted over a histogram of all CTTSs in our study of NGC 2264 that were observed by CoRoT in either of its observing runs. While the CTTSs in the whole sample show a tendency toward lower masses, the AA Tau-like stars are equally present in the whole range of masses considered. Therefore, though we find AA Tau-like light curves among CTTSs of all masses, the ratio of these stars to the total number of stars observed by CoRoT in that mass bin increases with increasing mass. This makes them relatively more common among higher mass stars (in the TTS mass range, i.e. up to $\sim 2 M_{\odot}$) than among lower mass stars (middle panel of Figure 4.18).

Inclination is a major factor in whether we observe the AA Tau-like phenomenon or not, so we know that the observed AA Tau-like systems are only a fraction of the total number of systems that present an inner disk warp. For stars of $M_* \lesssim 0.7 M_{\odot}$, we observe fewer than 10% of the CTTSs as AA Tau-like. If we consider that it is possible to view the occultations in systems of inclination between $\sim 60°$ and $77°$ (see Section 4.6) then, assuming random inclinations, this means that only at most 50% of the CTTSs in this mass range should possess an inner disk warp. For stars of $M_* \gtrsim 0.7 M_{\odot}$, about 35% present AA Tau-like behavior, meaning that if we assume random inclinations, all of these stars likely possess an inner disk warp at some point.

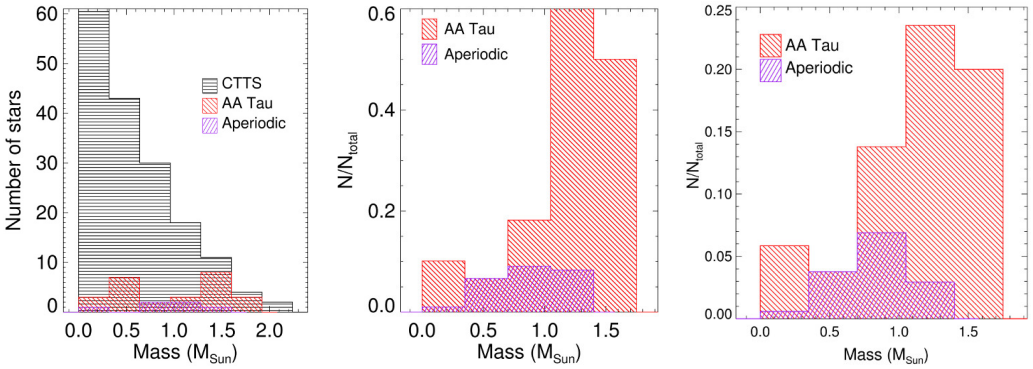

Figure 4.18: Left: mass histogram of all CTTSs observed by CoRoT (black), those with AA Tau-like light curves (red), and those whose CoRoT light curves are dominated by aperiodic extinction events (purple). Middle: number of AA Tau-like stars (red) and aperiodic extinction stars (purple), divided by the total number of CTTSs observed by CoRoT in that mass bin. Stars of both CoRoT observing runs were considered, and any star that presented AA Tau-like photometric behavior in either run was included in the AA Tau category. Right: number of AA Tau-like stars (red) and aperiodic extinction stars (purple), divided by the total number of CTTSs in the sample of Venuti et al. (2014), including those that were not observed by CoRoT.

The fraction of stars that present AA Tau-like light curves becomes unusually large as we approach even higher masses ($M_* \gtrsim 1.0 M_\odot$). Considering that we should only observe $\sim 20\%$ of the CTTSs as AA Tau-like, the fraction of AA Tau-like systems we find in this mass range is much larger than we would expect even if all CTTSs observed by CoRoT possessed an inner disk warp. This could be due to a selection bias, since the CoRoT targets were not selected randomly, but based on specific criteria, which in 2008 included periodicity and in 2011 prioritized many systems previously classified as AA Tau-like. Therefore, we compared with another sample. The right panel of Figure 4.18 shows a histogram of the number of AA Tau-like systems observed by CoRoT, this time normalized by the total number of CTTSs observed by the CFHT MegaCam (Venuti et al. 2014), including those that were not observed in the CoRoT campaigns. This histogram could present the opposite bias as the previous one, since some of the systems that were not observed by CoRoT could very well present AA Tau-like variability that would be unaccounted for. Still, we see that slightly over 20% of the stars in the mass range $1.0 M_\odot \lesssim M_* \lesssim 2.0 M_\odot$ present this type of variability. Extrapolating this amount to the systems where the inclinations prevent us from observing this tendency, nearly all of the systems with mass $1.0 M_\odot \lesssim M_* \lesssim 2.0 M_\odot$ and most ($\sim 75\%$) of the systems with mass $0.7 M_\odot \lesssim M_* \lesssim 1.0 M_\odot$ should present an inner disk warp at some point. For systems of $M_* \lesssim 0.7 M_\odot$, this fraction would be of only $\sim 25\%$.

One possible explanation for this trend is the stellar magnetic field configuration. The magnetic field's dipolar component is believed to be responsible for the strong interaction

with the inner disk that causes a warp to appear. As was discussed in Section 4.7, a stronger dipolar component leads to a larger truncation radius, which tends to favor stable accretion. Gregory et al. (2012) found that the magnetic field configuration of a CTTS depends strongly on its internal structure, and that for intermediate to high mass TTSs ($0.5M_{\odot} \lesssim M_{*} \lesssim 2.0M_{\odot}$), those that are fully convective or have as yet only developed a small radiative core tend to have strong dipoles. At the estimated age of 2 - 3 Myr of NGC 2264, Gregory et al. (2012) show that stars in this mass range are still developing a radiative core. It might then be reasonable that they possess strong dipolar components in their magnetic fields.

As for TTSs of smaller mass ($M_{*} \lesssim 0.5M_{\odot}$), there is still very little information available on magnetic fields because of observational constraints. At least one CTTS in this mass range has had its magnetic field topology measured (V2247 Oph, Donati et al. 2010b). It was found to have a weak dipolar component. Therefore, it is possible that among fully convective stars, a significant difference in magnetic field configurations may exist among these two mass ranges. For main sequence stars, Morin et al. (2010) showed that those of very low mass have considerably different magnetic field topologies than fully convective stars of higher mass. While the latter generally possess magnetic fields with strong dipoles, very low mass main sequence stars ($M_{*} \lesssim 0.2M_{\odot}$) can present a number of different magnetic topologies. They range from very strong, axisymmetric, nearly dipolar fields to weaker fields with a strong non-axisymmetric component and a strong toroidal component. This seems to indicate that a different magnetic field regime may dominate among stars of lower mass.

Our results alone are insufficient to determine whether a significant difference truly exists among magnetic field configurations of CTTSs of different masses. Other factors may be influencing our higher detection of AA Tau-like light curves among CTTSs of higher mass. For example, mass accretion rates tend to decrease toward lower masses (Venuti et al. 2014), which would cause the truncation radius to increase. This would favor a stable accretion mechanism, but could also cause the disk warp to be located farther away from the co-rotation radius than we assume. If they are located significantly farther away, we would require higher inclinations to observe the occultations in these systems, which would considerably reduce the number of AA Tau-like systems identified. This effect could also be the result of an observational bias. Assuming the stars in our sample are all at the same distance, those of lower mass should generally be fainter than those of higher mass. The signal from the CoRoT observations could simply be too low among stars below a certain mass limit for us to reliably identify AA Tau-like light curves.

Chapter 5

Spectral signatures of jets and outflows

In this chapter, we investigate the ejection phenomena that originate in the inner disks of classical T Tauri Stars and Herbig AeBe stars in NGC 2264 by analyzing the forbidden [OI] 6300Å emission line present in their spectra. This line is a strong tracer of jets and winds in YSOs, therefore characterizing the emission profiles allows us to infer properties of these jets and winds and search for associations with stellar and accretion properties. We can take advantage of the extensive knowledge available on the CTTSs belonging to NGC 2264 and search for correlations between the different components of the [OI] 6300Å line and stellar and/or disk properties.

Of the 487 stars that were included in the 2014 FLAMES campaign, which was centered on the [OI] line (described in Section 2.4), 483 are cataloged as members of NGC 2264 according to the criteria described in Section 3.1. Of these, 237 are WTTSs, 182 are classified as CTTSs according to the criteria described in Section 3.2, 2 are Herbig Ae/Be stars, and the remaining 62 are of unknown spectral types and have not shown any indication of accretion is previous studies. There is also one candidate CTTS among the stars that were not cataloged as members, according to Venuti et al. (2014).

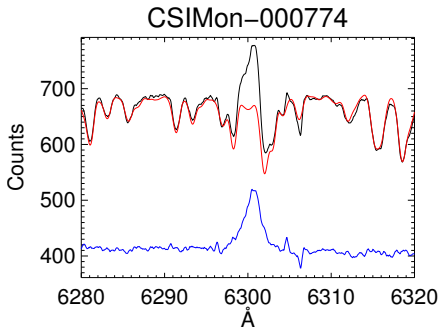

Figure 5.1: Example showing the photospheric contribution being removed from a CTTS spectrum in order to recover the intrinsic [OI] emission line profile. The veiled, broadened WTTS template is shown in red, plotted over the stellar spectrum in black. Below, the final product is shown in blue, shifted vertically to facilitate a comparison with the stellar spectrum. Note that the wings of this profile are recovered after removing the photospheric absorption lines.

5.1 Recovering the intrinsic [OI] λ6300Å line profile

In order to identify forbidden [OI] 6300Å emission in the stellar spectra, it is often necessary to eliminate the photospheric contribution to the spectrum, thus isolating the emission line. Photospheric absorption lines that lie close to the [OI] emitting region can affect the emission line and even bring it to levels below our detection rate, especially when the emission is weak. In order to remove this effect, we subtract a photospheric template from the stellar spectrum and recover the intrinsic [OI] line profile (see Figure 5.1). The photospheric template used for each star is a combination of a WTTS spectrum of the same (or nearly the same) spectral type, an extra continuum to replicate the CTTS's veiling, and artificial broadening in order for the absorption line widths to reproduce the CTTS's rotational broadening. These steps were described in more detail in Section 3.3.2. The template used was the one whose combination of WTTS, veiling and rotational broadening had the least residuals in comparison to the CTTS spectrum. This procedure was not performed for the 2 HAeBe stars, since they do not present any significant photospheric features in the region near the [OI] line which could interfere with the analysis.

After removing the photospheric contribution to the spectra, we searched for [OI] emission in our stars. We considered as a detection any emission with a peak above 3σ and full width at half maximum (FWHM) higher than the resolution of our spectra, which we measured as 11.3 km/s. Values of σ represent the noise in the spectra, measured from two regions of the continuum 5Å before and after the [OI] line. A few cases where a marginal detection was found in the exact region where the telluric emission line (described in Section 2.4) was originally located were considered as residual contamination from the telluric line and eliminated from the list of detections.

All profiles shown in this chapter have been shifted to the stellar rest velocity.

5.1.1 Completion

Among our 183 CTTSs (and CTTS candidates), 102 ($56\% \pm 6\%$[1]) show emission in the [OI] line, as well as both HAeBe stars in our sample. This low number is somewhat unexpected, since past studies have shown that most accreting T Tauri stars present emission in the forbidden [OI] 6300Å line (e.g. Cabrit et al. 1990; Hartigan et al. 1995; Natta et al. 2014). On the one hand, the sample studied by Hartigan et al. (1995, hereafter HEG95) was composed of stars with on average higher mass accretion rates than ours, which could explain their much higher detection rate[2]. We see this by comparing our distribution of accretion luminosities (L_{acc}) with those calculated by Rigliaco et al. (2013, hereafter R13), who obtained modern estimates of accretion luminosities for the sample of HEG95. Their values are mostly concentrated at $L_{acc} > 10^{-2.6} L_{\odot}$, with only 3/30 outliers at lower luminosities, whereas around 75% of our sample has higher accretion luminosities than this. Among stars of $L_{acc} > 10^{-2.6} L_{\odot}$, our detection rate is 69%, much higher than the global detection rate we find, but still lower than HEG95, who detected the [OI] 6300Å line in 100% of the CTTSs analyzed. On the other hand, Natta et al. (2014, hereafter N14) analyzed a sample of CTTSs with lower mass accretion rates than ours and still found a 91% detection rate in the [OI] 6300Å line among CTTSs. Therefore the mass accretion rates alone cannot account for our low detection rate of [OI] 6300Å emission.

Venuti et al. (2017b) investigate the possibility that NGC 2264 is composed of more than one subpopulation, as a consequence of sequential star formation. They show that the northern region, close to the O-type star S Mon, likely formed first (over 5 Myr ago) while the southern region, near the more embedded Cone Nebula, appears to be younger ($\lesssim 1$ Myr old). Sacco et al. (in prep) is currently investigating the distribution of radial velocities of the cataloged members of NGC 2264, which also suggests that more than one population may be present. We speculate that our low detection rate may reflect the existence of two subpopulations, in which the older one presents weaker outflows and therefore much less [OI] emission. However, when comparing the stars in our sample where [OI] was detected with those where it was not, K-S tests show no statistical difference between their ages or radial velocities. Therefore this scenario is also unable to account for our unusually low detection rate.

Our global detection rate of the [OI] emission line is not constant throughout the HR diagram, it is much higher in the upper left portion (among hotter, more luminous stars) and decreases towards lower effective temperatures (see Figure 5.2). Among stars of $M_* \leq 0.5 M_{\odot}$ (or $T_{eff} \lesssim 3800$K) the detection rate is only 38% (31/81), while for stars of $M_* > 0.5 M_{\odot}$ ($T_{eff} \gtrsim 3800$K) it is 70% (73/104). This could be the result of an observational bias if the cooler stars tend to present emission of lower intensity compared to the level of noise in

[1] The error given corresponds to the Poisson uncertainty, defined as $\sqrt{N_{det}}/N_{tot}$, where N_{tot} is the total number of objects considered and N_{det} is the number of detections.

[2] See Section 5.2 for a discussion on the connection between mass accretion and [OI] emission.

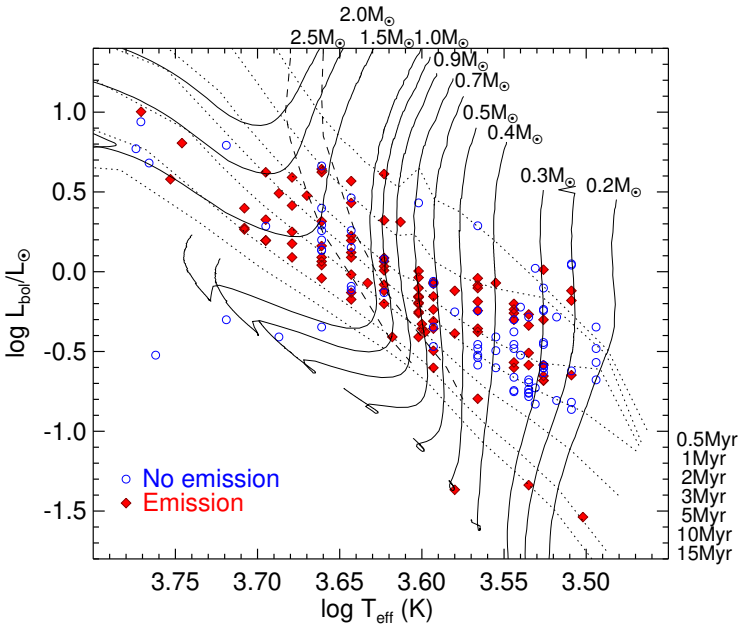

Figure 5.2: HR Diagram of the CTTSs in our sample that have detected [OI] emission (red filled diamonds) and that do not (blue open circles). Mass tracks and isochrones of Siess et al. (2000) are shown as solid and dashed lines, respectively.

their spectra, which falls below our detection threshold. One or more of the following factors could cause this:

- lower mass stars tend to have lower mass accretion rates (Venuti et al. 2014), which would result in lower intensity [OI] emission lines[2];
- cooler stars have more numerous and deeper photospheric absorption lines near the [OI] line that, even after subtracting a photospheric template, lead to higher levels of noise in the spectra; and
- stars of lower luminosity tend to have spectra with lower signal to noise ratios (S/N) in our sample, since all of the spectra were observed with the same integration time[3].

The third factor should be countered by a contrast effect: the lower a photosphere's luminosity, the higher the contrast between a jet's emission and the stellar continuum. This is possibly why we still detect emission in the lower right corner of the HR diagram, despite the sources being fainter. Another effect that can be interfering with the overall [OI] detection is the telluric [OI] emission line. If a star has only a weak component of low radial velocity which coincides closely with the radial velocity of the telluric emission line on the night of the observation, it will be impossible to recover the intrinsic profile.

[3]An exception to this are the stars that were observed in configuration A1 (see Section 2.4), which was observed a total of 4 times, resulting in spectra of better S/N than those observed in the other configurations. However the detection rate in this configuration was no different than the overall detection rate.

In an attempt to assess the level of observational bias, we plot in Figure 5.3 the flux of the continuum at 6300Å versus the star's effective temperature, showing in color the peak of the detected [OI] emission line, measured as the maximum flux minus the continuum flux at 6300Å. The flux is given in instrumental counts, since our data is not flux calibrated. We separate the stars observed in configuration A1 (bottom panels) from those observed in all other configurations (top panels). Configuration A1 was observed 4 times and the observations were combined to create an average spectrum for each star (Section 2.4), meaning that these spectra have better S/N than those that were observed only once. By separating them in Figure 5.3, we can verify if there is a difference in the detectability of the [OI] line in this configuration in comparison with all others. Detections are shown in the left panels of Figure 5.3 while in the right panels we present upper limits of the non-detections, defined as 3σ (where σ was measured from two regions of the spectrum 5Å above and below the [OI] line). Though the detections generally have much higher peaks than the upper limits, there are some that are very close to the 3σ threshold. This is especially true in the low end of the diagram, where our detection rate is the lowest, but also among some of the brightest stars, where a contrast effect may make it difficult to detect emission in [OI] (the more luminous the stellar photosphere, the stronger any [OI] emission from jets or outflows needs to be in order to have a high enough flux above the continuum to be detected). When analyzing only configuration A1, we see that there are also a few detections close to the 3σ threshold, though in this case they seem to separate more from non-detections. The global [OI] detection rate in this configuration is of 55%±9%, the same as the overall value, calculated considering all configurations (56%±6%).

From Figure 5.3, we judge that it is not possible to state for certain that the non-detections in our sample truly have no [OI] emission. Our heterogeneous detection rate across the HR diagram, as well as our overall low detection rate compared with other works, may be caused by an observational bias. To avoid any issues this may bring about, we include upper limits of non-detections in our analyses whenever possible.

5.1.2 Characterizing [OI] emission line profiles

The [OI] 6300Å emission line profile generally presents two distinct features: a low-velocity component (LVC), centered close to the stellar rest frame or blueshifted by up to $\sim$ 20 km/s, and a high-velocity component (HVC), blueshifted by $\sim$ 50 - 200 km/s from the stellar rest frame (HEG95). The HVC is believed to arise in the fast, bipolar jets that are associated with these young objects, while the LVC seems to originate in slower moving winds. The precise origin of the LVC is still under debate. The possible scenarios for its formation are: centrifugally driven magnetohydrodynamic (MHD) disk winds (HEG95, Kwan & Tademaru 1995); thermally driven disk winds, powered by photoevaporation from X-ray (Ercolano & Owen 2010, 2016) or extreme ultra-violet (EUV, Font et al. 2004) radiation from the central

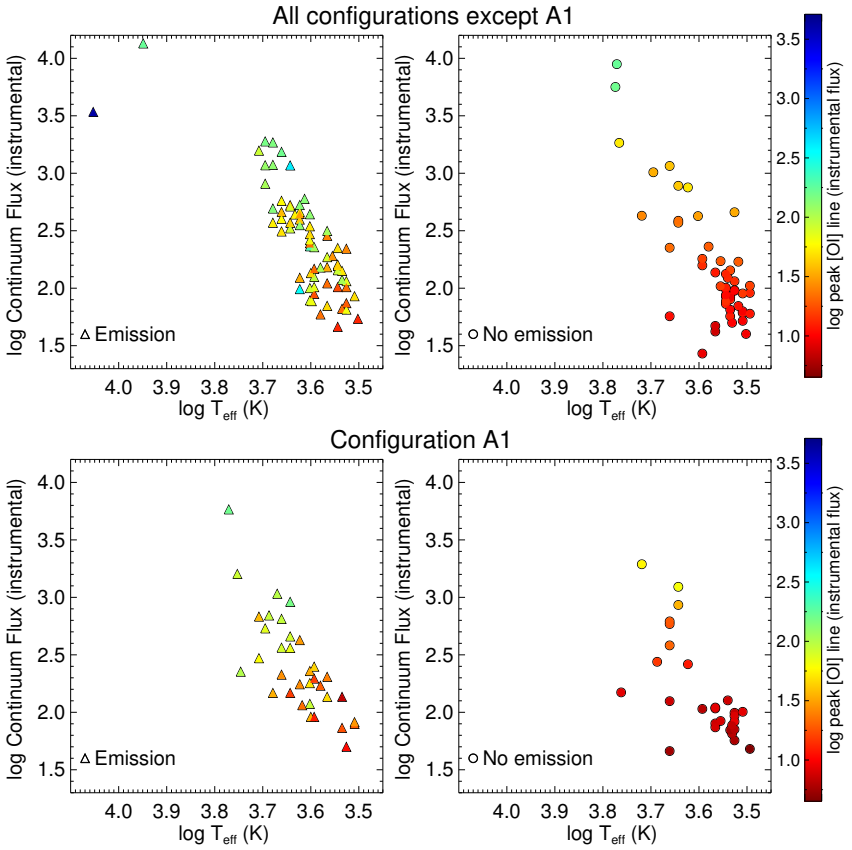

Figure 5.3: Instrumental flux of the continuum at 6300Å versus the effective temperature. Colors represent the peak of the detected [OI] emission line, measured as the maximum flux minus the continuum flux at 6300Å (in instrumental counts). Left panels show detections, while right panels show upper limits for the non-detections, taken as 3σ. Bottom panels show the A1 configuration, which was observed 4 times and has better S/N, while top panels show all other configurations.

object; non-thermal winds from a cooler disk region, where OH is photodissociated by far ultra-violet (FUV) radiation from the central object (e.g., Gorti et al. 2011); or bound gas in the disk under Keplerian rotation (R13). In their sample, N14 found that the forbidden line ratios are consistent with the LVC arising from slow (< 20 km/s), dense ($n_H > 10^8 cm^{-3}$), warm (T $\sim$ 5000K - 10000K), mostly neutral gas.

In recent studies (R13; Simon et al. 2016, hereafter S16), the LVC has been analyzed in more detail and is found to be often composed of two components itself, a narrow and a broad component (defined by S16 as having FWHM < 40 km/s and FWHM ≥ 40 km/s, respectively). S16 showed that the two components appear to originate in distinct regions of the accretion disk, with the broad component possibly coming from closer to the central object (at R $\sim 0.05 - 0.5$au) than the narrow component (at R $\sim 0.5 - 5$au). This result poses the following question: are the broad and narrow components of the [OI] 6300Å line low-velocity emission formed through the same physical mechanism but in different regions of the accretion disk, or does each arise from a distinct phenomenon? R13 proposed that

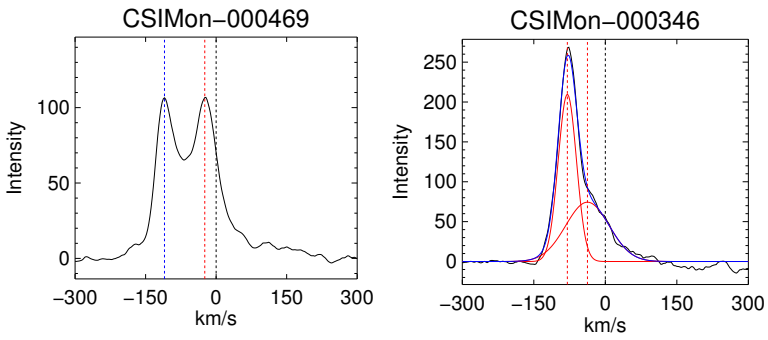

Figure 5.4: Two examples of [OI] emission line profiles found in our sample. Left: two distinct peaks can be identified, one close to the stellar rest velocity and the other blueshifted by over 100km/s (shown as red and blue dashed lines, respectively). The black dashed line shows stellar rest velocity. Right: Gaussian decomposition of a very asymmetric profile. Two separate Gaussians are shown in red, while the sum of the two is shown in blue, overplotted onto the observed profile (black).

the broad LVC may be tracing bound gas coming from a warm disk surface in Keplerian rotation around the star, while the narrow LVC may arise in a cool ($\sim$ 1000 K) molecular wind from farther out in the disk (R $\gtrsim$ 10 au), where [OI] gas becomes gravitationally unbound. In their paper, S16 investigate whether the narrow LVC could arise in a thermally driven photoevaporative wind, but argue that photoevaporation cannot occur at the radial distance where the broad LVC is believed to arise. They attribute the broad LVC emission to the base of an MHD disk wind. In this section we attempt to identify each of these features in our [OI] line profiles so that we can investigate their origins and their connection to stellar and disk properties. However, as we will show, it is not always trivial to separate them.

We observe various different morphologies in our [OI] 6300Å line profiles. For 17 stars we can clearly identify two or three distinct peaks (see the left panel of Figure 5.4 for an example). In all of these cases at least one peak is centered at a velocity higher than $\pm$48km/s from the stellar rest velocity (usually blueshifted by $v < -48$km/s, but in 4 cases a peak is redshifted by $v > 48$km/s). We identify these as high velocity components of the [OI] line. Among the profiles with only one clear peak, many are asymmetric or very broad at the base and an attempt to fit them with Gaussians showed that they require more than one component (right panel of Figure 5.4). We therefore performed a Gaussian decomposition of all profiles in order to find which ones consist of various components and estimate the centroid velocity and width of each one. To determine how many Gaussians are necessary to reproduce an emission profile, reduced χ^2 values were compared for fits with up to four Gaussians, and the number that resulted in χ^2 closest to 1 was taken. The Gaussian decomposition of all profiles are shown at the end of this chapter, in Figure 5.26 (page 122).

Figure 5.5 shows on the right panel the distribution of FWHM and centroid velocity (v_c) of all of the components derived from all of the Gaussian fits, and on the left panel a

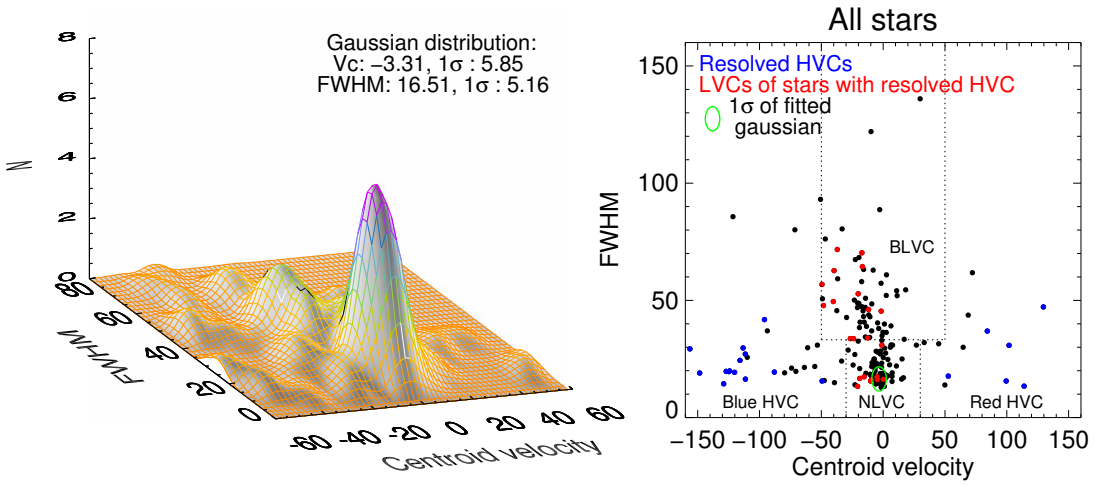

Figure 5.5: Right: distribution of FWHM and centroid velocity of all components from all profiles derived from the Gaussian fits. Dotted lines indicate approximately the separation between different components - narrow and broad LVC, red- and blueshifted HVC, according to our analysis (this is only an approximation, since there may be some overlap between different components). Left: surface plot of the central region of the distribution shown in the right panel, where the z axis represents the number of Gaussian components in square bins of 5km/s × 5km/s.

surface plot of the same distribution, with the z axis representing the number of Gaussian components in square bins of 5km/s × 5km/s. There is evidently a very high concentration of components at low, slightly blueshifted centroid velocities and low FWHM. We interpret this as the locus of the narrow LVCs studied by R13 and S16. A Gaussian fit around the surface plot (left panel of Figure 5.5) has a 1σ width represented in the right panel as a green ellipse. If this truly represents the locus of the narrow component of the LVC, then this component should typically have $v_c = -3.3 \pm 5.9$ km/s and FWHM $= 16.5 \pm 5.2$ km/s. If we consider a 3σ threshold, then components of -20.9 km/s $< v_c < 14.2$ km/s and FWHM < 32 km/s should represent narrow LVCs.

The cutoff in centroid velocity between LVCs and HVCs varies in the literature from 30km/s (S16) to 60km/s (HEG95) and is always somewhat arbitrary. In our sample the lowest centroid velocity of a HVC with a clearly resolved peak is -48.3km/s, but this does not necessarily represent the cutoff between low and high velocity components, only our ability to resolve separate peaks. For a first analysis we consider the cutoff at 30km/s, to compare with the results of S16. Therefore all components with $|v_c| > 30$km/s are initially considered HVCs, and those with $|v_c| \leq 30$km/s LVCs.

In order to better distinguish between the narrow and broad components of the LVC (NLVC and BLVC), we selected a sample of 25 stars whose profiles consist of two Gaussian components with centroid velocity below 30 km/s, in which one is clearly broader than the other. In Figure 5.6 we plot the distribution of centroid velocity and FWHM of the LVCs

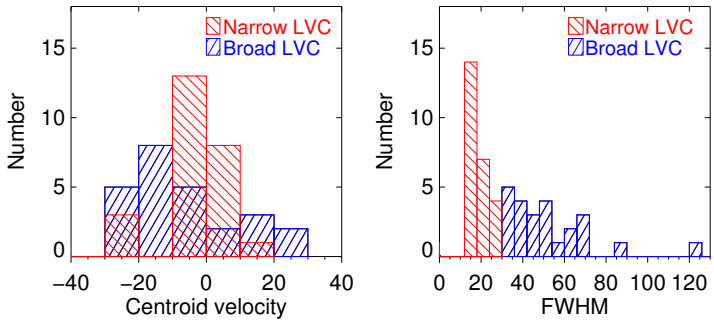

Figure 5.6: Distribution of centroid velocity (left) and FWHM (right) of the components from our Gaussian fits for a group of stars that present two low velocity components (two components with $|v_c| < 30$ km/s). Red represents the narrowest of the two components while blue represents the broadest.

of these 25 stars, red representing the narrowest of a profile's two components, and blue the broadest. We see that the NLVC is generally close to stellar rest velocity or slightly blueshifted, while the centroid velocity of the BLVC varies more. The FWHM of these NLVCs vary from 13.3 km/s to 28.4 km/s, with a mean of 19.2 km/s and standard deviation of 4.2 km/s; the FWHM of these BLVCs vary from 30.9 km/s to 136 km/s, with a mean of 55.5 km/s and standard deviation of 26.5 km/s. These values found for the narrow LVC are consistent with our characterization of this component from Figure 5.5.

We also selected a group of 15 stars whose profiles clearly show a HVC (with a resolved peak or not) and a broader component at lower centroid velocity, in order to study the relation between a star's HVC and its broad LVC. The HVCs were identified according to $|v_c| > 30$ km/s, but no cutoff was used to identify BLVCs, the only requirement was that its centroid velocity be lower than that of the HVC. Figure 5.7 shows the distribution of centroid velocity and FWHM of these two components. These HVCs have $|v_c|$ between 49.9 km/s and 156.3 km/s, with a mean of 104.7 km/s and standard deviation of 30.3 km/s; and FWHM between 13.9 km/s and 47.2 km/s, with a mean of 22.8 km/s and standard deviation 7.8 km/s. The BLVCs have v_c between -49.5 km/s and -1.6 km/s, with a mean of -27.4 km/s and standard deviation of 15.9 km/s; and FWHM between 38.9 km/s and 76.2 km/s, with a mean of 54.8 km/s and standard deviation of 11.7 km/s. Though these two components show clearly separate ranges of both centroid velocity and FWHM, there is a small overlap in FWHM, around 40-50 km/s. We also see that the BLVC can be blueshifted by up to ∼50 km/s, much more than the 30 km/s considered above. Therefore we repeated Figure 5.6, this time for a group of 32 stars that have two components of centroid velocity $|v_c| < 50$ km/s (Figure 5.8). The NLVC continues to show the same behavior, whereas the BLVC indeed extends to more blueshifted velocities. The NLVC shows centroid velocities between -24.3 km/s and 15.3 km/s in both Figures 5.6 and 5.8. In the latter its FWHM reaches 31 km/s, slightly overlapping with the lower limit of 30.9 km/s of the BLVC.

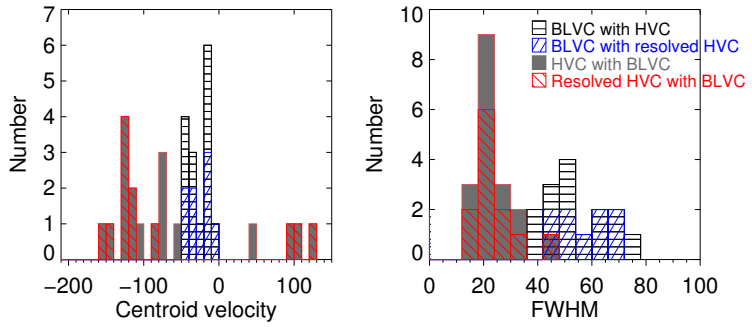

Figure 5.7: Distribution of centroid velocity (left) and FWHM (right) of the components from our Gaussian decomposition for a group of stars that present both a HVC and a broad LVC. Grey shaded bins represent HVCs, while black bins represent their corresponding BLVCs. Red represents only the HVCs that have a clearly resolved peak while blue represents their corresponding BLVCs.

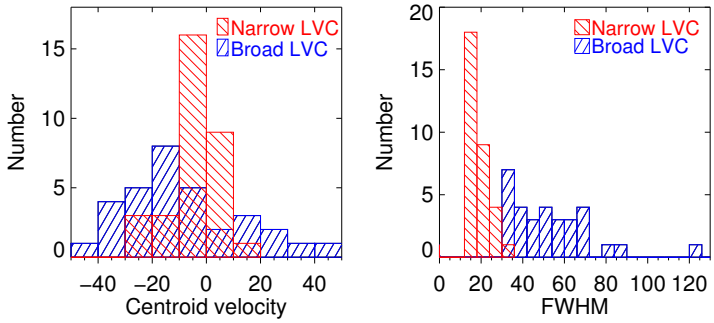

Figure 5.8: Same as Figure 5.6, but taking components with $|v_c| < 50$ km/s.

It is clear from all of these plots that the narrow LVC has centroid velocity less than 30 km/s. The cutoff in centroid velocity between the broad LVC and the HVC, however, is more difficult to determine. Our analysis seems to point to a value around 50 km/s, but for systems seen at high inclinations the [OI] emission coming from a high-velocity jet would be observed at lower projected velocities. If, for instance, a system is observed at an inclination of 80°, emission from a jet travelling at 200 km/s would be centered at 35 km/s ($V_{jet} * \cos i$). We appear to have a few cases like this in our sample. For example, the star Mon-228 shows a broad component centered close to rest velocity and a narrow component centered at -33.6 km/s, which is more blueshifted than a typical narrow LVC. We do not have direct measurements of inclination for the stars in this cluster, but we can deduce from its rotation period, $v \sin i$ and radius (using Equation 4.5) that Mon-228 is observed at a very high inclination. This component is therefore consistent with a HVC.

In the end, we used the following criteria to classify each component:

- All components with $|v_c| < 30$ km/s were classified as LVCs. When more than one component from an emission profile satisfied this condition, the broadest was classified as a broad LVC and the narrowest as a narrow LVC. When there was only one compo-

nent, it was classified as narrow if FWHM $\leq$ 32 km/s and broad if FWHM $>$ 32 km/s (from the analysis of Figure 5.5). There were no cases of more than two components in this velocity range.

- All components with $|v_c| > 50$ km/s were classified as HVCs.

- The components with centroid velocity between 30 km/s and 50 km/s were analyzed case-by-case. If, for a particular profile, a broad LVC of lower centroid velocity was already accounted for but a HVC was not, this component was classified as a HVC. For the opposite case, in which a HVC was already accounted for but a BLVC was not, it was classified as a BLVC provided its FWHM was greater than 30 km/s. When neither component had already been classified, two features were taken into account: the component's width and the system's inclination. For large FWHM ($>$ 40 km/s) it was classified as BLVC; for low FWHM ($<$ 30 km/s) it was classified as HVC; and for the intermediate case it was considered a HVC when there were indications that the system is observed at high inclination (high $\sin i$ calculated from stellar rotation properties, or light curves dominated by heavy circumstellar extinction) and a BLVC when there were not.

Of the 185 CTTSs and HAeBe stars observed in NGC 2264, we detected emission in the [OI] 6300Å line of 104 stars, all of which present a LVC. A HVC, however, was only detected in 34 of these profiles. This represents only 18% of all CTTSs and HAeBe stars observed, a much lower detection rate than was expected (previous studies, such as Edwards et al. 1987, HEG95, N14 and S16, have detected it in around 30% or more of CTTSs). Of these 34 profiles, 23 show only a blueshifted HVC, 5 only a redshifted HVC, and the remaining 6 profiles present both a blue and a redshifted HVC. For the LVCs, 33/104 profiles show both a narrow and broad component, while 39/104 show only a narrow component (for a total of 72 profiles, or 69% of detected [OI] emission, with a NLVC) and 32/104 show only a broad component (for a total of 65 profiles, or 63% of detected [OI] emission, with a BLVC). This means that 39% of the CTTSs and HAeBe stars in our sample present a NLVC and 35% present a BLVC. These rates are lower than those found by, e.g., S16, though the difference in the detection rate of the two studies is much more significant for the BLVC, which they found in 76% of their sample of CTTSs, than for the NLVC, which were detected in 55% of their CTTSs.

Table 5.1 lists the minimum and maximum values found for the centroid velocities (v_c) and FWHM of each of these components, as well as their mean, median, and standard deviation (1σ). We performed K-S tests between the distributions of FWHM and v_c of the different components and all proved to be statistically different, with a $<$ 1% probability that the distributions draw from the same population.

Table 5.1: Information about the centroid velocities (v_c) and FWHM of the several different components of the [OI] emission line.

		Min	Max	Mean	Median	1σ
NLVC:	v_c	-28.3	16.4	-3.5	-2.5	8.9
Detected: 72/185	FWHM	12.9	31.0	20.2	18.7	4.9
BLVC:	v_c	-49.5	44.9	-11.5	-13.5	19.7
Detected: 65/185	FWHM	30.9	136.0	51.5	47.0	20.8
Blueshifted HVC:	v_c	-156.3	-33.6	-93.7	-96.0	34.2
Detected: 29/185	FWHM	11.6	93.1	29.4	21.4	20.8
Redshifted HVC:	v_c	40.3	129.6	79.8	72.2	28.5
Detected: 11/185	FWHM	13.4	61.8	31.3	30.8	15.6

Notes. All values are in units of km/s.

5.2 Line luminosities and correlations with stellar/accretion properties

In order to estimate the luminosity of the [OI] emission lines, we began by measuring equivalent widths (EW) for each [OI] line profile. In order to estimate uncertainties, we added a random distribution of noise at the same level of the uncertainty in the flux and calculated the resulting EW. This was done 200 times, then we took the mean and standard deviation of these 200 values as our final value of EW and its uncertainty. We estimated the EW of the narrow and broad components of the LVC from their Gaussian fits, whereas for the HVC, we used the line's total value minus the EWs of all other components. This is to account for the fact that the HVC usually deviates from a Gaussian profile more than the narrow and broad components of the LVC and therefore using the value derived from the Gaussian fit may result in a larger error. For the 6 stars that present both a redshifted and a blueshifted HVC, we first estimated the EW of each of these components from their Gaussian fits. We then made a second estimate by subtracting the values of all other Gaussian components, including that of the other HVC, from the total [OI] line's EW. This slightly overestimates each HVC's EW because the residuals from both components as they deviate from a Gaussian profile are added to each component's measure of EW. Therefore to minimize this effect, we consider this value to be an upper limit and the estimate from the Gaussian fit to be a lower limit, and take the average of the two as the final value of the EW of each HVC.

Our spectra are not flux calibrated, therefore in order to retrieve [OI] line luminosities we estimated the continuum flux around 6300Å using the average r-band magnitude from the CFHT MegaCam 2012 campaign (described in 2.2.3). As an estimate of the error bar, we used the amplitude of variability from the CoRoT light curves. For the brighter stars that saturated in the CFHT observations, we used the CoRoT R magnitudes, which

were converted from the mean CoRoT flux using the photometric zero-point of 26.74, as determined by Cody et al. (2014). A comparison of the CFHT r and CoRoT R magnitudes in our sample shows that the two coincide very well among the brighter stars ($R \lesssim 14$) and therefore we introduce very little error by using the CoRoT magnitudes for the stars with no CFHT photometry. Magnitudes were corrected for extinction, then converted to flux using a distance to NGC 2264 of 760 pc (Sung et al. 1997; Gillen et al. 2014). The continuum flux was then multiplied by the measured equivalent widths in order to retrieve the luminosities of the [OI] line's individual components, which were then added together in order to retrieve the total [OI] line luminosity.

To correct for extinction we used the individual values derived for each star by Venuti et al. (2014). When no value was available, we used the average extinction towards the cluster of $A_R = 0.40$, estimated from the stars in our sample with measured extinction. This was done when calculating the luminosity of the [OI] line's LVCs. The HVC, however, is believed to arise from jets far enough above the disk midplane that it is likely only affected by interstellar extinction in our line-of-sight toward the cluster, and not by the circumstellar disk material of individual objects. Therefore, when calculating the flux in the [OI] line's blueshifted HVC, we used the average extinction toward the cluster for all stars rather than their individual values. As for the redshifted HVCs, which represent emission coming from the receding part of the protostellar jets, the extinction due to circumstellar disk material cannot be ignored, since the disk should intersect our line-of-sight to this part of the jet. Therefore when calculating the luminosity of the redshifted HVC, we used the individual values of extinction, as was done for the LVCs. Even so, their luminosities may often still be underestimated. In the cases where we find both a redshifted and blueshifted HVC in a star's [OI] line profile, the luminosity of the former is usually lower than that of the latter. Therefore care must be taken when analyzing luminosities of the redshifted HVC. In our analysis, when searching for correlations with other parameters, we consider only the luminosity of the blueshifted HVCs in order to eliminate this source of additional uncertainty.

The luminosities of the total [OI] line profiles, as well as those of each separate component, are given in Table 5.3 (page 118). We also give the upper limits determined for the CTTSs in which no [OI] emission was detected.

5.2.1 Correlations among [OI] luminosities and stellar/disk properties

Figures 5.9 to 5.15 show the relations between the [OI] line's total luminosity, as well as the luminosities of its individual components (NLVC, BLVC, and HVC), and different properties of the star, disk and accretion. Upper limits of non-detections are shown as green arrows in all plots and the luminosity of blueshifted and redshifted high velocity components are shown in different colors (blue and red, respectively). Light blue arrows in the HVC plots represent upper limits for HVC luminosities when only low velocity [OI] emission was detected.

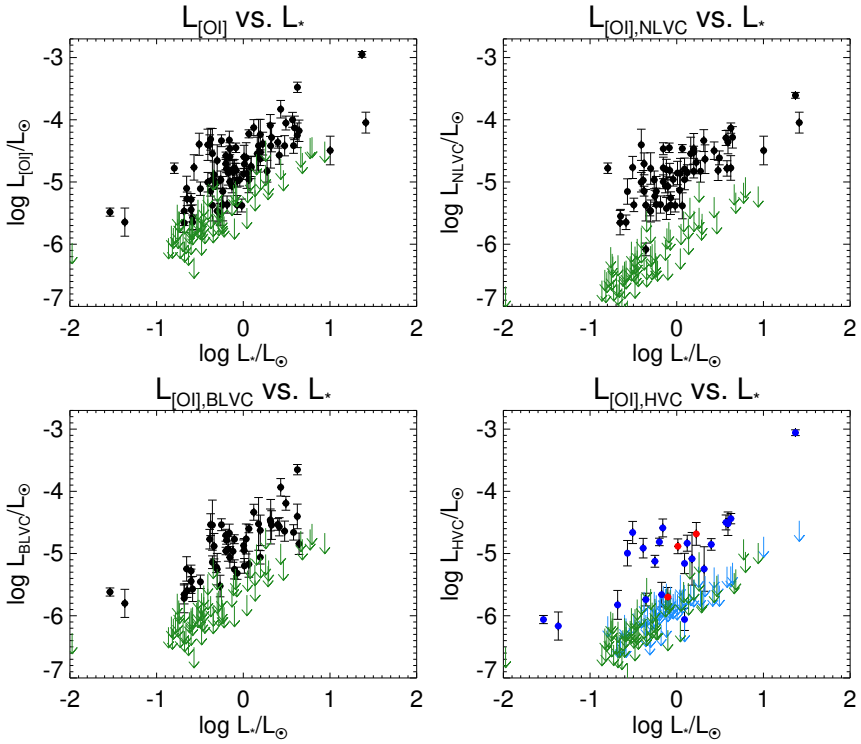

Figure 5.9: [OI] line luminosity and luminosity of each individual component versus stellar luminosity. Green arrows represent upper limits for [OI] line and component luminosities when no emission in [OI] was detected. In the HVC plot (lower right), blue dots represent blueshifted HVCs while red dots represent redshifted HVCs. In this plot, light blue arrows represent upper limits for HVC luminosities when only low velocity [OI] emission was detected.

In order to evaluate possible correlations between stellar, disk and accretion properties and the [OI] emission line and its different components, we used the ASURV (Astronomy SURVival) package[4] (Lavalley et al. 1992), which implements the methods described in Isobe et al. (1986). We chose these methods because they allow us to perform linear regression and correlation tests while taking into account the upper limits of our non-detections and thus diminishing possible observational biases.

We find a strong correlation between stellar luminosity and the luminosities of all [OI] components, especially the low velocity components (Figure 5.9). A Kendal τ test gives a probability of less than 0.001% that these correlations do not exist. This was also observed by N14 and S16 for the LVC. All components of the [OI] line also correlate well with the accretion luminosity, or similarly with the mass accretion rate (Figure 5.10), as has been noted in many previous studies (Cabrit et al. 1990, HEG95, R13, N14, S16). A Kendall τ test shows that the probability that there is no correlation with accretion luminosity is less than 0.001% for all components. However, for the HVC, if we examine only positive

[4] Available at http://astrostatistics.psu.edu/statcodes/sc_censor.html

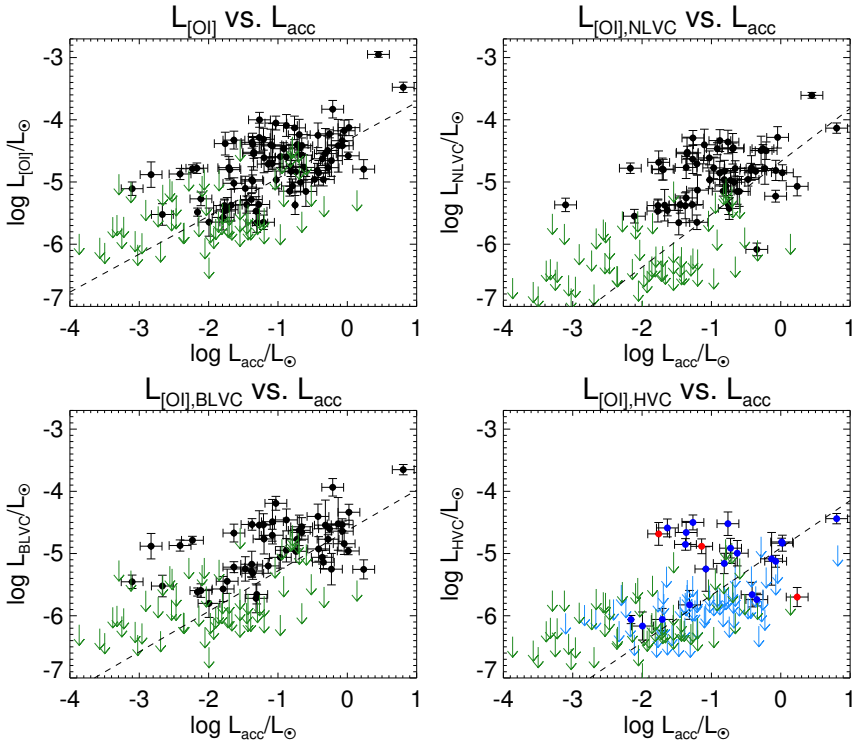

Figure 5.10: [OI] line luminosity and luminosity of each individual component versus accretion luminosity. Colors and symbols represent the same as in Figure 5.9.

detections this probability increases to 0.2%. Though still low enough to confirm that there is a correlation, the fact that this value is so much higher than when upper limits are taken into consideration shows how important it is to include them in this analysis. Figure 5.10 clearly shows that many non-detections of the [OI] line correspond to stars of low accretion luminosity, and therefore low mass accretion rates, meaning they were likely not detected because the [OI] emission line is lower than our detection threshold and not because of an actual lack of emission, leading to an observational bias. The accretion luminosities we used were those calculated from UV excess luminosity by Venuti et al. (2014) when available, and using Hα luminosity otherwise. Using the parametric EM algorithm available in ASURV, we find the following relations for each component of the [OI] 6300Å line:

$$\log L_{NLVC} = -4.67(\pm0.16) + 0.85(\pm0.11)\log L_{acc} \tag{5.1}$$

$$\log L_{BLVC} = -4.63(\pm0.13) + 0.65(\pm0.08)\log L_{acc} \tag{5.2}$$

$$\log L_{HVC} = -4.81(\pm0.19) + 0.83(\pm0.15)\log L_{acc}. \tag{5.3}$$

We can compare our correlations of the LVC with those of R13, N14 and S16. Figure 5.11 shows the luminosity of the full (narrow+broad) LVC of the [OI] line versus the stellar luminosity (left) and accretion luminosity (right) for all four samples. We consider the full LVC rather than the broad or narrow components individually in order to compare with R13, who only decomposed their LVC into separate components for two stars, and N14, who

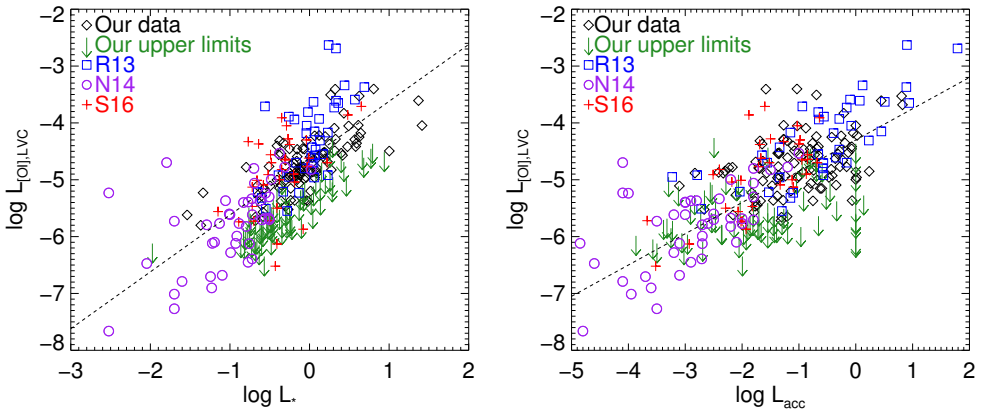

Figure 5.11: [OI] LVC luminosity versus stellar luminosity (left) and accretion luminosity (right). Black diamonds represent our sample, while green arrows represent our upper limits to the LVC luminosities when no emission in [OI] was detected. Blue squares, purple circles and red crosses represent the values given in R13, N14 and S16 for their samples, respectively. Dashed lines show the linear regression found for all 4 data sets put together, including our upper limits.

did not have enough spectral resolution to perform this decomposition. We see that all of the samples agree well in both relations, allowing us to establish a well-defined link between the [OI] line's LVC luminosity and the stellar luminosity over 4 orders of magnitude, as well as between the [OI] line's LVC luminosity and the accretion luminosity over 7 orders of magnitude. Using once again the EM method, we find the following for the combination of all four samples:

$$\log L_{LVC,all} = -4.30(\pm 0.06) + 0.55(\pm 0.03) \log L_{acc} \tag{5.4}$$

$$\log L_{LVC,all} = -4.62(\pm 0.04) + 1.00(\pm 0.06) \log L_{*}. \tag{5.5}$$

Equation 5.4 is in agreement with the relation found for only our sample, using the same method:

$$\log L_{LVC,ours} = -4.43(\pm 0.10) + 0.61(\pm 0.07) \log L_{acc}. \tag{5.6}$$

The relation between L_{LVC} and L_{acc} is also in agreement with those found by R13 and S16, though our slope is not as steep as the one found by N14 for their data.

Furthermore, in the right panel of Figure 5.11 we can see that, for stars of low accretion luminosities, our upper limits for the [OI] LVC luminosity are in the same range of values as the [OI] LVC luminosities found by N14 for stars in their sample with similar accretion luminosities. This helps to support the hypothesis presented in Section 5.1.1 that our low detection rate, particularly among stars of low mass accretion rates, may be due to an observational bias. Many (if not all) of the stars in our sample may have at least low velocity [OI] 6300Å emission which are simply too faint to be detected in our spectra.

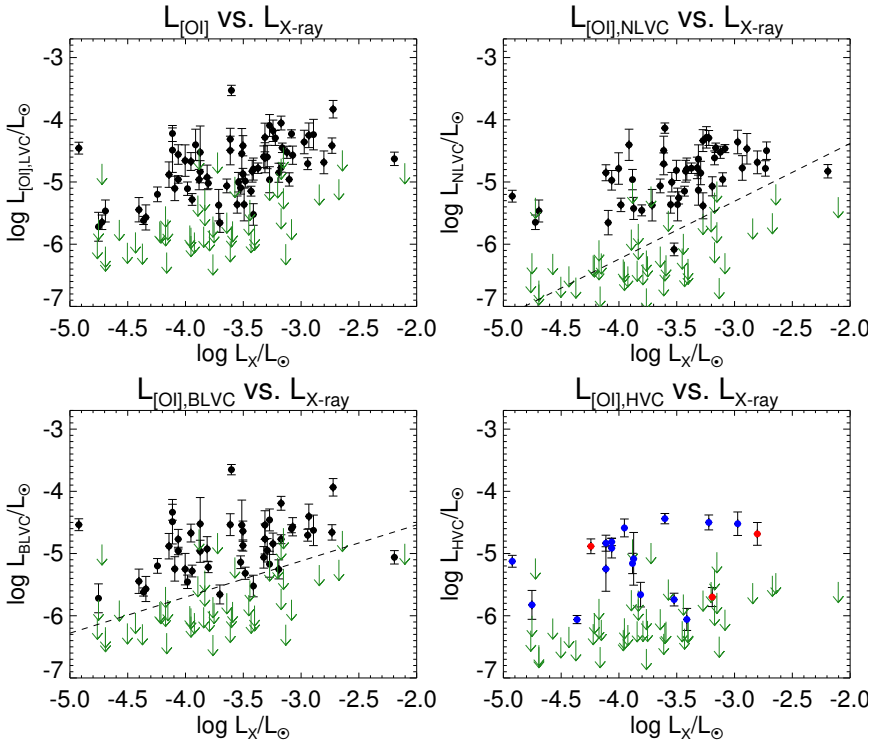

Figure 5.12: [OI] line luminosity and luminosity of each individual component versus X-ray luminosity. Colors and symbols represent the same as in Figure 5.9. Linear fits are shown for the narrow and broad LVCs and were calculated taking the upper limits into consideration.

Figure 5.12 shows the [OI] line luminosity in terms of X-ray luminosity (X-ray luminosity values are from Guarcello et al. 2017, and are shown in Table 5.3). The X-ray luminosity does not correlate with the luminosity of either the HVC or the total LVC. Similarly to S16, who found a 10.8% likelihood of no correlation between the X-ray luminosity and the LVC luminosity, we find that when considering the total LVC there is a 12% probability of no correlation. However, when we separate the contributions of the narrow and broad components, we find that there is only a 0.2% chance that the X-ray luminosity does not correlate with the broad LVC luminosity, and an even smaller one ($< 0.001\%$) that there is no correlation with the narrow LVC (Figure 5.12). However, since our data also show a correlation between the X-ray luminosity and the stellar luminosity (Figure 5.13), it is unclear to us whether the relationships found between L_X and $L_{NLVC,BLVC}$ are real or whether they are driven by an underlying correlation with the stellar luminosity, which is much stronger for the individual low velocity components than for the total LVC. In an attempt to remove the possible influence of L_*, we searched for a correlation between the X-ray luminosities and the [OI] line's NLVC and BLVC luminosities, with both normalized by the stellar luminosities (L_*). We find that there is no correlation between L_X/L_* and L_{NLVC}/L_* or L_{BLVC}/L_*. Furthermore, if either the NLVC or the BLVC originates in an X-ray driven photoevaporative wind, then we might expect there to be a correlation between their centroid velocities and the X-ray luminosities, if stronger X-rays result in faster flows (R13). We find no such

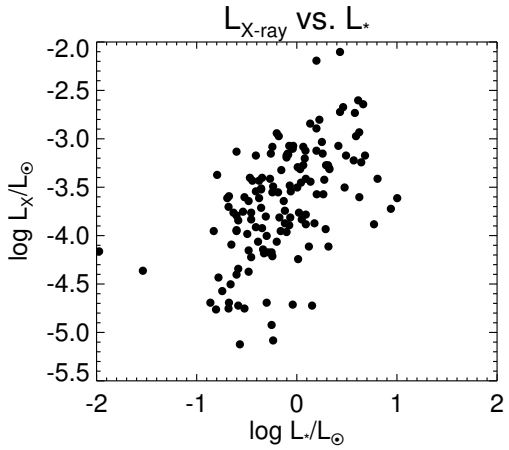

Figure 5.13: X-ray luminosity versus stellar luminosity for the stars in our sample with X-ray measurements. A Kendall τ test gives only a 2.5% probability that no correlation exists.

correlation in our sample, just as R13 found none in theirs. However, though the model of Ercolano & Owen (2010) predicts that, for [OI] emission originating in an X-ray driven photoevaporative wind, a correlation should exist between the [OI] luminosity and the X-ray luminosity, an updated version of this model predicts no such correlation (Ercolano & Owen 2016). Therefore, our results cannot rule out a photoevaporative wind as the source of either of the low-velocity components of the [OI] emission line.

Figures 5.14 and 5.15 show two indices that indicate the amount of dust present in the inner circumstellar disk. As was discussed in Section 4.2, the α_{IRAC} index corresponds to the slope of a star's spectral energy distribution between 3.6μm and 8μm and can be used to classify a system's inner ($\sim$ 0.1au) disk structure (Lada et al. 2006). The dashed line in Figure 5.14 represents the boundary between systems with optically thick inner disks (right) and systems with anemic disks (middle), while the dashed-dotted line represents the boundary between systems with anemic disks and naked photospheres (left). It is clear from the plot of L_{HVC} versus α_{IRAC} (lower right panel of Figure 5.14) that in order to possess high velocity [OI] 6300Å emission, a system must still have a considerable amount of dust in this region of the disk. All systems showing this emission have optically thick inner disks, with the exception of one star (Mon-250[5]) that has an anemic disk and presents a faint [OI] HVC. The NLVC, on the other hand, is present in a number of anemic disks systems and even some systems classified as naked photospheres, while the BLVC seems to show an intermediate behavior, having been observed in some anemic disk systems but not as many as the NLVC.

The K $-$ 3.6μm excess probes a region of the disk that is even closer to the star than α_{IRAC}. In the bottom right panel of Figure 5.15 there is an even clearer threshold for HVC emission: all systems showing any amount of this emission have E(K $-$ 3.6μm) $>$ 0.3, the

[5]This is the same star that was studied in some detail in Section 4.5, which presents AA Tau-like light curves in both 2008 and 2011.

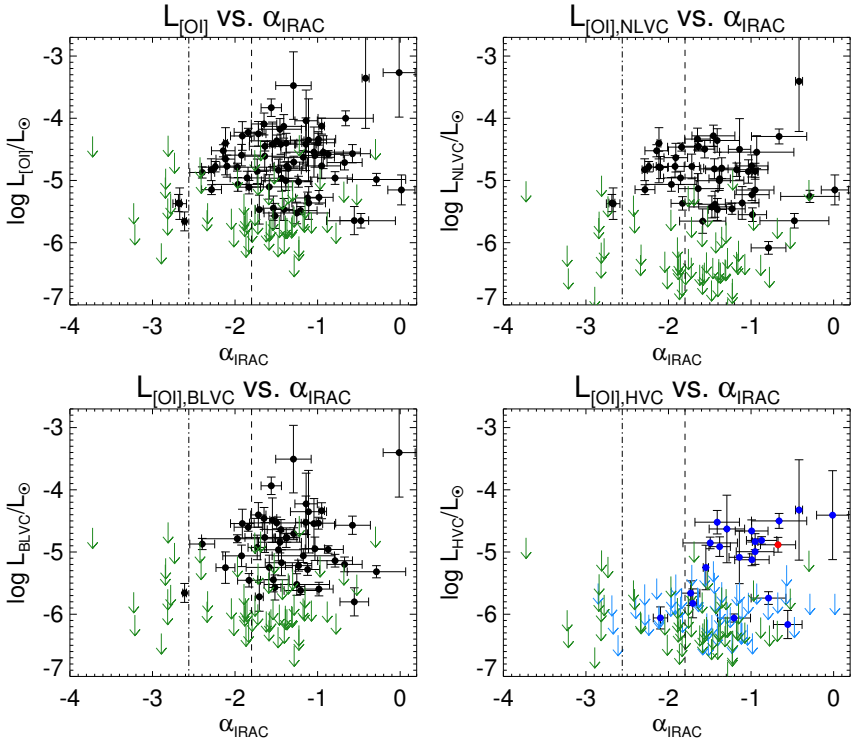

Figure 5.14: [OI] line luminosity and luminosity of each individual component versus the α_{IRAC} index. Colors and symbols represent the same as in Figure 5.9.

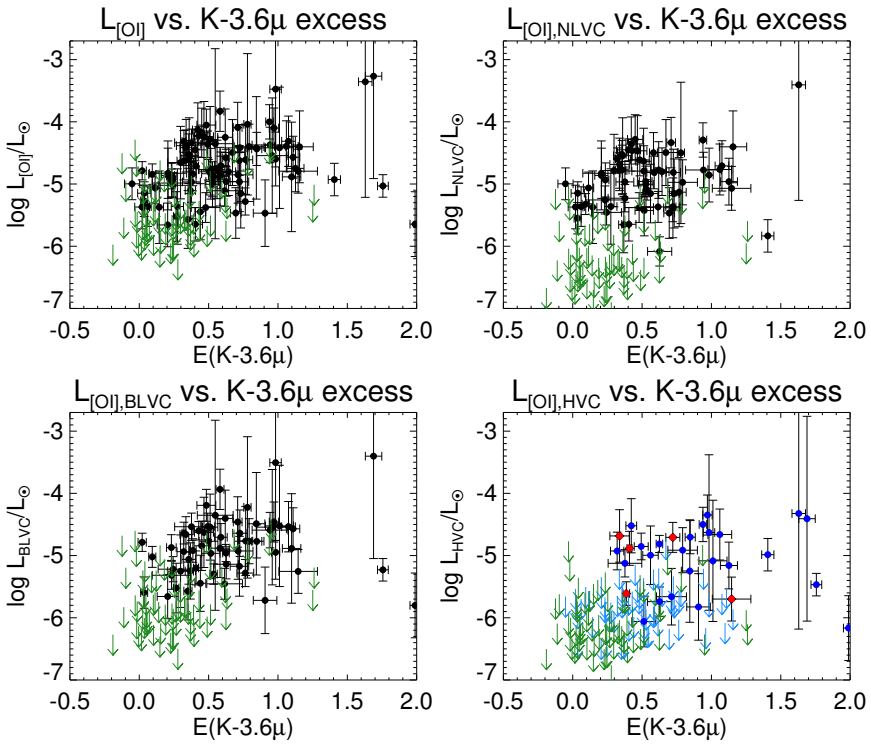

Figure 5.15: [OI] line luminosity and luminosity of each individual component versus K-IRAC$_{3.6\mu}$ excess. Colors and symbols represent the same as in Figure 5.9.

same conclusion reached by HEG95. This indicates that, in order for a high velocity jet to be launched, the system must have an optically thick inner disk. There is however no correlation between the amount of infrared excess and the jet's luminosity or velocity in our sample. The values of α_{IRAC} and $K - 3.6\mu m$ excess are given in Table 5.3.

5.3 Photometric variability and the [OI] line

Of the 104 stars in our sample that present [OI] emission, 88 were observed by the CoRoT satellite in either of its two observing runs in NGC 2264 (detailed in Chapter 2). The different groups of light curve morphology described in Section 3.4 can help shed light on certain properties of these systems, such as the observed disk geometry or in which regime the star is accreting matter. By combining this information with the observed [OI] line profiles, we can attempt to better understand how ejection processes occur in systems with each of these different light curve types.

We can at times use the light curve classification to infer system inclinations, which is very useful since we do not have direct inclination measurements for this cluster. As was discussed in Chapter 4, the systems that present AA Tau-like light curves in one CoRoT observing run or the other are consistent with being observed at high inclinations. We can also assume that this is the case for stars that show aperiodic extinction-dominated light curves in both observing runs, since optically thick material from the disk must intersect our line-of-sight in order to produce the occulting events. On the other hand, for the stars that show spot-like variability or flux burst-dominated light curves, we see no indication of optically thick disk material intersecting our line-of-sight. This means that these systems are probably observed at medium to low inclinations. Finally, the complex light curves, those that are more difficult to classify, probably represent an intermediate case, where we observe both extinction events and spots on the stellar surface. It is more complicated to make assumptions about the inclinations at which these systems are observed, except that they are probably neither too low or too high.

Figure 5.16 shows the average [OI] line profile for these three different cases: systems that present spot-like or flux burst-dominated light curves in either 2008 or 2011, those with light curves classified as complex in both 2008 and 2011 (or observed in only one CoRoT epoch and classified as complex), and those with AA Tau-like or aperiodic extinction-dominated light curves in either 2008 or 2011. Each profile was normalized by its maximum intensity, then the average of each group was taken. We can see that the low velocity components of the three profiles are very similar, whereas the high velocity components differ. The average profile of the stars that present spot-like or flux burst-dominated light curves shows a blueshifted HVC with a clearly separated peak. This is consistent with observing systems close to pole-on that are associated with fast bipolar jets. These jet velocities projected in our line-of-sight would be close to their terminal velocities, resulting in high velocity [OI]

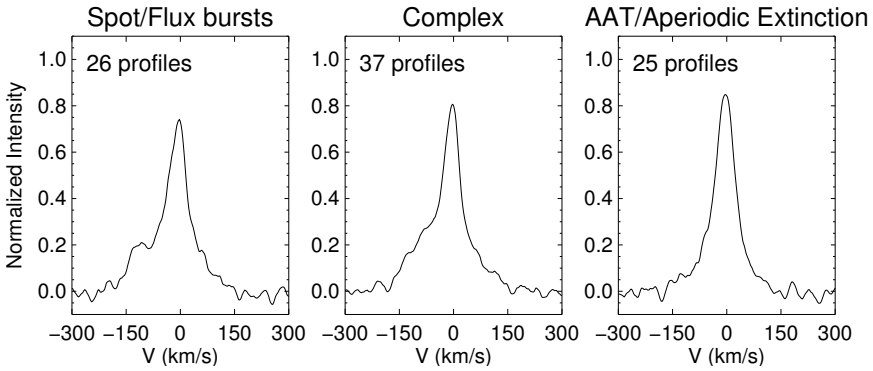

Figure 5.16: Average [OI] line profiles for different types of photometric variability that hint at the system's inclination. Left: stars that showed spot-like or flux burst-dominated light curves in either CoRoT observing run. These systems are generally seen at medium to low inclinations. Middle: stars with complex (difficult to classify) light curves. These are probably seen at intermediate inclinations. Right: stars that showed AA Tau-like or aperiodic extinction-dominated light curves in either CoRoT observing run. These are generally seen at high inclinations.

emission that is blueshifted enough that it can easily be distinguished from the low velocity [OI] emission.

The average profile of the stars that show complex photometric behavior also presents a blueshifted HVC, but it does not have a well-defined peak. Instead the high velocity emission is blended with the low velocity emission, resulting in a profile with an intense LVC accompanied by a less intense (less than about half the maximum intensity of the LVC), extended blue wing. This profile resembles the average [OI] line profile of all of the stars in our sample (see the bottom right panel of Figure 5.17). Finally, the average [OI] line profile for stars with AA Tau-like or aperiodic extinction-dominated light curves presents a typical LVC with a somewhat broad base and only a modest extended blue wing. This is consistent with a scenario in which these systems are observed nearly edge-on. In this case, even if there were fast jets present, they would be nearly perpendicular to our line-of-sight and the projected velocity would be so low that we would barely be able to distinguish the resulting HVC from a broad LVC.

The light curve classification can also help indicate in which way a CTTS is accreting matter. We have already seen that AA Tau-like photometric variability may be associated with a stable accretion regime (Bouvier et al. 2007; Romanova et al. 2013; McGinnis et al. 2015), in which case the inner disk warp invoked to explain the quasi-periodic flux dips would originate from the intense interaction between the inner disk and an inclined, strongly bipolar stellar magnetic field. In order to observe the AA Tau-like flux dips the system should be observed at a high inclination. However, if a system undergoing stable accretion is observed at a lower inclination, its light curve would probably be dominated by the rotational modulation of spots on the stellar surface, which would be stable over a few rotation cycles.

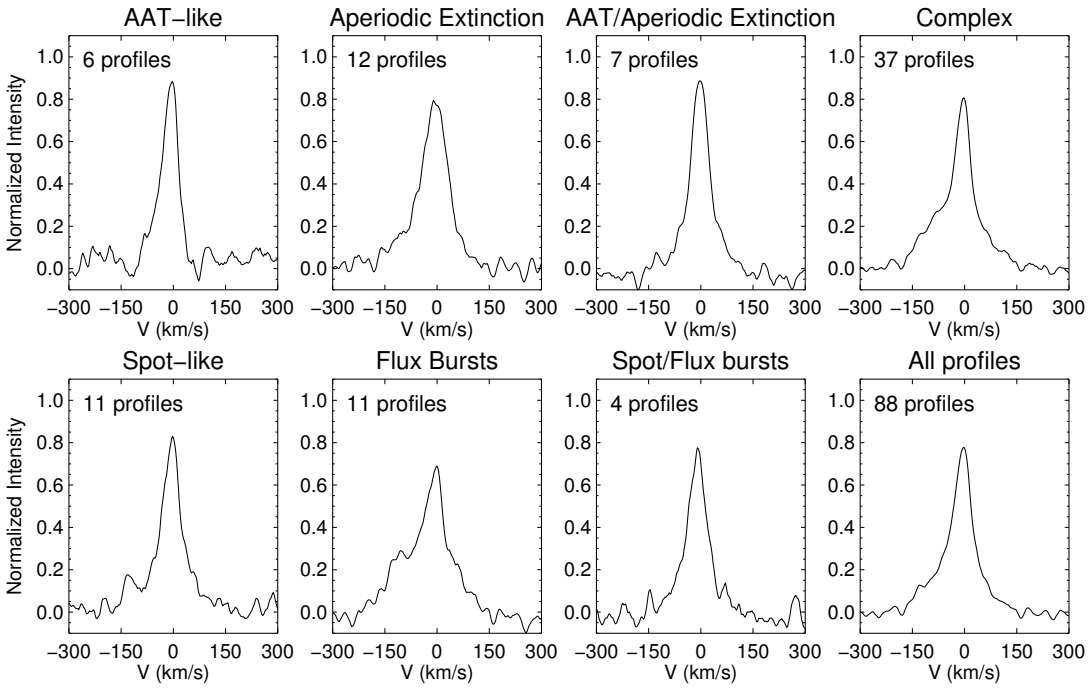

Figure 5.17: Average [OI] line profiles for different types of photometric variability. From left to right, top to bottom: stars that presented only AA Tau-like light curves in both CoRoT observations, stars that presented only aperiodic extinction-dominated light curves in both CoRoT observations, stars that alternated between AA Tau-like and aperiodic extinction between 2008 and 2011, stars with complex (difficult to classify) light curves, stars with spot-like light curves in both CoRoT observations, stars with light curves dominated by stochastic flux bursts in both CoRoT observations, stars that altered between spot-like and flux bursts between 2008 and 2011, and finally an average of all [OI] line profiles.

These could be either cold spots, owing to the strong bipolar stellar magnetic field, or hot spots owing to the intense accretion shocks associated with the stable accretion funnel flows (or a combination of both). On the other hand, for systems undergoing unstable accretion, Kurosawa & Romanova (2013) have shown that their photometric variability would likely be very stochastic, due to the various irregularly distributed hot spots on the stellar surface. In Chapter 4 and McGinnis et al. (2015), we propose that if these systems are observed at sufficiently high inclinations, these light curves could be dominated by irregular obscuration of the photosphere from material lifted above the disk midplane in the accretion "tongues". Therefore, we might assume that CTTSs that present periodic or quasi-periodic light curves (spot-like and AA Tau-like) are accreting in the stable regime, whereas those that present aperiodic light curves (dominated by flux bursts or extinction events) are accreting in the unstable regime.

It is important to remember that a CTTS's light curve morphology is not a permanent characteristic of that system, but rather a reflection of the system's current state, and as that system progresses through different phases of accretion and of its evolution, its light

curve morphology will change accordingly. Not only have we shown in Section 4.7 that many systems suffered a transition between AA Tau-like and aperiodic extinction-dominated photometric behavior between the two CoRoT observing runs, but Sousa et al. (2016) also noted that many systems suffered a transition between spot-like and flux burst-dominated photometric behavior in the same time. These transitions have been attributed to a change in these systems' accretion regimes in timescales of a few years. We recall that according to Kurosawa & Romanova (2013), systems undergoing a stable accretion regime tend to have lower mass accretion rates and more ordered magnetic fields, with stronger bipolar components, than those undergoing an unstable accretion regime. Therefore if any of these factors change over time, the star may transition from one regime to another.

In Figure 5.17, we again show the average profiles of different groups of our CTTSs that present [OI] emission. This time, we separated them according to their light curve morphology in both CoRoT epochs and according to whether they maintained a constant photometric behavior or transitioned between different classifications. Again we see that stars that present AA Tau-like light curves in one or both CoRoT epochs show a narrow profile, with only a broad base or a modest blue wing. Stars that present aperiodic extinction in both CoRoT epochs, however, show a much broader profile, with a more extended blue wing. In a similar fashion, stars with light curves dominated by flux bursts in both CoRoT epochs have a very broad profile and a clear blueshifted HVC with a distinct peak, whereas the stars with spot-like light curves in one epoch or another present a much weaker HVC, whether in the form of an extended blue wing or clearly separated from the LVC. This may be explained by the different mass accretion rates among these groups. Stars that consistently present irregular, aperiodic photometric variability during years probably have higher mass accretion rates that maintain them in a constant state of unstable accretion. This higher mass accretion rate would be connected to more intense jets and therefore stronger [OI] emission line HVCs, as the bottom right panel of Figure 5.10 suggests.

5.4 The low velocity component

Simon et al. (2016) investigated the possibility that the FWHM of the narrow and broad components of the LVC may derive from the system's inclination. Emission originating in the disk is subject to broadening by Keplerian rotation. It is the rotation velocity projected in our line-of-sight that determines the line broadening, therefore systems at different inclinations should present lines of different FWHM. S16 found that the FWHM of both the NLVC and the BLVC increases with inclination. They also found that the BLVC becomes less blueshifted at higher inclinations.

In order to search for these trends in our data, we first verify if there is any correlation between the FWHM of the NLVC and of the BLVC in the systems that present both. If the observed FWHM of both components are connected to the system's inclination, then

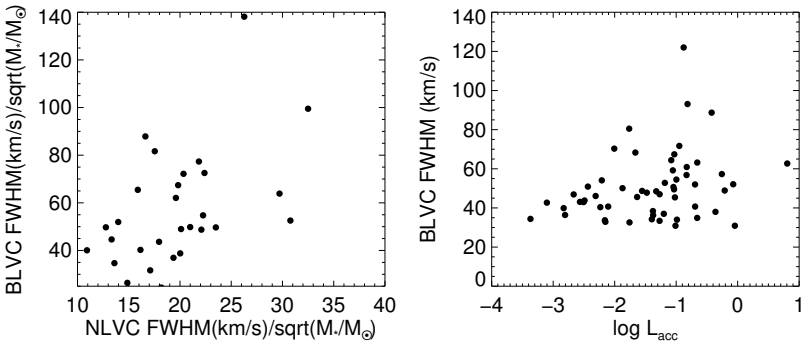

Figure 5.18: Left: FWHM of the broad LVC vs. FWHM of the narrow LVC, both normalized by the square root of the stellar mass, for the systems where both are detected. Right: FWHM of the broad LVC versus accretion luminosity.

we would expect a positive one to exist. In our sample, we do not find a clear correlation between these two components' FWHM, with a Kendall τ test giving a 13% probability of no correlation. However, the stellar mass is essential in determining the Keplerian rotation rate at a given disk radius (more specifically, the square root of the stellar mass), so we searched again for a correlation between these two components' FWHM, this time normalized by the square root of the stellar mass (left panel of Figure 5.18). In this case we find a correlation, with only a 0.1% chance that it is false. Nevertheless, Figure 5.18 shows that there is a significant spread in this relation, meaning that other factors besides the system inclination should be influencing the FWHM of one or both of these components. For the BLVC, we also find a positive correlation between the FWHM and the accretion luminosity (right panel of Figure 5.18). Though there is also a large spread in this distribution, a Kendall τ test gives only a 2% probability that this correlation is false. This is not the case for the NLVC, for which we found no correlation between the FWHM and any stellar or accretion property.

Unfortunately, we do not have direct measurements of the inclinations of our systems as S16 have for many of theirs. Therefore in order to compare with the FWHM and centroid velocities of our LVCs, we estimate system inclinations from stellar rotation properties, as was done in Section 4.6 for the AA Tau-like systems, using Equation 4.5. We use the periods obtained from the 2011 CoRoT light curves (Venuti et al. 2017a) or the 2008 CoRoT light curves (Alencar et al. 2010) and assume they represent stellar rotation periods. Stellar radii are given in Section 3.3.1, and the values of $v \sin i$ used in this Chapter are the ones that were determined directly from the same FLAMES spectra that contain the [OI] 6300Å line (see Section 3.3.2). As has been discussed in Section 4.6.2, this method for deriving inclinations is subject to a number of uncertainties and the resulting inclinations are very inaccurate (see, e.g., Appenzeller & Bertout 2013, for a comparisson between inclinations derived from rotation properties and those measured directly). Nevertheless, these estimates allow us to at least distinguish between systems observed at low inclinations from those observed at medium to high inclinations.

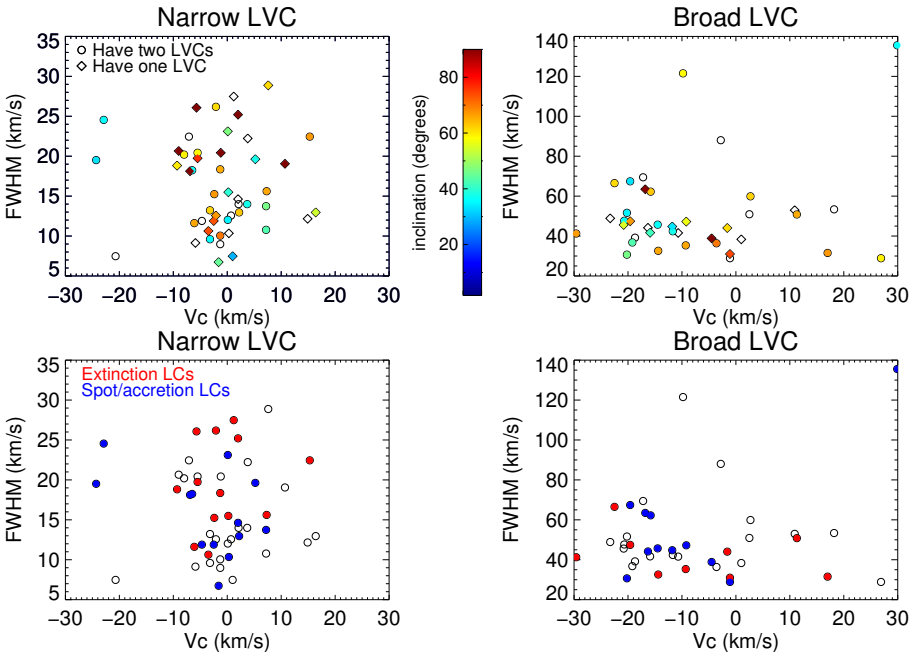

Figure 5.19: FWHM vs. centroid velocity for narrow LVCs (left) and broad LVCs (right). Upper panels: colors represent inclinations. Bottom panels: stars with extinction dominated light curves (expected to be observed at medium to high inclinations) are shown in red, while stars with spot-like or flux burst-dominated light curves (expected to be observed at low to medium inclinations) are shown in blue. Both methods show that systems observed at higher inclinations tend to show broader narrow LVCs than those observed at lower inclinations. They also show that systems observed at lower inclinations tend to have more blueshifted broad LVCs. A trend in the width of broad LVCs is difficult to find since our sample does not probe very large widths.

In Figure 5.19 we plot FWHM against centroid velocity for the narrow and broad LVCs. In the upper panels, colors represent inclinations estimated from the stellar rotation properties. In the bottom panels, we separate stars with AA Tau-like and/or aperiodic extinction dominated light curves, which are expected to be observed at medium to high inclinations, and stars with spot-like or flux burst-dominated light curves, which are expected to be observed at low to medium inclinations. We can see a general trend for the FWHM of the narrow LVC, in which systems observed at higher inclinations tend to present broader NLVCs than those observed at lower inclinations, in agreement with S16. For the broad LVC, we cannot distinguish any trend between the FWHM and system inclinations, which was observed by S16. However, our sample does not probe very large widths as theirs does, and this could be why we do not see the trend. On the other hand, the centroid velocities of the BLVC seem to show a tendency with inclination. Systems viewed at lower inclinations appear to present more blueshifted BLVCs on average than those viewed at higher inclinations, and the redshifted components seem to be associated with high inclinations (though there are few objects in this velocity bin with estimates of inclination, so we cannot conclude this

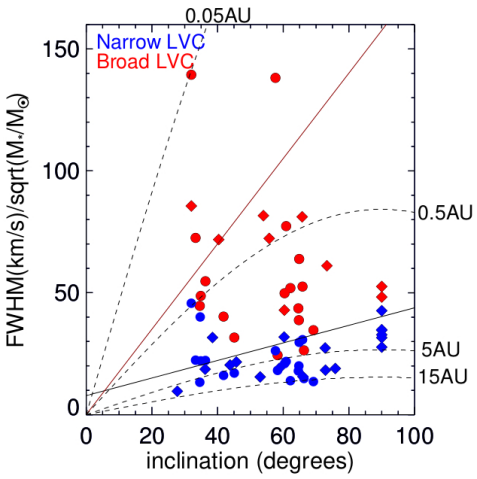

Figure 5.20: FWHM normalized by the square root of the stellar mass vs. inclination. Red symbols represents broad LVCs, while blue symbols represent narrow LVCs. Filled circles show cases where two LVCs were identified and filled diamonds show cases where only a BLVC or a NLVC was identified. Black dashed lines show line width as a function of inclination for Keplerian rotation at four different disk radii: 0.05au, 0.5au, 5au and 15au. The linear fits found by S16 for their broad and narrow components are shown as dark red and black lines, respectively. Our components are found in the same range as theirs, but on average lower in the diagram.

with certainty). The latter effect could represent a scenario in which the BLVC is produced in a disk wind and the system is viewed at a very specific, high inclination, such that the approaching (blueshifted) part of the wind is obscured by the outer flaring part of the disk but the receding (redshifted) part is unobstructed from view (S16).

Figure 5.20 shows the FWHM/$\sqrt{\text{mass}}$ of each component versus system inclinations, which describes the relation expected for Keplerian broadening. We do not find linear correlations for the two components as S16 did, but their inclinations are measured directly from spatially resolved disks, whereas ours are estimates subject to large uncertainties, meaning their results from this diagram are much more reliable than ours. In Figure 5.20 we plot their linear fit found for the broad LVC (in dark red) and for the narrow LVC (in black), in order to compare our data with their results. We see that our data lie in the same general region as theirs, but on average lower (toward narrower components), despite their spectra having better resolution than ours. It is possible that this difference is caused by the different methods used to decompose the observed profiles into Gaussians, which makes it difficult to compare the two. Since our values of inclination are so uncertain, it is also possible that the objects with the lowest values of FWHM/$\sqrt{\text{mass}}$ in our sample could in reality have much lower inclinations than we estimate and should therefore be located further to the left of the diagram than they are. Furthermore, for the BLVC we find very few components among the broadest range (FWHM $>$ 100km/s). This could be due to an observational bias; if the

noise in our spectra is large it may be masking these very broad components, which would tend to blend into the continuum. If this is the case, then our sample is incomplete at high FWHM for the BLVC.

Our values of mass were determined by Venuti et al. (2014) using the pre-main sequence evolution tracks of Siess et al. (2000), unlike those of S16 which were determined by Herczeg & Hillenbrand (2014) using the tracks of Baraffe et al. (2003) and Tognelli et al. (2011). The use of different evolutionary models to determine mass could induce a systematic error in the comparison of the values of FWHM/$\sqrt{\text{mass}}$. In order to investigate if this was the case, we calculated the masses in our sample in the same way as those of S16 had been calculated, then remade Figure 5.20. The resulting plot showed very little difference to the original one and maintained the observed trend. Therefore the difference in the way masses were determined cannot account for the differences observed between the two samples.

We cannot discard the possibility that the difference found between the widths of our low-velocity components and those of S16 represents a physical effect. If the widths of these components derive mostly from Keplerian broadening (as appears to be the case for the NLVC, at least), then this would mean that the low-velocity [OI] emission in our sample is coming from a region farther out in the accretion disk than in their sample. Since Taurus ($\sim$ 1 Myr) is younger than NGC 2264 ($\sim$ 3-5 Myr[6]), this could reflect the evolution of the accretion disks. This would mean that as a system gets older, its low-velocity [OI] emission would tend to come from larger disk radii.

Ercolano & Owen (2010) propose that the LVC of the [OI] 6300Å emission line may be produced in an X-ray driven photoevaporative disk wind. As has been shown by R13, this model cannot account for the widths of the [OI] low-velocity profiles. However, if we analyze only the narrow LVC, this is no longer the case. The newer models of Ercolano & Owen (2016) produce profiles with 14.36km/s $< FWHM <$ 32.89km/s, using very similar spectral resolution to our data. This range of values is comparable to the range we observe in the NLVCs of our [OI] profiles (12.9km/s $< FWHM <$ 31.0km/s).

We have seen in Figures 5.14 and 5.15 that the NLVC is much more commonly found among systems with a thin inner disk than the BLVC. This is consistent with S16's finding that the NLVC is often present in transition disks, whereas the BLVC rarely is. We do not have a list of systems with transition disks in our sample, nevertheless we have a preliminary list of candidates (Alana Sousa, private communication), 15 of which are among our sources with a detected [OI] 6300Å line. Around half of them (8) only show a NLVC, while only 2 show a BLVC alone. The remaining 5 show both components, with the NLVC considerably stronger than the BLVC. Ercolano & Owen (2010) predict that, if the [OI] 6300Å emission comes from a photoevaporative disk wind, then this emission would be approximately twice as luminous among sources with transition disks than among sources with primordial disks.

[6]There is, however, strong evidence for a significant age spread in this cluster (see Dahm 2008; Venuti et al. 2017b).

If the NLVC traces such a photoevaporative wind and the BLVC does not, then we could expect to detect much stronger NLVCs than BLVCs as the systems evolve.

In our sample, we find many more systems with a narrow LVC compared to the number of systems with a broad LVC than S16 found in Taurus (NGC 2264: NLVC/BLVC = 72/67 = 1.07, Taurus: NLVC/BLVC = 18/25 = 0.72). The higher fraction of NLVCs to BLVCs that we find may reflect the evolution of the disks, since Taurus is a younger star forming region (SFR) than NGC 2264.

Our BLVCs are generally more blueshifted than our NLVCs, which is not consistent with the scenario proposed by R13, in which the BLVC arises in bound gas in Keplerian rotation in the inner disk region. In their study, R13 decomposed the [OI] LVC into a broad and narrow component for only two stars, both of which showed BLVCs centered close to stellar rest velocity. This lead them to their conclusion. However, as Ercolano & Owen (2010) point out, though a blueshifted emission line is a clear sign of outflowing material, the lack of a blueshift does not necessarily mean the emission did not arise in an outflow. Our results show that many systems have a BLVC centered close to stellar rest velocity, but most are blueshifted by a few tens of km/s, which indicates that this emission likely arises in an inner disk wind rather than bound gas.

5.5 The high velocity component

In order to investigate which properties of the star-disk system are responsible for driving protostellar jets, we analyze the relationship between the luminosity of the HVC of the [OI] line and stellar/accretion properties. Figure 5.21 shows the HVC luminosity versus stellar mass, on the left, and versus mass accretion rates, on the right. We plot in this figure only the mass accretion rates derived from the UV excess and not the values derived from the Hα equivalent widths, in order to compare a more self-consistent sample[7]. We find no direct correlation between the HVC luminosity and stellar mass. The left panel of Figure 5.21 shows an almost bimodal behavior: some of the stars have [OI] HVC luminosities that fall in the same range as many of the upper limits of non-detections, while another group shows higher luminosities that are nearly constant among the entire mass range, with $\log L_{HVC}/L_{\odot} \sim -4.6$. The right panel, on the other hand, shows that there is a relation between the [OI] HVC and mass accretion, as has already been established here through the correlation between HVC luminosity and accretion luminosity in Section 5.2 and in other papers (Cabrit et al. 1990, HEG95). However, there is no clear separation between the two groups identified in the left panel.

[7] Determining mass accretion rates using these two different methods leads to slightly different values (see e.g., Sousa et al. 2016). UV excess is a more direct measurement of accretion, since the Hα line can have contributions from a wind and from accretion shocks, and does not necessarily originate only in accretion columns as is normally assumed when estimating $\dot{M}_{acc}$, whereas the UV excess originates only in the accretion shocks.

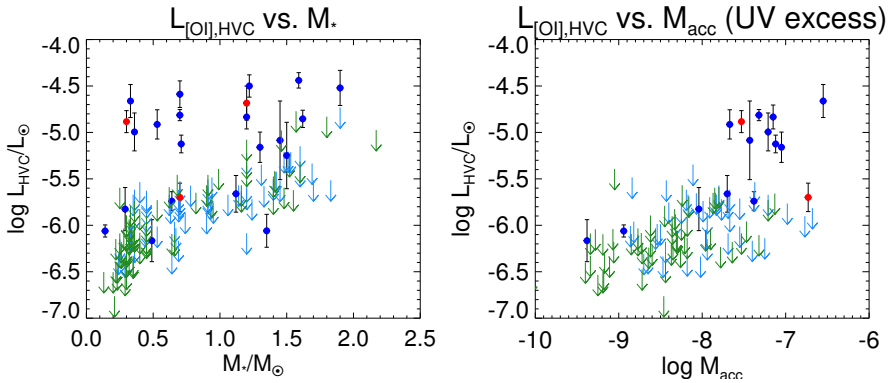

Figure 5.21: [OI] HVC luminosity versus stellar mass (left) and mass accretion rate derived from the UV excess (right).

It is possible that the two groups we see in the left panel of Figure 5.21 represent two slightly different populations that coexist in this SFR. As was mentioned in Section 5.1.1, Venuti et al. (2017b) find evidence for the coexistence of more than one subpopulation in NGC 2264. This could explain what we see in the relation between [OI] HVC luminosity and stellar parameters such as mass and temperature. However, we find no significant difference between the ages, radial velocities, or spatial distribution of the two groups we observe. We are, nonetheless, subject to low number statistics, therefore this does not necessarily rule out the possibility that they may belong to two different subpopulations of NGC 2264.

If rotationally driven stellar winds play a part in launching protostellar jets, then we may expect there to be a relation between the stellar rotation rate (or the stellar rotation rate as a function of the break-up velocity on the stellar surface) and the luminosity of the HVC of the [OI] line or the jet velocity. The left panel of Figure 5.22 shows the HVC luminosity as a function of the stellar rotation rate normalized by the break-up velocity. No correlation was found between the two in our sample. On the right panel of Figure 5.22 we plot the HVC luminosity as a function of the Keplerian velocity of the inner accretion disk at the co-rotation radius and again find no correlation.

In order to relate jet velocities with stellar/accretion parameters, we calculate the deprojected jet velocities from the HVC centroid velocities and from our estimates of inclinations, derived from stellar rotation properties. We assume that the centroid velocity of the [OI] emission line's HVC represents the propagation velocity of the jet responsible for the emission, projected in our line-of-sight. This is consistent with what we see in the left panel of Figure 5.23, which shows that the centroid velocity of the [OI] HVC tends to increase with increasing system inclination. Linear regression was performed on this plot, excluding the one outlier, Mon-1144, the only star that presents a high HVC centroid velocity but does not have a low estimated inclination (marked with a square in Figure 5.23). Since the jet is perpendicular to the accretion disk, then the deprojected jet velocity (V_{jet}) will be the HVC centroid velocity divided by the cosine of the system inclination ($V_{jet} = V_{c,HVC}/\cos i$). Since

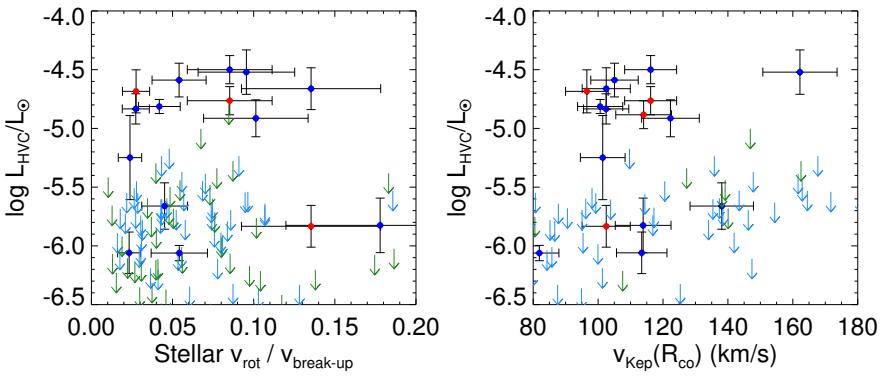

Figure 5.22: Left: [OI] HVC luminosity versus stellar rotation velocity normalized by the break-up velocity. Right: [OI] HVC luminosity versus the Keplerian velocity of the disk at co-rotation radius.

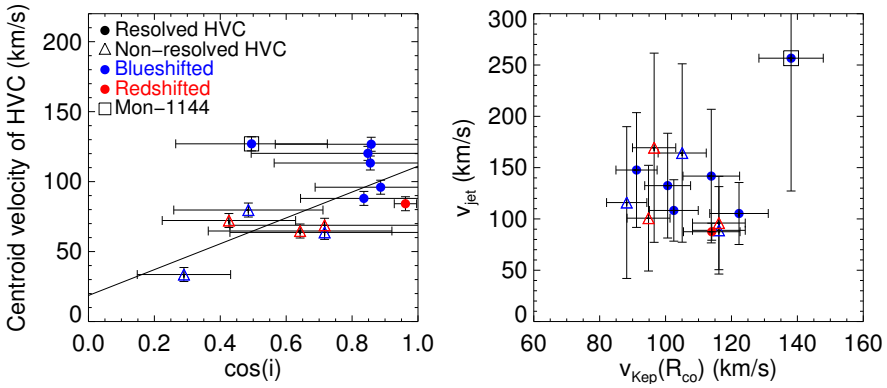

Figure 5.23: Left: centroid velocity of the HVC versus cosine of inclination. Right: deprojected jet velocity versus the Keplerian velocity of the disk at co-rotation radius.

deriving system inclinations from stellar rotation properties is subject to large uncertainties, our values of jet velocity are also very imprecise. We find that all of the jets in our sample appear to propagate at approximately the same velocity. In fact, the values we derive all agree within the uncertainties with the average value of $v_{jet} = 128(\pm 41)$ km/s. This is considerably lower than the average jet velocity found, for instance, in Taurus (∼200-300km/s, according to Appenzeller & Bertout 2013). The values of v_{jet} found are given in Table 5.2.

Figures 5.23 and 5.24 show no correlation between the jet propagation velocity and stellar rotation velocities, Keplerian rotation velocities at the inner disk (at the co-rotation radius), or stellar mass. However the very large error bars in jet velocity may be masking possible trends. Direct measurements of system inclinations are necessary to confirm the lack of correlations among these properties. Since we do not find a correlation between the jet propagation velocity and any stellar property, but find jet velocities that are lower than those measured in other SFRs, it is possible that a characteristic of the cluster itself, rather than the individual sources, is influencing the propagation velocities of protostellar jets. If, for instance, the age of the SFR is responsible for the difference between the jet velocities

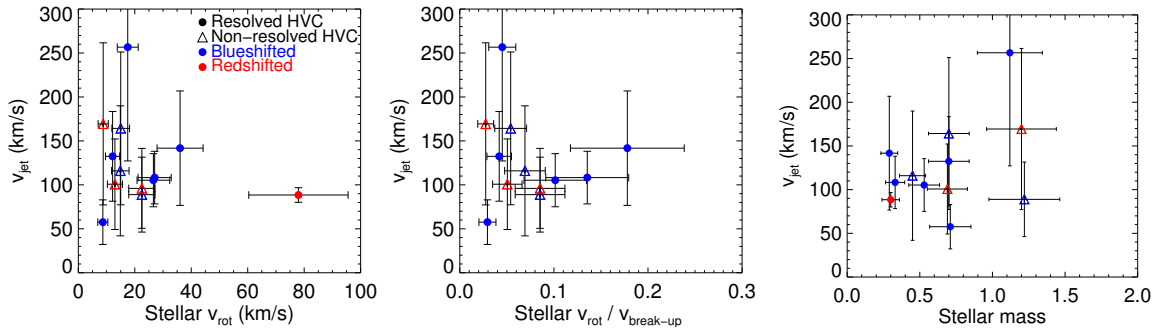

Figure 5.24: Left: deprojected jet velocity versus stellar rotation velocity. Middle: stellar rotation velocity is normalized by the break-up velocity. Right: deprojected jet velocity versus stellar mass.

in NGC 2264 and Taurus, then this would mean that jet velocities decrease with age, which would require the launching radii to increase with time. However, our results alone are not enough to reach such conclusion. For this we would need to compare the jet velocities of a large number of different SFRs.

We can estimate the mass loss rates $\dot{M}_{loss}$ through the protostellar jets in our sample using the relation between $\dot{M}_{loss}$ and the [OI] 6300Å line luminosity given in HEG95 (equation A17), scaled to a propagation velocity of 128 km/s. This results in the following equation:

$$\log \dot{M}_{loss} = -2.67 + \log\left(\frac{L_{[OI],HVC}}{L_{\odot}}\right). \tag{5.7}$$

These values likely represent upper limits to the mass loss rates, since this relation assumes that all [OI] high-velocity emission comes from one shock, whereas in reality they probably come from several shocks. We can see in Figure 5.25 (left panel) that these mass loss rates are indeed higher than we would expect, with many systems showing $\dot{M}_{loss} > \dot{M}_{acc}$. This is especially the case for systems where the HVC was not clearly resolved, and the separation via Gaussian decomposition may not have entirely removed the contribution of the LVC, resulting in overestimated HVC luminosities. A more accurate determination of $\dot{M}_{loss}$ requires knowledge of the physical conditions of the jets (e.g., electron density and temperature), which cannot be extracted from the [OI] 6300Å line alone. Our FLAMES spectra do not cover simultaneously other forbidden emission lines such as [OI] 5577Å, [NII] 6548Å/6583Å or [SII] 6716Å/6731Å, so we cannot use lines ratios to determine these physical conditions. The UVES spectra (described in Section 2.2.5) cover all of these lines, but unfortunately only four stars with [OI] emission were observed with this instrument, only one of which shows a HVC. Therefore, for the time being, we must rely on assumptions. The mass loss rates we find following Equation 5.7 are given in Table 5.2.

If we know the mass loss rates $\dot{M}_{loss}$, then we can estimate the mechanical luminosity transported by the jets $L_{mech}(jet)$. This can be calculated as:

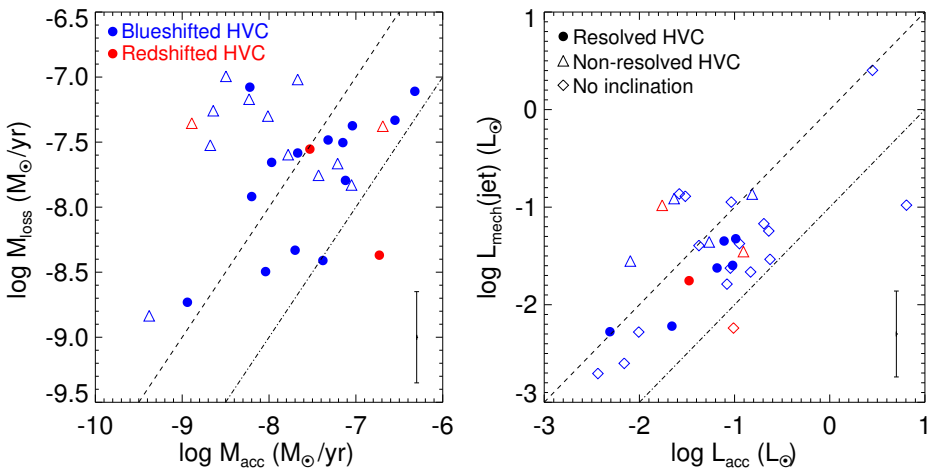

Figure 5.25: Left: mass loss rate versus mass accretion rate. The dashed line shows a one-to-one relation between $\dot{M}_{loss}$ and $\dot{M}_{acc}$ and the dashed-dotted line shows a relation of $\dot{M}_{loss} = 0.1\dot{M}_{acc}$. Right: mechanical luminosity transported by the jet ($L_{mech}(jet)$) versus accretion luminosity (L_{acc}). The dashed line shows $L_{mech}(jet) = L_{acc}$, while the dashed-dotted line represents $L_{mech}(jet) = 0.1L_{acc}$. Blue symbols represent systems for which the luminosity of the blueshifted HVC was used to estimate $\dot{M}_{loss}$, while red symbols represent systems that only present a redshifted HVC. A typical error bar is shown in the bottom right of each plot.

$$L_{mech}(jet) = \frac{1}{2}\dot{M}_{loss}V_{jet}^2, \tag{5.8}$$

where V_{jet} is the jet propagation velocity. In the right panel of Figure 5.25, we plot the jet mechanical luminosity against the accretion luminosity (derived in Section 3.3.4). In order to increase the number of systems analyzed in this plot, it is necessary to estimate jet velocities for the systems whose inclinations we do not know. As we have seen, our jet velocities all agree, within the uncertainties, with the average value found. Therefore we assume that this is also the case for the jets associated with the systems for which we have no inclination and estimate their $L_{mech}(jet)$ by taking $V_{jet} = 128(\pm41)$km/s. We can see from the right panel of Figure 5.25 that, if the mass loss rates through protostellar jets are proportional to the [OI] HVC luminosities and the propagation velocities are all approximately the same, then the mechanical luminosity transported by these jets correlates positively with the accretion luminosities measured in these systems. Our values of $L_{mech}(jet)$ can be found in Table 5.2.

We have seen that the HVC of the [OI] 6300Å line depends strongly on an optically thick inner disk and that its luminosity correlates well with the system's accretion luminosity. Our results in this section suggest that stellar properties such as effective temperature, mass, or stellar rotation, do not influence in a significant way the propagation velocity or luminosity of the jets that produce this high-velocity emission. It seems, therefore, that it is the disk, rather than the star, that governs the launching mechanism of protostellar jets.

Table 5.2: Jet parameters for the stars with detected high-velocity [OI] emission

CSIMon ID	$\dot{M}_{loss}$ ($M_\odot$/yr)	V_{jet} (km/s)	$L_{mech}(jet)$ ($L_\odot$)
CSIMon-000011	7.59e-08	-	0.10
CSIMon-000126	1.70e-06	-	2.29
CSIMon-000153	5.69e-08	142±65	0.09
CSIMon-000228	4.50e-07	116±74	0.50
CSIMon-000250	3.33e-08	349±218	0.33
CSIMon-000260	3.93e-07	148±56	0.11
CSIMon-000346	9.82e-07	164±87	2.19
CSIMon-000357	7.86e-07	169±92	1.85
CSIMon-000392	3.33e-05	-	44.99
CSIMon-000406	5.83e-07	132±51	0.84
CSIMon-000423	1.30e-07	-	0.17
CSIMon-000425	1.20e-06	89±43	0.78
CSIMon-000457	1.49e-06	-	2.01
CSIMon-000469	2.86e-07	-	0.39
CSIMon-000498	1.15e-06	95±51	0.86
CSIMon-000510	7.50e-07	-	1.01
CSIMon-000567	3.13e-07	-	0.42
CSIMon-000577	5.32e-07	-	0.72
CSIMon-000632	2.60e-08	-	0.04
CSIMon-000766	4.64e-07	105±30	0.42
CSIMon-000846	1.38e-06	-	1.87
CSIMon-000919	9.32e-08	87±48	0.06
CSIMon-000936	5.57e-07	-	0.75
CSIMon-000996	7.45e-07	101±52	0.62
CSIMon-001011	3.31e-08	-	0.04
CSIMon-001022	2.15e-07	-	0.29
CSIMon-001036	3.84e-07	-	0.52
CSIMon-001037	8.93e-07	-	1.20
CSIMon-001061	6.92e-08	-	0.09
CSIMon-001100	1.80e-06	-	2.44
CSIMon-001132	8.29e-07	108±30	0.80
CSIMon-001144	8.30e-08	257±129	0.45
CSIMon-001249	4.96e-07	88±8	0.31

Table 5.3: [OI] 6300Å line luminosities and stellar parameters

CSIMon ID	$L_{[OI]}$ ($L_\odot$)	L_{NLVC} ($L_\odot$)	L_{BLVC} ($L_\odot$)	$L_{HVC,blue}$ ($L_\odot$)	$L_{HVC,red}$ ($L_\odot$)	L_X ($L_\odot$)	α_{IRAC}	E(K-3.6μm)
CSIMon-000011	1.61e-05	8.52e-06	5.56e-06	-	2.00e-06	6.41e-04	-	1.15
CSIMon-000021	4.18e-06	4.18e-06	-	-	-	-	-	0.48
CSIMon-000056	<9.03e-06	-	-	-	-	-	-1.36	0.25
CSIMon-000062	<1.06e-05	-	-	-	-	-	-	0.12
CSIMon-000063	<2.51e-06	-	-	-	-	-	-1.37	-
CSIMon-000064	<5.29e-06	-	-	-	-	6.72e-04	-1.15	0.43
CSIMon-000090	<3.14e-06	-	-	-	-	8.26e-06	-0.88	-
CSIMon-000103	9.12e-05	3.17e-05	5.95e-05	-	-	2.50e-03	-1.14	0.78
CSIMon-000109	<3.14e-05	-	-	-	-	-	-1.76	-0.12
CSIMon-000117	<3.32e-06	-	-	-	-	-	-2.34	0.39
CSIMon-000119	1.09e-05	4.14e-06	6.73e-06	-	-	5.34e-04	-1.44	0.72
CSIMon-000120	2.21e-05	1.65e-05	5.61e-06	-	-	9.93e-05	-2.12	0.30
CSIMon-000123	<5.81e-06	-	-	-	-	1.73e-04	-	0.30
CSIMon-000126	7.95e-05	-	3.46e-05	4.48e-05	-	1.54e-04	-1.09	0.97
CSIMon-000131	3.42e-05	3.42e-05	-	-	-	-	-	11.94
CSIMon-000134	<2.95e-06	-	-	-	-	6.72e-05	-1.72	0.05
CSIMon-000136	<8.64e-06	-	-	-	-	1.28e-04	-0.53	0.36
CSIMon-000137	3.58e-06	-	3.58e-06	-	-	3.95e-05	-1.54	0.44
CSIMon-000153	3.40e-06	-	1.91e-06	1.50e-06	-	1.77e-05	-1.71	0.91
CSIMon-000168	9.92e-06	9.92e-06	-	-	-	2.87e-04	-1.38	0.53
CSIMon-000177	3.84e-05	1.65e-05	2.19e-05	-	-	1.85e-03	-	0.34
CSIMon-000192	<2.75e-06	-	-	-	-	1.11e-04	-1.31	-
CSIMon-000207	<3.53e-06	-	-	-	-	1.77e-05	-2.04	-0.02
CSIMon-000212	<3.15e-06	-	-	-	-	2.55e-04	-1.16	0.24
CSIMon-000219	<1.26e-06	-	-	-	-	2.03e-05	-1.87	0.24
CSIMon-000220	<2.20e-06	-	-	-	-	3.69e-04	-	0.05
CSIMon-000225	<2.26e-06	-	-	-	-	1.19e-04	-1.58	0.27
CSIMon-000228	2.34e-05	-	1.16e-05	1.18e-05	-	2.80e-04	-	0.32
CSIMon-000250	1.70e-05	1.61e-05	-	8.72e-07	-	3.86e-04	-2.10	0.51
CSIMon-000260	1.55e-05	1.35e-05	-	1.95e-06	-	7.03e-04	-0.93	1.41
CSIMon-000273	7.12e-06	7.12e-06	-	-	-	3.69e-04	-2.28	0.04
CSIMon-000279	<1.63e-06	-	-	-	-	2.44e-04	-1.59	0.15
CSIMon-000280	<1.60e-05	-	-	-	-	-	-1.97	0.18
CSIMon-000290	<3.85e-06	-	-	-	-	3.52e-04	-	0.33
CSIMon-000295	5.23e-06	-	5.23e-06	-	-	1.14e-04	-1.12	0.76
CSIMon-000296	3.00e-05	3.00e-05	-	-	-	7.54e-04	-2.14	0.35
CSIMon-000297	5.78e-05	3.42e-05	2.36e-05	-	-	1.28e-03	-	0.47
CSIMon-000314	2.20e-06	-	2.20e-06	-	-	1.98e-04	-2.61	0.20
CSIMon-000318	<1.55e-05	-	-	-	-	6.27e-04	-0.97	-
CSIMon-000326	<2.50e-06	-	-	-	-	3.95e-04	-1.39	0.06
CSIMon-000328	<2.71e-06	-	-	-	-	2.50e-04	-1.88	0.02
CSIMon-000330	<1.12e-05	-	-	-	-	-	-2.84	-0.10
CSIMon-000335	2.85e-05	2.85e-05	-	-	-	-	-0.93	0.36
CSIMon-000340	<5.15e-06	-	-	-	-	-	-2.82	0.11
CSIMon-000341	<5.94e-06	-	-	-	-	6.72e-05	-	0.63
CSIMon-000342	<2.19e-06	-	-	-	-	-	-1.79	0.37
CSIMon-000346	4.71e-05	-	2.13e-05	2.58e-05	-	1.11e-04	-	11.44

Table 5.3: [OI] 6300Å line luminosities and stellar parameters - continued

CSIMon ID	$L_{[OI]}$ ($L_\odot$)	L_{NLVC} ($L_\odot$)	L_{BLVC} ($L_\odot$)	$L_{HVC,blue}$ ($L_\odot$)	$L_{HVC,red}$ ($L_\odot$)	L_X ($L_\odot$)	α_{IRAC}	E(K-3.6μm)
CSIMon-000347	2.25e-06	2.25e-06	-	-	-	1.89e-05	-0.47	0.40
CSIMon-000349	4.87e-05	1.96e-05	2.91e-05	-	-	2.44e-04	-	1.08
CSIMon-000352	<3.38e-06	-	-	-	-	7.03e-05	-1.18	0.30
CSIMon-000356	<1.11e-06	-	-	-	-	2.03e-05	-1.23	0.23
CSIMon-000357	4.14e-05	2.07e-05	-	-	2.07e-05	1.57e-03	-	0.34
CSIMon-000358	7.88e-06	2.22e-06	5.66e-06	-	-	8.07e-05	-1.59	0.37
CSIMon-000359	2.55e-05	1.68e-05	8.68e-06	-	-	4.75e-04	-1.92	0.36
CSIMon-000361	<2.22e-06	-	-	-	-	3.69e-05	-1.62	0.19
CSIMon-000370	2.36e-05	1.49e-05	8.70e-06	-	-	6.41e-03	-1.17	11.16
CSIMon-000379	5.19e-05	2.33e-05	2.87e-05	-	-	4.87e-04	-1.91	0.51
CSIMon-000392	1.12e-03	2.47e-04	-	8.76e-04	-	-	-	-
CSIMon-000406	2.63e-05	-	1.10e-05	1.54e-05	-	8.65e-05	-0.87	0.63
CSIMon-000412	1.70e-05	-	1.70e-05	-	-	6.72e-04	-1.37	0.50
CSIMon-000423	9.31e-06	-	5.90e-06	3.41e-06	-	-	-0.57	1.76
CSIMon-000424	<3.08e-06	-	-	-	-	5.99e-05	-1.08	0.35
CSIMon-000425	9.98e-05	5.10e-05	-	3.16e-05	1.72e-05	5.99e-04	-0.66	0.94
CSIMon-000426	<2.80e-05	-	-	-	-	1.89e-05	-2.73	-0.02
CSIMon-000433	1.67e-05	1.67e-05	-	-	-	4.24e-04	-2.24	-
CSIMon-000434	3.00e-06	-	3.00e-06	-	-	3.86e-04	-1.25	0.27
CSIMon-000441	3.42e-06	3.42e-06	-	-	-	2.03e-05	-1.41	0.70
CSIMon-000448	1.31e-05	8.05e-06	5.04e-06	-	-	1.06e-03	-1.12	0.54
CSIMon-000456	<1.60e-05	-	-	-	-	2.67e-04	-	0.51
CSIMon-000457	5.41e-04	-	3.96e-04	3.91e-05	1.06e-04	3.86e-04	-0.01	1.69
CSIMon-000462	3.21e-05	3.21e-05	-	-	-	2.44e-04	-	0.67
CSIMon-000469	4.61e-05	5.91e-06	2.91e-05	7.51e-06	3.59e-06	1.19e-05	-0.99	0.38
CSIMon-000474	2.08e-04	9.06e-05	1.18e-04	-	-	3.21e-03	-	-
CSIMon-000484	<1.05e-06	-	-	-	-	6.87e-05	-	-
CSIMon-000491	2.69e-05	-	2.69e-05	-	-	8.46e-04	-0.58	1.11
CSIMon-000498	7.41e-05	4.39e-05	-	3.01e-05	-	1.06e-03	-1.41	0.42
CSIMon-000510	3.67e-05	-	1.69e-05	1.98e-05	-	8.46e-04	-0.97	0.85
CSIMon-000525	<4.46e-05	-	-	-	-	1.89e-04	-1.69	0.94
CSIMon-000530	<8.80e-06	-	-	-	-	-	-1.59	13.14
CSIMon-000553	<5.48e-05	-	-	-	-	1.17e-04	-1.22	0.95
CSIMon-000558	6.65e-05	5.22e-05	1.44e-05	-	-	5.72e-04	-1.46	0.45
CSIMon-000566	<1.83e-06	-	-	-	-	1.73e-05	-	0.37
CSIMon-000567	3.82e-05	-	3.00e-05	8.22e-06	-	1.34e-04	-1.14	1.01
CSIMon-000577	4.34e-05	-	2.94e-05	1.40e-05	-	-	-1.49	0.49
CSIMon-000578	<6.18e-06	-	-	-	-	-	-2.78	0.03
CSIMon-000590	<3.34e-06	-	-	-	-	6.13e-05	-1.89	0.19
CSIMon-000598	3.55e-05	3.55e-05	-	-	-	6.87e-04	-1.64	0.40
CSIMon-000613	8.10e-05	4.63e-05	3.47e-05	-	-	5.34e-04	-1.65	0.71
CSIMon-000619	2.86e-05	-	2.86e-05	-	-	3.07e-04	-1.04	0.96
CSIMon-000628	2.69e-06	-	2.69e-06	-	-	4.54e-05	-1.52	0.35
CSIMon-000631	9.00e-05	9.00e-05	-	-	-	-	-	-
CSIMon-000632	2.26e-06	-	1.58e-06	6.83e-07	-	-	-0.56	1.99
CSIMon-000636	<9.78e-06	-	-	-	-	2.87e-04	-0.68	1.26
CSIMon-000637	4.24e-06	4.24e-06	-	-	-	1.94e-04	-2.67	0.14

Table 5.3: [OI] 6300Å line luminosities and stellar parameters - continued

CSIMon ID	$L_{[OI]}$ ($L_\odot$)	L_{NLVC} ($L_\odot$)	L_{BLVC} ($L_\odot$)	$L_{HVC,blue}$ ($L_\odot$)	$L_{HVC,red}$ ($L_\odot$)	L_X ($L_\odot$)	α_{IRAC}	E(K-3.6μm)
CSIMon-000655	<3.09e-06	-	-	-	-	1.77e-04	-1.85	0.51
CSIMon-000660	<1.25e-05	-	-	-	-	1.44e-03	-1.72	0.60
CSIMon-000667	4.25e-05	4.25e-05	-	-	-	9.27e-04	-0.57	0.94
CSIMon-000676	<1.89e-05	-	-	-	-	-	-1.53	0.23
CSIMon-000681	3.82e-05	1.54e-05	2.29e-05	-	-	3.14e-04	-1.44	0.73
CSIMon-000685	<4.35e-06	-	-	-	-	-	-2.33	0.05
CSIMon-000697	<4.51e-06	-	-	-	-	2.28e-04	-	0.10
CSIMon-000717	1.46e-05	3.76e-06	1.09e-05	-	-	1.34e-04	-1.47	0.52
CSIMon-000718	<2.80e-06	-	-	-	-	-	-	11.72
CSIMon-000727	<1.85e-06	-	-	-	-	-	-2.01	0.04
CSIMon-000733	<1.00e-05	-	-	-	-	1.47e-04	-1.30	0.09
CSIMon-000736	9.54e-06	3.50e-06	6.04e-06	-	-	1.57e-04	-1.23	0.24
CSIMon-000753	<6.10e-07	-	-	-	-	7.54e-06	-1.28	0.28
CSIMon-000754	<2.85e-06	-	-	-	-	3.95e-04	-2.82	-0.11
CSIMon-000765	1.49e-05	1.49e-05	-	-	-	3.78e-04	-2.29	0.21
CSIMon-000766	3.98e-05	1.06e-05	1.70e-05	1.22e-05	-	8.65e-05	-1.38	0.79
CSIMon-000774	8.86e-05	2.44e-05	6.42e-05	-	-	6.72e-04	-	0.48
CSIMon-000795	5.63e-05	1.68e-05	3.95e-05	-	-	1.17e-03	-1.72	0.62
CSIMon-000796	1.31e-05	-	1.31e-05	-	-	7.20e-05	-	0.58
CSIMon-000798	<5.11e-05	-	-	-	-	1.31e-04	-3.73	-0.03
CSIMon-000804	1.04e-05	5.55e-06	4.82e-06	-	-	3.29e-04	-0.29	0.23
CSIMon-000808	1.10e-05	1.10e-05	-	-	-	7.89e-04	-1.85	0.53
CSIMon-000810	<1.55e-05	-	-	-	-	2.12e-03	-2.84	0.04
CSIMon-000811	2.45e-05	7.39e-06	1.72e-05	-	-	4.87e-04	-1.64	0.77
CSIMon-000823	<1.47e-06	-	-	-	-	7.36e-04	-	-0.00
CSIMon-000824	<1.35e-05	-	-	-	-	5.34e-04	-2.41	0.38
CSIMon-000836	<3.38e-06	-	-	-	-	2.67e-05	-1.54	0.14
CSIMon-000846	3.33e-04	7.34e-05	2.23e-04	3.64e-05	-	2.50e-04	-	9.75
CSIMon-000860	<4.34e-06	-	-	-	-	-	-3.23	-0.03
CSIMon-000861	4.45e-05	-	4.45e-05	-	-	6.56e-05	-1.11	0.55
CSIMon-000873	1.48e-04	3.18e-05	1.16e-04	-	-	1.89e-03	-1.56	0.58
CSIMon-000877	5.94e-05	3.44e-05	2.50e-05	-	-	8.26e-04	-1.84	0.43
CSIMon-000879	4.34e-06	4.34e-06	-	-	-	2.80e-04	-2.69	0.06
CSIMon-000893	<2.10e-06	-	-	-	-	-	-0.78	0.49
CSIMon-000904	3.96e-05	3.96e-05	-	-	-	1.22e-04	-2.12	1.16
CSIMon-000914	<5.20e-06	-	-	-	-	-	1.87	1.25
CSIMon-000919	1.45e-05	-	1.21e-05	-	2.45e-06	1.81e-04	-1.04	0.39
CSIMon-000926	<2.51e-06	-	-	-	-	1.61e-04	-1.57	0.07
CSIMon-000928	4.35e-06	4.35e-06	-	-	-	3.21e-04	-1.11	0.27
CSIMon-000931	<9.81e-07	-	-	-	-	1.73e-04	-2.89	0.15
CSIMon-000936	7.48e-05	1.41e-05	4.61e-05	1.47e-05	-	7.71e-05	-0.95	-
CSIMon-000937	1.35e-05	-	1.35e-05	-	-	3.14e-04	-2.40	0.23
CSIMon-000945	<7.37e-06	-	-	-	-	3.61e-04	-1.43	0.62
CSIMon-000996	2.39e-05	4.31e-06	-	-	1.96e-05	8.46e-04	-1.19	0.72
CSIMon-001003	5.36e-06	2.82e-06	2.54e-06	-	-	-	-0.98	0.04
CSIMon-001011	3.28e-06	-	2.41e-06	8.69e-07	-	4.34e-05	-1.21	-
CSIMon-001022	3.81e-05	-	3.25e-05	5.64e-06	-	7.71e-05	-1.55	0.84

Table 5.3: [OI] 6300Å line luminosities and stellar parameters - continued

CSIMon ID	$L_{[OI]}$ ($L_\odot$)	L_{NLVC} ($L_\odot$)	L_{BLVC} ($L_\odot$)	$L_{HVC,blue}$ ($L_\odot$)	$L_{HVC,red}$ ($L_\odot$)	L_X ($L_\odot$)	α_{IRAC}	E(K-3.6μm)
CSIMon-001031	<4.67e-05	-	-	-	-	7.03e-04	-0.30	0.68
CSIMon-001033	1.63e-05	-	1.63e-05	-	-	-	-1.97	0.02
CSIMon-001036	1.71e-05	7.02e-06	-	1.01e-05	-	-	-0.95	0.56
CSIMon-001037	3.35e-04	-	3.11e-04	2.35e-05	-	2.67e-04	-1.29	0.98
CSIMon-001038	7.80e-06	4.29e-06	3.51e-06	-	-	1.04e-04	-1.83	0.62
CSIMon-001053	2.52e-05	1.39e-05	1.13e-05	-	-	5.09e-04	-1.03	0.98
CSIMon-001054	1.97e-05	-	1.97e-05	-	-	1.14e-03	-1.29	0.59
CSIMon-001055	<2.39e-05	-	-	-	-	7.89e-03	-2.42	0.15
CSIMon-001059	<1.43e-06	-	-	-	-	4.24e-05	-1.40	0.39
CSIMon-001061	1.09e-05	8.25e-07	7.25e-06	1.82e-06	1.05e-06	3.00e-04	-0.79	0.63
CSIMon-001064	4.84e-05	2.54e-05	2.30e-05	-	-	1.94e-05	-0.68	0.32
CSIMon-001076	<2.74e-06	-	-	-	-	1.44e-04	-1.39	0.25
CSIMon-001094	8.64e-06	8.64e-06	-	-	-	2.28e-04	-1.96	0.11
CSIMon-001099	<2.96e-05	-	-	-	-	6.72e-04	-	0.78
CSIMon-001100	5.59e-04	3.93e-04	-	2.90e-05	1.37e-04	4.98e-04	-0.42	1.63
CSIMon-001114	4.27e-06	4.27e-06	-	-	-	-	-	0.02
CSIMon-001131	1.08e-05	1.08e-05	-	-	-	-	-	0.38
CSIMon-001132	4.04e-05	1.71e-05	-	2.18e-05	1.47e-06	-	-0.99	1.06
CSIMon-001140	1.38e-05	1.38e-05	-	-	-	-	-	0.21
CSIMon-001142	<6.12e-06	-	-	-	-	1.47e-04	-1.89	0.03
CSIMon-001144	1.40e-05	-	1.19e-05	2.18e-06	-	1.54e-04	-1.73	0.71
CSIMon-001149	<2.61e-06	-	-	-	-	1.09e-04	-1.46	0.44
CSIMon-001156	<1.98e-06	-	-	-	-	1.11e-04	-3.21	-0.02
CSIMon-001157	1.16e-05	1.16e-05	-	-	-	-	-0.79	0.24
CSIMon-001167	<3.78e-06	-	-	-	-	8.26e-04	-1.87	0.27
CSIMon-001171	1.01e-05	1.01e-05	-	-	-	-	-	-0.05
CSIMon-001174	7.05e-06	7.05e-06	-	-	-	-	0.01	0.73
CSIMon-001181	<1.51e-06	-	-	-	-	3.14e-05	-1.84	0.10
CSIMon-001187	<2.56e-06	-	-	-	-	-	-1.31	0.62
CSIMon-001197	<1.27e-06	-	-	-	-	-	-1.23	0.25
CSIMon-001199	1.30e-05	-	1.30e-05	-	-	1.65e-04	-1.53	1.10
CSIMon-001201	<1.03e-05	-	-	-	-	7.03e-04	-4.19	0.03
CSIMon-001203	1.53e-05	1.53e-05	-	-	-	-	-	0.59
CSIMon-001217	2.37e-05	1.09e-05	1.28e-05	-	-	1.31e-04	-	1.13
CSIMon-001219	<1.27e-06	-	-	-	-	-	-1.48	0.02
CSIMon-001223	<3.83e-06	-	-	-	-	-	-1.29	0.34
CSIMon-001234	1.58e-05	1.58e-05	-	-	-	-	-1.35	0.64
CSIMon-001241	<4.07e-06	-	-	-	-	1.73e-04	-1.76	0.28
CSIMon-001249	1.94e-05	-	6.33e-06	-	1.31e-05	5.72e-05	-0.67	0.41
CSIMon-001275	<3.77e-05	-	-	-	-	2.28e-03	-	0.49
CSIMon-001279	1.43e-05	4.76e-06	9.52e-06	-	-	7.54e-04	-2.85	0.09
CSIMon-001304	<5.30e-05	-	-	-	-	-	-2.81	10.45

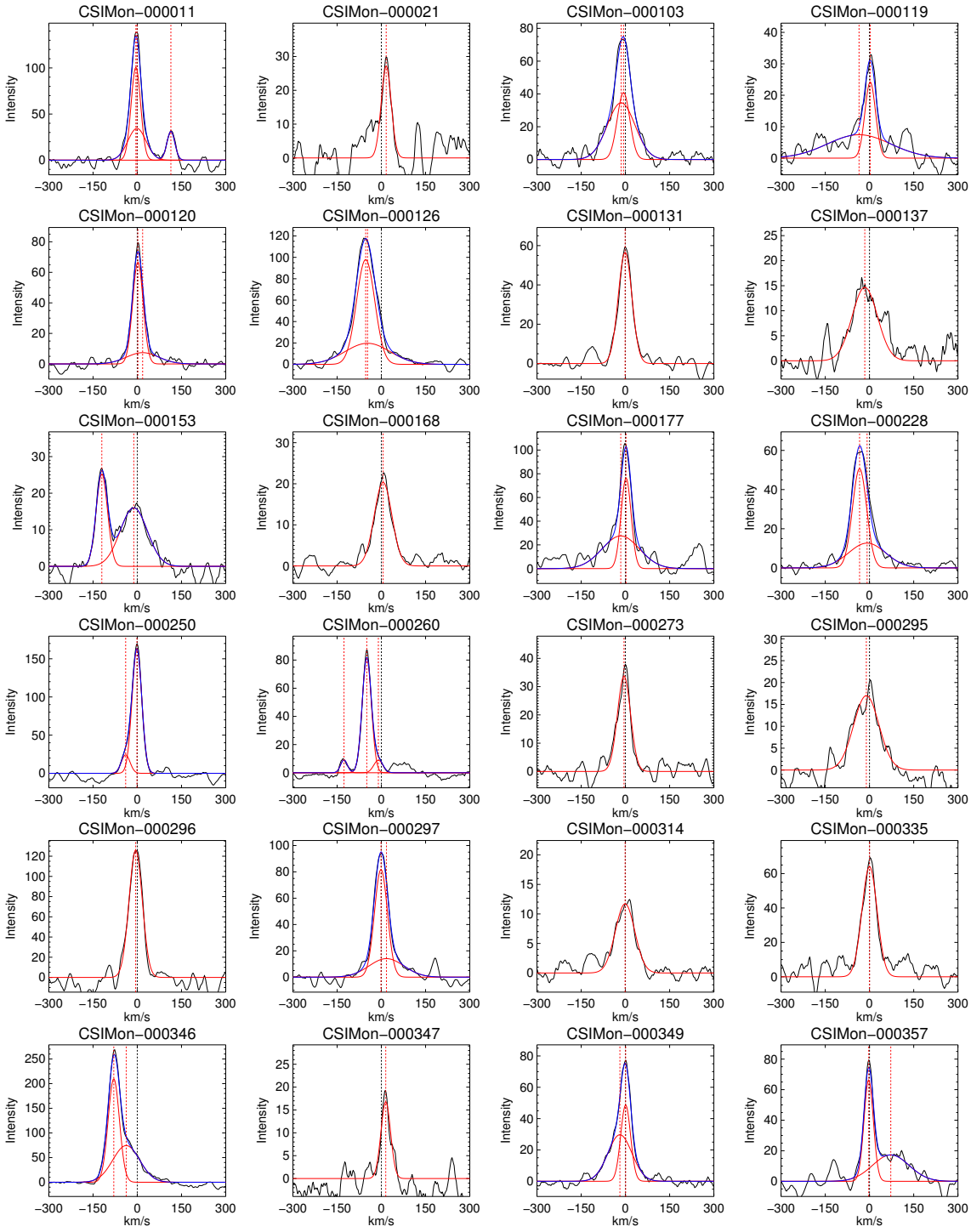

Figure 5.26: Gaussian decomposition of the [OI] 6300Å line profiles. Individual Gaussians are shown in red, while the sum of all Gaussians is shown in blue, plotted over the observed profile, in black.

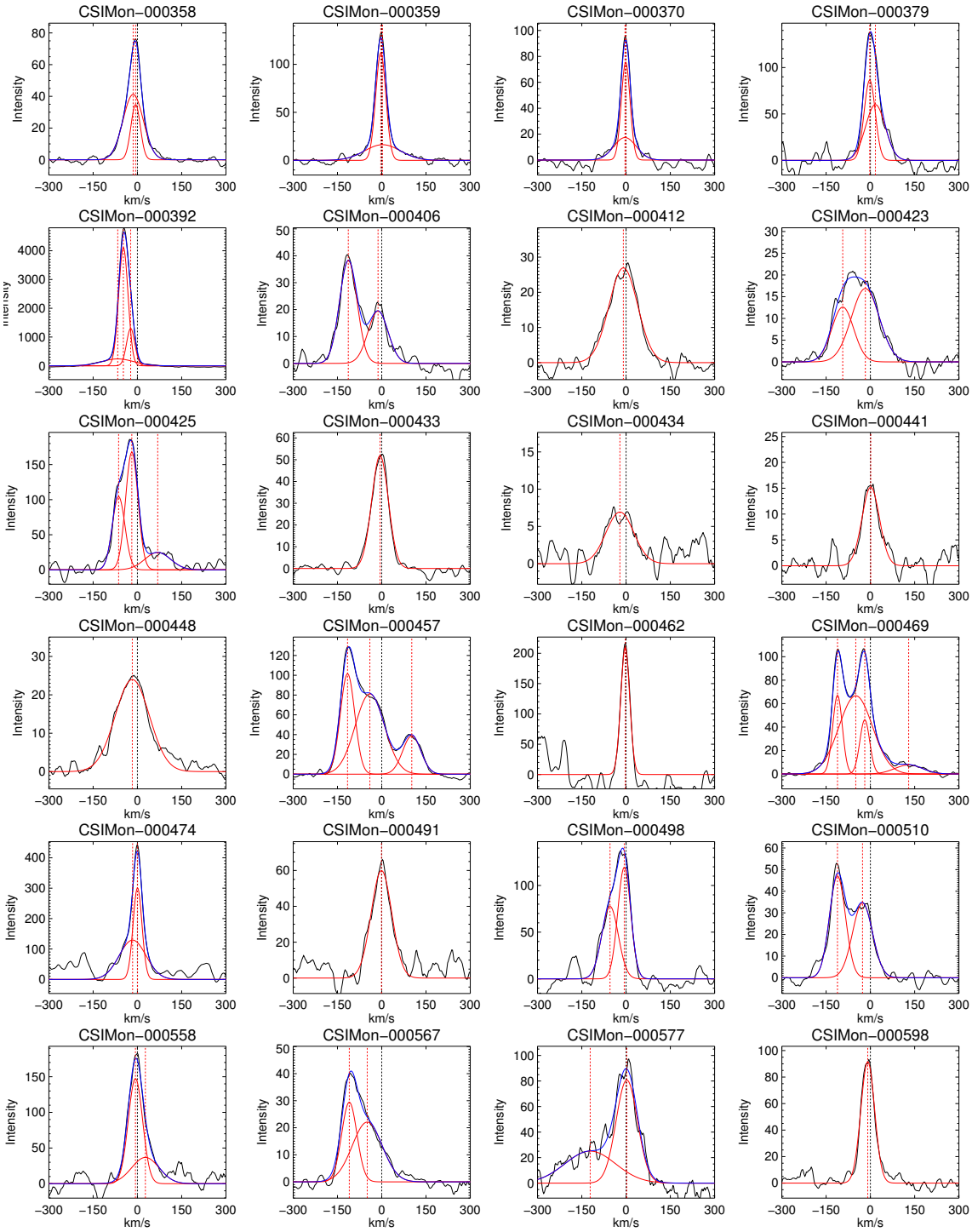

Figure 5.26: Continued.

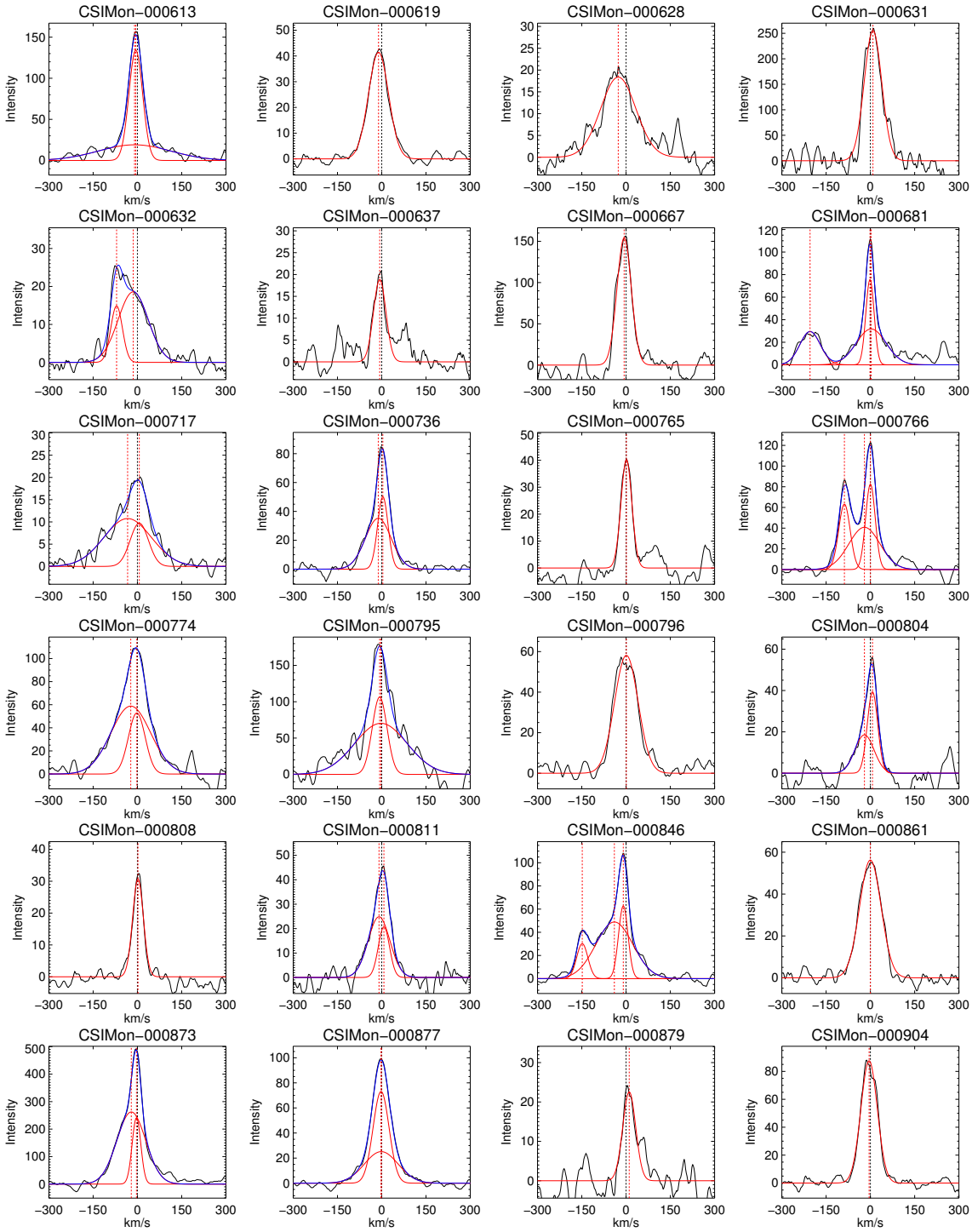

Figure 5.26: Continued.

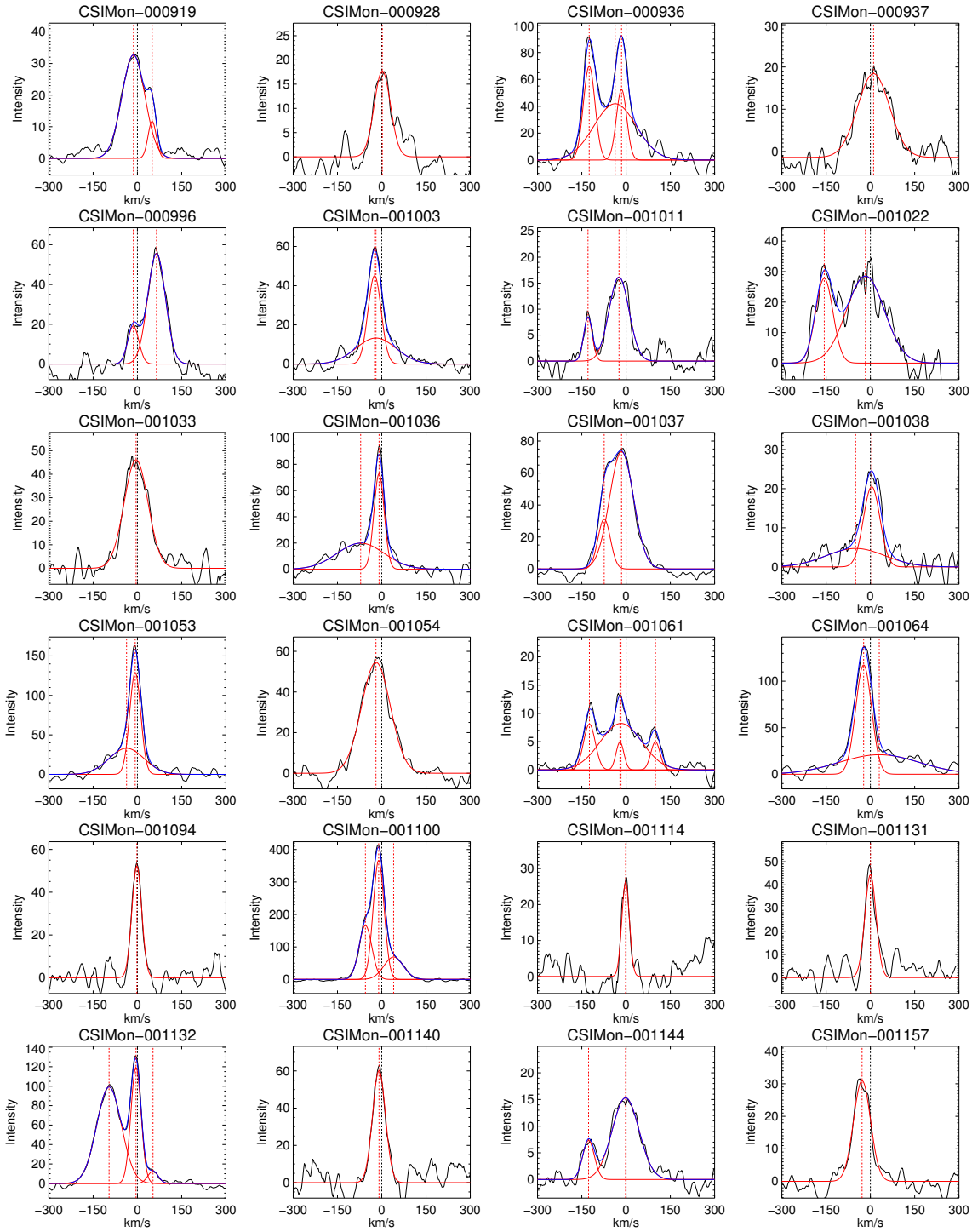

Figure 5.26: Continued.

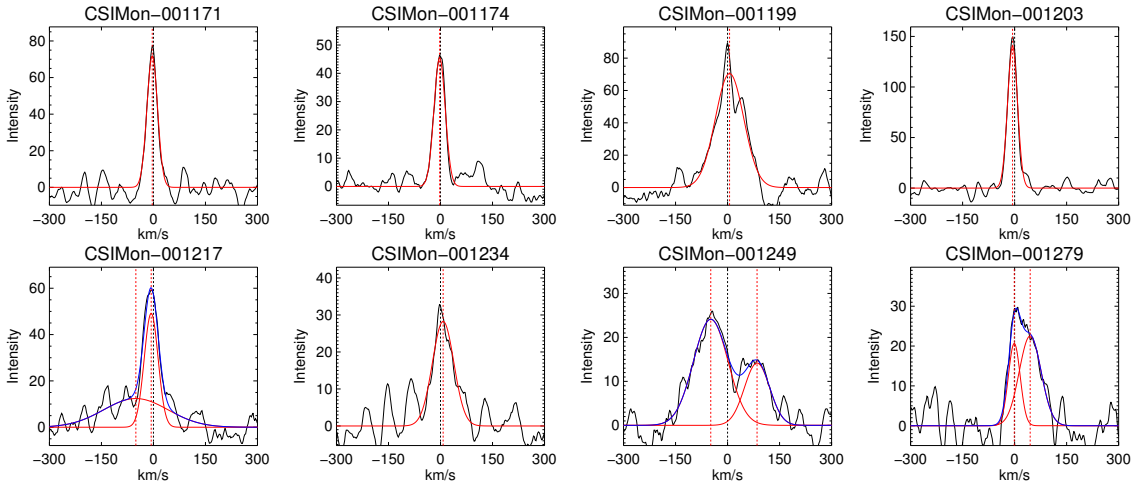

Figure 5.26: Continued.

Chapter 6

Conclusions and perspectives

Disentangling the physical processes that dominate the inner region of circumstellar disks around young stellar objects is currently a major challenge in the field of star formation. Among classical T Tauri stars, accretion is known to take place in the innermost part of the disk (few 0.1 au from the central object) and is strongly regulated by the interaction between the accretion disk and the stellar magnetic field. Properties of T Tauri jets also suggest a magnetic origin from the very inner au of the accretion disk and slow ($v \lesssim 50$ km/s) winds, detected among many classical T Tauri stars, often show signs of originating from a similar region. Accretion and outflow processes help regulate fundamental stellar properties such as mass and angular momentum, and strongly influence the evolution of circumstellar disks from which planets are formed. Therefore, understanding the dynamics of the inner accretion disk and its interaction with the stellar magnetic field is vital to fully comprehend the formation of solar-type stars and planetary systems. To that end, we have performed an analysis of the classical T Tauri star population of NGC 2264, in search of observational signatures of the accretion and ejection processes that occur or originate in the inner part of their circumstellar disks.

The first part of this work was devoted to the investigation of how accretion occurs through the interaction between the stellar magnetosphere and the inner accretion disk. We analyzed a group of stars that present a particular type of photometric behavior which could give us clues regarding this interaction. These stars' light curves are dominated by extinction events, caused by the stellar photosphere being obscured by disk material. There is evidence that these systems are observed at high inclinations (i.e., close to edge-on) and that the material obscuring the stellar photosphere is located in the innermost part of the accretion

disk, where the interaction with the stellar magnetosphere occurs and accretion columns are formed. We have found that stars that present this type of photometric behavior are common in this star forming region. Of 159 accreting T Tauri stars that were analyzed during this part of the study, 33 present CoRoT light curves dominated by extinction events, whether quasi-periodic, such as the AA Tau-like light curves, or with no obvious periodicity. This represents $21(\pm4)\%$[1] of the observed CTTSs. These objects give us insight into the phenomena that take place in the inner region of circumstellar disks, a region that is otherwise difficult to study due to its proximity to the star and to instrumental limitations. We find that, though an AA Tau-like light curve is only observed for a small fraction of the stars ($\sim 14\%$), the inner disk structure responsible for the occultations should be common to most CTTSs, assuming that the systems are observed at random inclinations, since the occultations can only observed in systems that are viewed close to edge-on.

We analyzed the optical CoRoT light curves of these systems along with simultaneously obtained infra-red *Spitzer* light curves, and found that extinction laws significantly different from those typically found in the interstellar medium are necessary to account for the ratios between the amplitudes of the optical and IR light curves. In particular, it seems that the inner disk should contain dust grains considerably larger than those of the interstellar medium, which suggests that grain growth has occurred in these disks.

When comparing photometric variability with veiling and color information, we have found that many of our systems show an increase of hot spots on the stellar surface at the same times as the flux dips appear in the light curve. This indicates that there is a spatial association between the structure that is causing the occultation events and accretion shocks on the stellar surface. Most of these systems present quasi-periodic photometric behavior resembling that of the CTTS AA Tau, when it was studied by Bouvier et al. (1999). This association between the occulting structure and accretion shocks is consistent with the scenario proposed to explain AA Tau's variability. In this scenario, the occultation events are caused by an inner disk warp, located at the base of the funnel flows that are associated with a stable accretion regime, periodically intersecting our line-of-sight. In two cases, we have also found this increase of hot spots during flux dips for stars with aperiodic light curves. This suggests that a similar mechanism is at work in these systems. These aperiodic extinction events may be caused by material lifted above the disk midplane at the base of randomly distributed accretion streams, such as the ones associated with an unstable accretion regime.

For the stars with AA Tau-like light curves, we tested the model that was proposed for AA Tau itself, to verify if it would be capable of reproducing their light curves as it did AA Tau's. This model consists of an optically thick warp in the inner circumstellar disk region of a system viewed at a high inclination. This warp occults the stellar photosphere periodically

[1] The error given corresponds to the Poisson uncertainty, defined as $\sqrt{N_{det}}/N_{tot}$, where N_{tot} is the total number of objects considered and N_{det} is the number of detections.

as the system rotates, causing flux dips in the light curve. It is a simple geometrical model, aimed at reproducing the general morphology of these light curves. This occultation model was shown to be successful at reproducing the widths and amplitudes of AA Tau-like flux dips in the light curves of most of these stars, using warp parameters that are similar to those found for AA Tau. Only one star in our initial sample of possible AA Tau-like systems (Mon-1131, which appears to be viewed at a low inclination) does not fit within the AA Tau-like scenario.

Typical ratios between the warp's maximum height h_{max} and the radius R_w at which it is located in the disk were found to be between $h_{max}/R_w = 0.2$ and 0.3. This range is consistent with the values found by Bouvier et al. (1999) for AA Tau and by Fonseca et al. (2014) for V354 Mon (Mon-660), though it is higher than the values of disk scale height traditionally used in disk models ($\sim 0.05 - 0.1R$, Bertout et al. 1988; Duchêne et al. 2010). The warp's height and azimuthal extension were shown to be variable on a timescale of days, presenting typical variations of 10 - 20% between rotation cycles. Despite the dynamic nature of this warp, there is strong evidence that it can persist over timescales of a few years. We have shown that, when this is the case, the warp maintains similar height and azimuthal extension during that time and remains at about the same radial distance.

For the few cases where the occultation model is unable to reproduce an AA Tau-like light curve using a classical inner disk warp, we have proposed a scenario in which more than one accretion funnel flow may exist in each hemisphere, as predicted for the ordered unstable accretion regime by the MHD simulations of Blinova et al. (2016). This can account for the multiple flux dips per stellar rotation seen in the light curves. In many cases, even when a single accretion column in the visible hemisphere is able to account for the main features of an AA Tau-like light curve, we observe various narrow, shallow dips alongside the deeper, broader AA Tau-like flux dips. We attribute these traits to the existence of secondary accretion streams that coexist with the main accretion funnel flows, that are also capable of lifting dust above the disk plane at other locations around the star.

We ascribe AA Tau-like light curves to a stable accretion regime, and light curves that present aperiodic extinction events to an unstable accretion regime, and have shown that a star may suffer a transition from one to the other in the few years that separate our two CoRoT observing runs. We have also shown that AA Tau-like light curves are more common among stars of intermediate to high mass within the CTTS range ($0.7M_\odot \lesssim M_* \lesssim 2.0M_\odot$) than among those of lower mass ($M_* \lesssim 0.7M_\odot$). We speculate that this aspect may be linked to stellar magnetic field configurations, but further investigation is necessary to confirm this.

Having studied these systems in detail, we then proceeded to the second part of this work, in which we searched for ejection signatures in the spectra of CTTSs and Herbig Ae/Be stars in NGC 2264. We focused on the forbidden [OI] 6300Å emission line, well-known for tracing jets and winds associated with young, accreting objects. A total of 181 CTTSs and 2 HAeBe stars, members of NGC 2264, were observed in this line with the FLAMES spectrograph.

Of these, we detected [OI] 6300Å emission in 102 CTTSs and both HAeBe stars.

Our detection rate among accreting T Tauri stars is only 56%±6%, which is low compared to previous studies of this forbidden emission line, that detected it in over 90% of CTTSs (Cabrit et al. 1990; Hartigan et al. 1995; Natta et al. 2014; Simon et al. 2016). Our detection rate is not uniform across the HR diagram, but decreases toward lower masses, reaching only 38% for $M_* \leq 0.5 M_\odot$ (the detection rate is 70% for $M_* > 0.5 M_\odot$). We find no statistical difference between the ages or radial velocities of the systems in which we detect [OI] and those in which we do not, leading us to conclude that our low detection rate probably does not reflect the existence of more than one subpopulation in NGC 2264. Since other studies have detected [OI] emission in stars of similar luminosity and mass accretion rates as ours and found [OI] line luminosities in the same range where the upper limits of our non-detections lie, we are lead to believe that we were unable to properly probe the [OI] emission of stars of low luminosity and/or mass accretion rates. This has likely lead to an observational bias, which we believe is the cause for our unusually low detection rate.

We performed a Gaussian decomposition of the [OI] line profiles and identified up to four different components: a narrow low-velocity component (NLVC), a broad low-velocity component (BLVC), a blueshifted high-velocity component (HVC), and a redshifted high-velocity component. The NLVC was detected in 72 stars (among 183 CTTSs and HAeBe stars analyzed), with an average FWHM of 20.2(±4.9) km/s and average centroid velocity (v_c) of -3.5(±8.9) km/s. The BLVC was detected in 67 stars, with an average FWHM of 52.1(±21.3) km/s and average v_c of -12.1(±20.1) km/s. The HVC was detected in 33 stars, 22 of which showed only a blueshifted HVC, 5 only a redshifted HVC, and 6 showed both a red- and blueshifted HVC. The HVC has an average FWHM of 28.3(±16.6) km/s and average $|v_c|$ of 90.9(±32.8) km/s.

We searched for correlations between the luminosity of the [OI] line and its different components and stellar parameters, and found that the luminosities of both LVCs and of the HVC all correlate with the stellar luminosity L_* and with the accretion luminosity L_{acc}. Neither the luminosity of the HVC nor of the total LVC correlates with the stellar X-ray luminosity L_X, nevertheless there is a positive correlation between L_X and the luminosities of the individual narrow and broad components of the LVC. It is not clear, however, if this correlation is real or if it is driven by an underlying correlation with the stellar luminosity, since we have also shown that L_X correlates weakly with L_*.

The HVC of the [OI] line is only detected among objects with significant infrared excess ($K - 3.6\mu m > 0.3$), in agreement with (Hartigan et al. 1995). This indicates that an optically thick inner disk is necessary to be able to power the strong bipolar jets from which this component is emitted. The NLVC, on the other hand, is detected in many sources with optically thin inner disks ($K - 3.6\mu m$ down to 0 and α_{IRAC} indices that classify the systems as naked photospheres), and has been shown to be present among systems with transition disks (Simon et al. 2016). The BLVC represents an intermediate case: it is detected in a

few systems with little infrared excess, but only rarely (less than 5% of the total number of BLVCs found are in systems with $K - 3.6\mu m < 0.2$).

We compared the [OI] line profiles of stars belonging to different groups of light curve morphology, in order to investigate the connection between photometric variability and [OI] emission. We found that the average [OI] line profiles of stars that present aperiodic photometric behavior (dominated by either flux bursts or flux dips) in their CoRoT light curves are on average broader and present much more extended blue wings than the average profiles of stars that show periodic (spot-like or AA Tau-like) behavior. These aperiodic light curves have been associated with stars accreting in an unstable regime, which generally present higher mass accretion rates and more complex stellar magnetic fields than those accreting in a stable regime. Our results indicate that these systems undergoing unstable accretion tend to present broader LVCs and stronger HVCs than the ones undergoing stable accretion, whose [OI] line profiles are dominated by the NLVC.

We have also found that the systems with light curves dominated by stable spots or flux bursts show much more pronounced HVCs in their [OI] line profile than the ones with light curves dominated by AA Tau-like or aperiodic flux dips. The average [OI] line profile of the former shows a HVC with a resolved peak, while the average profile of the latter shows only a small extended blue wing. This is consistent with a scenario in which the stars that present spot-like or flux burst dominated light curves are viewed at much lower inclinations than those with AA Tau-like or aperiodic extinction-dominated light curves, as was originally proposed as part of the interpretation of these light curve classifications.

We have seen that the NLVC tends to be broader among systems viewed at higher inclinations, in accordance with studies in other star forming regions (Simon et al. 2016). We do not identify a similar trend in the FWHM of the BLVC, however we do find a possible trend in its centroid velocity. The BLVC appears to be, on average, more blueshifted in systems viewed at lower inclinations. We also find a positive correlation between the width of the BLVC and the accretion luminosity, which was observed in the Taurus star forming region as well (Simon et al. 2016). The very blueshifted velocities of the BLVC are not consistent with this emission coming from bound gas in the inner disk, as was suggested by Rigliaco et al. (2013). Instead, our results seem to support an inner disk wind as the origin of this component.

We found narrower [OI] BLVCs and NLVCs on average than Simon et al. (2016) found in Taurus, despite their better spectral resolution. Since NGC 2264 is older than Taurus, this could be an indication that, as a system evolves, its [OI] low-velocity emission tends to come from farther out in the accretion disk. We have also found a larger fraction of NLVC/BLVC than they have, which could also reflect the evolution of the disks, since it has been shown that the NLVC is much more common than the BLVC among systems with thin inner disks, being often found in systems with transition disks.

As for the [OI] HVC, believed to originate in bipolar jets, we observe an unusual behavior

when comparing its luminosity with stellar parameters like mass or effective temperature. We have found that one group of stars show nearly constant HVC luminosities around $L_{[OI],HVC} \sim 10^{-4.7} L_\odot$ for nearly the full range of T Tauri masses ($0.3 M_\odot \lesssim M_* \lesssim 2 M_\odot$), while another group shows lower HVC luminosity, mostly $\lesssim 10^{-5.5} L_\odot$, in the same range as most upper limits of our non-detections. This bimodal behavior could indicate that we are measuring two subpopulations of NGC 2264 with slightly different characteristics, however we found no statistical difference between the ages or radial velocities of these two groups. Nevertheless, in this case, we are subject to low number statistics and therefore cannot exclude this possibility.

We have estimated the maximum velocities of the jets in our sample by deprojecting the centroid velocities of the [OI] HVCs from our line-of-sight. The jet velocities we found do not seem to correlate with any stellar or accretion properties, however we are subject to large uncertainties in the jet velocities because we do not have directly measured system inclinations. Therefore, we cannot entirely exclude the possibility that a correlation may exist with some stellar parameter, which is masked within our uncertainties. The derived jet velocities all agree, within the error bars, with the average value of $v_{jet} = 128(\pm 41)$ km/s. This value is lower than the average jet velocities measured in the younger star forming region Taurus (see Appenzeller & Bertout 2013).

Finally, we have found that, if the mass ejection rate through the jet is proportional to the [OI] HVC luminosity and the jet velocities are approximately constant (as appears to be the case among our sources), then the mechanical luminosity transported by the jet is proportional to the accretion luminosity.

6.1 Perspectives

The work that was developed during this doctoral program can be extended to other star forming regions. In 2016 another young, open cluster known as NGC 6530 (associated with M8 - the Lagoon Nebula) was targeted in a new coordinated campaign including simultaneous observations with K2 (the extended Kepler mission - another satellite based telescope aimed at high-precision, high-cadence photometry), *Spitzer* and FLAMES (in the Hα and LiI 6707Å region). This will lead to the identification of a number of new systems belonging to the different light curve classifications, allowing us to further investigate the physical mechanisms responsible for each one. We will be able to conduct tests of the inner disk warp that we previously could not, since more FLAMES spectra were observed simultaneously with high-precision photometry in NGC 6530 than had been in NGC 2264. For example, we will verify if the height of the inner disk warp scales with the mass accretion rate and how one varies as a function of the other. A proposal to map the known CTTSs and HAeBe stars in this cluster in the [OI] 6300Å line has also been approved by ESO and is awaiting execution.

The targets in NGC 6530 are of slightly larger stellar masses and earlier spectral types

than the NGC 2264 sample, with many more intermediate mass CTTSs and HAeBe stars, which will allow us to probe a region of the HR diagram that was poorly sampled in the current work. It is in this region of the HR diagram that the stars evolve from fully convective to having significant radiative cores, and the properties of the stellar magnetic field and its role in accretion/ejection processes is expected to change dramatically. We will be able to investigate how this reflects in the accretion and ejection signatures we observe.

Several intermediate mass CTTSs from both NGC 6530 and NGC 2264 have been observed with the UVES spectrograph, which contains many permitted (Hα, Hβ, HeI, NaD) and forbidden ([OI] 5577Å, [NII] 5755Å, [OI] 6300,6363Å, [NII] 6548,6584Å, [SII] 6716,6731Å) emission lines that trace accretion and ejection. A study of the simultaneous variability of these lines will allow us to characterize the physical conditions in which they are produced and test the connection between accretion and ejection.

This coordinated study of star forming regions will also be extended to the Taurus association. An observational campaign with K2 is currently underway, which will provide high quality light curves for 215 of its members. Among them, a group of 5 stars will also have spectropolarimetric observations taken with ESPaDOns at the CFHT. This technique allows one to determine the intensity and topology of the magnetic field on the stellar surface (Donati 2001; Donati et al. 2006). This will be the first time that information on the stellar magnetic field will be available for young, accreting stars together with high-precision, high-cadence photometry, since spectropolarimetric data was not possible to be obtained for either NGC 2264 or NGC 6530, due to the faintness of the sources. It is strongly believed that the stellar magnetic field is crucial in driving accretion and ejection processes in young stellar objects, therefore this new data will bring unprecedented information to light.

Appendix A

Papers resulting from this thesis

The following papers are the result of the work described in this thesis. The first paper was published by Astronomy & Astrophysics in May 2015, while the second paper (for which only the first page is shown here) has been submitted to the same journal in July 2017.

A&A 577, A11 (2015)
DOI: 10.1051/0004-6361/201425475
© ESO 2015

Astronomy & Astrophysics

CSI 2264: Probing the inner disks of AA Tauri-like systems in NGC 2264⋆,⋆⋆

P. T. McGinnis[1], S. H. P. Alencar[1], M. M. Guimarães[2], A. P. Sousa[1], J. Stauffer[3], J. Bouvier[4,5], L. Rebull[3], N. N. J. Fonseca[1,4], L. Venuti[4], L. Hillenbrand[6], A. M. Cody[3], P. S. Teixeira[7], S. Aigrain[8], F. Favata[9], G. Fűrész[10], F. J. Vrba[11], E. Flaccomio[12], N. J. Turner[13], J. F. Gameiro[14], C. Dougados[4], W. Herbst[15], M. Morales-Calderón[16], and G. Micela[12]

[1] Departamento de Física – ICEx – UFMG, Av. Antônio Carlos, 6627, 30270-901 Belo Horizonte, MG, Brazil
e-mail: pauline@fisica.ufmg.br
[2] Departamento de Física e Matemática – UFSJ – Rodovia MG 443, KM 7, 36420-000, Ouro Branco, MG, Brazil
[3] Spitzer Science Center, California Institute of Technology, Pasadena, CA 91125, USA
[4] Univ. Grenoble Alpes, IPAG, 38000 Grenoble, France
[5] CNRS, IPAG, 38000 Grenoble, France
[6] Astronomy Department, California Institute of Technology, Pasadena, CA 91125, USA
[7] University of Vienna, Department of Astrophysics, Türkenschanzstr. 17, 1180 Vienna, Austria
[8] Department of Astrophysics, Denys Wilkinson Building, University of Oxford, Oxford OX1 3RH, UK
[9] European Space Agency, 8-10 rue Mario Nikis, 75738 Paris, Cedex 15, France
[10] MIT Kavli Institute for Astrophysics and Space Research, 77 Mass Ave 37-582f, Cambridge, MA 02139, USA
[11] U.S. Naval Observatory, Flagstaff Station, 10391 West Naval Observatory Road, Flagstaff, AZ 86001, USA
[12] INAF – Observatorio Astronomico di Palermo, Piazza del Parlamento 1, 90134 Palermo, Italy
[13] Jet Propulsion Laboratory, California Institute of Technology, Pasadena, CA 91109, USA
[14] Instituto de Astrofísica e Ciências Espaciais and Faculdade de Ciências, Universidade do Porto, Rua das Estrelas, 4150-762 Porto, Portugal
[15] Astronomy Department, Wesleyan University, Middletown, CT 06459, USA
[16] Centro de Astrobiología, Departamento de Astrofísica, INTA-CSIC, PO BOX 78, ESAC Campus, 28691 Villanueva de la Cañada, Madrid, Spain

Received 5 December 2014 / Accepted 6 February 2015

ABSTRACT

Context. The classical T Tauri star (CTTS) AA Tau has presented photometric variability that was attributed to an inner disk warp, caused by the interaction between the inner disk and an inclined magnetosphere. Previous studies of the young cluster NGC 2264 have shown that similar photometric behavior is common among CTTS.
Aims. The goal of this work is to investigate the main causes of the observed photometric variability of CTTS in NGC 2264 that present AA Tau-like light curves, and verify if an inner disk warp could be responsible for their observed variability.
Methods. In order to understand the mechanism causing these stars' photometric behavior, we investigate veiling variability in their spectra and $u - r$ color variations and estimate parameters of the inner disk warp using an occultation model proposed for AA Tau. We also compare infrared *Spitzer* IRAC and optical CoRoT light curves to analyze the dust responsible for the occultations.
Results. AA Tau-like variability proved to be transient on a timescale of a few years. We ascribe this variability to stable accretion regimes and aperiodic variability to unstable accretion regimes and show that a transition, and even coexistence, between the two is common. We find evidence of hot spots associated with occultations, indicating that the occulting structures could be located at the base of accretion columns. We find average values of warp maximum height of 0.23 times its radial location, consistent with AA Tau, with variations of on average 11% between rotation cycles. We also show that extinction laws in the inner disk indicate the presence of grains larger than interstellar grains.
Conclusions. The inner disk warp scenario is consistent with observations for all but one star with AA Tau-like variability in our sample. AA Tau-like systems are fairly common, comprising 14% of CTTS observed in NGC 2264, though this number increases to 35% among systems of mass $0.7\ M_{\odot} \lesssim M \lesssim 2.0\ M_{\odot}$. Assuming random inclinations, we estimate that nearly all systems in this mass range likely possess an inner disk warp. We attribute this to a possible change in magnetic field configurations among stars of lower mass.

Key words. accretion, accretion disks – stars: pre-main sequence – techniques: photometric – techniques: spectroscopic

⋆ Based on data from the *Spitzer* and CoRoT missions, as well as the Canada France Hawaii Telescope (CFHT) MegaCam CCD, the European Southern Observatory (ESO) Very Large Telescope, and the US Naval Observatory. The CoRoT space mission was developed and operated by the French space agency CNES, with participation of ESA's RSSD and Science Programmes, Austria, Belgium, Brazil, Germany, and Spain. MegaCam is a joint project of CFHT and CEA/DAPNIA, at the Canada-France-Hawaii Telescope (CFHT), operated by the National Research Council (NRC) of Canada, the Institut National des Sciences de l'Univers of the Centre National de la Recherche Scientifique (CNRS) of France, and the University of Hawaii.

⋆⋆ Figures 21–24 are available in electronic form at http://www.aanda.org

1. Introduction

Magnetospheric accretion models account for most of the observed characteristics of classical T Tauri stars (CTTS), such as their strong ultraviolet (UV) and optical excess, as well as broad emission lines and forbidden emission lines (Shu et al. 1994; Hartmann et al. 1994; Muzerolle et al. 2001; Kurosawa et al. 2006; Lima et al. 2010). These stars have also been observed to have strong magnetic fields (Johns-Krull et al. 2001) and X-ray emission (e.g., Preibisch et al. 2005). Magnetohydrodynamics (MHD) models suggest that the stellar magnetosphere truncates the inner circumstellar disk at a distance of a few stellar radii, where the disk's matter stress equals the magnetic stress, forcing the material within this truncation radius to be accreted onto the star, following the magnetic field lines (Bessolaz et al. 2008). This forms what are called accretion columns, which are responsible for the broad emission lines observed, particularly those of the hydrogen Balmer series. When the free-falling material reaches the stellar surface, accretion shocks result in hot spots near the magnetic poles of the stars, causing the observed UV and optical excess. Part of the material from the disk can also be ejected in a disk wind, resulting in forbidden emission lines. These stars also present a strong infrared (IR) excess with regard to the photospheric flux because of the absorption and reemission at longer wavelengths of stellar radiation by the circumstellar disk.

Magnetohydrodynamics models (e.g., Kulkarni & Romanova 2009; Romanova et al. 2009, 2013; Kurosawa & Romanova 2013) have proposed that CTTS can accrete matter from their circumstellar disks through a stable or an unstable regime. In the stable regime, a misalignment between the star's magnetic field and the star's rotation axis causes the material present in the region near the disk's truncation radius to fall onto the star via two main accretion columns, following the magnetic field lines connecting the disk to the star (Fig. 1). This interaction may also lift dust above the disk midplane, creating an optically thick warp in the inner disk region near the truncation radius, located at the base of these accretion columns. At the other end of each accretion column, an accretion shock on the stellar surface results in a hot spot, located at a high latitude. Observations of the magnetic fields of CTTS have shown that this misalignment between the star's magnetic field and the star's rotation axis is common (Gregory et al. 2012).

Magnetohydrodynamics models also predict that the stellar magnetic field interacts with the disk at and near the co-rotation radius. Differential rotation between the star and the disk, and throughout the accretion columns, results in a distortion of the magnetic field lines, causing them to inflate and eventually disconnect and reconnect, restoring the original field configuration (Zanni & Ferreira 2013).

Accretion through an unstable regime occurs when Rayleigh-Taylor instabilities between an accretion disk and a stellar magnetosphere cause matter to accrete onto the star via streams or tongues in random locations around the star, causing stochastic photometric variability (see Fig. 1 in Kurosawa & Romanova 2013).

If a star undergoing stable accretion is seen at a medium or low inclination, its light curve should show periodic variability due to the modulation of its main hot spot. If it is seen at a high inclination (yet not so high that the flared outer disk completely occults the star), the inner disk warp will occult the stellar photosphere periodically, causing flux dips in the star's light curve. If a star undergoing unstable accretion is seen at a medium or low inclination, its light curve will show stochastic variability due to the many hot spots on the stellar surface (Stauffer et al. 2014). These hot spots are due to the various accretion shocks around the star. If these stars are seen at high inclinations, we can expect to observe stochastic occultations of the photosphere by dust lifted above the disk plane near the base of the accretion tongues whenever one passes in front of our line of sight, leading to light curves dominated by aperiodic extinction events. These aperiodic extinction events could also be due to occultation by dust that is lifted above the disk plane as a result of magnetorotational instabilities (Turner et al. 2010).

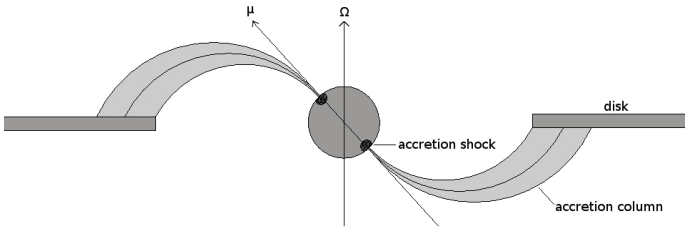

Fig. 1. When there is a misalignment between the axis of the (predominately dipolar) magnetic field (μ) and the stellar rotation axis (Ω), magnetospheric accretion may occur via the stable accretion mechanism, where two main accretion columns form at the regions where the stellar magnetic pole is closest to the disk. Two main hot spots due to accretion shocks are located near the magnetic poles.

During a study of the photometric and spectroscopic variability of the CTTS AA Tauri, conducted between 1995 and 2007 (Bouvier et al. 1999, 2003, 2007), a simple geometrical model was presented to explain the behavior of AA Tau's light curve, characterized by a relatively constant level of brightness interrupted by quasi-periodic dips of around 1.4 mag (see Fig. 9 in Bouvier et al. 1999). This variability was attributed to periodic occultations by an inner disk warp spatially associated with two major accretion columns, as in the stable accretion regime. This result provided great support for MHD models.

It is interesting to note that after over 20 years of observations often showing the same quasi-periodic behavior, AA Tau's light curve suddenly changed quite drastically when its average brightness level decreased by over 2 mag in 2011 (Bouvier et al. 2013), at which point it lost its periodicity. This indicates that, though the inner disk warp structure may be stable over the course of many years, it can disappear in a timescale of less than one year.

There are many possible scenarios in which a warp can appear within the circumstellar disk of a T Tauri star besides the one described here (see, e.g., Terquem & Papaloizou 2000; Flaherty & Muzerolle 2010). In this paper, we treat the case of CTTS, which are actively subject to ongoing magnetospheric accretion, with inner disk warps located at or near the disk's corotation radius (see discussion in Sect. 3.5). It is reasonable to assume that a warp at this location is due to the interaction between an inclined magnetosphere and the inner disk, and therefore associated with the accretion columns, as was considered for AA Tau in Bouvier et al. (2007). For the stars in this paper, we will consider this to be the main mechanism responsible for the inner disk warp.

1.1. The occultation model proposed for AA Tau

Bouvier et al. (1999) considered that the dynamic interaction between the inclined magnetic field of the star and its inner disk region would cause the material in this part of the disk to be lifted, preferentially where the stellar magnetic dipole is closest

to the disk, resulting in two arch-shaped walls located opposite to each other. This warp, located at or near the co-rotation radius (R_{co}) of the accretion disk, eclipses the stellar photosphere when it passes through the observer's line of sight. It has an azimuthal extension of ϕ_w and a maximum height of h_{max} from the disk's mid plane, which occults the stellar photosphere at phase 0.5, provoking a minimum in the light curve.

The model uses simple geometric principles to reproduce a synthetic light curve where an optically thick clump of given maximum height h_{max} and azimuthal extension ϕ_w, present at the co-rotation radius R_{co}, occults the stellar photosphere of a system seen at inclination i. The height of the clump is assumed to vary according to

$$h(\phi) = h_{max} \left| \cos\left(\frac{\pi(\phi - \phi_0)}{\phi_w} \right) \right| \quad (1)$$

for values of $-\phi_w/2 \leq \phi \leq \phi_w/2$, where ϕ_0 is the azimuth of maximum disk height. The clump height is equal to zero for all values of $|\phi| > \phi_w/2$. In the case of AA Tau, the warp found to best reproduce its light curve had a maximum height of $h_{max} = 0.3R_{co}$, and an azimuthal extension of 360°.

1.2. AA Tau-like light curves in NGC 2264

In a study of CTTS in the young cluster NGC 2264 using light curves from the CoRoT satellite (Convection, Rotation and planetary Transits, Baglin et al. 2006), various CTTS with light curves similar to that of AA Tau were found (Alencar et al. 2010). NGC 2264 is a young stellar cluster of approximately 3 Myr situated in the Orion spiral arm, around 760 pc from the Sun (for a review of the cluster, see Dahm 2008). Of the stars in the region observed by the CoRoT satellite in 2008, 301 were confirmed as members of the cluster, and of these 83 were classified as CTTS by Alencar et al. (2010).

The 83 CTTS were separated into three groups, according to the morphology of their light curves. The first group consisted of 28 periodic, nearly sinusoidal light curves, whose variabilities were attributed to long-lived cold spots; the second group consisted of 23 light curves with the same characteristics as those of AA Tau, periodic but with varying amplitude and shape of dips; and the third group consisted of 32 non-periodic light curves. Two examples of the AA Tau-like light curves, shown in full and folded in phase, can be seen in Fig. 2.

In the same study that identified these light curves, *Spitzer* IRAC single epoch photometry was used to determine whether there is dust in the inner disk region of these stars, by identifying near-infrared excess emission. Of the 83 CTTS, 68 were also observed by *Spitzer*. All of the stars with AA Tau-like light curves that were observed by *Spitzer* and CoRoT were shown to present dust in the inner disk region. This is consistent with the assumption that the photometric behavior of these stars is due to obscuration by optically thick material in their inner disks.

In order to better understand the physical processes that govern CTTS variability, a new observational campaign of NGC 2264 was organized in December 2011. The Coordinated Synoptic Investigation of NGC 2264 (CSI 2264, Cody et al. 2014)[1] is composed of simultaneous observations on fifteen telescopes (eleven ground-based and four space-based telescopes), including the CoRoT satellite, the *Spitzer* Infrared Array Camera

[1] The CoRoT and *Spitzer* light curves for all probable NGC 2264 members, as well as our broad band photometry for these stars, are available at http://irsa.ipac.caltech.edu/data/SPITZER/CSI2264.

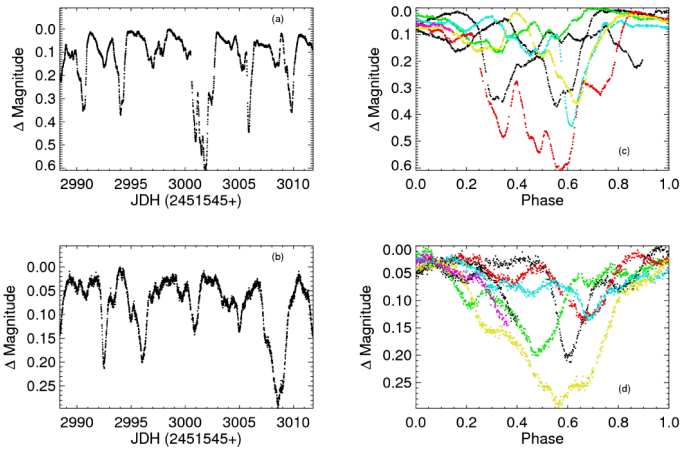

Fig. 2. Two examples of AA Tau-like light curves found for CTTS in NGC 2264 by Alencar et al. (2010). **c)** and **d)** show the light curves **a)** and **b)**, respectively, folded in phase. Different colors correspond to different rotation cycles.

(IRAC, Fazio et al. 2004), the Canada-France-Hawaii Telescope (CFHT) MegaCam (Boulade et al. 2003), and the FLAMES multi-object spectrograph on the Very Large Telescope (VLT, Pasquini et al. 2002). This campaign provided us with simultaneous photometric and spectroscopic information in a wide range of wavelengths. New CTTS were identified according to their UV excess (Venuti et al. 2014), and various new stars with AA Tau-like light curves were found, in addition to stars with newly identified types of photometric behavior (Stauffer et al. 2014, 2015).

Because of the large number of previous studies of NGC 2264, it was possible to establish reliable criteria for cluster membership, as discussed in Alencar et al. (2010). As probable cluster members, we used photometric Hα and variability from Lamm et al. (2004) following their criteria; X-ray detection from Ramírez et al. (2004) and Flaccomio et al. (2006) and location on the cluster sequence in the $(I, R-I)$ diagram, when available; spectroscopic Hα equivalent width greater than a spectral type dependent threshold (White & Basri 2003); and Hα emission line width at 10% intensity greater than 270 km s^{-1}, as proposed by White & Basri (2003) to identify accreting T Tauri stars.

In this study we present a multi-wavelength analysis of the CTTS members of NGC 2264 that appear to have extinction dominated photometric behavior. In Sect. 2 we present the observations used in this study, while in Sect. 3 we show the analysis of our data and our results. In Sect. 4 we present a discussion on the proposed cause of these stars' photometric variabilities, and in Sect. 5 we present our conclusions.

2. Observations

2.1. CoRoT data

The first CoRoT short run occurred in March 2008, when the young cluster NGC 2264 was observed for 23 days uninterruptedly. Nearly four years later, during the CSI 2264 campaign, the cluster was observed once again by CoRoT from 2011 December 1, to 2012 January 3, during the satellite's fifth short run. CoRoT's field of view is larger than the full extent of the cluster, which fits entirely into one of the CCDs designed for studying exoplanets. Stars of magnitude down to $R \sim 18$ were observed, with a cadence of 512 s. In some cases the data were

taken with exposure times of 32 s to provide high cadence light curves. All of the light curves from the first epoch were rebinned to 512 s.

CoRoT observes in a white light bandpass of approximately 3700 Å to 10 000 Å. It can, in principle, provide three-color photometry by passing the stellar light through a low-resolution spectral dispersing prism, but for the purpose of this paper we used only the integrated white light flux.

After undergoing standard CoRoT pipeline procedures, detailed in Samadi et al. (2006), the data were subsequently processed to remove unwanted effects, such as those caused by Earth eclipses, and to remove measurements affected by the South Atlantic Anomaly, using a sigma-clipping filter. Care was taken not to remove flaring events. In some cases, jumps due to detector temperature jumps were present in the photometry, and when possible they were removed manually (for more details on the correction of CoRoT light curve systematics, see Cody et al. 2014).

2.2. Spitzer IRAC data

The *Spitzer* Space Telescope mapped a region of ~0.8° × 0.8° centered at RA 06:40:45.0, declination +09:40:40, from 2011 December 3, to 2012 January 1. Targets were observed approximately twelve times a day in the IRAC 3.6 μm and 4.5 μm channels in its Warm Mission mode. Most of the objects have data from both bands, but around 40% of the objects fall near the edges of the mapping region, and only have data from one band. A staring mode was also used around the beginning of the run for a region near the center of the cluster. A cadence of approximately 15 s was obtained during four blocks of 20, 26, 16, and 19 h, on 2011 December 3, December 5, 6, December 7, 8, and December 8, 9.

The IRAC data reduction procedures and production of IRAC light curves are explained in detail in Cody et al. (2014) and Rebull et al. (2014).

2.3. CFHT MegaCam data

NGC 2264 was observed using the Canada France Hawaii Telescope's wide-field imager MegaCam (Boulade et al. 2003) between 2012 February 14 and 2012 February 28. The MegaCam's field of view spans a full 1×1 square degree, covering the cluster with only one pointing. Data were taken in the u and r bands on 30 epochs. Reduction of these data is explained in Venuti et al. (2014).

2.4. USNO data

On the order of 900 epochs of I-band photometric observations of NGC 2264 were obtained at the US Naval Observatory 40″ telescope from December 2011 to March 2012. A field of view of $23' \times 23'$, centered approximately on the cluster center, was observed. The data underwent standard reduction procedures using bias and dome flat images that were obtained at the beginning of each night. Aperture photometry was performed for all stars in each image, and a set of non-variable stars was identified in order to establish zero-points for each CCD frame and construct light curves of the targets using differential photometry.

2.5. Spectroscopy

For some stars in our sample, 20−22 epochs of VLT FLAMES spectra were obtained between 2011 December 4, and 2012 February 29. Of these, we have four to six epochs of simultaneous FLAMES spectroscopy and CoRoT photometry.

FLAMES can obtain medium- and high-resolution spectra for multiple objects over a field of view 25 arcmin in diameter. Since this is much smaller than the extent of NGC 2264, even with two pointings, only the central part of the cluster was observed (one pointing centered at RA 06:41:04.8, declination +09:45:00, the other centered at RA 06:40:58.8, declination +09:21:54). We used the HR15N grating of the GIRAFFE/MEDUSA mode, which covers Hα and Li 6707 Å with a resolution of 17 000. A few of the brighter stars were observed with the UVES (Ultraviolet and Visual Echelle Spectrograph) red mode, which covers the region from 4800 Å to 6800 Å with a resolution of 38 700. Only one of the stars treated in this paper was observed with UVES.

Where FLAMES spectra were not available, we used high-resolution Hectochelle spectra from 2004−2005 provided by Gábor Fűrész (Fűrész et al. 2006). They used the 190Å wide order centered at Hα, with a resolution of $R \sim 34\,000$. These spectra were used for eight stars.

3. Data analysis and results

3.1. Initial selection of candidates for extinction dominated light curves

Throughout this paper we are concerned with stars that present extinction events due to circumstellar material eclipsing the stellar photosphere. This requires that the stars in our sample be CTTS, with at least some optically thick dust still present in the disk. Therefore, after selecting the probable members of NGC 2264 following criteria described in Alencar et al. (2010), a subset of stars with CoRoT observations in either epoch was classified as CTTS based on the following criteria: Hα width at 10% intensity greater than 270 km s^{-1}, Hα equivalent width higher than a spectral type dependent criterion proposed by White & Basri (2003), or U-V excess greater than a spectral type dependent threshold described in Alencar et al. (2010). A new group of CTTS candidates proposed by Venuti et al. (2014) based on UV excess measured with the CFHT Megacam during the CSI 2264 campaign was also taken into consideration. We also consider the two stars Mon-56 and Mon-14132 as candidate CTTS since they have IR excess and photometric variability characteristic of the CTTS studied in this paper, though we do not have enough spectral information to classify them as CTTS and they present no considerable UV excess.

Of the ~300 confirmed members observed in 2008, we classified 95 as CTTS or CTTS candidates, 12 more than had been considered by Alencar et al. (2010). Of the ~500 confirmed members observed in 2011, 148 were classified as CTTS or candidates. Of all of these CTTS and CTTS candidates, 84 were observed in both epochs. Therefore our initial sample of possible CTTS is of 159 cluster members, observed with CoRoT in either 2008, 2011, or both. Sousa et al. (in prep.) performed an in-depth study of all of these CTTS, focusing on the VLT spectroscopy.

The CoRoT light curves of these 159 stars were separated into different groups based on their visual morphologies. This was done based solely on the CoRoT light curves, with no color information. One of these groups consists of AA Tau-like light curves, which present a relatively stable maximum brightness

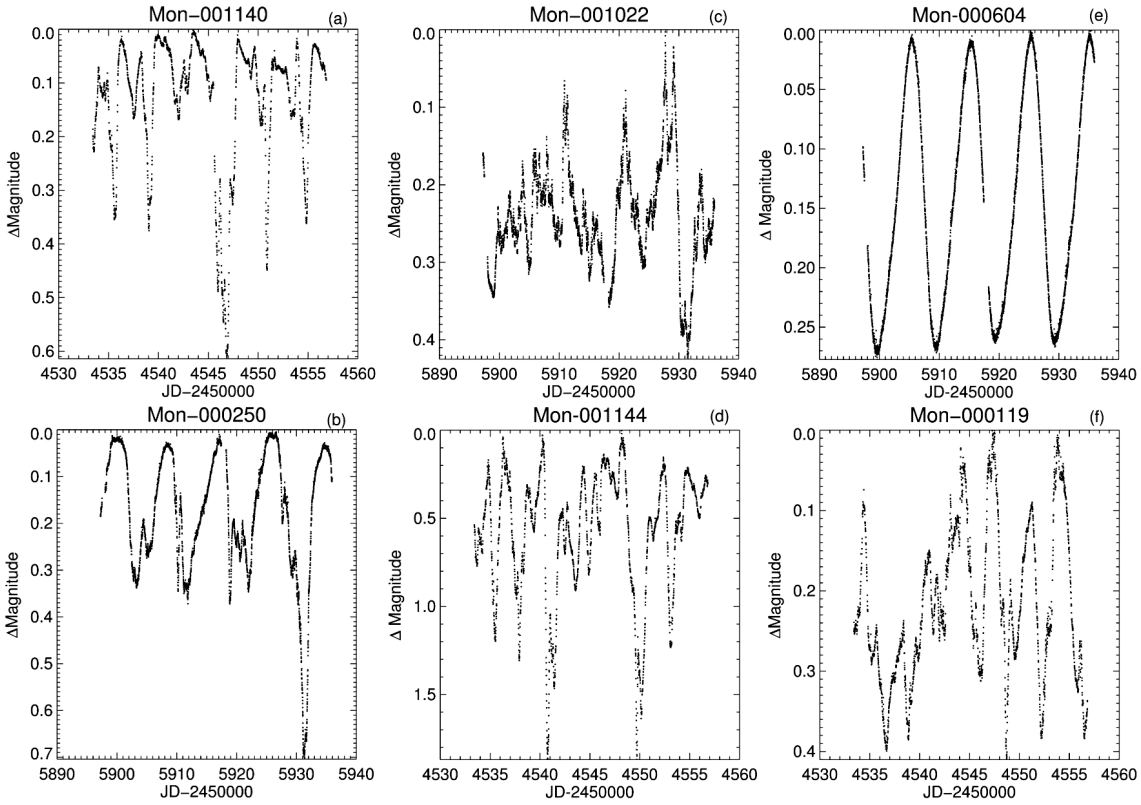

Fig. 3. Examples of different light curve morphologies found in CTTS in NGC 2264. **a)** and **b)** show periodic light curves attributed to circumstellar extinction, **c)** shows an accretion burst dominated light curve, **d)** shows a light curve dominated by aperiodic extinction, **e)** shows a spot-like light curve, and **f)** shows a light curve whose morphology is very complex, probably as a result of a combination of processes.

level interrupted by quasi-periodic flux dips that are neither spot-like nor eclipse-like in nature. The term quasi-periodic means that the flux dips present a stable period but vary in shape and/or amplitude between rotation cycles. They vary by on average 25% in width and 30% in amplitude from one rotation cycle to the next. Their periods range from 3 to 10 days and are consistent with Keplerian rotation near the co-rotation radius (see Fig. 13 and discussion in Sect. 3.5). They are usually accompanied by other narrower, shallower flux dips that are not necessarily periodic and can have significant structures within the main flux dips.

Bouvier et al. (2007) showed that the photometric behavior of the star AA Tau varied significantly between observations separated by a few years, showing at times the quasi-periodic flux dips attributed to the inner disk warp, at times more than one flux dip per stellar rotation period, and at times with almost no variability (see Fig. 15 in Bouvier et al. 2007). The light curves we have described as AA Tau-like are based on the observations of AA Tau from 1995. There are, however, some light curves that are similar to the 1995 AA Tau light curve, but that either do not have a well-defined maximum brightness, or show relatively weak periodicity (for example, see star Mon-1054 in Fig. 20). Cody et al. (2014) do not classify these as AA Tau-like light curves, but they are important in the context of this paper because they may represent systems that are undergoing events similar to those that AA Tau underwent during its other phases. Therefore, we consider stars that present these light curves in one CoRoT observation or the other to be candidate AA Tau systems along with the stars that have classical AA Tau-like light curves. We analyze their photometric variability in the same way as we do the AA Tau-like light curves, in order to establish whether the stable accretion mechanism viewed at a high inclination could also be responsible for their variability.

Another group that is of interest to this study is composed of light curves with similar characteristics to the AA Tau-like light curves, but that show no obvious periodicity. These light curves appear to be dominated by aperiodic extinction events. These two groups can easily be distinguished from the periodic, nearly sinusoidal, variability attributed to long-lived cold spots, or the nearly symmetric, narrow flux bursts described in Stauffer et al. (2014) and attributed to stochastic accretion events. A few examples of different types of variability are shown in Fig. 3. For a detailed discussion of these and other light curve morphologies, including a statistical analysis of symmetry in the flux and periodicity, see Cody et al. (2014).

Figure 4 shows the CoRoT light curve and USNO *I*-band light curve, shifted to coincide in magnitude, of two AA Tau-like stars. It is evident from this figure, though the *I*-band photometry coincides closely with the CoRoT photometry, that the lower cadence makes it difficult for AA Tau-like behavior to be identified using only ground-based data. This shows the importance of high cadence space-based photometry to better understand the phenomena that occur among these young stellar objects.

Table 1 shows information on the stars in our sample that are considered to have AA Tau-like or aperiodic extinction dominated light curves in either epoch. The CSIMon ID is an internal naming scheme devised for the CSI 2264 campaign (see Cody et al. 2014), and comprises all cluster members, candidates and field stars in the NGC 2264 field of view (for brevity, throughout the text, we eliminate 'CSI' and the leading zeros and replace, for instance, CSIMon-000250 with Mon-250). The CoRoT ID is the identification number assigned by the CoRoT satellite to all

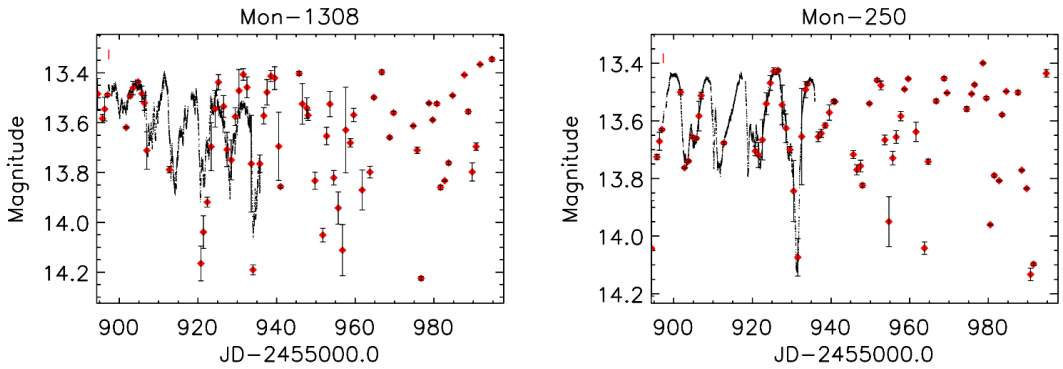

Fig. 4. *I*-band and CoRoT photometry, shifted in magnitude to coincide, for the AA Tau-like stars Mon-1308 and Mon-250. The high cadence space-based observations allow the AA Tau-like flux dips to be easily identified, while with even high quality ground-based photometry it is difficult to obtain enough information for the variability to be quantified.

objects it has observed. In some cases where the same star was observed in both epochs, two different CoRoT IDs were assigned to the same star. For these stars we present the ID from the 2008 observation. The 2MASS identification is also presented.

The sixth and seventh columns of Table 1 show how the light curve was classified in one epoch or the other. Those labeled with AAT present AA Tau-like light curves, those labeled with AATc are those that were not classified as AA Tau-like by Cody et al. (2014), but that we consider to be candidate AA Tau systems, and those labeled as Ap show aperiodic light curves. For six stars, a possible AA Tau-like variability was found in both epochs, meaning the mechanism responsible for this variability can be stable on a timescale of a few years. Four stars that present AA Tau-like variability were only observed in one epoch. There are thirteen stars that were observed in both epochs and classified as AA Tau-like in one and aperiodic in the other. Of these, five displayed AA Tau-like behavior in 2008, yet in 2011 presented aperiodic variability, while the other eight showed the opposite trend. This points to a possible change from a stable accretion regime to one of unstable accretion (or vice-versa) in a matter of less than four years. This is discussed in Sect. 3.3. Another five stars were classified as having an aperiodic extinction dominated light curve in both epochs. Five more stars with aperiodic extinction dominated light curves were only observed in 2011.

It is interesting to note that, though many stars suffered a transition between AA Tau-like and aperiodic extinction dominated light curves, no star whose light curve was classified as AA Tau-like in one CoRoT observing run was classified as spot-like in the other. This could be due to inclinations, since high inclinations would favor extinction events and possibly hide any variability due to spots on the stellar surface.

Another group of stars with what appear to be short duration extinction events present in their CoRoT light curves is studied by Stauffer et al. (2015). These stars present narrow flux dips that are generally shallower than in AA Tau-like light curves, and nearly Gaussian shaped, while AA Tau-like light curves usually show very irregularly shaped dips, often with significant structure in the minima. The narrow dip stars are periodic over timescales of tens of days, with periods that are consistent with Keplerian rotation periods of the inner disk region. Stauffer et al. (2015) argue that the inner disk warp is not adequate to explain these flux dips because of their short durations and regular shapes, and propose alternate scenarios to account for the variabilities. Two of the stars in our sample of AA Tau-like light curves are considered in their paper as well. They are Mon-56 and Mon-1131, and they present a rather complex photometric behavior. Therefore they are studied therein through different points of view, in order to investigate other possible causes for their variabilities. There are also some stars with AA Tau-like light curves that at times present these narrow flux dips along with the broader ones. These features of their light curves are also discussed in Stauffer et al. (2015).

3.2. Veiling and variability

3.2.1. Correlation between photometric variability and veiling

Veiling occurs as a result of a strong UV and optical excess produced in the accretion shocks on the stellar surface of CTTS. It is present in spectra when the hot spot caused by these accretion shocks is visible to the observer. This UV excess results in an added blue continuum to the photosphere's spectra, resulting in somewhat shallower absorption lines than those from a pure photosphere. For the CTTS in NGC 2264 for which we obtained FLAMES spectra, we measured the veiling and its variability, using the equivalent widths of the Li I 6707.8 Å and Fe I 6633.4 Å lines. These lines were chosen since they are the absorption lines with the best signal-to-noise ratio in our spectra. As veiling increases, the equivalent widths we measure will decrease.

Many of these CTTS show a certain amount of variability in their measured veiling. We verified whether there was a correlation between this variability and the photometric variability. In principle, a correlation or anti-correlation should exist in some cases, depending on the physical processes occurring on the stellar photosphere. If, for instance, the variability is due to obscuration of the photosphere by an inner disk warp that is associated with accretion columns, we can expect two possible scenarios. When the accretion shocks on the stellar surface are not visible, or the veiling is too small to be accurately measured, there will be no considerable variability in the observed line equivalent widths. If, on the other hand, accretion shocks appear in our line of sight and produce measurable veiling, they should appear along with the inner disk warp, since both are associated with the accretion columns. In this case, when the inner disk warp occults the star causing brightness minima, the veiling should increase thanks to the appearance of the hot spots caused by accretion shocks. Therefore, for an AA Tau-like light curve, the equivalent width of Li I (LiIEW) or Fe I (FeIEW) should either remain relatively constant or increase with increasing brightness. In the latter case, this could be evidence that the star's photometric

Table 1. Stars with AA Tau-like and variable extinction dominated light curves.

CSIMon ID	CoRoT ID	2MASS	RA	Dec	Sp type	LC type (2008)	LC type (2011)	P (days) (2008)	P (days) (2011)	$v \sin i$ (km s^{-1})	$\alpha_{\rm IRAC}$	$[F(\rm disk)/F(\rm star)]_{4.5\ \mu m}$
CSIMon–000056[a]	223994760	06415315+0950474	6:41:53.16	+9:50:47.4	K5	AAT	AAT	5.71	5.86	11.1 ± 2.2	–1.21	1.0
CSIMon–000126	616895876	06405783+0941201	6:40:57.84	+9:41:20.1	M0	–	Ap	–	0.35[b]	14.0 ± 2.0	–1.04	4.8
CSIMon–000250*	223980688	06410050+0945031	6:41:00.50	+9:45:03.1	K3	AATc	AAT	8.32	8.93	9.8 ± 2.2	–2.10	2.1
CSIMon–000296*	500007209	06405059+0954573	6:40:50.59	+9:54:57.3	K2	Ap	AAT	2.51[b]	3.91	17.3 ± 2.6	–2.14	1.6
CSIMon–000297*	223976747	06404516+0928444	6:40:45.16	+9:28:44.4	K2	AAT	Ap	3.16	–	30.8 ± 1.8	–2.24	1.6
CSIMon–000314	500007930	06404459+0932261	6:40:44.59	+9:32:26.2	M3	Ap	Ap	–	3.38[b]	24.0 ± 2.0	–2.61	0.7
CSIMon–000325[a]	605538641	06405934+0955201	6:40:59.34	+9:55:20.2	G5V[c]	–	Ap	–	–	–	–1.38	–
CSIMon–000358	400007959	06410673+0947275	6:41:06.73	+9:47:27.6	M3	Ap	AAT	–	5.86	–	–1.55	1.3
CSIMon–000379*	223981811	06410497+0950460	6:41:04.97	+9:50:46.1	K2	Ap	AATc	3.73[b]	3.68	25.0 ± 1.2	–1.91	2.2
CSIMon–000433	616919770	06410111+0934522	6:41:01.11	+9:34:52.2	M1	–	Ap	–	–	–	–2.05	–
CSIMon–000441*	223980048	06405809+0936533	6:40:58.10	+9:36:53.3	M2	AAT	Ap	4.06	–	–	–1.41	1.0
CSIMon–000456	616872585	06405154+0943242	6:40:51.54	+9:43:24.2	K4	–	AAT	–	5.03	19.3 ± 1.5	–1.62	2.5
CSIMon–000498*	500007120	06404750+0949289	6:40:47.50	+9:49:28.9	K3	AATc	AAT	4.23	4.28	24.1 ± 2.4	–1.41	2.9
CSIMon–000619	603402479	06411475+0934134	6:41:14.75	+9:34:13.4	K8.5	Ap	Ap	–	–	–	–1.11	11.5
CSIMon–000654*	500007610	06405949+0929517	6:40:59.50	+9:29:51.7	M3	AATc	Ap	4.66	–	18.0 ± 3.0	–0.92	–
CSIMon–000660*	223980693	06410051+0929159	6:41:00.51	+9:29:15.9	K4	AAT	AAT	5.25	5.25	21.4 ± 2.5	–1.72	3.4
CSIMon–000667*	223987997	06412878+0938388	6:41:28.78	+9:38:38.8	K3	Ap	Ap	–	–	24.0 ± 2.0	–0.54	1.5
CSIMon–000717	616943877	06411511+0926443	6:41:15.11	+9:26:44.3	M0.5	–	Ap	–	–	–	–1.43	1.4
CSIMon–000774[†]	223980264	06405884+0930573	6:40:58.84	+9:30:57.3	K2.5	AAT	Ap	3.46	–	30.7 ± 1.3	–1.25	2.1
CSIMon–000811*	500007460	06404321+0947072	6:40:43.21	+9:47:07.2	K6	Ap	AAT	–	7.88	13.5 ± 1.7	–1.08	3.0
CSIMon–000824*	223981023	06410183+0938411	6:41:01.84	+9:38:41.1	K4	AAT	–	7.05	–	14.8 ± 1.4	–2.02	–
CSIMon–000928*	223987178	06412562+0934429	6:41:25.62	+9:34:43.0	M0	AAT	Ap	9.92	–	20.1 ± 2.8	–1.11	1.4
CSIMon–001037	223973200	06403086+0934405	6:40:30.86	+9:34:40.5	K1	Ap	Ap	–	8.93[b]	32.0 ± 3.0	–1.29	11.3
CSIMon–001038	602095739	06402262+0949462	6:40:22.62	+9:49:46.3	M0	–	Ap	–	–	–	–1.73	3.0
CSIMon–001054*	400007538	06403652+0950456	6:40:36.52	+9:50:45.6	M2	Ap	AATc	–	4.08	20.4 ± 2.0	–1.10	2.0
CSIMon–001131	223957455	06393441+0954512	6:39:34.41	+9:54:51.2	M2	Ap	AAT	5.15[b]	5.18	8.8 ± 1.7	–1.38	1.4
CSIMon–001140	223959618	06394147+0946196	6:39:41.47	+9:46:19.7	K4	AAT	AAT	3.87	3.90	19.8 ± 2.3	–2.37	0.8
CSIMon–001144*	223971231	06402309+0927423	6:40:23.09	+9:27:42.3	K5	Ap	Ap	–	–	24.0 ± 3.0	–1.73	3.75
CSIMon–001167*	400007528	06403787+0934540	6:40:37.87	+9:34:54.0	M3	Ap	AATc	8.30[b]	8.78	11.3 ± 2.1	–1.87	1.2
CSIMon–001296	223948127	06390374+0940234	6:39:03.75	+9:40:23.4	K7	Ap	AAT	–	9.75	11.0 ± 1.6	–1.47	–
CSIMon–001308	223964667	06395924+0927245	6:39:59.24	+9:27:24.5	M0	AAT	AAT	6.45	6.68	9.9 ± 2.0	–1.87	0.7
CSIMon–006986	223950070	06390996+1005127	6:39:09.96	+10:05:12.7	K7:M1	AATc	–	6.16	–	–	–1.22	–
CSIMon–014132[a]	602070634	06390355+0916159	6:39:03.55	+9:16:16.0	M3.5	–	AAT	–	4.48	–	–1.50	–

Notes. The first three columns show the identification of each star using our internal CSI 2264 naming scheme, the identification assigned to each star by the CoRoT satellite, and the respective 2MASS identification. In the cases where a star was observed twice by CoRoT and assigned a different identification in each epoch, we use the one given in the first epoch. An asterisk following the CSIMon ID indicates that we have FLAMES/GIRAFFE spectra, and a dagger indicates that we have FLAMES/UVES spectra, both simultaneous with the second CoRoT epoch. The fourth and fifth columns show each star's coordinates, and the sixth column shows their spectral types, taken from Venuti et al. (2014), except where specified. The seventh and eighth columns show the classification given to the light curve (LC) in each epoch (2008 March observations and 2011 December observations). The ninth and tenth columns show the periods that were measured for each CoRoT light curve in the first (2008) and second (2011) epochs. The eleventh column shows the values of projected rotational velocity $v \sin i$ measured using FLAMES spectra when available, or Hectochelle spectra otherwise. The twelfth column shows the $\alpha_{\rm IRAC}$ index calculated for each star, which corresponds to the slope of the spectral energy distribution between 3.6 μm and 8 μm. The thirteenth column shows the ratio of disk flux to stellar flux at 4.5 μm, estimated from each star's SED. [(a)] There is not enough spectral information to classify these stars as CTTS, though they have IR excess and show variability characteristic of CTTS. [(b)] Low probability periods found during a periodogram analysis of the light curves. [(c)] Spectral type from Young (1978).

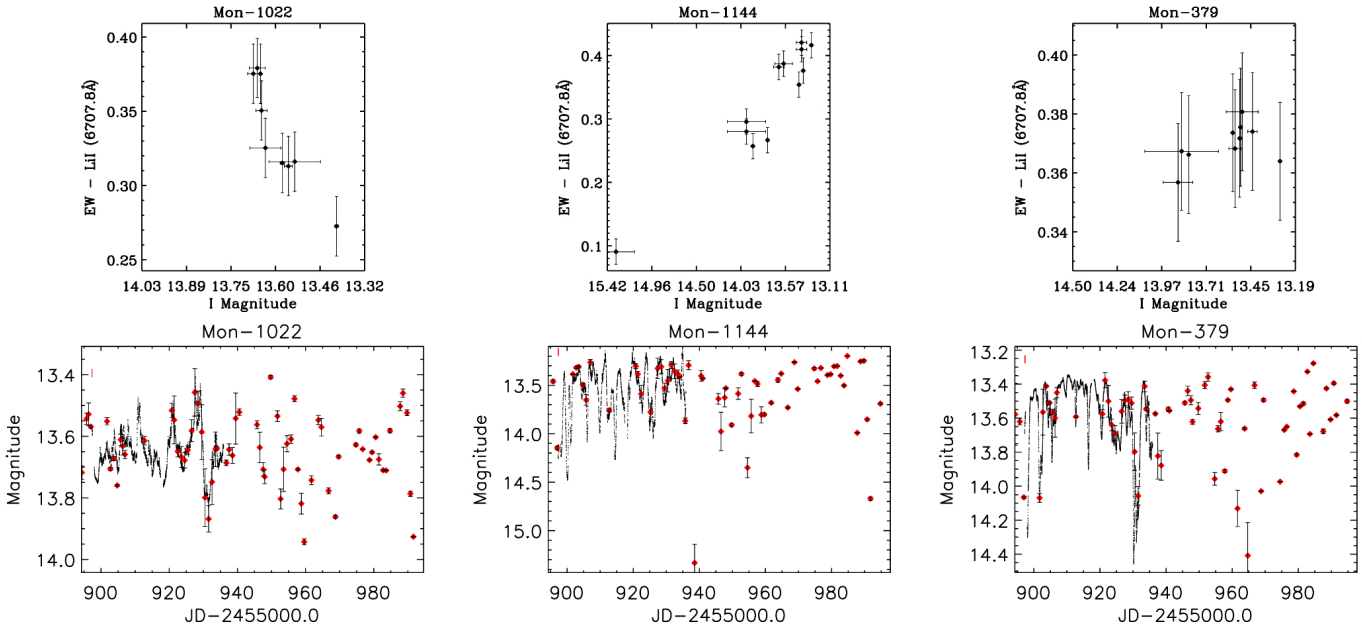

Fig. 5. *Top*: LiIEW vs. *I* magnitude for three different stars. *Bottom*: *I*-band and CoRoT light curves, shifted in magnitude to coincide, of the same three stars. *Left panels*: the star has an accretion-burst dominated light curve, and veiling variability that supports the variable accretion scenario. *Middle panels*: the star has a light curve that presents aperiodic extinction events, and veiling variability that supports a scenario in which the occulting structures are associated with accretion shocks. *Right panels*: the star has a light curve with AA Tau-like characteristics, while its near lack of veiling variability can neither confirm nor refute the hypothesis that it is an AA Tau-like system.

variability is due to obscuration by an inner disk warp that is spatially associated with the accretion columns.

For photometric variability that is due mainly to a configuration of hot spots on the stellar surface, the veiling should increase with increasing brightness, and therefore FeIEW and LiIEW should decrease with increasing brightness. This is the case for the accretion-driven flux bursts discussed by Stauffer et al. (2014). The reoccurring narrow increases in brightness are likely due to an increase in accretion luminosity and are therefore associated with an increase in veiling.

If the star's photometric variability is due simply to the rotational modulation of a stable, cold spot on the photosphere, the veiling would not be expected to vary, since cold spots do not cause veiling.

Measures of veiling using the FeI 6633.4 Å line are much less accurate than LiI 6707.8 Å, since it is shallower in these stars and therefore suffers more from noise in the spectra. For this reason veiling was only measured using FeI for a small subset of these stars with FLAMES spectroscopy. In these cases the observed tendencies agree with those determined using the LiI line.

We made plots of LiIEW vs. USNO *I*-band magnitudes for the stars in our sample where both data were available. The *I*-band light curves were used rather than the CoRoT light curves because they had better time coverage, despite the lower cadence. There are at most six FLAMES spectra of each star obtained simultaneously with the CoRoT observations, whereas the USNO observations spanned the entire FLAMES campaign. In order to construct the plots, *I*-band measurements taken on the same night were averaged and matched with the equivalent width found using the FLAMES spectrum taken on that night. The USNO and VLT are separated by little more than 40° in longitude, so the observations were likely taken within a few hours of each other on most nights.

Figure 5 shows plots of LiIEW vs. *I*-band magnitudes (top panels) for three different examples, along with the corresponding CoRoT and *I*-band light curves (bottom panels). The left panels of Fig. 5 show a star whose veiling increases with increasing brightness. We can see from its light curve that it is dominated by flux bursts attributed to variable accretion events. The middle panels of Fig. 5 show a star whose veiling increases with decreasing brightness, a tendency we attribute to occultation of the photosphere by an inner disk warp associated with the accretion mechanism. Its light curve morphology shows variability that could be explained by this scenario. The right panels of Fig. 5 show a star whose veiling does not vary considerably, which can mean the photometric variability is due to a configuration of cold spots on the surface, or to obscuration by an inner disk warp that either fully occults the accretion shocks associated with it, leaving the veiling unaltered during eclipses, or the accretion is relatively low, and only a small hot spot is present, not capable of generating a large UV excess or veiling. The light curve agrees with the inner disk warp scenario, since cold spots would result in a much more regular photometric variability, but the veiling can neither confirm nor disprove this hypothesis. This star also presents little UV excess, consistent with either of these scenarios.

The star Mon-811 was outside the USNO field, and therefore we have no *I*-band information for it. For this one star, we made a plot of LiIEW vs. CoRoT flux counts instead. This plot was not nearly as well sampled, since very few FLAMES spectra were taken during the CoRoT observations, but it shows a tendency similar to the middle panels of Fig. 5.

Figure 6 shows plots of LiI equivalent width vs. *I* magnitude for some of the AA Tau-like or aperiodic extinction stars in our sample (plots of the missing stars can be found in Fig. 21). In many cases the veiling variability is very irregular, and we cannot see a clear pattern (e.g., Mon-498). For the star Mon-379 (shown in the right panels of Fig. 5), the veiling is relatively constant. For six stars, we see an apparent decrease in veiling

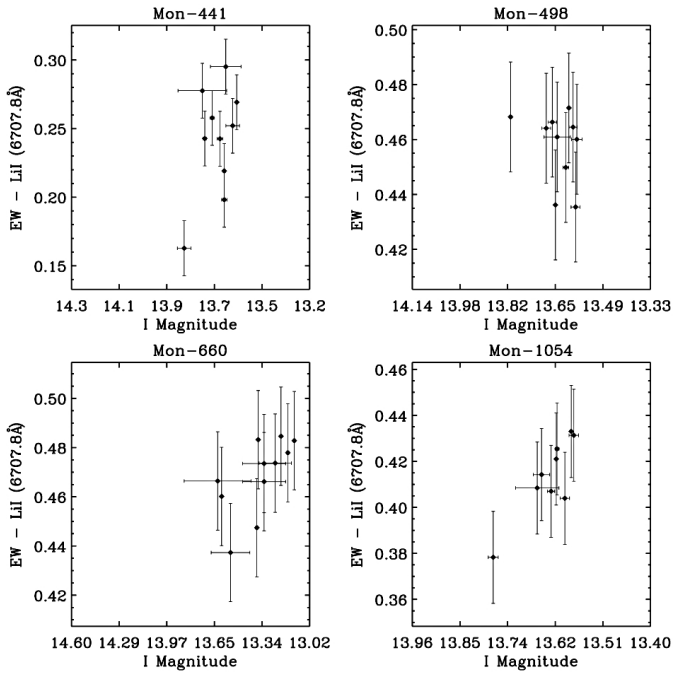

Fig. 6. LiIEW vs. *I* magnitude for some of the stars in our sample. The star Mon-1054 is an example of a candidate AA Tau system that shows increasing LiIEW with decreasing magnitude. The star Mon-441 shows similar behavior, though its photometric behavior is aperiodic. The star Mon-660 is an AA Tau-like system that appears to show increasing LiIEW with decreasing magnitude, though the uncertainties are quite large, and the star Mon-498 is an example of a system with very irregular veiling that shows no obvious pattern.

(increase in LiI equivalent width) as the star's brightness increases, which could indicate that the mechanism responsible for their photometric variability is obscuration by an inner disk structure associated with accretion columns. This is the case for Mon-250, Mon-441, Mon-660, Mon-811, Mon-1054, and Mon-1144. The last has the largest variability amplitude in veiling (~0.3 Å), meaning there should be significant hot spots on the stellar surface. It is the star with the highest UV excess among the stars in our sample where veiling was measured, which could be expected, since the hot spots associated with the accretion shocks on the surface of the star should produce a considerable UV excess when visible.

Two of the stars that show an increase in veiling during the minima in their light curves have aperiodic photometric variability (Mon-441 and Mon-1144). This provides support for our hypothesis that the occultations in these light curves are caused by dust lifted above the disk plane at the base of unstable accretion streams, since these should be associated with accretion shocks on the stellar surface in a manner analogous to the stable accretion funnels. If these stars are undergoing unstable accretion, they should show no obvious periodicity in their light curves, but if they are seen at high enough inclinations, they should share other similarities with AA Tau-like systems, such as the one we see here.

3.2.2. The specific case of Mon-250

We analyzed the Hα line profile of the star Mon-250 during different rotational phases (Fig. 7b), and note a redshifted absorption component (indicated by an arrow in the figure) that appears in several spectra during the light curve minima that is not present in other phases. This is clear evidence that the accretion

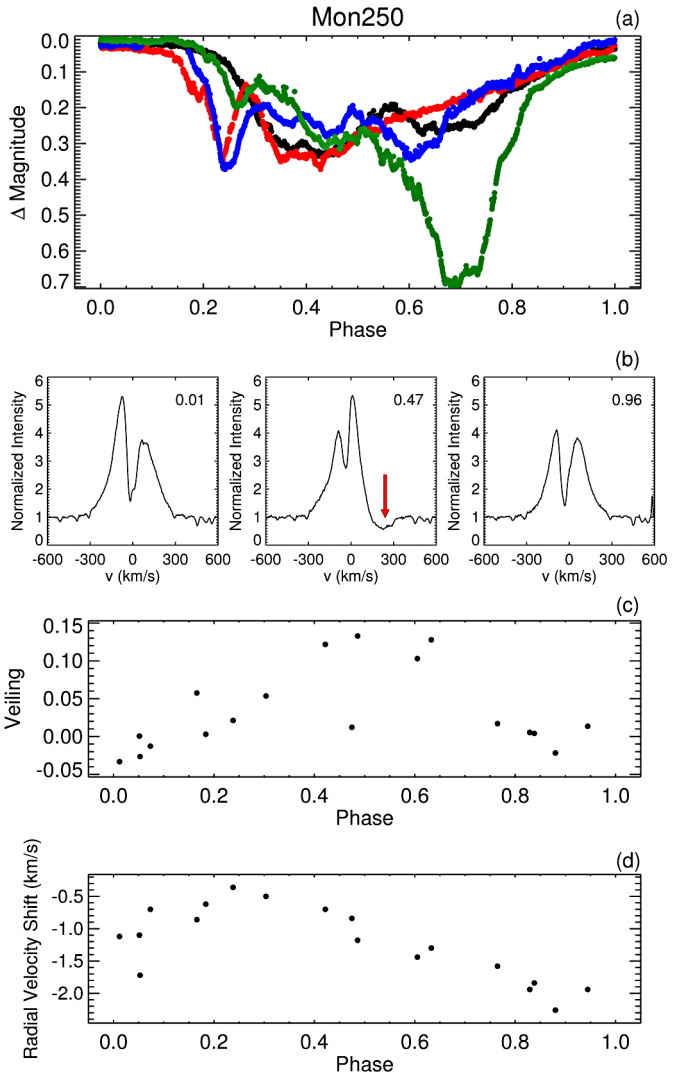

Fig. 7. Mon-250. **a)** 2011 CoRoT light curve folded in phase. **b)** Hα line profile during different rotational phases, indicated in each panel. A redshifted absorption component seen only near phase 0.5 is indicated by a red arrow. **c)** Measured veiling folded in phase. **d)** Shift in radial velocity measured from photospheric lines in the spectra, folded in phase. In all four panels, the same period of 8.6 days, determined from the radial velocity variation of photospheric lines, was used to calculate the phase. The same initial date was also used.

funnel and hot spot appear in front of our line of sight during the photometric flux dips, since the infalling material responsible for the absorption is moving away from us.

This star's veiling variability also points to the appearance of accretion shocks during occultations. For this particular star, we were able to measure veiling in all 20 FLAMES epochs by comparing line depths to those of a weak line T Tauri star of the same spectral type, to determine what fraction of the observed continuum should be due to the hot spot. Figure 7c shows a plot of veiling folded in phase, using the rotation period determined from radial velocity shifts of photospheric lines in the spectra (Fig. 7d). It can be seen that there is almost always an increase in veiling as the light curve undergoes a minimum in brightness. This is evidence of the appearance of a hot spot on the stellar surface, one large enough to produce measurable veiling, during occultations. The rotation period found from the variability of radial velocities measured in the Mon-250 photospheric lines was of 8.6 ± 0.5 days, consistent with the period

found from the CoRoT light curve observed at the same epoch of 8.93 ± 0.50 days. This shows that the occulting structure is located at or near the disk's co-rotation radius, as was the case for AA Tau. Unfortunately, this type of analysis was only possible for this star since it was the only one with a high enough variability amplitude in veiling and radial velocity of photospheric lines to draw significant conclusions.

We attribute these phenomena, which were also observed for AA Tau (Bouvier et al. 2007), to the appearance of a major accretion funnel and accretion shock associated with it, at the moment of occultation by the inner disk warp. This shows the association between the inner disk warp and the stable accretion columns, and provides support to our hypothesis that in these cases, the same interaction between the inclined stellar magnetic field and the inner disk that is causing the material to accrete onto the star via two major accretion columns is also responsible for lifting dust from the disk plane, creating a warp in the disk near the co-rotation radius.

3.3. Stable and unstable accretion regimes

In this section, we discuss the main differences between the quasi-periodic AA Tau-like stars and the stars whose light curves are dominated by circumstellar extinction, but have no obvious periodicity. We propose that the former may be undergoing accretion via a stable regime, while the latter could be accreting via an unstable regime. Kurosawa & Romanova (2013) cite the parameters that are important in determining through which of these regimes a star will accrete. They are mass accretion rate ($\dot{M}_{\rm acc}$), truncation radius, stellar rotation rate, the inclination angle β between the stellar rotation axis and the axis of the magnetic field (Ω and μ, respectively, in Fig. 1), and the α-parameter, which describes viscosity in the disk.

Kurosawa & Romanova (2013) mention a possible transition between regimes, which can occur if one or a few of the factors that determine instability change with time within a certain system. For instance, if the truncation radius $R_{\rm mag}$ becomes smaller than the co-rotation radius $R_{\rm co}$, due for example to a change in the stellar magnetic field, accretion flows tend to become unstable. The mass accretion rate can also affect the ratio $R_{\rm mag}/R_{\rm co}$, since a higher mass accretion rate leads to a smaller truncation radius, therefore leading to a more unstable configuration. The viscosity parameter (α) controls the global mass accretion rate. The higher α is, the higher the mass accretion rate is, leading to more instabilities. According to Kulkarni & Romanova (2009), the transition from a stable to an unstable regime occurs around critical values of mass accretion rates. They state typical critical values for stars with $R_{\rm mag} \approx 2{-}3R_*$ to be around $\dot{M}_{\rm acc} = 1.7 \times 10^{-7}$, and for stars with $R_{\rm mag} \approx 4{-}5R_*$, around $\dot{M}_{\rm acc} = 2.1 \times 10^{-8}$.

A smaller angle β also leads to less stable configurations, since at large β the magnetic poles become closer to the inner disk rim, lowering the potential barrier in the vertical direction that the material must overcome to be lifted into the accretion funnels. According to Kulkarni & Romanova (2009), values of $\beta > 25°$ usually lead to stable configurations (see also Romanova et al. 2014).

Venuti et al. (2014) showed that mass accretion rates in CTTS can vary considerably over time. They calculated mass accretion rates for stars in NGC 2264 using data from 2010 December and 2012 January, the latter being nearly simultaneous with the CoRoT observations. They show that many of the stars in our sample had mass accretion rates vary by up to 50% in

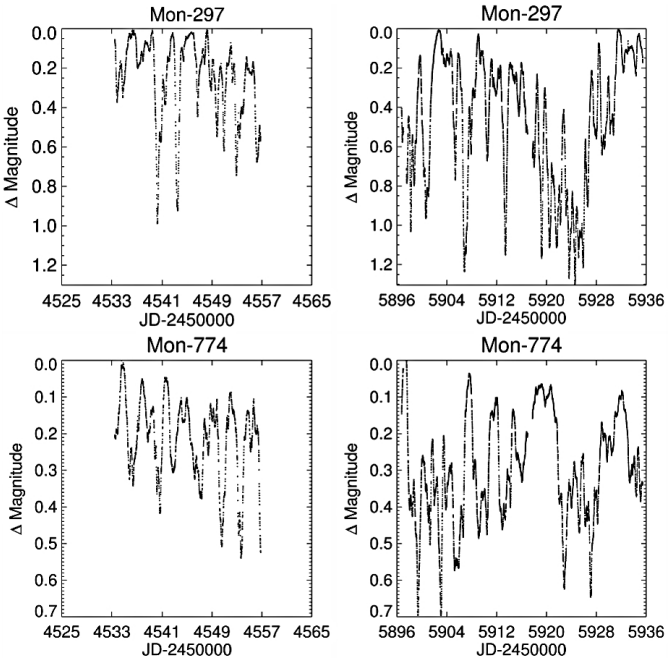

Fig. 8. CoRoT light curves of Mon-297 and Mon-774 during their AA Tau phases (*left*) and aperiodic phases (*right*).

little over one year. Unfortunately, there is no estimate of mass accretion rate simultaneous with the 2008 CoRoT observations, but it is possible that a variation such as this contributed to a transition between accretion regimes. However, Venuti et al. (2014) also show that long term changes in mass accretion rates are not necessarily larger than short term changes.

Magnetic field configurations may also be responsible for these transitions. It is possible for the magnetic field of a CTTS to change significantly in a few years. This has been observed, for example, in the CTTS V2129 Oph (Donati et al. 2011). Its magnetic field was measured in two different epochs, nearly four years apart, and the magnetic field strength varied greatly from one epoch to the other. The dipolar component was found to be about 3 times stronger in the second epoch, and the octupolar component 1.5 times stronger than four years earlier. Donati et al. (2011) found that the ratio $R_{\rm mag}/R_{\rm co}$ nearly doubled in that time.

In this study we have seen that $38\%^{+14\%}_{-11\%}$ (5/13) of the stars that were observed in 2008 as having photometric variability similar to AA Tau were observed again in 2011, showing aperiodic variability due to extinction from circumstellar material. Of the stars that were observed in 2008 as having aperiodic photometric variability due to circumstellar extinction, $62\%^{+11\%}_{-15\%}$ (8/13) were observed again in 2011, then showing variability similar to AA Tau. If our proposed scenario is true, then this points to a transition from a stable to an unstable accretion regime, or vice-versa, in a matter of less than four years, for $57\%^{+9\%}_{-11\%}$ of our sample of possible AA Tau-like stars, i.e., (5+8)/23. An example of two of the stars that appear to have undergone this transition is shown in Fig. 8.

We also performed a periodogram analysis of the light curves of these 13 stars that changed between periodic and aperiodic photometric behavior. The periodograms of each epoch were analyzed separately and compared. For 11 stars, during the epoch of unstable accretion at least a weak signal was present at the period found for the AA Tau phase, believed to be the stellar rotation period. For eight of these, this peak was the only one

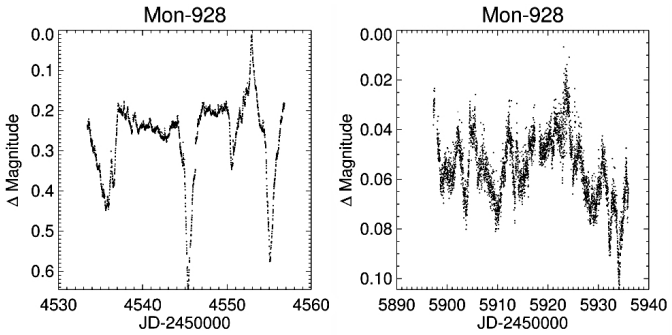

Fig. 9. CoRoT light curves of Mon-928 in 2008 (*left*) and 2011 (*right*).

present, or the strongest, despite being much weaker than the one present during the AA Tau phase. One exception is the star Mon-441, which shows a weak signal during its unstable phase, but this signal does not correspond to the period found in the AA Tau phase, or to a multiple of it.

In most cases the variable depths of the flux dip amplitude in a star's light curve during its aperiodic phase are smaller than those measured in its AA Tau phase by 20% to 60%. However, for 4 of the 13 stars that underwent a transition between AA Tau-like and aperiodic light curve, the flux dip depths remained nearly the same in both epochs, and for 2 more stars the variability amplitude during their aperiodic phase was larger by 20% to 30%. This means that, at least in some cases, during the unstable accretion phase dust must be lifted above the disk plane at similar, and sometimes even higher, altitudes as during the stable accretion phase.

As for the star Mon-928, the flux dips present in 2008 disappear entirely in 2011. The light curve we observe in the second epoch is not characteristic of circumstellar extinction. The period of 9.92 days found during the first epoch is very similar to periods previously measured for this star in the literature (Lamm et al. 2005), yet it is non-existent in the 2011 light curves (see Fig. 9). One possibility is that in 2011 the inner disk warp did not reach high enough altitudes above the disk to occult the stellar photosphere. At the inclination of 71° found by us for this system (see Sect. 3.5), our simulations using the occultation model show that if the warp found to best reproduce the 2008 CoRoT light curve decreases in height by at least 26%, the occultations observed in 2008 would no longer occur. This amount of variation in warp height is well within the range we observe for these objects (see Sect. 3.5). This star is also one of the two that appear to have undergone a small increase in mass accretion rate from 2010 December to 2012 January (Venuti et al. 2014); therefore, it is possible that a higher mass accretion rate led to a more unstable configuration during the 2011 observations, resulting in a less pronounced disk warp.

Kurosawa & Romanova (2013) also predict that for a more unstable regime, one should observe a higher frequency of flux peaks per stellar rotation period in the light curves of stars of medium or low inclinations thanks to the presence of a larger number of accretion shocks on the photosphere. It is fair to assume that, for systems seen at high inclinations, a higher frequency of flux dips would also be observed for more unstable scenarios because of the larger number of accretion streams present around the star, whose base could contain dust that can occult the photosphere. Of the stars in our sample that changed from one regime to the other, most show two to three flux dips per stellar rotation period during the unstable accretion phase, while some show up to seven flux dips per rotation period. This may be an indication of the degree of instability of each star-disk system. The two stars that show the highest frequencies of flux dips during their unstable accretion phases are the two that have the lowest masses in our sample of possible AA Tau-like stars. As is discussed in Sect. 3.7, low mass stars appear to present more unstable accretion, possibly as a result of magnetic field configurations. These higher frequencies of flux dips can also be caused by dust lifted above the disk plane because of magnetorotational instabilities that do not necessarily lead to accretion streams (Turner et al. 2010; Hirose & Turner 2011).

Of the 23 stars that present AA Tau-like behavior, only six maintain this behavior in both 2008 and 2011. Many appear to show some signs of weak instability even during their AA Tau phase, sometimes presenting two or three flux dips in one rotation cycle. A few examples are Mon-297, Mon-456, and Mon-824 (Fig. 10). Most show many small secondary flux dips present in the light curve, indicating a possible coexistence of secondary accretion streams with the main accretion funnels.

3.4. Comparing optical and infrared light curves

Of the 33 stars in our sample of AA Tau-like or aperiodic extinction dominated CoRoT light curves, 29 were observed almost simultaneously with *Spitzer* in mapping mode. Figure 11 shows a few examples of *Spitzer* IRAC 3.6 μm and 4.5 μm light curves, plotted along with the respective CoRoT light curves. The CoRoT flux was transformed into magnitude using its greatest value as magnitude zero, then shifted to overlap the *Spitzer* IRAC data. Figure 22 shows the light curves of all other stars in our sample.

We see that 4 of the 29 stars show very similar behavior in both bands, and present AA Tau-like modulation in the infrared as well as the optical. These stars are Mon-660, Mon-811, Mon-1140, and Mon-1308. Another five show similar behavior, with minima and maxima generally coinciding in the infrared and optical, but these light curves do not overlap perfectly. These are Mon-297, Mon-314, Mon-433, Mon-441, and Mon-456.

There are nine stars that correlate in some parts of their infrared and optical light curves, while other parts behave differently, or even anti-correlate at times. Stars Mon-56, Mon-126, Mon-358, Mon-654, Mon-717, Mon-774, Mon-1054, Mon-1144, and Mon-1167 show this behavior. The 10 stars Mon-296, Mon-325, Mon-379, Mon-498, Mon-619, Mon-667, Mon-928, Mon-1037, Mon-1038, and Mon-1131 have entirely different infrared and optical light curves, with very little or no features in common.

The star Mon-250 has *Spitzer* IRAC light curves that almost anti-correlate with its CoRoT light curve. Most of the *Spitzer* IRAC maxima coincide with CoRoT minima, meaning this variability cannot possibly be the consequence of a hot or cold spot on the stellar surface, since any variability on the surface should be present in all wavelengths. To explain why there is more IR emission during the optical eclipses, we propose the following scenario. The stable accretion regime assumes that there are two main accretion funnels opposite each other, one in each hemisphere. Each of these funnels is associated with a hot spot on the stellar surface, where the accretion shock is located. The base of each accretion funnel is associated with part of the inner disk warp. When one part of the warp occults the stellar photosphere in our line of sight, the hot spot opposite it, as well as the rest of the stellar photosphere on that side of the star, illuminates the corresponding part of the inner disk warp. The dust located there absorbs the light from the hot spot and photosphere and reemits it at longer wavelengths, causing an increase in emission

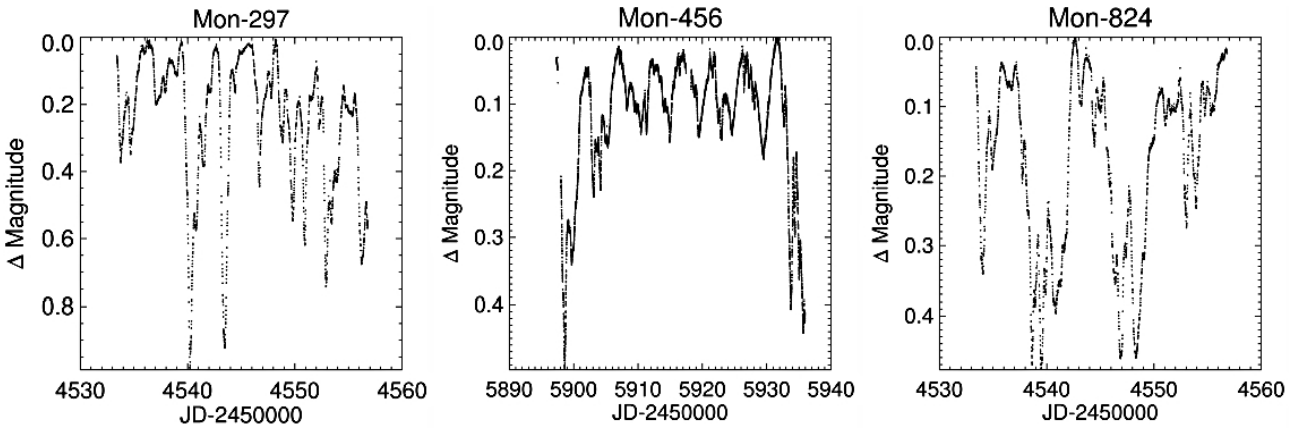

Fig. 10. CoRoT light curves of Mon-297, Mon-456, and Mon-824 during their AA Tau phase. These stars sometimes present two, or even three, flux dips per rotation period, and often secondary flux dips are present alongside the main flux dips, indicating a possible coexistence between unstable accretion streams and stable accretion funnels.

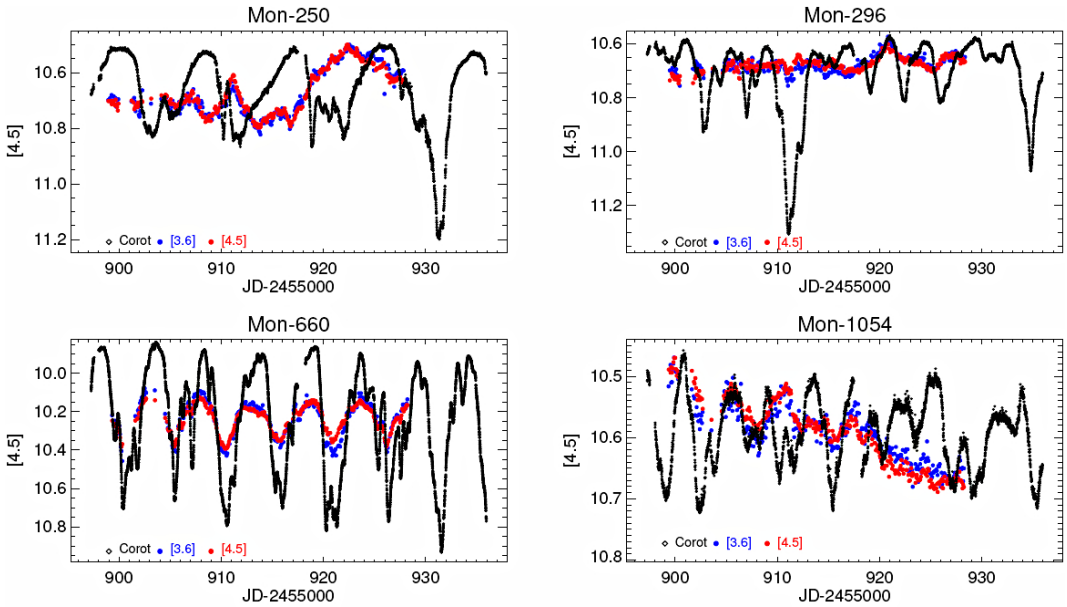

Fig. 11. *Spitzer* IRAC 3.6 μm and 4.5 μm light curves (blue and red filled circles, respectively) overplotted on CoRoT light curves (black circles). The CoRoT and IRAC 3.6 μm light curves were shifted in magnitude for easier comparison.

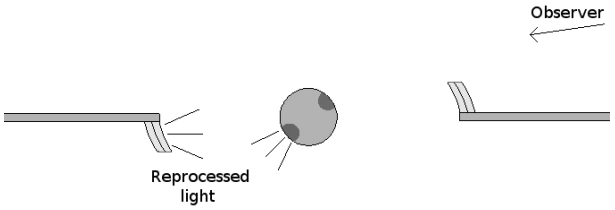

Fig. 12. When one side of the inner disk warp occults the stellar photosphere, the hot spot and photosphere on the opposite side illuminate the part of the warp on that side. The light is absorbed by the dust and is re-emitted at longer wavelengths.

in the infrared (Fig. 12). This emission in the infrared is predicted by the radiation transfer model of Whitney et al. (2013) when applied to an accretion hot spot associated with an inner disk warp. This behavior is also observed in a few other light curves, during one or two rotation cycles (see, e.g., Mon-1054 in Fig. 11, between MJD 55 909 and MJD 55 913).

The $\alpha_{\rm IRAC}$ index is a good indicator of the amount of dust present in the inner accretion disk. It corresponds to the slope of the spectral energy distribution (SED) between 3.6 μm and 8 μm. Unfortunately, there were no *Spitzer* IRAC observations in 8 μm simultaneously with the 2011 CoRoT-*Spitzer* campaign, since by this time *Spitzer* was already operating in its warm mission. We do, however, have $\alpha_{\rm IRAC}$ values from Teixeira et al. (2012) for 14 of these 29 stars with simultaneous CoRoT and *Spitzer* light curves, and archival IRAC and Multiband Imaging Photometry for *Spitzer* (MIPS) data (for details see Cody et al. 2014), which enabled us to calculate values of $\alpha_{\rm IRAC}$ for the stars that were not included in Teixeira et al. (2012). These values are given in Table 1. Lada et al. (2006) established a criterion to classify the inner disk structures of systems according to the $\alpha_{\rm IRAC}$ index. Stars with $\alpha_{\rm IRAC} < -2.56$ are classified as naked photospheres (systems devoid of dust within a few 0.1 AU), those with $-2.56 < \alpha_{\rm IRAC} < -1.80$ have anemic disks (their inner disk region is optically thin), those with $-1.8 < \alpha_{\rm IRAC} < -0.5$ have optically thick inner disks, stars with $-0.5 < \alpha_{\rm IRAC} < 0.5$ are flat

spectra sources, and stars with $\alpha_{\rm IRAC} > 0.5$ are Class I protostellar objects.

We note that the objects in our sample whose CoRoT and *Spitzer* light curves correlate best have values of $\alpha_{\rm IRAC}$ between -1.4 and -1.9, meaning they are generally in the transition region between optically thin and optically thick inner disks. If there is too much dust within a few AU of the star (higher values of $\alpha_{\rm IRAC}$), the *Spitzer* light curves would be dominated by emission from warm circumstellar dust, rather than eclipses of the stellar photosphere. On the other hand, if the portion of the disk occulting the star is not optically thick, then the flux dips at IRAC wavelengths could be much shallower than for the case where we assume optically thick absorption at all bands. This seems to be the case for Mon-296, whose *Spitzer* light curve remains relatively steady except for a very shallow dip occurring at the same time as the optical light curve's lowest minimum, and a small burst near one of its maxima (top right panel in Fig. 11). This star's $\alpha_{\rm IRAC}$ shows that it has an anemic disk. The star Mon-250, mentioned in the discussion above, also has an anemic disk. It has a value of $\alpha_{\rm IRAC} = -2.10$, one of the lowest in our sample.

Another useful quantity is the ratio of the disk flux to the stellar flux at 4.5 μm, estimated from the slope of each star's SED as compared to an estimate of the photospheric flux based on the star's spectral type and the Kurucz-Lejeune models (Lejeune et al. 1997), normalized to the observed J-band and assuming an appropriate amount of reddening customized to each object. This indicates what fraction of the 4.5 μm flux originates at the disk, and should relate directly to how well the light curves correlate. If this ratio is zero, then the optical and infrared light curves should coincide. If it is considerably larger, very little of the infrared flux comes from the star, and the flux dips present in the optical light curves should be absent from the infrared light curves. The values of $F_{4.5\ \mu{\rm m}}({\rm disk})/F_{4.5\ \mu{\rm m}}({\rm star})$ estimated for our stars are shown in Table 1.

We see some of these predicted tendencies, but the relationship is not as direct as one would expect. The stars with the lowest fractions of disk flux at 4.5 μm tend to have well correlated light curves, and generally very similar variability amplitudes in the optical and infrared, while those with a very high value of disk flux per stellar flux have uncorrelated, or weakly correlated, optical and infrared light curves. For the intermediate values, however, we find all sorts of scenarios. Mon-660, for instance, has an estimated ratio of disk flux to stellar flux of $F_{4.5\ \mu{\rm m}}({\rm disk})/F_{4.5\ \mu{\rm m}}({\rm star}) = 3.4$, and very strongly correlated light curves, while for Mon-928 $F_{4.5\ \mu{\rm m}}({\rm disk})/F_{4.5\ \mu{\rm m}}({\rm star}) = 1.4$, and its optical and infrared light curves are completely different. This could be due to uncertainties in the SED fits caused by poor or time variable data, or could simply be due to the time variable nature of the SEDs. There could have been some changes in the disk emission between the *Spitzer* cryogenic mission, from whence the values used to plot the SEDs were taken, and the 2011 CoRoT and *Spitzer* observing campaign.

For the stars where a correlation can be identified, we calculated which extinction law is necessary to transform the optical to the infrared light curve, assuming an optically thin regime. Extinction laws A_λ/A_R, where $\lambda = 3.6$ μm and 4.5 μm, were found to be between 0.28 and 0.77. According to Cardelli et al. (1989), we can derive values of A_λ/A_V for a given R_V (where R_V is defined as $A_V/E(B-V)$). A value of $R_V = 3.1$, typically used for interstellar matter (ISM), translates to $A_{3.6}/A_V = 0.05$ and $A_{4.5}/A_V = 0.04$. Transforming to A_R, since the CoRoT filter is centered close to the center of the R Johnson filter, we would have $A_{3.6}/A_R = 0.07$ and $A_{4.5}/A_R = 0.05$. These extinction laws are much lower than those found for the stars in our sample, implying that the distribution of dust grains in the inner circumstellar disk region is quite different from ISM, possibly containing fewer small grains. In addition, the observed dip depth ratio should be corrected for the fraction of IR light emitted by the disk. This would only increase our values of A_λ/A_R.

3.5. Modeling the CoRoT light curves

In this section we use the occultation model proposed for AA Tau in Bouvier et al. (1999) (described in Sect. 1.1) to attempt to reproduce the AA Tau-like light curves in our sample. If the optical photometric variability observed is due to periodic occultations by an inner disk warp, as we propose, then this geometrical model should be capable of reproducing the general trend of these light curves. We vary the model's main parameters in an attempt to obtain the configuration that most closely matches the observed variability. In this way we determine which values of warp height and azimuthal extension are needed to explain these stars' variability and how they must change from one rotation cycle to another in order to account for the changes in width and amplitude of each flux dip (see also Fonseca et al. 2014, for a detailed study of the light curve of V354 Mon−Mon-660).

As was mentioned in Sect. 1.1, the parameters of the occultation model are the star-disk system's inclination i, the radius $R_{\rm w}$ at which the warp is located, and the warp's maximum height $h_{\rm max}$ and azimuthal extension $\phi_{\rm w}$.

We assume that the periods we measured from the CoRoT light curves are the Keplerian periods of the occulting material orbiting the star; therefore, if we know the star's mass, we can use Kepler's third law in the following form to calculate the radius at which the warp is located,

$$R_{\rm w}^3 = GM_* \left(\frac{P_{\rm kep}}{2\pi}\right)^2, \tag{2}$$

where M_* is the star's mass, $P_{\rm kep}$ is the Keplerian rotation period, and G is the gravitational constant. To calculate the inclination we use the following relation between $v \sin i$, stellar radius R_*, and stellar rotation period $P_{\rm rot}$:

$$v \sin i = \frac{2\pi R_*}{P_{\rm rot}} \sin i. \tag{3}$$

We used stellar masses and radii determined by Venuti et al. (2014), who compared effective temperatures and bolometric luminosities placed on the Hertzsprung-Russell diagram to pre-main sequence model grids of Siess et al. (2000). The values are shown in Table 2, along with our values of Keplerian periods found from CoRoT light curves in each epoch, and the corresponding Keplerian rotation radius.

Values of the stars' projected rotational velocities ($v \sin i$) were obtained comparing FLAMES spectra, when available, and Hectochelle spectra otherwise, to synthetic spectra using the program Spectroscopy Made Easy (SME, Valenti & Piskunov 1996) and Oleg Kochukhov's Binmag3[2], as well as the spectrum synthesis code Synth3 (Kochukhov 2007) and atomic line files extracted from the *Vienna Atomic Line Database* (VALD)[3] (Piskunov et al. 1995; Ryabchikova et al. 1997; Kupka et al. 1999, 2000). We used photospheric lines to estimate the values of $v \sin i$ shown in Tables 1 and 2. For a few of our stars either no

[2] http://www.astro.uu.se/~oleg/

[3] http://vald.astro.uu.se/

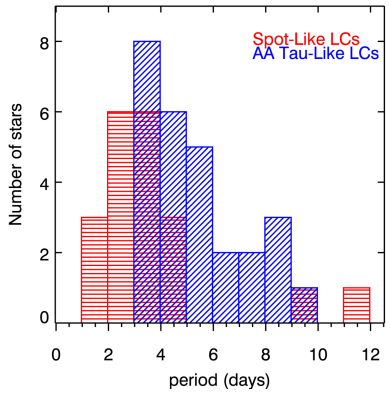

Fig. 13. Period histogram of CTTS in NGC 2264 whose CoRoT light curves were classified as AA Tau-like (blue) or spot-like (red). The periods of spot-like light curves represent stellar rotational periods, while those of AA Tau-like light curves represent Keplerian rotation periods at the warp location. The periods of spot-like light curves were taken from the 2011 data, while AA Tau-like light curves from both 2008 and 2011 were used.

spectrum was available, or the signal-to-noise ratio of the photospheric lines was insufficient for this analysis and therefore no value is given.

Co-rotation radius. A stellar rotation period independent of CoRoT light curves was measured for only one star in our sample, Mon-250, by determining the variability of the radial velocity of photospheric lines in the FLAMES spectra (Fig. 7). This method was unsuccessful for the other stars, since their radial velocities did not present significant variability within our errors. The spectroscopic period found for Mon-250 was $P_{\rm rot} = 8.6 \pm 0.5$ days, a value consistent with the periods found from its CoRoT light curves of $P_{\rm kep} = 8.3 \pm 1.0$ days in 2008 and $P_{\rm kep} = 8.9 \pm 0.5$ days in 2011. The same period of 8.6 days was found by Sousa et al. (in prep.) in both the Hα and the HeI 6678 Å lines. This indicates that the structure responsible for the occultations in the CoRoT light curves is located at or near the co-rotation radius.

This was found to be true for the star AA Tau as well, when Bouvier et al. (2007) measured its rotational period using the radial velocity of the HeI 5876 Å emission line and photospheric lines and found a value consistent with their photometric period. Therefore we find it reasonable to assume that the inner disk warp is located at the disk's co-rotation radius for the other AA Tau-like systems. Since we do not have an accurate measure of stellar rotation periods for the stars in our sample besides Mon-250, we use the periods determined from their CoRoT light curves in Eq. (2) to calculate their inclinations.

In order to further investigate whether these Keplerian periods can also represent the stars' rotation periods, we made a period histogram of all of the CTTS in NGC 2264 with CoRoT light curves classified as spot-like or AA Tau-like (see Fig. 13). The spot-like light curves are due to rotational modulation of stable configurations of spots on the stellar surface, and therefore these values represent the stars' rotational periods. The values from AA Tau-like light curves represent the Keplerian rotation periods of the inner disk material that occults the stellar photosphere. We see that, though the distributions are not identical, the values for AA Tau-like light curves fall within the region where rotational periods are found.

Inclination. We calculate $\sin i$ of each star using Eq. (3) and taking the period found from the CoRoT light curve as $P_{\rm rot}$, except in the case of Mon-250, for which the spectroscopic period was used. For those stars observed to be periodic in both epochs, but for which a slightly different period was found in 2008 and 2011, the value with the smallest error was used, i.e., the one whose periodogram presented a peak with smaller width at half maximum and higher intensity. The results are shown in Table 2.

It is important to note that the inclination is a very difficult parameter to determine precisely, especially when dealing with high inclinations. In these cases a relatively small error in $\sin i$ is translated into a large error in i. Unfortunately our errors in $\sin i$ themselves are relatively large to begin with, therefore our values for i are very imprecise.

Hartmann (2001) and Rebull et al. (2002) discuss the difficulties in obtaining precise values of luminosity, temperature, and radius for TTSs because of their strong variabilities, spectrum veiling, surface spots, and uncertainties in calculating the distance. The former showed that typical errors in radius determination are on the order of 20%, while the latter show errors of typically 12% for TTSs in the spectral range K5-M2. In this study we consider errors of 20% in radius.

Errors in period and $v \sin i$ vary from one star to another. For periods, we adopted the half width at half maximum of the peak in each periodogram as the uncertainty, which is typically around 5% to 7%. Our errors in $v \sin i$ are typically on the order of 10−12%. This leads to errors around 35% in $\sin i$, which is rather high, but consistent with other studies of TTS inclinations (e.g., Artemenko et al. 2012).

Although the actual values of inclination are imprecise, it is not difficult to distinguish between systems with low inclinations and those with medium to high inclinations, since for low inclinations errors in $\sin i$ do not translate into such large errors in i as with high inclinations. We see from Table 2 that the star Mon-1131 is seen at a low inclination, and we can consequently rule out the proposed occultation mechanism as the primary cause for the light curve variations. However, it is possible that there are two structures in each hemisphere, separated by 180°, obscuring the photosphere and making it seem as if the period were half the true value. If this were the case its inclination would be $64^{\circ}{}^{+26}_{-36}$, though further investigation is needed to determine its true rotation period. For the time being this star has been excluded from further investigation using the occultation model, though it is studied in Stauffer et al. (2015), where different mechanisms are proposed to explain its variability.

For the other stars in our sample for which an inclination can be estimated, they tend toward high values, at least within the uncertainties (see Table 2). There are many stars for which the value of $\sin i$ found was larger than 1. In some cases a reasonable interval of values within the error bars falls under 1, in which case we argue that the system's inclination should be anywhere between the inverse sine of the lowest value ($\sin i - \Delta \sin i$, where $\Delta \sin i$ is the uncertainty in $\sin i$) and 90°. We then consider the inclination to be the mean value in this interval (for example, a star of $\sin i = 1.07 \pm 0.32$ has an inclination of $69^{\circ} \pm 21^{\circ}$, since the inverse sine of the lowest value, $\sin i = 1.07 - 0.32 = 0.75$, is 48°).

For the star Mon-928, its value of $\sin i$ is much larger than 1, even when considering the error bars. It is possible that the material occulting this star is located farther away from the star than its co-rotation radius, in which case the Keplerian period we calculated using the CoRoT light curves is larger than the stellar rotation period, resulting in a larger value of $\sin i$. It is also possible that the true period is half the value used. There is an additional,

Table 2. Stellar parameters initially calculated for the AA Tau-like candidates.

CSIMon ID	L_{bol} ($L_\odot$)	M_* ($M_\odot$)	R_* ($R_\odot$)	P_1 (days)	P_2 (days)	$v \sin i$ (km s^{-1})	$\sin i$	Inclination (°)	$R_{w,1}$ (R_*)	$R_{w,2}$ (R_*)
CSIMon-000056	0.77	1.16	1.52	5.71	5.86	11.1 ± 2.2	0.85 ± 0.38	58^{+32}_{-30}	9.29	9.45
CSIMon-000250	1.23	1.35	1.63	8.32	8.93	9.8 ± 2.2	1.02 ± 0.49	62 ± 28	11.71	12.28
CSIMon-000296	1.57	1.42	1.71	–	3.91	17.3 ± 2.6	0.78 ± 0.33	51^{+39}_{-24}	5.11	6.86
CSIMon-000297	1.57	1.42	1.71	3.16	–	30.8 ± 1.8	1.13 ± 0.40	69 ± 21	5.95	–
CSIMon-000358†	0.22	0.29	1.39	–	5.86	–	–	–	–	6.51
CSIMon-000379	2.12	1.60	1.99	–	3.68	25.0 ± 1.2	0.91 ± 0.30	66^{+24}_{-28}	5.95	5.89
CSIMon-000441†	0.50	0.36	1.92	4.06	–	–	–	–	3.97	–
CSIMon-000456	1.58	1.41	2.00	–	5.03	19.3 ± 1.5	0.96 ± 0.21	74^{+16}_{-33}	–	6.92
CSIMon-000498	3.85	1.90	2.88	4.23	4.28	24.1 ± 2.4	0.71 ± 0.26	45^{+31}_{-19}	4.73	4.77
CSIMon-000654	0.47	0.30	2.03	4.66	–	18.0 ± 3.0	0.82 ± 0.37	55^{+35}_{-28}	3.87	–
CSIMon-000660	1.36	1.40	1.86	5.25	5.25	21.4 ± 2.5	1.16 ± 0.44	68 ± 22	7.64	7.50
CSIMon-000774	3.10	1.83	2.49	3.46	–	30.7 ± 1.3	0.84 ± 0.28	57^{+33}_{-23}	4.73	–
CSIMon-000811	1.08	0.91	1.97	–	7.88	13.5 ± 1.7	1.07 ± 0.35	64 ± 26	–	8.19
CSIMon-000824	1.96	1.48	2.23	7.05	–	14.8 ± 1.4	0.92 ± 0.40	68^{+22}_{-37}	7.90	–
CSIMon-000928	0.58	0.63	1.65	9.92	–	20.1 ± 2.8	2.38 ± 1.05	90	10.09	–
CSIMon-001054	0.63	0.36	2.17	–	4.08	20.4 ± 2.0	0.76 ± 0.28	49^{+41}_{-28}	–	3.52
CSIMon-001131	0.55	0.36	2.01	–	5.18	8.8 ± 1.7	0.45 ± 0.21	27 ± 14	4.44	4.46
CSIMon-001140	1.10	1.31	1.67	3.87	3.90	19.8 ± 2.3	0.91 ± 0.34	66^{+24}_{-35}	6.79	6.83
CSIMon-001167	0.56	0.30	2.23	–	8.78	11.3 ± 2.1	0.88 ± 0.42	62^{+28}_{-35}	5.18	5.37
CSIMon-001296	0.91	0.69	1.99	–	9.75	11.0 ± 1.6	1.07 ± 0.48	63 ± 27	–	8.52
CSIMon-001308	0.53	0.63	1.59	6.45	6.68	9.9 ± 2.0	0.82 ± 0.37	55^{+35}_{-28}	7.86	8.04
CSIMon-014132†	0.37	0.28	1.88	–	4.48	–	–	–	–	3.98

Notes. $P1$ and $P2$ are the Keplerian periods found from the CoRoT light curves in 2008 and 2011, respectively, while $R_{w,1}$ and $R_{w,2}$ are the co-rotation radii found using $P1$ and $P2$, respectively. The stars identified with a † either have no observed spectrum, or the signal-to-noise ratio is too low to determine $v \sin i$, and so we cannot calculate their inclinations.

smaller, flux dip in its 2008 light curve located between the second and third larger flux dips (see Fig. 9), which justifies using a period of 4.96 days, rather than 9.92 days, though we gave preference to the latter since it coincides with the period found in the literature of 9.48 ± 2.34 (Lamm et al. 2005). If the period were indeed half the value we considered, this would lead to an inclination of 66° ± 24°. In either case, it is probably safe to consider that this system has a high inclination. Therefore, we used the occultation model described in Sect. 1.1 to find which interval of inclinations results in the best fit for the light curve, and consider this as the system's inclination. We did this as well for the three stars for which we have no measure of $v \sin i$, where we assume without proof that the systems are seen nearly edge-on. The new values are presented in Table 3.

For the rest of the AA Tau-like stars, we used the occultation model in a similar fashion as a fine tuning for the inclination. We noticed that in many cases we were not able to successfully reproduce the observed widths in flux dips using the whole range of values of i initially calculated, unless we used other parameters that were unphysical (such as azimuthal extension $\phi_w > 360°$). Therefore, we took all values of i within the error bars and chose only the interval that could successfully reproduce the widths of the observed light curves with physically possible values of ϕ_w. This restricted the inclinations much more than the original calculation, resulting in much smaller error bars, as can be seen in Table 3. Figure 14 shows an example of the best fits for a light curve using the originally calculated value of inclination (with $\phi_w \leq 360°$) and the new value presented in Table 3. It is easy to see that this value reproduces the widths of the flux dips much more closely.

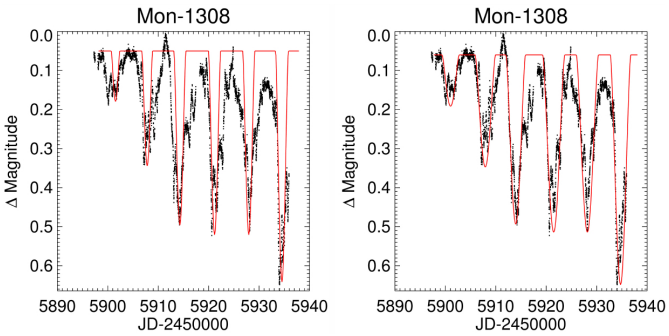

Fig. 14. Fitted light curves of the star Mon-1308 using an inclination of 55° (*left*) and 75° (*right*). In both cases the values of warp maximum height and azimuthal extension were set to those that best fit the width and amplitude of the minima without extrapolating to unphysical values.

Warp parameters and fitted light curves. The occultation model was used interactively to simulate the CoRoT light curves using the values given in Table 2 for stellar mass, radius, and co-rotation radius, with the warp maximum height and azimuthal extension as free parameters, and inclination as a semi-free parameter, constrained to values within the error bars presented in Table 2. Each minimum of each light curve was fitted independently to account for slight changes in the warp from one rotation cycle to another. Some examples of the synthetic light curves reproduced by the occultation model are shown in Fig. 15 (synthetic light curves of all other stars are shown in Fig. 23). Inclinations were determined first, as described above,

Table 3. Occultation model parameters found for the AA Tau-like candidates.

CSIMon ID	Epoch	$R_w(R_*)$	h_{max}/R_w	$\phi_w(^\circ)$	Inclination (°)
CSIMon-000056	2008	9.29	0.24–0.25 (±0.10)	320 (±40)–360	71 ± 6
CSIMon-000056	2011	9.45	0.24–0.26 (±0.10)	290 (±70)–360	71 ± 6
CSIMon-000250	2008	11.71	0.23–0.28 (±0.05)	140 (±30)–360	74 ± 3
CSIMon-000250	2011	12.28	0.24–0.27 (±0.05)	270 (±30)–360	74 ± 3
CSIMon-000296	2011	6.86	0.21–0.31 (±0.09)	290 (±40)–360	72 ± 5
CSIMon-000297	2008	5.95	0.17–0.28 (±0.04)	180 (±30)–360	75 ± 2
CSIMon-000358	2011	6.51	0.17–0.19 (±0.06)	210 (±50)–360	73 ± 4
CSIMon-000379	2011	5.89	0.22–0.34 (±0.12)	110 (±30)–270 (±90)	70 ± 7
CSIMon-000441	2008	3.97	0.17–0.23 (±0.11)	160 (±20)–310 (±50)	70 ± 7
CSIMon-000456	2011	6.92	0.18–0.24 (±0.05)	360	74 ± 3
CSIMon-000498	2008	4.73	0.17–0.21 (±0.10)	145 (±35)–165 (±15)	70 ± 6
CSIMon-000498	2011	4.77	0.19–0.22 (±0.10)	130 (±50)–165 (±15)	70 ± 6
CSIMon-000654	2008	3.87	0.10–0.13 (±0.06)	180 (±60)–310 (±50)	73 ± 4
CSIMon-000660	2008	7.64	0.25–0.33 (±0.04)	260 (±20)–360	74 ± 3
CSIMon-000660	2011	7.50	0.27–0.29 (±0.05)	200 (±30)–360	74 ± 3
CSIMon-000774	2008	4.73	0.15–0.21 (±0.03)	220 (±40)–360	75 ± 2
CSIMon-000811	2011	8.19	0.26–0.28 (±0.08)	360	72 ± 5
CSIMon-000824	2008	7.90	0.24–0.27 (±0.08)	260 (±40)–360	72 ± 5
CSIMon-000928	2008	6.36	0.28–0.30 (±0.10)	120–300 (±60)	71 ± 6
CSIMon-001054	2011	3.52	0.16–0.21 (±0.09)	270 (±70)–360	70 ± 5
CSIMon-001140	2008	6.79	0.16–0.24 (±0.03)	190 (±20)–360	75 ± 2
CSIMon-001140	2011	6.83	0.14–0.24 (±0.03)	190 (±20)–360	75 ± 2
CSIMon-001167	2011	5.37	0.15–0.18 (±0.05)	330 (±30)–360	74 ± 3
CSIMon-001296	2011	8.52	0.31–0.34 (±0.13)	260 (±80)–330 (±30)	69 ± 8
CSIMon-001308	2008	7.86	0.28–0.30 (±0.06)	330 (±30)–360	73 ± 4
CSIMon-001308	2011	8.04	0.20–0.27 (±0.06)	340 (±20)–360	73 ± 4
CSIMon-014132	2011	3.98	0.18–0.32 (±0.14)	120 (±40)–290 (±80)	68 ± 9

Notes. R_w is the radius where the warp is located, assumed to be at the co-rotation radius (i.e., $R_w = R_{co}$); h_{max} is the maximum warp height found for each flux dip, expressed in stellar radii R_*; and ϕ_w is the azimuthal extension of the warp found for each flux dip. The inclinations shown here were constrained using the occultation model.

by verifying for which values we were able to reproduce the width of each minima without having to resort to unphysical values of azimuthal extension. We used a maximum inclination of 77°, since for inclinations larger than this the outer flared disk would overshadow the inner disk region[4], making it impossible to observe the stellar photosphere (Bertout 2000). Error bars in warp maximum height and azimuthal extension were calculated by modeling the minima with the value of inclination fixed at its lowest and highest possible values, and finding the best fit in each case.

Table 3 shows the final values obtained for the model parameters. Since they vary from one rotation cycle to another, we present the intervals of the values found for each light curve. Most of the values found for the warp's maximum height and azimuthal extension are similar to those found for AA Tau. The average ratio between the warp's maximum height and the radius at which it is located is $h_{max}/R_w = 0.23$, though individual values range from 0.10 to 0.34 (for comparison we note that the value used for AA Tau in Bouvier et al. 1999 was of $h_{max}/R_w = 0.30$). The average value of the warp's azimuthal extension is $\phi_c = 300°$, but is often a full 360°, the same as AA Tau, and can be as low as 110°. Inclinations generally need to be greater than ~65° for the occultation model to successfully reproduce the widths of the minima, but in some cases may be as low as 60° for relatively large warp heights and shallow flux dips.

We see that the warp maximum height should vary between rotation cycles by on average 11%, and at times by up to 57%, to account for the variations in amplitude of the light curves. The azimuthal extension of the warp should vary by on average 17%, and up to 65%, between rotation cycles to account for the variations in width of the minima present in the CoRoT light curves. If the photometric variability of these stars is truly due to occultations by an inner disk warp caused by the interaction between the magnetosphere and the inner disk region, as we propose, then these values show how dynamic this interaction is, as has been predicted by MHD models.

3.6. Color–magnitude diagrams and color variation

We constructed color magnitude diagrams of the stars in our sample (both those that present AA Tau-like light curves and those that present aperiodic extinction dominated light curves), to search for trends characteristic of extinction. We used data taken simultaneously with CoRoT and *Spitzer*, plotting CoRoT magnitude against CoRoT magnitude minus *Spitzer* $IRAC_{4.5\ \mu m}$ magnitude. It is not possible to use this method to clearly

[4] This effect may not be as significant for sources that have anemic disks, since they may possess flatter outer disks. However, this would only be relevant for the star Mon-314, which has aperiodic photometric behavior and therefore is not analyzed using the occultation model at any rate.

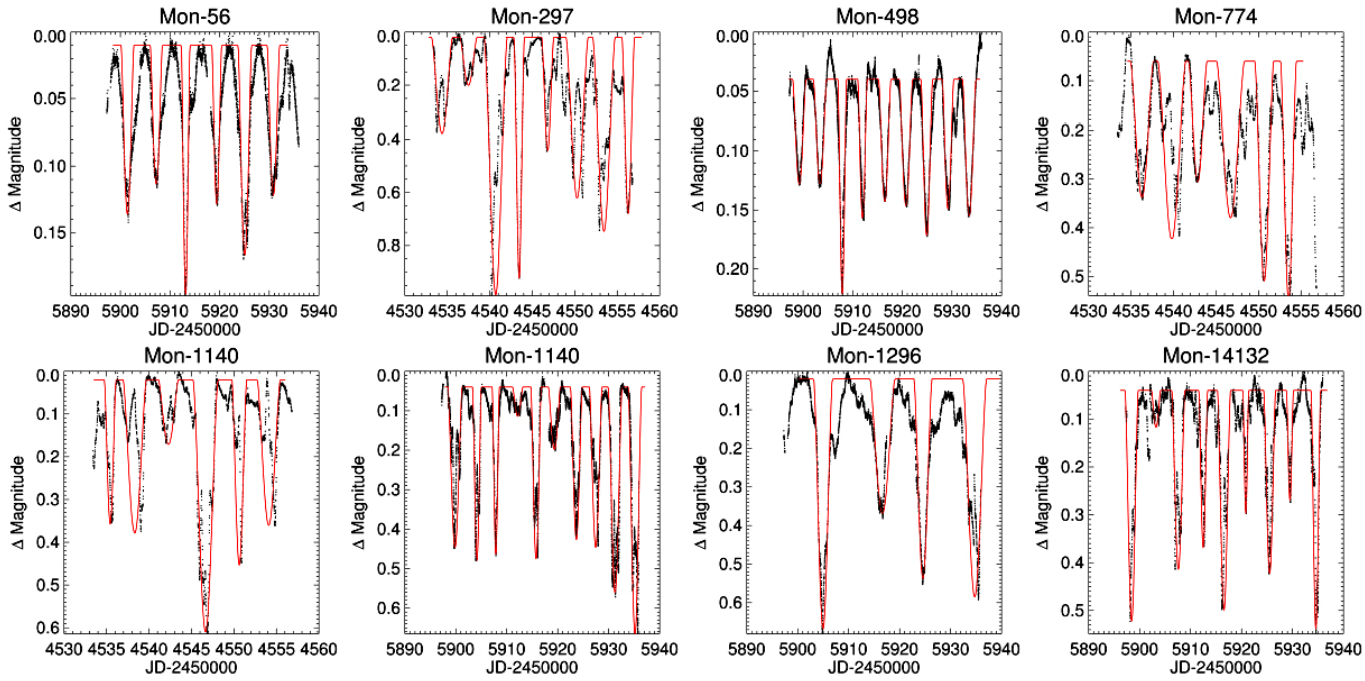

Fig. 15. Examples of simulated light curves of AA Tau-like stars (red) plotted over CoRoT light curves (black).

distinguish if the photometric variability is due to extinction or a configuration of spots on the surface, but if we assume that extinction is the main source of the flux dips present in both the CoRoT and IRAC light curves, then we can estimate extinction laws from the slopes of the distributions (Fig. 16).

In order to be sure that we are analyzing parts of the light curve where the same phenomenon is responsible for the variability in the optical and infrared bands, we calculated slopes using linear regression only for the parts of the data where the CoRoT and IRAC light curves correlate reasonably well. We also separated these parts in order to calculate slopes for different flux dips and different parts of the flux dips, as shown in Fig. 16, in order to verify if different extinction laws could be found for different parts of the disk warp. We find that entrances into and exits from the occultations show the same slopes, within the uncertainties. In one case, Mon-456 (see left panels of Fig. 16), slightly different slopes were found during different flux dips. This might indicate a small variability in the grain distribution of the inner disk warp during rotation cycles, or it could be due to other factors, such as variable disk emission, interfering with the IRAC light curves.

We were able to estimate extinction laws for ten of the stars in our sample using this method, finding values between those consistent with ISM ($A_{4.5\ \mu m}/A_R \sim 0.05$) and up to $A_{4.5\ \mu m}/A_R \sim 0.29 \pm 0.04$. Slopes of values less than 1 were not considered, since extinction laws derived would be unphysical. In these cases, other factors, such as variable disk emission in 4.5 μm or a configuration of hot or cold spots on the stellar surface, could be strongly influencing the distribution of points in the color magnitude diagrams. It is possible that variable disk emission is also influencing our derived extinction laws, causing us to find lower slopes and therefore lower extinction laws than were estimated in Sect. 3.4. More accurate estimates will require a more extensive study of these and other color magnitude diagrams, which will be treated in a future paper.

To check for color variation in the periodic and quasi-periodic stars in our sample, we compared CoRoT and I-band light curves with $u-r$ for the stars whose light curves were classified as AA Tau-like or AA Tau candidates in 2011. We plotted these light curves in phase, using the periods determined from the CoRoT data (Table 1). The same initial date was taken for all three plots for easy comparison. Though the CFHT data were not taken simultaneously with CoRoT, by folding the light curves in phase, using the same initial date and period, we can see how the color varies during the flux dips. For most stars, we see a reddening at phase 0.5 during the eclipses, as is to be expected from an extinction event.

For four stars (Mon-250, Mon-358, Mon-456, and Mon-1054), we can observe a bluing at phase 0.5 for one or two rotation cycles, while the other cycles either maintain relatively constant color or become slightly redder. This effect was observed in AA Tau (Bouvier et al. 2003), which showed little color variation except during some minima, when it became bluer. This was attributed to the appearance of part of the hot spot associated with the accretion shocks on the stellar surface, during eclipses from the inner disk warp. This shows very strong evidence that these four stars are undergoing the same physical processes as AA Tau did during its stable accretion phase.

Three stars undergo an interesting phenomenon where they become slightly bluer during the beginning of the eclipses and then become redder. This could also be evidence that the hot spot associated with the accretion shock is partially showing, but in this case it is soon occulted by the inner disk warp. These stars are Mon-1140, Mon-1308, and Mon-1167. For two stars, Mon-56 and Mon-14132, we see little or no change in color. Figure 17 shows some of these light curves and $u-r$ color diagrams folded in phase. The others are shown in Fig. 24.

3.7. Other characteristics of AA Tau-like stars

Figure 18, top left panel, shows a mass histogram of AA Tau-like stars (red) and stars with aperiodic extinction dominated light curves (purple), plotted over a histogram of all CTTS in our

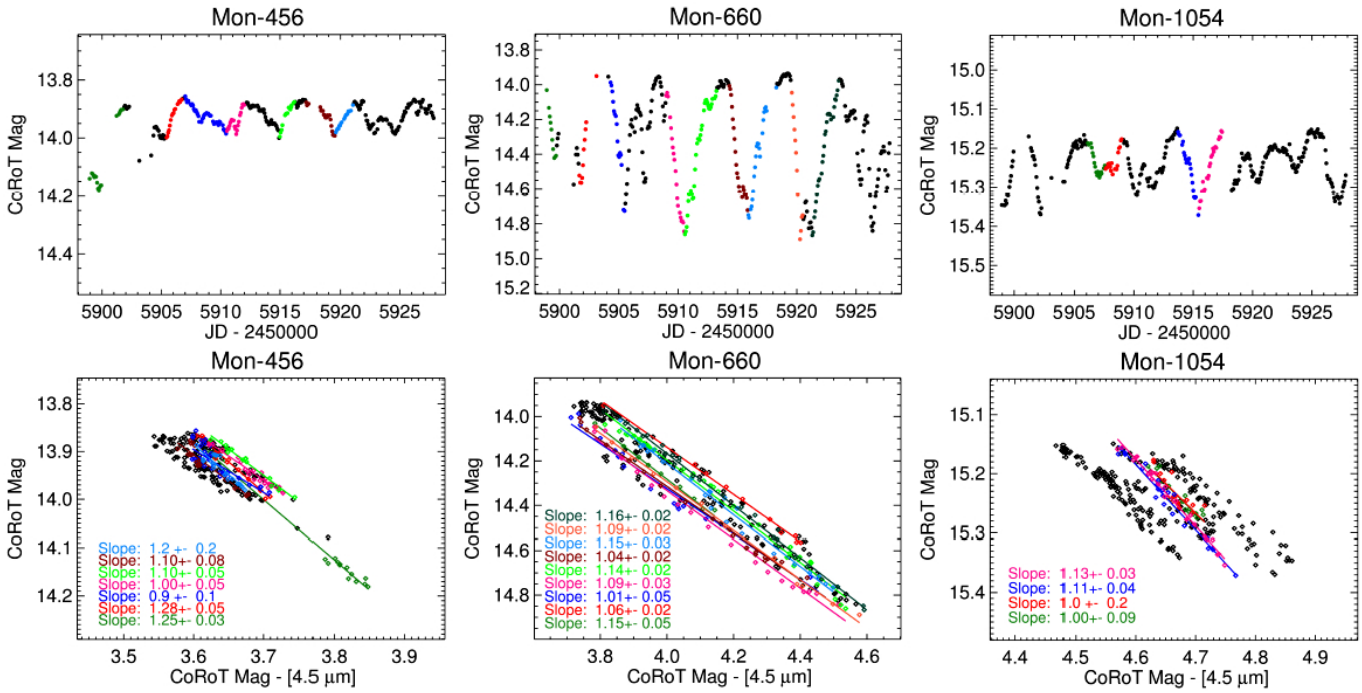

Fig. 16. *Top*: CoRoT light curve of the stars Mon-456, Mon-660, and Mon-1054. *Bottom*: CoRoT vs. CoRoT-IRAC$_{4.5\ \mu m}$ color magnitude diagrams of the same stars. The slopes were calculated for various parts of the light curves where CoRoT and *Spitzer* IRAC data best correlate. Different colors show different parts of the light curves for which slopes were calculated.

study of NGC 2264 that present CoRoT light curves from either observing run. While the CTTS show a tendency toward lower masses, the number of stars declining rapidly for larger masses, the AA Tau-like stars are equally present in the whole range of masses considered. Therefore, though there are AA Tau-like stars of all masses in the CTTS range, the ratio of these stars to the total number of stars in that mass bin increases with increasing mass, meaning they are relatively more common among higher mass stars than lower mass ones (top right diagram in Fig. 18). Stars that present AA Tau-like photometric behavior in either 2008 or 2011 were included in the AA Tau category.

Inclination is a major factor in whether we observe AA Tau-like events or not; therefore, we know that the observed AA Tau-like stars are only a fraction of the total number of stars that present an inner disk warp. For stars of $M \lesssim 0.7\ M_{\odot}$, fewer than 10% are observed as AA Tau-like. If we consider that it is possible to view the occultations at angles between ~60° and 77°, as was shown using the occultation model, then only at most 50% of stars in this mass range possess an inner disk warp with two major accretion funnels. For stars of $M \gtrsim 0.7\ M_{\odot}$, about 35% show AA Tau-like behavior, meaning that if we assume random inclinations, all of these stars likely possess an inner disk warp during some part of their evolution.

The fraction of stars that present AA Tau-like photometric behavior is quite large as we approach even higher masses ($M \gtrsim 1.0\ M_{\odot}$), much larger than we would expect if all CTTS observed by CoRoT possessed an inner disk warp, given that when we consider random inclinations we should only see ~20% of AA Tau-like systems. This is possibly due to a selection bias, since the CoRoT targets are not selected randomly, but based on specific criteria, which included many systems with known periodicity, and in 2011 included systems previously classified as AA Tau-like. Therefore, to compare with a less biased sample, we plotted a histogram of the number of AA Tau-like systems observed by CoRoT compared to the total number of CTTS observed by the CFHT MegaCam (presented in Venuti et al. 2014), including those that were and were not observed by CoRoT. This plot, shown in the bottom panel of Fig. 18, may also have a biased tendency, since it is possible that some of the systems not observed by CoRoT also present AA Tau-like variability that would be unaccounted for. Even so, we see that slightly over 20% of stars with mass $M \gtrsim 1.0\ M_{\odot}$ present this type of variability. Extrapolating this amount to the systems where the inclinations prevent us from observing this tendency, we still conclude that nearly all of the systems with mass $1.0\ M_{\odot} \lesssim M \lesssim 2.0\ M_{\odot}$ and most (~75%) of the systems with mass $0.7\ M_{\odot} \lesssim M \lesssim 1.0\ M_{\odot}$ should present an inner disk warp, while for systems of $M \lesssim 0.7\ M_{\odot}$ this fraction would be of only ~25%.

This may be due to different stellar magnetic field configurations. The dipolar component of the magnetic field is responsible for the interaction with the inner disk, and a stronger dipolar component leads to a larger truncation radius. As was discussed in Sect. 3.3, a larger truncation radius tends to favor a stable accretion regime. Gregory et al. (2012) found that the magnetic field configuration of a star depends strongly on its internal structure, and that for intermediate to high mass T Tauri Stars ($0.5\ M_{\odot} \lesssim M_{*} \lesssim 2.0\ M_{\odot}$), those that are fully convective, or have as yet only developed a small radiative core, tend to have strong dipoles. At the estimated age of 2−3 Myr of NGC 2264, Gregory et al. (2012) show that stars in this mass range have not yet developed a significant radiative core. They should therefore possess strong dipolar components in their magnetic fields.

There is still very little information available on magnetic fields of T Tauri stars of smaller mass ($M_{*} \lesssim 0.5\ M_{\odot}$), because of observational constraints. At least one T Tauri star in this mass range, V2247 Oph, has had its magnetic field topology measured and was found to have a weak dipolar component (Donati et al. 2010). Therefore, it is possible that among fully convective stars, a significant difference in magnetic field configurations

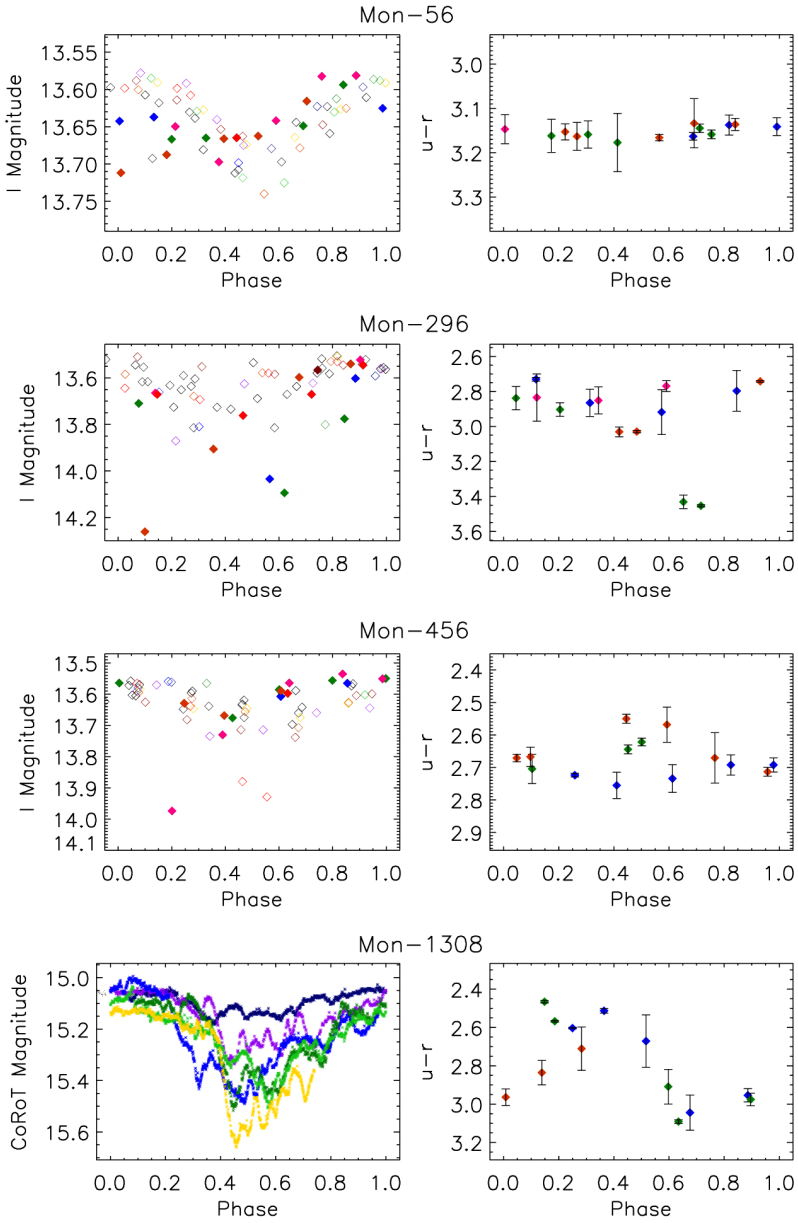

Fig. 17. Examples of I-band and $u-r$ light curves folded in phase. The colors used for $u-r$ represent the same rotation cycle as the filled diamonds of the same color in I. Mon-56 shows no measurable variability in $u-r$; Mon-296 shows reddening events in $u-r$ during its eclipses in the I-band; Mon-456 shows a slight reddening during one of its I-band minima (blue diamonds) and bluing events during the other I-band minima (orange and green diamonds); and Mon-1308 shows a bluing, followed by a reddening event during its minima in the CoRoT light curve. It was not possible to identify flux dips in the phase-folded I-band light curve of Mon-1308 because of insufficient cadence, so the phase-folded CoRoT light curve is shown instead. The same period and initial date were used for CoRoT and $u-r$, though in this case colors do not represent the same phase in both plots.

may exist among these two mass ranges. Morin et al. (2010) showed that among main sequence stars, those of very low mass show magnetic field topologies that differ considerably from fully convective stars of somewhat higher mass. While the latter generally possess magnetic fields with strong dipoles, main sequence stars of very low mass ($M_* \lesssim 0.2\ M_\odot$) show a number of different magnetic topologies, ranging from very strong, axisymmetric, nearly dipolar fields to weaker fields with a strong non-axisymmetric component, and a strong toroidal component. This supports the idea that a different magnetic field regime may dominate among stars of lower mass.

However, our results alone are insufficient to conclude that a significant difference exists among magnetic field configurations in these two mass ranges. There are other factors that may influence our higher detection of AA Tau-like systems among those of somewhat higher mass. For instance, mass accretion rates tend to decrease toward lower masses (Venuti et al. 2014), which would increase the truncation radius at this mass range. This would favor a stable accretion mechanism, but could also lead to the disk warp being located farther away from the co-rotation radius than we have assumed. If they are located significantly farther away, we would need higher inclinations to observe the eclipses in these systems, making it more difficult to do so.

It is also possible that this effect is simply the result of an observational bias. Stars of lower mass are generally fainter than those of higher mass, and the signal from the CoRoT

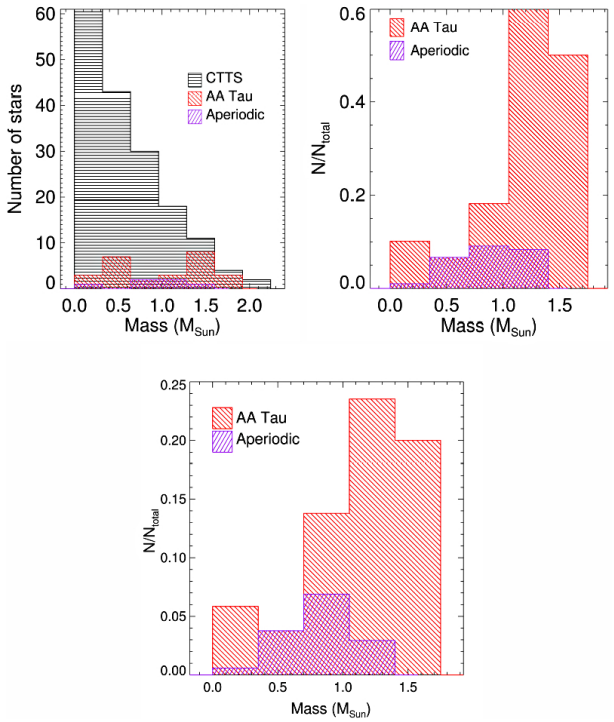

Fig. 18. *Top left*: mass histogram of all CTTS with CoRoT light curves (black), stars with AA Tau-like light curves (red), and stars whose CoRoT light curves are dominated by aperiodic extinction events (purple). *Top right*: number of AA Tau-like stars (red) and aperiodic extinction stars (purple), divided by the total number of CTTS observed by CoRoT in that mass bin. Stars of both CoRoT observing runs were used, and any star that presented AA Tau-like photometric behavior in either run was included in the AA Tau category. *Bottom*: number of AA Tau-like stars (red) and aperiodic extinction stars (purple), divided by the total number of CTTS in the sample of Venuti et al. (2014), including those that were not observed by CoRoT.

observations could be too low among stars below a certain mass limit to allow an accurate classification of AA Tau-like light curves.

4. Discussion

The occultation model initially proposed for the star AA Tau appears to be adequate at reproducing the general aspects of the flux dips of the stars listed in Table 3. It is capable of reproducing their widths and amplitudes using values of inclination, warp maximum height, and azimuthal extension that are consistent with those found for AA Tau itself, with only a few stars showing values of warp height and azimuthal extension that are significantly lower.

We note that for stars whose light curves are classified as AA Tau-like in both CoRoT observing runs (2008 and 2011), the values found for warp maximum height and azimuthal extension in one epoch are always within the same range as those found in the other. This means that, although the occulting structure should be variable on a timescale of days to weeks because of the dynamic interactions, it should be stable enough to persist on a timescale of a few years. We also note that, for these stars, the periods found in each observing run are very similar to each other. Most are equal within their uncertainties. In all of these cases the radius where the occulting structure should be located differs by less than 4% from one epoch to the other, and most by less than 2%, which is within their respective uncertainties.

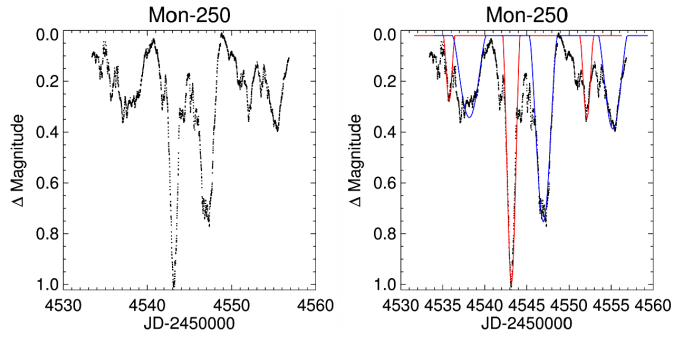

Fig. 19. *Left*: 2008 CoRoT light curve of Mon-250. *Right*: synthetic light curves generated with the occultation model for two separate accretion funnels (blue and red) overplotted on the 2008 CoRoT light curve of Mon-250.

It is possible that the structures move somewhat in radius over timescales of a few years, but they should do so by very little.

Though it can reproduce the widths and amplitudes of light curve minima, the occultation model is unable to account for the exact shape of the flux dips, which are much more complex than the nearly Gaussian shapes that it reproduces. This model is based on a symmetric warp of homogeneous optical thickness, which likely does not reflect the reality of these systems. For AA Tau, short term brightening episodes were seen to occur during the occultation events, and were attributed to inhomogeneities of reduced optical thickness in the occulting material (Bouvier et al. 1999). We observe these brightening episodes in many of the light curves in our sample. In most cases the light curve minima present significant structure, which could be due to these inhomogeneities, to the existence of a configuration of hot spots visible during the occultations, or to non-steady accretion within the funnel flows, which would lead to variable emission during the flux dips.

In some cases we observe two minima where we would expect to see one, such as in the 2008 CoRoT light curve of the star Mon-250 (left panel of Fig. 19). We know from its 2011 CoRoT light curve and spectra that this star's rotation period is on the order of 8.6 days (Fig. 7); therefore, the 2008 light curve spans only three rotation cycles, though we see more than three flux dips. We can speculate that the two middle dips are part of one structure, as the last two dips would be, and that there is significant emission from the hot spot associated with the accretion shock superimposed onto the extinction from the base of the accretion funnel, or simply that the warp was very inhomogeneous. Unfortunately, there is no color information simultaneous with this light curve to verify these scenarios. However, the occultation model is incapable of reproducing one flux dip that would encompass both middle dips seen in the light curve using physically plausible parameters. We are able to reproduce each dip separately, however, if we consider that there are two accretion funnels, separated by 160°, i.e., nearly opposite each other (right panel of Fig. 19). We propose that it is possible for the main accretion funnel to at times give way to two accretion funnels as a result of an increase in instabilities.

This same behavior was observed in AA Tau in 1999, when its quasi-periodic flux dips gave way to two flux dips per stellar rotation (see Fig. 15 in Bouvier et al. 2007). We may also be seeing this in the star Mon-1054, whose veiling features support the AA Tau-like scenario as the primary cause for its photometric variability (see Sect. 3.2). The left panel of Fig. 20 shows its 2011 CoRoT light curve. Arrows point to moments where we observe two flux dips when we would expect to see only one in a

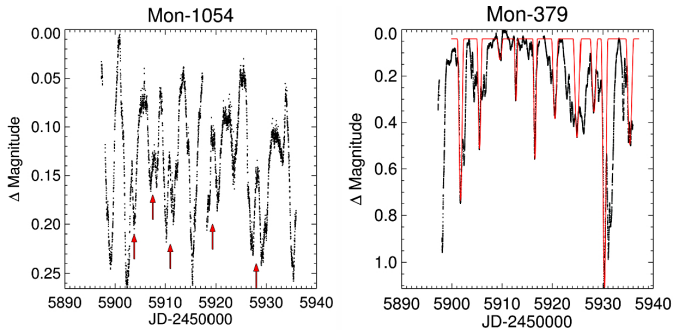

Fig. 20. *Left*: 2011 CoRoT light curve of Mon-1054. Arrows show moments when two flux dips are present where we would expect to see only one in a typical AA Tau-like scenario. *Right*: simulated light curve (red) overplotted on the 2011 CoRoT light curve of Mon-379 (black).

typical AA Tau-like scenario. The occultation model is capable of reproducing some of these double dips with only one accretion funnel, assuming that another mechanism is responsible for the emission within the dip, but it is not able to do so for the fifth double dip indicated in the left panel of Fig. 20. In this case, only two funnels (separated by 160° of similar height and azimuthal extension) can successfully reproduce both minima in the light curve. This may be an indication that this star is undergoing a transition between a stable and an unstable accretion regime, or that it is in an intermediate state of some instability.

This may be the case as well for the star Mon-379 during the 2011 CoRoT observations (Fig. 20, right panel), where we can observe periodic AA Tau-like dips that are easily reproduced by the occultation model accompanied by other extinction events. These additional extinction events may be due to random accretion streams characteristic of an unstable accretion regime, as was discussed in Sect. 3.3, that coexist with the main stable accretion funnel. We also note that for this particular star some of the dips are quite narrow and the best fit found with the occultation model has azimuthal extension as low as 110°, unlike the majority of other stars where this value is between 260° and 360°. This may also be an indication of this star's declining stability.

The phenomenon observed in the aperiodic light curves is similar to those observed in UX Ori-type objects, which exhibit deep, non-periodic algol-like minima caused by extinction from circumstellar material in the observer's line of sight (see the review by Grinin 2000). Both our aperiodic stars and the UX Ori-type objects show evidence of being seen at high inclinations, which is favorable for circumstellar material located near the disk plane to intersect our line of sight. UX Ori flux dips typically present larger amplitudes and longer duration than the stars in our sample, probably because of larger scale disk instabilities. They are also much more common among Herbig AeBe stars, though a few CTTS have been classified as UXors (Herbst & Shevchenko 1999; Grinin 2000). It is possible that some of the stars in our sample with aperiodic behavior could be considered UXors, though a study of color variability and polarization would be required to determine this.

5. Conclusions

CTTS that present extinction dominated light curves, such as the quasi-periodic AA Tau-like behavior or aperiodic extinction events, are common in NGC 2264. Of 159 cluster members that show signs of accretion, 33 present one of these two behaviors, i.e., $(21 \pm 4)\%$. These objects give us insight into the phenomena that take place in the inner region of circumstellar disks, a region that is otherwise difficult to study because of its proximity to the star and to instrumental limitations.

Extinction laws that include dust grains considerably larger than those found typically for the interstellar medium are necessary to account for the ratios between amplitudes in optical and IR light curves. This suggests that grain growth has occurred in these disks.

A model proposed to explain the light curve of the CTTS AA Tau, in which at the base of an accretion column there is an optically thick warp in the inner circumstellar disk region that occults the stellar photosphere periodically, was tested on 21 CTTS in NGC 2264. This occultation model was shown to be successful at reproducing the widths and amplitudes of AA Tau-like flux dips in the light curves of most of these stars, using warp parameters that are similar to those used for AA Tau. Typical ratios between this warp's maximum height and the radius at which it is located were found to be between $h_{\max}/R_{\rm w} = 0.2$ and $h_{\max}/R_{\rm w} = 0.3$. The warp's height and azimuthal extension were shown to be variable on a timescale of days, presenting typical variations of 10–20% between rotation cycles, though there is strong evidence that the occulting structure can exist over timescales of a few years. We have shown that, when this is the case, the warp maintains similar parameters during that time and remains at about the same radial distance.

For the few cases where the occultation model is unable to reproduce an AA Tau-like light curve using a classical inner disk warp, we have proposed a scenario where more than one accretion column exists in each hemisphere, and dust is lifted above the disk plane at other locations around the disk, all of which occult the star. This can account for the multiple flux dips per stellar rotation seen in the light curves. In many cases, even when a single accretion column in the visible hemisphere is able to account for the main features of an AA Tau-like light curve, we observe various narrow, shallow dips alongside the deeper, broader flux dips attributed to occultation by the warp associated with the main accretion column. We attribute these traits to the existence of secondary accretion streams that coexist with the main accretion funnel flows.

We ascribe AA Tau-like light curves to a stable accretion scenario, and light curves that present aperiodic extinction events to an unstable accretion scenario, and have shown that a star may suffer a transition from one to the other in the few years that separate our two CoRoT observing runs. For two stars with aperiodic extinction dominated light curves, we find evidence of hot spots associated with occultations, through an increase in veiling during light curve minima. We have also shown that AA Tau-like light curves are more common among stars of intermediate to high mass within the CTTS range ($0.7\ M_\odot \lesssim M_* \lesssim 2.0\ M_\odot$) than among those of lower mass ($M_* \lesssim 0.7\ M_\odot$), an aspect we believe may be linked to stellar magnetic field configurations.

We have shown that all but one star in our initial sample of possible AA Tau-like systems (Mon-1131, which is seen at a low inclination) fit very well within the AA Tau-like scenario. For nine of these stars we see clear evidence of a hot spot appearing simultaneously, or nearly so, with the occultation, either through an increase in veiling in the spectra or through a bluing effect observed in the color photometry. This strongly supports the idea that the flux dips observed in the CoRoT light curves are due to occultation by an inner disk warp that is associated with stable accretion funnel flows. We can therefore state with reasonable confidence that these are AA Tau-like systems.

Acknowledgements. The authors thank the referee V. Grinin for his contribution to the discussion. This work is based on data collected by the CoRoT satellite, and in part on observations made with the *Spitzer* Space Telescope, operated by the Jet Propulsion Laboratory, California Institute of Technology, under a contract with NASA. Support for this work was provided by NASA through an award issued by JPL/Caltech. PTM, SHPA, MMG, APS and NNJF acknowledge funding support from CAPES, CNPq, FAPEMIG, and Cofecub. J.B. acknowledges funding support from Cofecub, CNES, and the grant ANR 2011 Blanc SIMI5-6 020 01.

References

Alencar, S. H. P., Teixeira, P. S., Guimarães, M. M., et al. 2010, A&A, 519, A88
Artemenko, S. A., Grankin, K. N., & Petrov, P. P. 2012, Astron. Lett., 38, 783
Baglin, A., Auvergne, M., Barge, P., et al. 2006, in ESA SP 1306, eds. M. Fridlund, A. Baglin, J. Lochard, & L. Conroy, 33
Bertout, C. 2000, A&A, 363, 984
Bessolaz, N., Zanni, C., Ferreira, J., Keppens, R., & Bouvier, J. 2008, A&A, 478, 155
Boulade, O., Charlot, X., Abbon, P., et al. 2003, in Instrument Design and Performance for Optical/Infrared Ground-based Telescopes, eds. M. Iye & A. F. M. Moorwood, SPIE Conf. Ser., 4841, 72
Bouvier, J., Chelli, A., Allain, S., et al. 1999, A&A, 349, 619
Bouvier, J., Grankin, K. N., Alencar, S. H. P., et al. 2003, A&A, 409, 169
Bouvier, J., Alencar, S. H. P., Boutelier, T., et al. 2007, A&A, 463, 1017
Bouvier, J., Grankin, K., Ellerbroek, L. E., Bouy, H., & Barrado, D. 2013, A&A, 557, A77
Cardelli, J. A., Clayton, G. C., & Mathis, J. S. 1989, ApJ, 345, 245
Cody, A. M., Stauffer, J., Baglin, A., et al. 2014, AJ, 147, 82
Dahm, S. E. 2008, in Handbook of Star Forming Regions, Vol. I., ed. B. Reipurth, 966
Donati, J.-F., Skelly, M. B., Bouvier, J., et al. 2010, MNRAS, 402, 1426
Donati, J.-F., Bouvier, J., Walter, F. M., et al. 2011, MNRAS, 412, 2454
Fazio, G. G., Hora, J. L., Allen, L. E., et al. 2004, ApJS, 154, 10
Flaccomio, E., Micela, G., & Sciortino, S. 2006, A&A, 455, 903
Flaherty, K. M., & Muzerolle, J. 2010, ApJ, 719, 1733
Fonseca, N. N. J., Alencar, S. H. P., Bouvier, J., Favata, F., & Flaccomio, E. 2014, A&A, 567, A39
Fűrész, G., Hartmann, L. W., Szentgyorgyi, A. H., et al. 2006, ApJ, 648, 1090
Gregory, S. G., Donati, J.-F., Morin, J., et al. 2012, ApJ, 755, 97
Grinin, V. P. 2000, in Disks, Planetesimals, and Planets, ed. G. Garzón, C. Eiroa, D. de Winter, & T. J. Mahoney,ASP Conf. Ser., 219, 216
Hartmann, L. 2001, AJ, 121, 1030
Hartmann, L., Hewett, R., & Calvet, N. 1994, ApJ, 426, 669
Herbst, W., & Shevchenko, V. S. 1999, AJ, 118, 1043
Hirose, S., & Turner, N. J. 2011, ApJ, 732, L30
Johns-Krull, C. M., Valenti, J. A., Piskunov, N. E., Saar, S. H., & Hatzes, A. P. 2001, in Magnetic Fields Across the Hertzsprung-Russell Diagram, eds. G. Mathys, S. K. Solanki, & D. T. Wickramasinghe, ASP Conf. Ser., 248, 527
Kochukhov, O. P. 2007, in Physics of Magnetic Stars, eds. I. I. Romanyuk, D. O. Kudryavtsev, O. M. Neizvestnaya, & V. M. Shapoval, 109
Kulkarni, A. K., & Romanova, M. M. 2009, MNRAS, 398, 701
Kupka, F., Piskunov, N., Ryabchikova, T. A., Stempels, H. C., & Weiss, W. W. 1999, A&AS, 138, 119
Kupka, F. G., Ryabchikova, T. A., Piskunov, N. E., Stempels, H. C., & Weiss, W. W. 2000, Baltic Astron., 9, 590
Kurosawa, R., & Romanova, M. M. 2013, MNRAS, 431, 2673
Kurosawa, R., Harries, T. J., & Symington, N. H. 2006, MNRAS, 370, 580
Lada, C. J., Muench, A. A., Luhman, K. L., et al. 2006, AJ, 131, 1574
Lamm, M. H., Bailer-Jones, C. A. L., Mundt, R., Herbst, W., & Scholz, A. 2004, A&A, 417, 557
Lamm, M. H., Mundt, R., Bailer-Jones, C. A. L., & Herbst, W. 2005, A&A, 430, 1005
Lejeune, T., Cuisinier, F., & Buser, R. 1997, A&AS, 125, 229
Lima, G. H. R. A., Alencar, S. H. P., Calvet, N., Hartmann, L., & Muzerolle, J. 2010, A&A, 522, A104
Morin, J., Donati, J.-F., Petit, P., et al. 2010, MNRAS, 407, 2269
Muzerolle, J., Calvet, N., & Hartmann, L. 2001, ApJ, 550, 944
Pasquini, L., Avila, G., Blecha, A., et al. 2002, The Messenger, 110, 1
Piskunov, N. E., Kupka, F., Ryabchikova, T. A., Weiss, W. W., & Jeffery, C. S. 1995, A&AS, 112, 525
Preibisch, T., Kim, Y.-C., Favata, F., et al. 2005, ApJS, 160, 401
Ramírez, S. V., Rebull, L., Stauffer, J., et al. 2004, AJ, 127, 2659
Rebull, L. M., Makidon, R. B., Strom, S. E., et al. 2002, AJ, 123, 1528
Rebull, L. M., Cody, A. M., Covey, K. R., et al. 2014, AJ, 148, 92
Romanova, M. M., Ustyugova, G. V., Koldoba, A. V., & Lovelace, R. V. E. 2009, MNRAS, 399, 1802
Romanova, M. M., Ustyugova, G. V., Koldoba, A. V., & Lovelace, R. V. E. 2013, MNRAS, 430, 699
Romanova, M. M., Lovelace, R. V. E., Bachetti, M., et al. 2014, in Eur. Phys. J. Web Conf., 64, 5001
Ryabchikova, T. A., Piskunov, N. E., Kupka, F., & Weiss, W. W. 1997, Baltic Astron., 6, 244
Samadi, R., Fialho, F., Costa, J. E. S., et al. 2006, in ESA SP 1306, eds. M. Fridlund, A. Baglin, J. Lochard, & L. Conroy, 317
Shu, F., Najita, J., Ostriker, E., et al. 1994, ApJ, 429, 781
Siess, L., Dufour, E., & Forestini, M. 2000, A&A, 358, 593
Stauffer, J., Cody, A. M., Baglin, A., et al. 2014, AJ, 147, 83
Stauffer, J., Cody, A. M., McGinnis, P., et al. 2015, AJ, accepted
Teixeira, P. S., Lada, C. J., Marengo, M., & Lada, E. A. 2012, A&A, 540, A83
Terquem, C., & Papaloizou, J. C. B. 2000, A&A, 360, 1031
Turner, N. J., Carballido, A., & Sano, T. 2010, ApJ, 708, 188
Valenti, J. A., & Piskunov, N. 1996, A&AS, 118, 595
Venuti, L., Bouvier, J., Flaccomio, E., et al. 2014, A&A, 570, A82
White, R. J., & Basri, G. 2003, ApJ, 582, 1109
Whitney, B. A., Robitaille, T. P., Bjorkman, J. E., et al. 2013, ApJS, 207, 30
Young, A. 1978, PASP, 90, 144
Zanni, C., & Ferreira, J. 2013, A&A, 550, A99

Pages 23 to 27 are available in the electronic edition of the journal at http://www.aanda.org

Astronomy & Astrophysics manuscript no. OI_profiles_in_NGC2264
July 23, 2017
©ESO 2017

Ejection processes in the young open cluster NGC 2264 - A study of the [OI] 6300Å emission line⋆

P. McGinnis[1,2], C. Dougados[2], S. H. P. Alencar[1], J. Bouvier[2], and S. Cabrit[3]

[1] Departamento de Física - ICEx - UFMG, Av. Antônio Carlos, 6627, 30270-901 Belo Horizonte, MG, Brazil
e-mail: pauline@fisica.ufmg.br
[2] Univ. Grenoble Alpes, CNRS, IPAG, F-38000 Grenoble, France
[3] LERMA, Observatoire de Paris, CNRS, 61 Av. de l'Observatoire, 75014 Paris, France

July 23, 2017

ABSTRACT

Context. The [OI] 6300Å line is a well-known tracer of jets and winds in young stars, often showing three features: a high-velocity component (HVC), believed to originate in bipolar, collimated jets; and a broad and narrow low-velocity component (BLVC and NLVC), whose origins are still under debate.
Aims. We exploit the vast dataset available for the young, open cluster NGC 2264, in order to search for correlations between the different components of the [OI] 6300Å line and stellar/disk/accretion properties. With this, we aim to investigate different outflow processes that occur within the circumstellar environment of young stars.
Methods. We analyze FLAMES spectra of 184 classical T Tauri stars (CTTS) and Herbig AeBe stars in NGC 2264 and identify the different components of the [OI] line. We calculate line luminosities and jet propagation velocities, then compare these values with known stellar and accretion parameters.
Results. The HVC is only detected among systems with optically thick inner disks and the BLVC is found in few systems that present anemic disks, while the NLVC is common among systems with thin inner disks. It seems that as a system evolves, the NLVC tends to dominate the [OI] emission. The luminosity of the [OI] line and all of its components correlate positively with the stellar and accretion luminosity. A comparison of [OI] profiles with CoRoT light curves shows that the HVC is found most often among sources with irregular, aperiodic photometric variability. CTTSs accreting in an unstable regime appear to have broader LVCs and stronger HVCs than those accreting in a stable regime. An analysis of the HVC shows that the mechanical luminosity transported by protostellar jets correlates positively with the accretion luminosity. However no stellar properties, such as effective temperature, mass or stellar rotation, appear to significantly influence any property of these jets.
Conclusions. The NLVCs in our sample have centroid velocities and widths consistent with what is expected for photoevaporative disk winds, while our BLVCs present blueshifts compatible with an origin in inner disk winds, likely connected to the accretion process. The lack of correlations between the HVC and stellar parameters suggests that it is the disk, rather than the star, that governs the launching of protostellar jets. However, our large uncertainties in jet velocity may be masking possible trends.

Key words. accretion, accretion disks – line: formation – stars: jets – stars: pre-main sequence – stars: winds, outflows

1. Introduction

Outflows are a ubiquitous aspect of star formation. Powerful, highly collimated, bipolar jets are commonly found in association with YSOs of different evolutionary stages. The many similarities between jets emanating from these different sources suggest that the same physical mechanism is at work in different stages of star formation (Cabrit 2002). Though it has been well established that these ejection phenomena are closely associated with disk accretion (Cabrit et al. 1990; Hartigan et al. 1995, hereafter HEG95), likely occuring as the byproduct of magnetic acceleration from the inner accretion disk (Ferreira et al. 2006; Ray et al. 2007), the exact mechanism which drives them is not yet well understood. It is yet to be determined if these winds originate at the interface between stellar magnetosphere and accretion disk (the X-wind model, Shang et al. 2007), or in a wide range of disk radii up to a few AU from the star (the magneto-centrifugal disk wind, or D-wind model, Pudritz et al. 2007). Statistical studies to test which stellar (or disk) properties scale with jet properties can help shed light on the matter.

Slow winds are also present in young, accreting, low-mass stars (e.g., HEG95, Natta et al. 2014, hereafter N14). These objects, known as classical T Tauri stars (hereafter, CTTS), are optically visible, thus allowing us to obtain good estimates of stellar and accretion properties. They are Class II objects, meaning they are associated with well-characterized Keplerian disks. These aspects make them ideal sites for testing mass ejection models and for performing statistical studies to search for correlations between jet/wind properties and stellar/disk properties.

One of the strongest spectroscopic tracers of jets and winds in CTTSs is the forbidden [OI] 6300Å emission line. This line profile has traditionally been separated into two distinct features: a low-velocity component (LVC), centered close to the stellar rest frame or blueshifted by up to ~ 20 km/s, and a high-velocity component (HVC), blueshifted by ~ 50 - 200 km/s from the stellar rest frame (HEG95). The HVC is believed to arise in the fast, bipolar jets that are associated with these young objects, while the LVC seems to originate in slower moving winds. The

⋆ Tables 5, 4 and 7 and Figure 23 are only available in electronic form.

Appendix B

Papers published during the CSI 2264 campaign

Some of the work performed during the development of this thesis contributed to the following papers during the CSI 2264 collaboration.

The Astronomical Journal, 149:130 (30pp), 2015 April doi:10.1088/0004-6256/149/4/130
© 2015. The American Astronomical Society. All rights reserved.

CSI 2264: CHARACTERIZING YOUNG STARS IN NGC 2264 WITH SHORT-DURATION PERIODIC FLUX DIPS IN THEIR LIGHT CURVES*

John Stauffer[1], Ann Marie Cody[1,19], Pauline McGinnis[6], Luisa Rebull[1], Lynne A. Hillenbrand[2], Neal J. Turner[3], John Carpenter[2], Peter Plavchan[1], Sean Carey[1], Susan Terebey[4], María Morales-Calderón[5], Silvia H. P. Alencar[6], Jerome Bouvier[7], Laura Venuti[7], Lee Hartmann[8], Nuria Calvet[8], Giusi Micela[9], Ettore Flaccomio[9], Inseok Song[10], Rob Gutermuth[11], David Barrado[5], Frederick J. Vrba[12], Kevin Covey[13], Debbie Padgett[14], William Herbst[15], Edward Gillen[16], Wladimir Lyra[3,20], Marcelo Medeiros Guimaraes[18], Herve Bouy[5], and Fabio Favata[17]
[1] Spitzer Science Center, California Institute of Technology, Pasadena, CA 91125, USA; stauffer@ipac.caltech.edu
[2] Astronomy Department, California Institute of Technology, Pasadena, CA 91125, USA
[3] Jet Propulsion Laboratory, California Institute of Technology, Pasadena, CA 91109, USA
[4] Department of Physics and Astronomy, 5151 State University Drive, California State University at Los Angeles, Los Angeles, CA 90032, USA
[5] Centro de Astrobiología, Dpto. de Astrofísica, INTA-CSIC, PO BOX 78, E-28691, ESAC Campus, Villanueva de la Cañada, Madrid, Spain
[6] Departamento de Física—ICEx—UFMG, Av. Antônio Carlos, 6627, 30270-901, Belo Horizonte, MG, Brazil
[7] Université de Grenoble, Institut de Planétologie et d'Astrophysique de Grenoble (IPAG), F-38000 Grenoble, France; CNRS, IPAG, F-38000 Grenoble, France
[8] Department of Astronomy, University of Michigan, 500 Church Street, Ann Arbor, MI 48105, USA
[9] INAF—Osservatorio Astronomico di Palermo, Piazza del Parlamento 1, I-90134, Palermo, Italy
[10] Department of Physics and Astronomy, The University of Georgia, Athens, GA 30602–2451, USA
[11] Department of Astronomy, University of Massachusetts, Amherst, MA 01003, USA
[12] U.S. Naval Observatory, Flagstaff Station, 10391 West Naval Observatory Road, Flagstaff, AZ 86001, USA
[13] Department of Physics and Astronomy (MS-9164), Western Washington Univ., 516 High St., Bellingham, WA 98225, USA
[14] NASA/Goddard Space Flight Center, Code 665, Greenbelt, MD 20771, USA
[15] Astronomy Department, Wesleyan University, Middletown, CT 06459, USA
[16] Department of Physics, University of Oxford, Keble Road, Oxford, OX1 3RH, UK
[17] European Space Agency, 8-10 rue Mario Nikis, F-75738 Paris Cedex 15, France
[18] Departamento de Física e Matemática-UFSJ-Rodovia MG 443, KM 7, 36420-000, Ouro Branco, MG, Brazil
[19] NASA Ames Research Center, *Kepler* Science Office, Mountain View, CA 94035, USA
Received 2014 December 1; accepted 2015 January 23; published 2015 March 16

ABSTRACT

We identify nine young stellar objects (YSOs) in the NGC 2264 star-forming region with optical *CoRoT* light curves exhibiting short-duration, shallow periodic flux dips. All of these stars have infrared excesses that are consistent with their having inner disk walls near the Keplerian co-rotation radius. The repeating photometric dips have FWHMs generally less than 1 day, depths almost always less than 15%, and periods ($3 < P < 11$ days) consistent with dust near the Keplerian co-rotation period. The flux dips vary considerably in their depth from epoch to epoch, but usually persist for several weeks and, in two cases, were present in data collected in successive years. For several of these stars, we also measure the photospheric rotation period and find that the rotation and dip periods are the same, as predicted by standard "disk-locking" models. We attribute these flux dips to clumps of material in or near the inner disk wall, passing through our line of sight to the stellar photosphere. In some cases, these dips are also present in simultaneous *Spitzer* IRAC light curves at 3.6 and 4.5 microns. We characterize the properties of these dips, and compare the stars with light curves exhibiting this behavior to other classes of YSOs in NGC 2264. A number of physical mechanisms could locally increase the dust scale height near the inner disk wall, and we discuss several of those mechanisms; the most plausible mechanisms are either a disk warp due to interaction with the stellar magnetic field or dust entrained in funnel-flow accretion columns arising near the inner disk wall.

Key words: circumstellar matter – open clusters and associations: individual (NGC 2264) – stars: pre-main sequence – stars: variables: T Tauri, Herbig Ae/Be

1. INTRODUCTION

Understanding how young stellar objects (YSOs) assemble themselves and how the accretion process works requires understanding the structure and evolution of the inner disk on size scales <0.1 AU. Even with the advent of infrared (IR) and radio interferometry, imaging of even the nearest YSOs to detect structure on these size scales is impractical. It therefore becomes necessary to infer the spatial structure and composition on these size scales indirectly from, for example, spectral energy distributions (SEDs), high-resolution spectra, or variability studies.

SEDs have provided some of the most important insights into the structure and evolution of the inner disks of YSOs. These SEDs have been used not only to argue for the presence of an inner disk wall, located roughly at the dust sublimation boundary, but also that the upper edge of the wall is in most cases curved (McClure et al. 2013). Some YSOs have both

* Based on data from the *Spitzer* and *CoRoT* missions, as well as the Canada France Hawaii Telescope (CFHT) MegaCam CCD, and the European Southern Observatory Very Large Telescope, Paranal Chile, under program 088.C-0239. The *CoRoT* space mission was developed and is operated by the French space agency CNES, with participation of ESA's RSSD and Science Programmes, Austria, Belgium, Brazil, Germany, and Spain. MegaCam is a joint project of CFHT and CEA/DAPNIA, which is operated by the National Research Council (NRC) of Canada, the Institute National des Sciences de l'Univers of the Centre National de la Recherche Scientifique of France, and the University of Hawaii.
[20] NASA Sagan Fellow.

A&A 586, A47 (2016)
DOI: 10.1051/0004-6361/201526599
© ESO 2016

Astronomy & Astrophysics

CSI 2264: Accretion process in classical T Tauri stars in the young cluster NGC 2264⋆

A. P. Sousa[1], S. H. P. Alencar[1], J. Bouvier[2,3], J. Stauffer[4], L. Venuti[2,3], L. Hillenbrand[5], A. M. Cody[6], P. S. Teixeira[7], M. M. Guimarães[8], P. T. McGinnis[1], L. Rebull[4], E. Flaccomio[9], G. Fürész[10], G. Micela[9], and J. F. Gameiro[11]

[1] Departmento de Física-Icex-UFMG Antônio Carlos, 6627, 31270-90 Belo Horizonte, MG, Brazil
e-mail: alana@fisica.ufmg.br
[2] Univ. Grenoble Alpes, IPAG, 38000 Grenoble, France
[3] CNRS, IPAG, 38000 Grenoble, France
[4] Spitzer Science Center, California Institute of Technology, 1200 East California Boulevard, Pasadena, CA 91125, USA
[5] Astronomy Department, California Institute of Technology, Pasadena, CA 91125, USA
[6] NASA Ames Research Center, Kepler Science Office, Mountain View, CA 94035, USA
[7] Universität Wien, Institut für Astrophysik, Türkenschanzstrasse 17, 1180 Vienna, Austria
[8] Departmento de Física, Universidade Federal de Sergipe, SE 49100-000 Aracaju, Brazil
[9] INAF–Osservatorio Astronomico di Palermo, Piazza del Parlamento 1, 90134 Palermo, Italy
[10] MIT Kavli Institute for Astrophysics and Space Research, 77 Mass Ave 37-582f, Cambridge, MA 02139, USA
[11] Instituto de Astrofísica e Ciências Espaciais and Faculdade de Ciências Universidade do Porto, CAUP, Rua da Estrelas, 4150-762 Porto, Portugal

Received 25 May 2015 / Accepted 4 September 2015

ABSTRACT

Context. NGC 2264 is a young stellar cluster (~3 Myr) with hundreds of low-mass accreting stars that allow a detailed analysis of the accretion process taking place in the pre-main sequence.
Aims. Our goal is to relate the photometric and spectroscopic variability of classical T Tauri stars to the physical processes acting in the stellar and circumstellar environment, within a few stellar radii from the star.
Methods. NGC 2264 was the target of a multiwavelength observational campaign with CoRoT, MOST, *Spitzer*, and *Chandra* satellites and photometric and spectroscopic observations from the ground. We classified the CoRoT light curves of accreting systems according to their morphology and compared our classification to several accretion diagnostics and disk parameters.
Results. The morphology of the CoRoT light curve reflects the evolution of the accretion process and of the inner disk region. Accretion burst stars present high mass-accretion rates and optically thick inner disks. AA Tau-like systems, whose light curves are dominated by circumstellar dust obscuration, show intermediate mass-accretion rates and are located in the transition of thick to anemic disks. Classical T Tauri stars with spot-like light curves correspond mostly to systems with a low mass-accretion rate and low mid-IR excess. About 30% of the classical T Tauri stars observed in the 2008 and 2011 CoRoT runs changed their light-curve morphology. Transitions from AA Tau-like and spot-like to aperiodic light curves and vice versa were common. The analysis of the Hα emission line variability of 58 accreting stars showed that 8 presented a periodicity that in a few cases was coincident with the photometric period. The blue and red wings of the Hα line profiles often do not correlate with each other, indicating that they are strongly influenced by different physical processes. Classical T Tauri stars have a dynamic stellar and circumstellar environment that can be explained by magnetospheric accretion and outflow models, including variations from stable to unstable accretion regimes on timescales of a few years.

Key words. stars: formation – stars: variables: T Tauri, Herbig Ae/Be – open clusters and associations: individual: NGC 2264 – accretion, accretion disks

1. Introduction

Classical T Tauri stars (CTTSs) are young, low-mass stars ($M_* \leq 2\ M_\odot$), with spectral types from F to M. They are surrounded by a circumstellar disk from which they are still accreting material. They present strong and broad emission lines in their spectra and show emission excess with respect to the stellar photosphere that goes from the radio to the ultraviolet (Bouvier et al. 2007b). CTTSs have strong magnetic fields (Johns-Krull et al. 1999; Johnstone et al. 2014) that disrupt the accretion disk at a few stellar radii from the star and channel the accreting material, forming accretion columns. The accreting gas hits the stellar surface and creates hot spots. CTTSs also present cold spots at the stellar surface; these are caused by magnetic activity (Bouvier et al. 1995). Part of the gas in the inner disk region is ejected as a wind from the star-disk system along open magnetic field lines that may form collimated jets (e.g., Ferreira et al. 2006). In a few million years, before reaching the main sequence, CTTSs lose their disks and become weak-lined T Tauri stars (WTTSs), which no longer show detectable signs of accretion (e.g., Meyer 2009).

A characteristic of CTTSs is the photometric and spectroscopic variability at various wavelengths. The photometric variability occurs from X-ray to infrared on a timescale from a few minutes to several years and is usually irregular (e.g., Appenzeller & Mundt 1989). Some stars, however, show periodic behavior, which may be due to the presence of stable

⋆ Full Tables 2 and 3 are only available at the CDS via anonymous ftp to cdsarc.u-strasbg.fr (130.79.128.5) or via http://cdsarc.u-strasbg.fr/viz-bin/qcat?J/A+A/586/A47

The Astronomical Journal, 151:60 (30pp), 2016 March doi:10.3847/0004-6256/151/3/60
© 2016. The American Astronomical Society. All rights reserved.

CSI 2264: CHARACTERIZING YOUNG STARS IN NGC 2264 WITH STOCHASTICALLY VARYING LIGHT CURVES*

John Stauffer[1], Ann Marie Cody[2], Luisa Rebull[1], Lynne A. Hillenbrand[3], Neal J. Turner[4], John Carpenter[3], Sean Carey[1], Susan Terebey[5], María Morales-Calderón[6], Silvia H. P. Alencar[7], Pauline McGinnis[7], Alana Sousa[7], Jerome Bouvier[8,9], Laura Venuti[8,9], Lee Hartmann[10], Nuria Calvet[10], Giusi Micela[11], Ettore Flaccomio[11], Inseok Song[12], Rob Gutermuth[13], David Barrado[6], Frederick J. Vrba[14], Kevin Covey[15], William Herbst[16], Edward Gillen[17], Marcelo Medeiros Guimarães[18], Herve Bouy[6], and Fabio Favata[19]
[1] Spitzer Science Center, California Institute of Technology, Pasadena, CA 91125, USA; stauffer@ipac.caltech.edu
[2] NASA Ames Research Center, *Kepler* Science Office, Mountain View, CA 94035, USA
[3] Astronomy Department, California Institute of Technology, Pasadena, CA 91125, USA
[4] Jet Propulsion Laboratory, California Institute of Technology, Pasadena, CA 91109, USA
[5] Department of Physics and Astronomy, 5151 State University Drive, California State University at Los Angeles, Los Angeles, CA 90032, USA
[6] Centro de Astrobiología, Dpto. de Astrofísica, INTA-CSIC, P.O. BOX 78, E-28691, ESAC Campus, Villanueva de la Cañada, Madrid, Spain
[7] Departamento de Física—ICEx—UFMG, Av. Antônio Carlos, 6627, 30270-901, Belo Horizonte, MG, Brazil
[8] Université de Grenoble, Institut de Planétologie et d'Astrophysique de Grenoble (IPAG), F-38000 Grenoble, France
[9] CNRS, IPAG, F-38000 Grenoble, France
[10] Department of Astronomy, University of Michigan, 500 Church Street, Ann Arbor, MI:48105, USA
[11] INAF—Osservatorio Astronomico di Palermo, Piazza del Parlamento 1, I-90134, Palermo, Italy
[12] Department of Physics and Astronomy, The University of Georgia, Athens, GA 30602-2451, USA
[13] Department of Astronomy, University of Massachusetts, Amherst, MA 01003, USA
[14] U.S. Naval Observatory, Flagstaff Station, 10391 West Naval Observatory Road, Flagstaff, AZ 86001, USA
[15] Department of Physics and Astronomy (MS-9164), Western Washington Univ., 516 High St., Bellingham, WA 98225, USA
[16] Astronomy Department, Wesleyan University, Middletown, CT 06459, USA
[17] Department of Physics, University of Oxford, Keble Road, Oxford, OX1 3RH, UK
[18] Departamento de Física—UFS—Rod. Marechal Rondon, 49100-000, São Cristovão, SE, Brazil
[19] European Space Agency, 8-10 rue Mario Nikis, F-75738 Paris Cedex 15, France
Received 2015 October 12; accepted 2016 January 7; published 2016 February 18

ABSTRACT

We provide *CoRoT* and *Spitzer* light curves and other supporting data for 17 classical T Tauri stars in NGC 2264 whose *CoRoT* light curves exemplify the "stochastic" light curve class as defined in 2014 by Cody et al. The most probable physical mechanism to explain the optical variability within this light curve class is time-dependent mass accretion onto the stellar photosphere, producing transient hot spots. Where we have appropriate spectral data, we show that the veiling variability in these stars is consistent in both amplitude and timescale with the optical light curve morphology. The veiling variability is also well-correlated with the strength of the He I 6678 Å emission line, predicted by models to arise in accretion shocks on or near the stellar photosphere. Stars with accretion burst light curve morphology also have variable mass accretion. The stochastic and accretion burst light curves can both be explained by a simple model of randomly occurring flux bursts, with the stochastic light curve class having a higher frequency of lower amplitude events. Members of the stochastic light curve class have only moderate mass accretion rates. Their Hα profiles usually have blueshifted absorption features, probably originating in a disk wind. The lack of periodic signatures in the light curves suggests that little of the variability is due to long-lived hot spots rotating into or out of our line of sight; instead, the primary driver of the observed photometric variability is likely to be instabilities in the inner disk that lead to variable mass accretion.

Key words: circumstellar matter – open clusters and associations: individual (NGC 2264) – stars: pre-main sequence – stars: protostars – stars: variables: T Tauri, Herbig Ae/Be

1. INTRODUCTION

The published literature on the photometric variability of T Tauri stars now extends back in time more than 150 years (Schmidt 1861, 1866), predating by nearly 100 years the general acceptance that T associations are sites of recent/current star formation (Ambartsumian 1954; Salpeter 1954), and therefore that the photometric variability of T Tauri stars is likely a signpost of youth (Walker 1956). Haro & Herbig (1955) and Walker (1956) discovered that many of the photometrically variable T Tauri stars also had UV excesses and abnormally weak photospheric absorption lines (now usually described as spectral "veiling"); the former authors concluded that the UV excesses might originate from a small hot spot on or near the stellar photosphere. However, it was not until the 1970s that the modern paradigm for young stellar objects (YSOs) began to develop, first by linking the photospheric hotspots to accretion from a disk (Walker 1972; Wolf et al. 1977), and eventually by having the accretion stream be channeled by magnetic field lines connecting the star and inner disk (Ghosh & Lamb 1978; Königl 1991).

Based on photometry derived from visual observations or photographic plates, Joy (1945) made photometric variability

* Based on data from the *Spitzer* and *CoRoT* missions, as well as the Canada–France–Hawaii Telescope (CFHT) MegaCam CCD, and the European Southern Observatory Very Large Telescope, Paranal Chile, under program 088.C-0239. The *CoRoT* space mission was developed and is operated by the French space agency CNES, with particpiation of ESA's RSSD and Science Programmes, Austria, Belgium, Brazil, Germany, and Spain. MegaCam is a joint project of CFHT and CEA/DAPNIA, which is operated by the National Research Council (NRC) of Canada, the Institute National des Sciences de l'Univers of the Centre National de la Recherche Scientifique of France, and the University of Hawaii.

Bibliography

Adams, M. T., Strom, K. M., & Strom, S. E. 1983, ApJS, 53, 893 [1.4]

Affer, L., Micela, G., Favata, F., Flaccomio, E., & Bouvier, J. 2013, MNRAS, 430, 1433 [1.4]

Alencar, S. H. P., Teixeira, P. S., Guimarães, M. M., et al. 2010, A&A, 519, A88 [(document), 1.3, 1.4, 1.10, 3.1, 3.2, 3.4, 5.4]

Ambartsumian, V. A. 1947, Acad. Sci. Armenian S.S.R., Yerevan [1.2]

Ambartsumian, V. A. 1954, Memoires of the Societe Royale des Sciences de Liege, 1, 293 [1.2]

Appenzeller, I. & Bertout, C. 2013, A&A, 558, A83 [5.4, 5.5, 6]

Artemenko, S. A., Grankin, K. N., & Petrov, P. P. 2012, Astronomy Letters, 38, 783 [4.6.2]

Baglin, A., Auvergne, M., Barge, P., et al. 2006, in ESA Special Publication, Vol. 1306, ESA Special Publication, ed. M. Fridlund, A. Baglin, J. Lochard, & L. Conroy, 33 [1.4]

Baraffe, I., Chabrier, G., Barman, T. S., Allard, F., & Hauschildt, P. H. 2003, A&A, 402, 701 [5.4]

Bertout, C. 2000, A&A, 363, 984 [4.6.3]

Bertout, C., Basri, G., & Bouvier, J. 1988, ApJ, 330, 350 [6]

Bessell, M. S., Castelli, F., & Plez, B. 1998, A&A, 333, 231 [3.3.1]

Bessolaz, N., Zanni, C., Ferreira, J., Keppens, R., & Bouvier, J. 2008, A&A, 478, 155 [1.2.1]

Blinova, A. A., Romanova, M. M., & Lovelace, R. V. E. 2016, MNRAS, 459, 2354 [4.7, 6]

Boss, A. P. 1995, in Revista Mexicana de Astronomia y Astrofisica Conference Series, Vol. 1, Revista Mexicana de Astronomia y Astrofisica Conference Series, ed. S. Lizano & J. M. Torrelles, 165 [1.1]

Boulade, O., Charlot, X., Abbon, P., et al. 2003, in Society of Photo-Optical Instrumentation Engineers (SPIE) Conference Series, Vol. 4841, Instrument Design and Performance for Optical/Infrared Ground-based Telescopes, ed. M. Iye & A. F. M. Moorwood, 72–81 [2.2,

2.2.3]

Bouvier, J., Alencar, S. H. P., Boutelier, T., et al. 2007, A&A, 463, 1017 [1.3, 1.8, 3.4, 4.1, 4.5, 4.6.1, 4.7, 5.3]

Bouvier, J., Chelli, A., Allain, S., et al. 1999, A&A, 349, 619 [1.3, 1.6, 1.3, 1.7, 3.4, 4.1, 4.6, 4.6, 4.6.3, 6]

Bouvier, J., Grankin, K., Ellerbroek, L. E., Bouy, H., & Barrado, D. 2013, A&A, 557, A77 [1.3, 4.1]

Bouvier, J., Grankin, K. N., Alencar, S. H. P., et al. 2003, A&A, 409, 169 [1.3, 3.4, 4.1, 4.4, 4.5, 4.6.1]

Bouvier, J., Lanzafame, A. C., Venuti, L., et al. 2016, A&A, 590, A78 [1.4]

Burgasser, A. J., Kirkpatrick, J. D., Reid, I. N., et al. 2003, ApJ, 586, 512 [8]

Cabrit, S. 2002, in EAS Publications Series, Vol. 3, EAS Publications Series, ed. J. Bouvier & J.-P. Zahn, 147–182 [1.2.2]

Cabrit, S., Edwards, S., Strom, S. E., & Strom, K. M. 1990, ApJ, 354, 687 [1.2.2, 5.1.1, 5.2.1, 5.5, 6]

Cardelli, J. A., Clayton, G. C., & Mathis, J. S. 1989, ApJ, 345, 245 [4.2]

Cody, A. M., Stauffer, J., Baglin, A., et al. 2014, AJ, 147, 82 [1.4, 2.1, 2.2, 2.2.2, 3, 3.3.4, 3.4, 4.1, 4.1, 4.1, 4.5, 5.2]

Cohen, M. & Kuhi, L. V. 1979, ApJS, 41, 743 [3.3.1]

Costigan, G., Vink, J. S., Scholz, A., Ray, T., & Testi, L. 2014, MNRAS, 440, 3444 [4.7]

Covey, K. R., Ivezić, Ž., Schlegel, D., et al. 2007, AJ, 134, 2398 [3.3.1]

Cox, A. W., Grady, C. A., Hammel, H. B., et al. 2013, ApJ, 762, 40 [1.3, 4.1]

Dahm, S. E. 2008, The Young Cluster and Star Forming Region NGC 2264, ed. B. Reipurth, 966 [1.9, 1.4, 6]

Dahm, S. E. & Simon, T. 2005, AJ, 129, 829 [1.4, 3.3.1, 3.1]

Donati, J.-F. 2001, in Lecture Notes in Physics, Berlin Springer Verlag, Vol. 573, Astrotomography, Indirect Imaging Methods in Observational Astronomy, ed. H. M. J. Boffin, D. Steeghs, & J. Cuypers, 207 [6.1]

Donati, J.-F., Bouvier, J., Walter, F. M., et al. 2011, MNRAS, 412, 2454 [1.2, 1.2.1, 4.7]

Donati, J.-F., Howarth, I. D., Jardine, M. M., et al. 2006, MNRAS, 370, 629 [6.1]

Donati, J. F., Moutou, C., Malo, L., et al. 2016, Nature, 534, 662 [1]

Donati, J.-F., Skelly, M. B., Bouvier, J., et al. 2010a, MNRAS, 409, 1347 [1.2, 1.3]

Donati, J.-F., Skelly, M. B., Bouvier, J., et al. 2010b, MNRAS, 402, 1426 [1.2.1, 4.8]

Duchêne, G., McCabe, C., Pinte, C., et al. 2010, ApJ, 712, 112 [6]

Edwards, S., Cabrit, S., Strom, S. E., et al. 1987, ApJ, 321, 473 [5.1.2]

Edwards, S., Fischer, W., Hillenbrand, L., & Kwan, J. 2006, ApJ, 646, 319 [1.2.2]

Ercolano, B. & Owen, J. E. 2010, MNRAS, 406, 1553 [1.2.2, 5.1.2, 5.2.1, 5.4]

Ercolano, B. & Owen, J. E. 2016, MNRAS, 460, 3472 [1.2.2, 5.1.2, 5.2.1, 5.4]

Fang, M., van Boekel, R., Wang, W., et al. 2009, A&A, 504, 461 [3.3.4]

Fazio, G. G., Hora, J. L., Allen, L. E., et al. 2004, ApJS, 154, 10 [2.2]

Ferreira, J., Dougados, C., & Cabrit, S. 2006, A&A, 453, 785 [1, 1.2.2]

Fűrész, G., Hartmann, L. W., Szentgyorgyi, A. H., et al. 2006, ApJ, 648, 1090 [1.4, 2.5, 3.1]

Flaccomio, E., Micela, G., & Sciortino, S. 2006, A&A, 455, 903 [1.2, 1.4, 3.1]

Flaccomio, E., Micela, G., Sciortino, S., et al. 1999, A&A, 345, 521 [1.4]

Fonseca, N. N. J. 2016, PhD thesis, Universidade Federal de Minas Gerais, Brazil [4.2]

Fonseca, N. N. J., Alencar, S. H. P., Bouvier, J., Favata, F., & Flaccomio, E. 2014, A&A, 567, A39 [1.4, 6]

Font, A. S., McCarthy, I. G., Johnstone, D., & Ballantyne, D. R. 2004, ApJ, 607, 890 [5.1.2]

Gillen, E., Aigrain, S., McQuillan, A., et al. 2014, A&A, 562, A50 [1.4, 3.3.1, 3.4, 5.2]

Gilmore, G., Randich, S., Asplund, M., et al. 2012, The Messenger, 147, 25 [2.5]

Gorti, U., Hollenbach, D., Najita, J., & Pascucci, I. 2011, ApJ, 735, 90 [5.1.2]

Gregory, S. G., Donati, J.-F., Morin, J., et al. 2012, ApJ, 755, 97 [1.2.1, 4.8]

Grinin, V. P. 2000, in Astronomical Society of the Pacific Conference Series, Vol. 219, Disks, Planetesimals, and Planets, ed. G. Garzón, C. Eiroa, D. de Winter, & T. J. Mahoney, 216 [4.1]

Guarcello, M. G., Flaccomio, E., Micela, G., et al. 2017, A&A, 602, A10 [1.4, 5.2.1]

Gullbring, E., Hartmann, L., Briceño, C., & Calvet, N. 1998, ApJ, 492, 323 [1.2.1, 3.3.4, 3.3.4]

Haro, G. 1952, ApJ, 115, 572 [1.2.2]

Hartigan, P., Edwards, S., & Ghandour, L. 1995, ApJ, 452, 736 [1.2.2, 5.1.1, 6]

Hartmann, L. 2001, AJ, 121, 1030 [4.6.2]

Hartmann, L. 2009, Accretion Processes in Star Formation: Second Edition (Cambridge University Press) [1.1, 1.2, 1.2.2]

Hartmann, L., Herczeg, G., & Calvet, N. 2016, ARA&A, 54, 135 [1.2]

Hartmann, L., Hewett, R., & Calvet, N. 1994, ApJ, 426, 669 [1.2.1]

Herbig, G. H. 1951, ApJ, 113, 697 [1.2.2]

Herbig, G. H. 1960, ApJS, 4, 337 [1.1]

Herbst, W. & Shevchenko, V. S. 1999, AJ, 118, 1043 [4.1]

Herczeg, G. J. & Hillenbrand, L. A. 2014, ApJ, 786, 97 [5.4]

Hirose, S. & Turner, N. J. 2011, ApJL, 732, L30 [4.7]

Horne, J. H. & Baliunas, S. L. 1986, ApJ, 302, 757 [4.7]

Isobe, T., Feigelson, E. D., & Nelson, P. I. 1986, ApJ, 306, 490 [5.2.1]

Johns-Krull, C. M., Valenti, J. A., Piskunov, N. E., Saar, S. H., & Hatzes, A. P. 2001, in Astronomical Society of the Pacific Conference Series, Vol. 248, Magnetic Fields Across the Hertzsprung-Russell Diagram, ed. G. Mathys, S. K. Solanki, & D. T. Wickramasinghe, 527 [1.2]

Joy, A. H. 1945, ApJ, 102, 168 [1.1, 1.2]

Kendall, T. R., Bouvier, J., Moraux, E., James, D. J., & Ménard, F. 2005, A&A, 434, 939 [1.4]

Kochukhov, O. P. 2007, in Physics of Magnetic Stars, ed. I. I. Romanyuk, D. O. Kudryavtsev, O. M. Neizvestnaya, & V. M. Shapoval, 109–118 [3.3.3]

Kulkarni, A. K. & Romanova, M. M. 2009, MNRAS, 398, 701 [1.2.1, 4.7]

Kulkarni, A. K. & Romanova, M. M. 2013, MNRAS, 433, 3048 [4.6.3]

Kupka, F., Piskunov, N., Ryabchikova, T. A., Stempels, H. C., & Weiss, W. W. 1999, A&AS, 138, 119 [3.3.3]

Kupka, F. G., Ryabchikova, T. A., Piskunov, N. E., Stempels, H. C., & Weiss, W. W. 2000, Baltic Astronomy, 9, 590 [3.3.3]

Kurosawa, R., Harries, T. J., & Symington, N. H. 2006, MNRAS, 370, 580 [1.2.1]

Kurosawa, R. & Romanova, M. M. 2013, MNRAS, 431, 2673 [1.2.1, 1.4, 4.7, 4.7, 5.3]

Kurosawa, R., Romanova, M. M., & Harries, T. J. 2011, MNRAS, 416, 2623 [1.2.2]

Kwan, J. & Tademaru, E. 1995, ApJ, 454, 382 [1.2.2, 5.1.2]

Lada, C. J., Muench, A. A., Luhman, K. L., et al. 2006, AJ, 131, 1574 [4.2, 5.2.1]

Lamm, M. H., Bailer-Jones, C. A. L., Mundt, R., Herbst, W., & Scholz, A. 2004, A&A, 417, 557 [1.4, 3.1]

Lamm, M. H., Mundt, R., Bailer-Jones, C. A. L., & Herbst, W. 2005, A&A, 430, 1005 [4.6.2, 4.7]

Lavalley, M. P., Isobe, T., & Feigelson, E. D. 1992, in BAAS, Vol. 24, Bulletin of the American Astronomical Society, 839–840 [5.2.1]

Lim, B., Sung, H., Kim, J. S., et al. 2016, ApJ, 831, 116 [1.4]

Lima, G. H. R. A., Alencar, S. H. P., Calvet, N., Hartmann, L., & Muzerolle, J. 2010, A&A, 522, A104 [1.2.1, 1.2.2]

Luhman, K. L., Stauffer, J. R., Muench, A. A., et al. 2003, ApJ, 593, 1093 [3.3.1]

Mariñas, N., Lada, E. A., Teixeira, P. S., & Lada, C. J. 2013, ApJ, 772, 81 [1.4]

Matt, S. & Pudritz, R. E. 2005, ApJL, 632, L135 [1.2.2]

Mayor, M., Lovis, C., & Santos, N. C. 2014, Nature, 513, 328 [1]

McGinnis, P. T., Alencar, S. H. P., Guimarães, M. M., et al. 2015, A&A, 577, A11 [1.3, 1.4, 3.3.3, 3.4, 4.1, 4.2, 4.5, 4.7, 5.3]

Morales-Calderón, M., Stauffer, J. R., Hillenbrand, L. A., et al. 2011, ApJ, 733, 50 [1.4]

Morin, J., Donati, J.-F., Petit, P., et al. 2010, MNRAS, 407, 2269 [4.8]

Muzerolle, J., Calvet, N., & Hartmann, L. 2001, ApJ, 550, 944 [1.2.1]

Natta, A., Testi, L., Alcalá, J. M., et al. 2014, A&A, 569, A5 [5.1.1, 6]

O'Sullivan, M., Truss, M., Walker, C., et al. 2005, MNRAS, 358, 632 [1.3]

Palla, F. 1999, in NATO Advanced Science Institutes (ASI) Series C, Vol. 540, NATO Advanced Science Institutes (ASI) Series C, ed. C. J. Lada & N. D. Kylafis, 375 [1.1]

Palla, F. & Stahler, S. W. 1999, ApJ, 525, 772 [1.1]

Park, B.-G., Sung, H., Bessell, M. S., & Kang, Y. H. 2000, AJ, 120, 894 [3.3.1]

Pasquini, L., Avila, G., Blecha, A., et al. 2002, The Messenger, 110, 1 [2.2]

Pecaut, M. J. & Mamajek, E. E. 2013, ApJS, 208, 9 [3.3.1]

Piskunov, N. E., Kupka, F., Ryabchikova, T. A., Weiss, W. W., & Jeffery, C. S. 1995, A&AS, 112, 525 [3.3.3]

Preibisch, T., Kim, Y.-C., Favata, F., et al. 2005, ApJS, 160, 401 [1.2]

Pudritz, R. E., Ouyed, R., Fendt, C., & Brandenburg, A. 2007, Protostars and Planets V, 277 [1.2.2]

Ramírez, S. V., Rebull, L., Stauffer, J., et al. 2004, AJ, 127, 2659 [1.4, 3.1]

Randich, S., Gilmore, G., & Gaia-ESO Consortium. 2013, The Messenger, 154, 47 [2.5]

Ray, T., Dougados, C., Bacciotti, F., Eislöffel, J., & Chrysostomou, A. 2007, Protostars and Planets V, 231 [1, 1.2.2]

Rebull, L. M., Cody, A. M., Covey, K. R., et al. 2014, AJ, 148, 92 [1.4, 2.2.2]

Rebull, L. M., Makidon, R. B., Strom, S. E., et al. 2002, AJ, 123, 1528 [1.4, 3.3.1, 4.6.2]

Rigliaco, E., Pascucci, I., Gorti, U., Edwards, S., & Hollenbach, D. 2013, ApJ, 772, 60 [5.1.1, 6]

Romanova, M. M., Lovelace, R. V. E., Bachetti, M., et al. 2014, in European Physical Journal Web of Conferences, Vol. 64, European Physical Journal Web of Conferences, 5001 [4.7]

Romanova, M. M. & Owocki, S. P. 2016, Accretion, Outflows, and Winds of Magnetized Stars, ed. V. S. Beskin, A. Balogh, M. Falanga, M. Lyutikov, S. Mereghetti, T. Piran, & R. A. Treumann, 347 [1]

Romanova, M. M., Ustyugova, G. V., Koldoba, A. V., & Lovelace, R. V. E. 2009, MNRAS, 399, 1802 [1.2.1, 1.2.2]

Romanova, M. M., Ustyugova, G. V., Koldoba, A. V., & Lovelace, R. V. E. 2013, MNRAS, 430, 699 [1.2.1, 1.3, 4.7, 5.3]

Ryabchikova, T. A., Piskunov, N. E., Kupka, F., & Weiss, W. W. 1997, Baltic Astronomy, 6, 244 [3.3.3]

Samadi, R., Fialho, F., Costa, J. E. S., et al. 2006, in ESA Special Publication, Vol. 1306, ESA Special Publication, ed. M. Fridlund, A. Baglin, J. Lochard, & L. Conroy, 317 [2.1]

Shang, H., Li, Z.-Y., & Hirano, N. 2007, Protostars and Planets V, 261 [1.2.2]

Shu, F., Najita, J., Ostriker, E., et al. 1994, ApJ, 429, 781 [1.2.1]

Shu, F. H. 1977, ApJ, 214, 488 [1.1]

Siess, L., Dufour, E., & Forestini, M. 2000, A&A, 358, 593 [3.3.1, 5.2, 5.4]

Simon, M. N., Pascucci, I., Edwards, S., et al. 2016, ApJ, 831, 169 [1.2.2, 5.1.2, 5.4, 6]

Sousa, A. P., Alencar, S. H. P., Bouvier, J., et al. 2016, A&A, 586, A47 [1.4, 3.3.4, 3.3.4, 4.1, 4.5, 4.6.1, 5.3, 7]

Stauffer, J., Cody, A. M., Baglin, A., et al. 2014, AJ, 147, 83 [1.4, 3.4, 4.5]

Stauffer, J., Cody, A. M., McGinnis, P., et al. 2015, AJ, 149, 130 [1.4, 3.3.3, 3.4, 4.1, 4.1, 4.6.2]

Stauffer, J., Cody, A. M., Rebull, L., et al. 2016, AJ, 151, 60 [1.4, 3.3.3, 3.4]

Sung, H., Bessell, M. S., Chun, M.-Y., Karimov, R., & Ibrahimov, M. 2008, AJ, 135, 441 [3.1]

Sung, H., Bessell, M. S., & Lee, S.-W. 1997, AJ, 114, 2644 [1.4, 1.4, 3.3.1, 3.3.4, 4.6, 5.2]

Sung, H., Stauffer, J. R., & Bessell, M. S. 2009, AJ, 138, 1116 [1.4, 3.1]

Teixeira, P. S., Lada, C. J., Marengo, M., & Lada, E. A. 2012, A&A, 540, A83 [1.4, 4.2]

Tognelli, E., Prada Moroni, P. G., & Degl'Innocenti, S. 2011, A&A, 533, A109 [5.4]

Turner, D. G. 2012, Astronomische Nachrichten, 333, 174 [3.3.1]

Turner, N. J., Carballido, A., & Sano, T. 2010, ApJ, 708, 188 [1.2.1, 4.7]

Valenti, J. A. & Piskunov, N. 1996, A&AS, 118, 595 [3.3.1]

Venuti, L., Bouvier, J., Cody, A. M., et al. 2017a, A&A, 599, A23 [1.4, 5.4]

Venuti, L., Bouvier, J., Flaccomio, E., et al. 2014, A&A, 570, A82 [1.4, 2.2.3, 3.1, 3.2, 3.3.1, 3.2, 3.3.1, 3.1, 3.3.4, 3.3.4, 4.7, 4.18, 4.8, 5, 5.1.1, 5.2, 5.2.1, 5.4]

Venuti, L., Bouvier, J., Irwin, J., et al. 2015, A&A, 581, A66 [1.4, 4.1]

Venuti, L., Prisinzano, L., Sacco, G. G., et al. 2017b, submitted to A&A [1.4, 5.1.1, 6, 5.5]

Walker, M. F. 1956, ApJS, 2, 365 [1.4, 3.3.1]

White, R. J. & Basri, G. 2003, ApJ, 582, 1109 [3.2]

Whitney, B. A., Robitaille, T. P., Bjorkman, J. E., et al. 2013, ApJS, 207, 30 [4.2]

Zanni, C. & Ferreira, J. 2013, A&A, 550, A99 [(document), 1.5, 1.2.2, 1.3]

Zwintz, K., Moravveji, E., Pápics, P. I., et al. 2017, A&A, 601, A101 [1.4]